STUDIES ON THE STRUCTURAL AND ELECTRONIC PROPERTIES OF THIOLATE-PROTECTED GOLD NANOCLUSTERS BY X-RAY SPECTROSCOPY

by

Daniel M. Chevrier

Submitted in partial fulfilment of the requirements
for the degree of Doctor of Philosophy

at

Dalhousie University
Halifax, Nova Scotia
December 2016

Table of Contents

List of Tables

Appendix Tables

List of Figures

Appendix Figures

Abstract

Thiolate-protected gold nanoclusters (Au(SR) NCs) exhibit molecule-like properties that are both remarkable and unusual for metal-based nanoparticles. The ultra-small particle size and high stability enables Au(SR) NCs to be synthesized with atomic precision, where distinct particles have an exact composition of Au atoms and thiolate ligands. Recently, crystal structures of atomically-precise Au(SR) NCs (*e.g.*, $Au_{25}(SR)_{18}$ and $Au_{102}(SR)_{44}$) have been elucidated. This structural information enables their fascinating structure and properties to be examined in great detail, allowing for the effect of structural components, such as core, surface and metal-ligand interface, on the molecule-like properties to be addressed. Working towards this remaining challenge, experimental X-ray spectroscopy (mainly X-ray absorption spectroscopy) and supporting techniques were utilized as a suitable means to study the structure and electronic properties of Au(SR) NCs and other NC systems from an element- and site-specific perspective.

Herein, studies were devoted to understanding the effect of core structure and protecting ligands on the structure and properties of Au(SR) NCs. The influence of core size and geometry is first examined for icosahedral-based and face-centred cubic (FCC)-based Au(SR) NCs. It is shown that a difference of only a few Au atoms in the core can modulate the valence electronic structure and restructure the surface of icosahedral-based Au(SR) NCs. Au(SR) NCs with a FCC core geometry are found to have a common Au_4 core structural component that directs the molecule-like electronic properties and temperature-dependent bonding properties that are unique to FCC-based Au(SR) NCs. Examining the effect of ligand head group, structurally analogous selenolate-protected Au NCs reveal the predominate effect of Se on the electronic and bonding properties of Au NCs through more covalent Au-ligand interactions. The role of water-soluble glutathione ligands on the structure and photoluminescence of Au(SR) NCs were then investigated along with a comparison to organo-soluble Au(SR) NCs of the same composition. Finally, experimental and investigative techniques developed throughout this work were extended to study the structure and properties of protein-protected Au NCs and thiolate-protected Ag NCs.

List of Abbreviations and Symbols Used

3-D	Three-dimensional
2-D	Two-dimensional
APS	Advanced Photon Source
CLS	Canadian Light Source
CN	Coordination number
DFT	Density functional theory
DOS	Density of states
EXAFS	Extended X-ray absorption fine structure
FCC	Face-centred cubic
FT	Fourier-transformed
HCP	Hexagonal close-packed
HOMO	Highest occupied molecular orbital
IR	Infrared
LMCT	Ligand to metal charge transfer
LMMCT	Ligand to metal-metal charge transfer
LUMO	Lowest unoccupied molecular orbital
LT	Low temperature
MS	Mass spectrometry
MD	Molecular dynamics
MM	Molecular mechanics
NC	Nanocluster

NIR	Near-infrared
NP	Nanoparticle
p-MBA	*para*-mercaptobenzenoic acid
PL	Photoluminescence
QM	Quantum mechanics
QY	Quantum yield
RT	Room temperature
SeR	Selenolate
SAM	Self-assembled monolayer
SG	Glutathione
SPR	Surface plasmon resonance
SR	Thiolate
TEM	Transmission electron microscopy
UV	Ultraviolet
Vis	Visible
WT	Wavelet-transformed
XAFS	X-ray absorption fine structure
XANES	X-ray absorption near-edge structure
XRD	X-ray diffraction
XPS	X-ray photoelectron spectroscopy
E_0	Absorption edge energy
S_0^2	Amplitude reduction factor
l	Angular momentum quantum number

δ	Average spacing between valence energy levels
k_B	Boltzmann constant
R	Bond length
σ^2	Debye-Waller factor
E_F	Fermi energy
$\chi(k)$	Modulation of the photoelectron wave
k	Photoelectron wavenumber
$\mu(E)$	X-ray absorption coefficient

Acknowledgements

First, and foremost, I would like to acknowledge the support and guidance I received from Dr. Peng Zhang and Dr. Amares Chatt. I am grateful for their dedicated mentoring and for introducing me to world of nanoscience and synchrotron spectroscopy.

There were many graduate students, honours students and research assistants that came and went over the years in the Zhang group. These individuals not only contributed to my understanding of nanoparticles and synchrotron spectroscopy in some capacity, but were amazing peers and co-workers. Specifically, I have to thank Paul Duchesne, Dan Padmos, Mark MacDonald, Steve Christensen and Zac Cormier. They were excellent teachers and role models. My time as a graduate student was undoubtedly enriched by their intelligence and equally by their humour.

During the course of my PhD, my mother was working towards her PhD in English. She was a constant inspiration for me to keep working, to stay focused and to take pride in my research. My father and sister were also incredibly supportive. I thank them for always believing in me and for sending me their love over the years.

I would like to acknowledge the help and support received by fellow researchers and collaborators, beamline scientists, NSERC, faculty and staff from the Department of Chemistry at Dalhousie, coffee, the Internet, friends and additional family. Finally, I would to thank Jeremy Smith (my grade 11/12 chemistry teacher) and Dr. Fritz Grein (my first research supervisor) for kick-starting and encouraging my scientific curiosity.

Chapter 1 - Introduction

1.1 Metal Nanoparticles

A particle that has at least one length dimension between 1 to 100 nm is considered to be a nanoparticle (NP). NPs are not limited to spherical particles, they also exist in many different shapes or forms, such as rods, cubes or prisms.[1,2] They can consist of organic and/or inorganic constituents, but often have an organic surface protecting layer.[3,4] The possible combinations of shape and composition are extensive, making NPs a versatile class of materials for application across several scientific disciplines.[5–9] NPs are regarded as important materials that will hopefully advance technologies crucial to the sustainability of humankind, such as energy storage and medical technology.[7,10,11] Thus, identifying the potential of NP properties and their corresponding structures is an exciting and important area of chemical research.

As alluded to above, there are several kinds of NP compositions and structures. One main distinction is the type of material used to form the core (*i.e.*, bulk) of the NP, broadly categorized as organic (*e.g.*, polymers and lipids), inorganic (*e.g.*, mineral-based or metal-sulfide) or metal NPs (*e.g.*, transition metals). Organic and inorganic NPs are a diverse class of NP with promising applications, such as drug delivery devices and semiconducting materials for solar cells.[12,13] However, their properties do not change as dramatically as for metal NPs when the size, shape or composition is modified, nor can the surface structure and shape of organic and inorganic NPs be controlled to the same extent as metal NPs.[14] Metal NPs, on the other hand, exhibit an extensive range of optoelectronic and physicochemical properties that are scalable and sensitive to NP dimensions and composition.[8] As a result, metal NPs are promising for a broader spectrum of applications including catalysis,[15–19] nanoelectronics,[20] biomedical imaging[21,22] and therapeutic devices.[23,24]

On the nanoscale, some metals can exhibit properties that are distinct from the bulk-phase. Many of the unique physical, chemical, electronic and optical properties occur because of a high surface area-to-volume ratio and under-coordinated surface metal atoms (*e.g.*, edge or corner of a surface lattice plane).[8,25] Importantly, these properties can be further controlled or modified through the design of NP size, shape, surface structure and metal composition.[26,27] For metal-based NPs, noble metals (d^9 and d^{10} metals such as Pd, Ag, Pt and Au) have been more extensively studied in comparison to early transition metals because of their strong metallic bonding and resistance to oxidation or corrosion. Although costlier, noble metal NPs are stable and exhibit a strong response to incident light and external stimuli, making them excellent systems to study the properties of nano-sized metals.

1.1.1 Gold nanoparticles

Of the noble metals, Au is a favourable choice for NP research and developing NP applications because of its resistance to surface oxidation and general ease of NP preparation.[28] Remarkable properties of Au NPs include electrical conductivity, magnetism, strong quantum-size effects, a broad range of optical activity and biocompatibility.[28,29] Importantly, the optical, physical and electronic properties are tunable by changing the size, shape and surface morphology.[1,24,30,31]

The fascinating properties of Au NPs have been documented periodically throughout history, but one of the most significant contributions was by Faraday in 1857, when he investigated the optical properties of colloidal Au solutions.[32] Almost one hundred years later, Turkevich *et al.*[33] reported on the nucleation and growth properties of colloidal Au using transmission electron microscopy (TEM) while collecting some of the first images of Au NPs. The study of Au NPs was reinvigorated in the later part of the 20th century, when various bottom-up or solution-phase synthesis approaches reported better control over size, shape and properties.[28] For example, the Brust-Schiffrin synthesis was a monumental advancement in the solution-phase synthesis of highly stable Au NPs protected by a surface monolayer of thiolate molecules.[34] Despite the long history of Au NP research, this area continues to grow and remains a major focus in many scientific fields.[24,35–38]

1.1.1.1 Structure and properties

Although metal NPs can be produced with a "top-down" approach through physical means (*e.g.*, ball-milling),[39] "bottom-up" approaches through solution-phase chemical reactions have better control over Au NP size, shape and surface structure.[1,35] A solution-phase Au NP synthesis typically includes protecting molecules or surfactants to prevent particle aggregation, which leads to narrower particle size distributions. The surface layer of protecting molecules can also influence the properties of Au NPs and is an important consideration for the final intended application. There are several types of protecting molecules suitable for the surface passivation of Au NPs, commonly including amines, phosphines and thiols.[28,40,41] An example of a ligand-protected Au NP is presented in Figure 1.1 to generally illustrate the metal core and protecting ligand layer components. A closer look at the protecting ligand layer shows that the head group of the ligand interacts with the NP surface and the tail group is directed away from the NP surface. The tail group of the protecting molecule can range from hydrocarbon chains or branches to hydrophilic or amphiphilic molecular substituents, which provides additional protection of the Au NP surface and/or includes functionalization for interactions with other systems.[4]

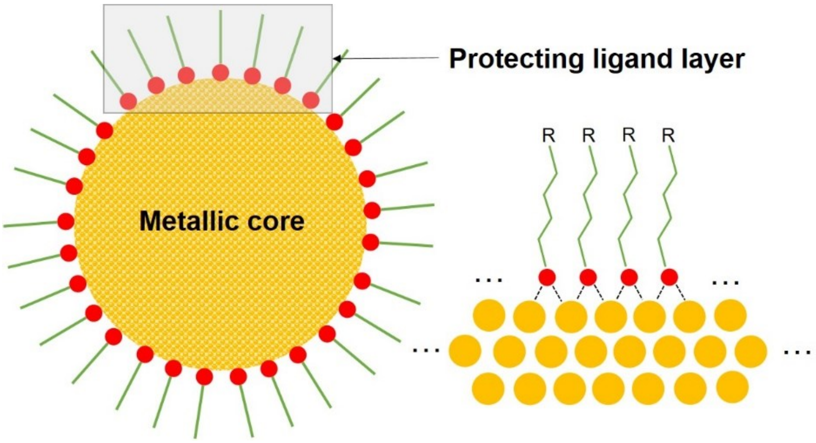

Figure 1.1 Generalized model of a ligand-protected gold nanoparticle with cross-section and surface views (metal atoms are yellow, ligand head groups are red and ligand tail groups are green lines with a functional moiety (R)).

In solution, Au NPs can interact with light to create what is known as a surface plasmon resonance (SPR). SPR occurs when Au NPs (and other noble metal NPs) absorb incident electromagnetic radiation, usually in the visible (Vis) spectrum, that induces a collective and resonant oscillation of free conduction electrons on the surface of Au NPs, creating a dipole resonance.[8] For spherical Au NPs, the SPR feature is typically seen as an intense and broad peak around 520 nm.[26] The effect of Au NP dimension and size is exemplified by comparing the SPR from spherical NPs with Au nanorods and nanoprisms.[31,42,43] For Au nanorods and nanoprisms, the SPR is red-shifted by 100 to 200 nm, depending on the aspect ratio of the nanorod or the edge length of the nanoprism.[44,45] A useful application of Au NP SPR is for surface enhanced Raman spectroscopy; when Au NPs are used as a substrate on the probe, SPR can enhance the detection of vibrational energies from small molecules.[43,44] Combining the biocompatibility of Au and Au NP surface functionalization, several biomedical applications related to diagnostics, biolabelling, photothermal therapy and drug delivery are also promising.[23,24,46]

When the diameter of Au NPs is small, around 2 to 3 nm, the SPR feature diminishes and electronic properties begin to deviate from metal particle behaviour.[47] For Au NPs of this size, the relative ratio of surface atoms to core atoms increases dramatically. Along with this decrease in Au NP size comes a drastic change in electronic properties. Semi-continuous valence bands of larger Au NPs transition to discontinuous or quantized valence energy levels. As a result, the properties of the Au particle appear more molecule-like in nature, compared to larger Au NPs. This class of ultra-small Au NPs is commonly referred to as Au nanoclusters (Au NCs).

1.2 Gold Nanoclusters

The study of Au NCs and other metal NCs has expanded the possibilities of metals on the nanoscale. Instead of size- and shape-dependent properties for Au NPs, the exact number of Au atoms per particle can have a significant influence on the properties of Au NCs. This is generally caused by the extremely small Au NC sizes (*e.g.*, Au_{13}, Au_{25}), where valence electrons reside in molecule-like electronic levels that are sensitive to structure and composition. Achieving single-sized Au NCs and other metal NCs is especially important for nanoscience and nanotechnology as it allows for important fundamental studies of structure-property relationships of metals on the nanoscale.

1.2.1 Electronic properties

Au NCs were initially examined in the gas-phase before sophisticated solution-phase syntheses were developed.[48,49] Experimental insights into the electronic properties of Au NCs were gained without surface protecting molecules or ligands. At the time, bare metal NCs were of significant interest since they existed between organometallic complexes and larger metal NPs, and also showed promise as catalysts when deposited on substrates.[50] Free and substrate-supported Au, and other metal NCs, are now widely recognized as high performance catalysts.[17,51,52] Before a deeper understanding behind the stability and electronic properties of Au NCs, however, gas-phase Na clusters were investigated to reveal remarkable order in size abundance, and electronic structure that resembled electron shell closings.[49] Select sizes of Na_n clusters were detected in higher proportions ($n = 8, 20, 40, 58$). Interestingly, it was later found that Au NCs in the gas-phase displayed similar properties with regard to stable clusters of specific size.[48]

The valence electronic structure of Au NCs is more semi-conducting or insulating in nature, compared to the semi-continuous band structure of larger Au NPs and conduction band of bulk Au. Au NCs of sufficiently small size have single-electron transitions between highest occupied molecular orbital (HOMO) and lowest unoccupied molecular orbital (LUMO) energy levels, similar to molecular systems.[53–55] This transformation in electronic structure is illustrated in Figure 1.2 and is generally explained by taking into account quantum confinement effects of electrons that appear as the particle size or the number of atoms per particle decreases. According to free electron theory, the appearance of quantum confinement effects can be approximated by calculating the average spacing between valence energy levels (δ) with the following relation,

$$\delta \approx \frac{E_F}{N} \tag{1.1}$$

where E_F is the Fermi energy of Au and N is number of gold atoms in the cluster or particle.[56] Quantum confinement effects are predicted when δ is greater than k_BT (where k_B is Boltzmann constant and T is temperature) at room temperature, which represents background thermal energy.[57] From this simple relation, these effects are apparent for Au when clusters are less than ~2 nm in diameter or less than ~170 Au atoms in size.[55] Considering Eqn. 1.1, even a small change to the Au NC size, or N in this case, can alter the valence electronic structure, affecting optical and physicochemical properties.

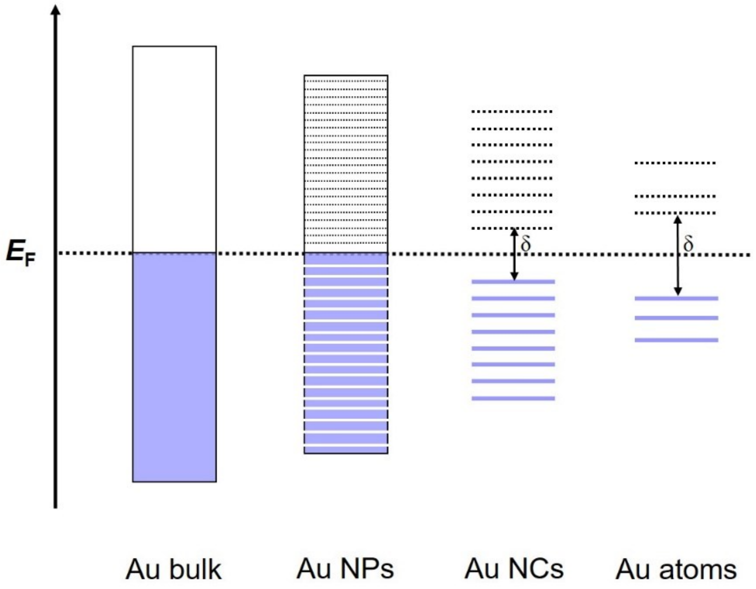

Figure 1.2 Generalized valence electronic structure for Au bulk, Au NPs, Au NCs and Au atoms, where E_F is Fermi energy and δ is the energy gap between highest occupied and lowest unoccupied levels.

The molecule-like electronic optical properties of Au NCs were suitably demonstrated with the size-dependent photoluminescence (PL) of dendrimer-protected Au NCs. Au NCs weakly protected within dendritic polymers, ranging from Au_5 to Au_{31} in size, were found to have emission energies that changed from blue to NIR when the

Au NC size increased.[58] To account for these size-dependent emissions, the electronic potential that describes the bare Au particle changes from a harmonic (Au_5) to a square well (Au_{31}) potential when the Au NC size increased.[58–60]

1.2.2 Ligand-protected gold nanoclusters

Gas-phase and weakly-protected Au NCs offered initial insights into the highly quantized electronic structure,[49] but without good surface protection their stability was extremely low or limited. Hence, ligand-protected Au NCs in condensed phases were desirable and allowed for further study and characterization. Phosphine and chloride co-protected Au NCs, $[Au_{39}(PPh_3)_{14}Cl_6]Cl_2$ and $Au_{55}(PPh_3)_{12}Cl_6$,[61,62] were some of the first ligand-protected Au NCs produced via solution-phase syntheses. Au atoms in the core of $Au_{39}(PPh_3)_{14}Cl_6]Cl_2$ (Au_{39}) were arranged in an unexpected hexagonal close-packed (HCP) structure that represented a new cluster-phase unique from the face-centred cubic (FCC) bulk-phase of Au. Au_{39} also carried an overall 2+ charge on the NC (two Cl^- counterions),[61] which demonstrated the distinct charge state property of some Au NCs. Although the structure of the metal core and surface ligand arrangement of $Au_{55}(PPh_3)_{12}Cl_6$ (Au_{55}) have not been unambiguously determined, various characterizations have suggested a two-shell cuboctahedron core (1+12+42 atom shells) for Au_{55} with an arrangement of Cl and PPh_3 ligands on surface facets, edges and corners of the Au_{55} core.[63] Notably, Au_{55} NCs showed exceptional resistance to oxidation in comparison to smaller Au NCs and larger Au NPs.[64] There was also evidence of molecule-like electronic structure with discrete valence energy levels.[65,66] However, the phosphine and chloride co-protected Au NCs suffered from low stability, low yield and difficult synthesis procedures.

A short time after the elucidation of Au_{39} and Au_{55}, the inclusion of thiolate ligands to protect the Au NC surface was demonstrated. The compositions and structures of $Au_{13}(PPh_3)_4(SR)_2Cl_2$ and $Au_{25}(PPh_3)_{10}(SR)_5Cl_2$ NCs (where SR represents an abbreviated thiolate molecule) revealed the new potential for thiolate protecting ligands and the icosahedral-based Au core geometry as a new cluster-phase.[67–69] Consistent with previous ligand-protected Au NC studies, molecule-like properties were detected using optical and electrochemical measurements.

In general, a variety of protecting ligands, such as polymers, phosphines, biomolecules and thiols,[58,70–72] have been shown to protect and stabilize the surface of Au NCs, but not all can be used to synthesize atomically-precise Au NCs with exact compositions of ligands and Au atoms. Following breakthrough in thiol self-assembled monolayers (SAMs) on Au[73–75] and the Brust-Schiffrin synthesis,[34] thiol molecules became better recognized as strong and suitable protecting ligands for Au NCs.

1.2.3 Thiolate-protected gold nanoclusters

The Brust-Schiffrin synthesis eventually became a well-known protocol for the formation of thiolate-protected Au NPs,[34] and later for thiolate-protected Au NCs. This method achieved low polydispersity of particle size, uniform particle shape and long-term stability in solution or in solid form.[76] The synthesis is a two-phase reaction (commonly toluene and water) that involves the reduction of Au(III) precursors to Au(I) and Au(0) with subsequent thiolate surface protection of the Au particle. The synthesis of atomically-precise thiolate-protected Au NCs (abbreviated as $Au_n(SR)_m$ NCs, wherein n and m denote a specific and consistent number of Au atoms and SR ligands per NC) came from developments and modifications of this synthesis protocol.

By controlling the SR:Au precursor ratio and the rate of reduction, Alvarez *et al.*[77] demonstrated that narrow size distributions of thiolate-protected Au NP and NC reaction products could be synthesized and then separated with chromatography. Discrete sizes (reported as detected masses) of $Au_n(SR)_m$ NCs were identified using mass spectrometry (MS) (*e.g.*, 93 kDa, 57 kDa, 45 kDa, 29 kDa, 8 kDa). This suggested specific sizes or compositions of $Au_n(SR)_m$ NCs were more stable than others.[78] Comparing the optical properties of each $Au_n(SR)_m$ NC product, the SPR absorption feature diminished with decreasing size, which initially demonstrated the transition of optoelectronic properties from Au NPs to Au NCs.[47] The onset of quantum confinement effects and molecule-like electronic behaviour was not fully recognized at this time, however, there was a small size distribution for each separated product, which smeared-out the absorption features for each $Au_n(SR)_m$ NC. Thus, the synthesis of single-sized $Au_n(SR)_m$ NCs was imperative in order to understand the sensitive change of optical and physical properties with size, structure and composition.

Another synthetic development for $Au_n(SR)_m$ NCs was the one-phase aqueous preparation of glutathione-protected Au NCs ($Au_n(SG)_m$ NCs).[79,80] Using polyacrylamide gel electrophoresis, discrete sizes of $Au_n(SG)_m$ NCs were separated from the reaction mixture and isolated for individual characterization, similar to the work with organo-soluble $Au_n(SR)_m$ NCs.[77] Here, Au NC sizes were identified with even better precision, ranging from $Au_{10}(SG)_{10}$ to $Au_{39}(SG)_{24}$. This allowed for careful characterization of their optical and electronic properties, which clearly displayed the molecule-like nature of $Au_n(SR)_m$ NCs. However, the synthesis yielded several sizes of $Au_n(SR)_m$ that had to be separated, and as a result the yield of each NC size was low.

To improve product yields and focus on certain $Au_n(SR)_m$ sizes without chromatographic separation, one-pot synthesis approaches were developed.[81–83] In a typical synthesis, a high SR:Au ratio was used to first produce Au(I)-SR aggregates. The conditions for mixing these aggregates and the thiolate ligand type can both have an effect on the target $Au_n(SR)_m$ NC size and structure. A strong reducing agent was then slowly added drop-wise to control the nucleation of the Au NCs. The high SR:Au ratio kept the Au(0) core sizes small and additional mixing caused $Au_n(SR)_m$ NCs of lesser stability to be destroyed or converted to the most favourable size. (Details on syntheses of $Au_n(SR)_m$ NCs studied in this thesis are presented in Section 2.5.)

1.2.3.1 Characterization and structure

Due to the 1 to 2 nm diameter size of $Au_n(SR)_m$ NCs, limitations in the imaging resolution of TEM prevent accurate and reliable determination of particle size. As a result, applying electrospray ionization and matrix-assisted laser desorption ionization MS techniques for the identification of $Au_n(SR)_m$ NCs was monumental for this research area.[84,85] From the combination of new synthesis strategies and characterization, an impressive series of $Au_n(SR)_m$ NCs have been synthesized and identified.[86–88] However, not all have been structurally characterized to understand how their properties change with composition, size, structure and ligand.

Au_{55} and SAMs of thiols on Au surfaces did offer some insight on the Au NC core structure and the ligand-metal interface on the nanoscale. However, it was uncertain whether these structures would directly translate to $Au_n(SR)_m$ NCs because of the different chemical interaction between S and Au, and extremely small core structures with a high degree of curvature. Fortunately, the total structure elucidation (*i.e.,* determination of atomic positions of Au, S and other atoms pertaining to the thiolate ligand) was achieved for some $Au_n(SR)_m$ NCs by growing crystals of a single-sized product for X-ray diffraction (XRD) measurements. This has led to a deeper understanding of thiolate-protected Au NC structure and detailed structure-property relationships.

Considered a scientific breakthrough across materials science, chemistry and physics, the crystal structures of atomically-precise $Au_{102}(SR)_{44}$, $Au_{38}(SR)_{24}$ and $Au_{25}(SR)_{18}$ were obtained within a few years of each other, which elucidated the core and surface structures of thiolate-protected Au NCs for the first time.[89–92] Several important discoveries were made from these crystal structures, including the icosahedral or decahedral core packing geometry of Au atoms and distinctive surface Au(I)-SR oligomeric capping units that defied earlier concepts of thiolate-bonding motifs (*e.g.*, on-top, bridging, and three-fold hollow site).[68,75,93,94] The elucidation of this $Au_n(SR)_m$ NC series allowed for some of the first correlations of structure (*i.e.*, structure-specific, not size-specific) with electronic and optical properties. An important finding from the crystal structure of $Au_{25}(SR)_{18}$ was the presence of a tetraoctylammonium ion (charge of 1+) in the crystal, which balanced the overall 1- charge on the $Au_{25}(SR)_{18}$ NC.[92,95] This led to a better understanding of charge states for $Au_n(SR)_m$ NCs, particularly when they are studied by electrochemical means.[82,96,97]

For a closer inspection of surface and core structure for icosahedral-based $Au_n(SR)_m$ NCs, the crystal structure[92] of $Au_{25}(SC_2H_4Ph)_{18}$ is shown in Figure 1.3. In this structure, there are 13 Au atoms arranged in a highly symmetric icosahedral core, with the remaining 12 Au atoms in 6 -SR-Au(I)-SR-Au(I)-SR- oligomer structures protecting the surface. Only one Au atom out of the 25 total Au atoms is surrounded by 12 surface Au atoms and has no interaction with thiolate ligands. The 12 Au atoms on the surface of the icosahedron have a partial Au(I) oxidation state from the electron withdrawing effect of the thiolate ligand. Au atoms interacting with two thiolate ligands on the surface in oligomer structures have a valence state of Au(I).[73,94] Because of the shape and surface-capping nature of the Au(I)-SR oligomeric components, they are referred to as “staple-like” motifs (“staples”, for short). The discovery of these surface structures on $Au_{102}(SR)_{44}$, $Au_{38}(SR)_{24}$ and $Au_{25}(SR)_{18}$ offered further explanation for the molecule-like electronic structure and remarkable stability of thiolate-protected Au NCs and possibly larger thiolate-protected Au NPs. In addition to strong metallic Au-Au bonding in the core, aurophilic interactions between Au atoms on the surface contribute to the stability and favourable geometric structure of the Au NC.[94,98]

$Au_{25}(SR)_{18}$ is one of the most thermodynamically stable compositions of $Au_n(SR)_m$ NCs.[99] It is often used as a model system for reference or to demonstrate structure-property relationships (as is done in Chapter 3 and Chapter 6). $Au_{25}(SR)_{18}$ also contains the basic structural anatomy of many $Au_n(SR)_m$ NCs. $Au_{25}(SR)_{18}$ has three distinct sites for Au atoms: centre, surface and staple. This introduces four types of Au-Au bonding that range from 2.7 to 3.5 Å; listed from shortest to longest, they are: centre-surface, surface-surface, surface-staple and staple-staple. For $Au_{25}(SR)_{18}$ NCs, the surface is stabilized by double (dimeric) staple units, exclusively, whereas $Au_{38}(SR)_{24}$ NCs is stabilized with a mixture of single (monomeric, SR-Au(I)-SR) and double staples, and $Au_{102}(SR)_{44}$ NCs have only single staples. Depending on the size of the Au core and the type of protecting thiolate, there are various combinations and configurations of Au(I)-SR oligomer surface structures possible.

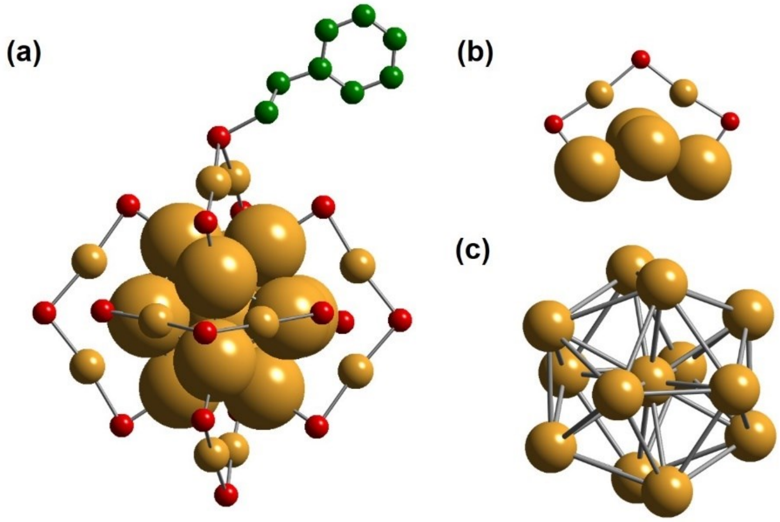

Figure 1.3 (a) $Au_{25}(SC_2H_4Ph)_{18}$ crystal structure with one complete phenylethanethiolate ligand (H atoms omitted), (b) isolated double staple structure and (c) Au_{13} icosahedral core. Au atoms are yellow, S atoms are red and C atoms are green.

Although icosahedral core structures and surface staple units consistently appeared for the first series $Au_n(SR)_m$ NC structures, the FCC-ordered core structure of $Au_{36}(SR)_{24}$ changed the architectural possibilities for the $Au_n(SR)_m$ NC framework.[100] The crystal structure for $Au_{36}(SC_6H_4C(CH_3)_3)_{24}$ is displayed in Figure 1.4 ($Au_{36}(SR)_{24}$ NCs are studied in Chapter 4). There are 28 Au atoms assembled into an FCC-ordered structure with four central Au atoms and a shell of 24 Au atoms that are surface Au sites. The surface is protected by 4 double staple units (8 Au atoms) and 12 bridging thiolates, where the thiolate ligand bonds with two surface Au atoms.

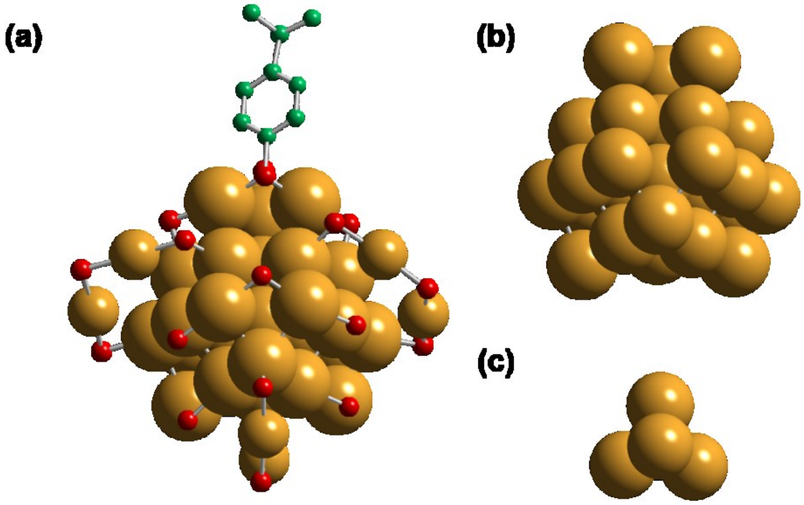

Figure 1.4 (a) $Au_{36}(SC_6H_4C(CH_3)_3)_{24}$ crystal structure with one complete bridging thiolate ligand (H atoms omitted), (b) isolated FCC-ordered Au_{28} core and (c) central Au_4 structure.

Another class of $Au_n(SR)_m$ NC structure types consist of Au_4 cluster units as the core structure. These core structures have neither icosahedral nor FCC-ordered symmetry because of their small size, and are considered as building blocks for the smallest $Au_n(SR)_m$ NC core structures (*e.g.*, $Au_{15}(SR)_{13}$ and $Au_{20}(SR)_{16}$).[101,102] With smaller core structures, longer Au(I)-SR oligomers (equivalent to triple or quadruple staple structures) interlock and/or wrap around to protect the Au core surface. These structural features have been experimentally verified for $Au_{24}(SR)_{20}$[103] and $Au_{20}(SR)_{16}$,[104] and predicted for $Au_{22}(SR)_{18}$.[105] With a variety of core structure geometries and Au(I)-SR surface protecting motifs constantly being elucidated, there is a need to identify the influence of each structural feature on the electronic and bonding properties. Importantly, the correlation between structural feature and property is possible given the study of distinct $Au_n(SR)_m$ NCs.

1.2.3.2 Gold-sulfur bonding

Although a general description of Au NC electronic structure was given in Figure 1.2, the high relative ratio of SR:Au per $Au_n(SR)_m$ NC and strong S-Au bonding have a considerable influence the electronic properties. The specific orbital interaction between S and Au occurs because of the unique Au valence electronic structure induced by relativistic effects.[106,107] These effects cause 6s and 6p orbitals to contract and the 5d orbital to expand. As a result, Au 6s and 5d orbitals become closer in energy (enabling s-d hybridization). Hybridized $3sp^3$ orbitals from S form a bond with 6s orbitals with some contribution from 5d.[108] Similar to other metal-thiolate and metal-phosphine complexes, π-π back-bonding will also transfer electron density from 5d of Au to the 3p orbitals of S.[109] Due to the covalent bonding nature of Au-S and the higher electronegativity of S, electron density is generally transferred from Au atoms on the NC surface to S. As seen from the surface structure of $Au_{25}(SR)_{18}$ and $Au_{36}(SR)_{24}$ (Figure 1.3 and Figure 1.4), there are several Au atoms with a valence state of 1+, which provides aurophilic interactions between Au atoms from closed-shell $5d^{10}$-$5d^{10}$ orbitals and further contributes to the stability of the NC.[110]

Finally, the electronic structure of $Au_n(SR)_m$ NCs is also affected by unique Au core structures or Au-Au bonding environments. Since Au atoms are not in typical FCC arrangements, other configurations of Au-Au packing and bonding can modulate the occupancy of electrons in Au valence energy levels. For example, under-coordinated Au atoms on NP surfaces or in small clusters experience less s-p-d hybridization than bulk Au, which increases the amount of electron density in the 5d valence region for Au.[111,112] Overall, the interplay from surface Au(I)-SR interactions and Au core structures affect the electronic structure of $Au_n(SR)_m$ NCs and are both examined in this thesis.

1.2.3.3 Optical properties and photoluminescence

As mentioned above, discrete electronic transitions occur between valence levels for Au NCs. Such electronic transitions are evident for $Au_n(SR)_m$ NCs as absorption features detected in the UV to the near-infrared (NIR) region.[88] Even large $Au_n(SR)_m$ NCs like $Au_{144}(SR)_{60}$ can exhibit many single-electron transitions despite having a significant metal core component, and are therefore more molecule-like than metal-like with regard to optoelectronic properties.[113] The optical and electronic properties of $Au_n(SR)_m$ NCs are sensitive to a number of factors including size and symmetry of Au core structures, Au(I)-SR surface structures and the thiolate ligand type.[88] Therefore, the absorption energy, intensity and spacing of features in the UV-Vis-NIR region will change based on the specific $Au_n(SR)_m$ NC being measured. In this regard, the absorption spectrum can be used as a diagnostic tool for determining the $Au_n(SR)_m$ NC product or monitoring the stability in solution.[88,114] An example of an absorption spectrum for $Au_{25}(SC_2H_4Ph)_{18}$ NCs is shown in Figure 1.5.

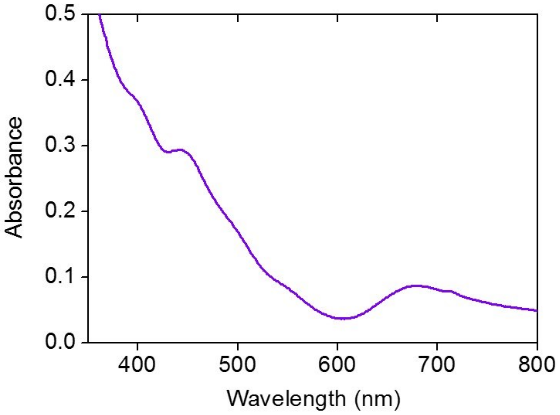

Figure 1.5 UV-Vis absorption spectrum of $Au_{25}(SC_2H_4Ph)_{18}$ NCs in toluene.

Au-S surface interactions play a significant role in stabilizing $Au_n(SR)_m$ NCs and, depending on thiolate ligand type, can influence the valence electronic structure. Density functional theory (DFT) calculations performed on $Au_{25}(SR)_{18}$ NCs have confirmed the origin of several absorption features of those seen in Figure 1.5 and determined the relative contribution of Au and S (ligand) atoms to each HOMO and LUMO energy level.[55,115] It was shown that the S 3p contribution to several HOMO-LUMO levels is significant and the selection of the stabilizing thiolate ligand can affect the electronic properties and optical properties.[95]

The PL of thiolate-protected Au NCs is distinct from larger Au NPs and polymer-protected Au NCs, which exhibit a size-dependent emission property.[116,117] Early studies on a diverse selection of thiolate-protected Au NCs demonstrated the emission energy and intensity to be independent of the core and the amount of ligand protection.[118] This suggested that the emission for Au NCs with strong thiolate ligand protection was more complicated than a simple core size-dependent property. Negeshi *et al.*[80] reported a similar composition-dependent emission property for a series of $Au_n(SG)_m$ NCs.

The role of the ligand and specific core-surface structures on the PL was examined in more detail after the structural elucidation of $Au_{25}(SR)_{18}$. Wu *et al.*[119] identified that charge transfer from the thiolate ligand to Au core via Au-S bonding and the donation of delocalized electrons to the Au core both contribute to the PL. This result supported ligand-to-metal charge transfer (LMCT) as a general concept to understand the photo-excited energy transfer mechanism for $Au_n(SR)_m$ NC PL. Furthermore, the excited state dynamics of $Au_{25}(SR)_{18}$ was studied in comparison to larger Au NCs, which revealed that relaxation from both Au core and Au(I)-SR electronic states account for emission at 500 nm and 700 nm, repsectively.[120] Although the quantum yield (QY) for

$Au_{25}(SR)_{18}$ is high for a metallic particle (QY = ~0.001%),[120] other $Au_n(SR)_m$ NCs have been synthesized with QYs of at least 5%.[103]

Rigidified or aggregated Au(I)-SR surface structures were more recently proven to account for the highly luminescent character of some $Au_n(SR)_m$ NCs. Rigidified or aggregated Au(I)-SR oligomers induce more radiative energy loss from a photo-excited state by preventing non-radiative energy loss through processes such as vibrations or rotations of Au-S bonds and thiolate ligands.[121,122] This has been observed mainly with $Au_n(SR)_m$ NCs that have a high Au(I)/Au(0) ratio and small core structure. Luo *et al.*[123] were the first to connect aggregation-induced emission with the enhanced PL of certain $Au_n(SR)_m$ NCs. Specific structural components are also responsible for the high emission property. In particular, interlocking Au(I)-SR oligomer structures have been predicted and verified for highly luminescent $Au_{22}(SG)_{18}$ (QY = 8%) and $Au_{24}(SR)_{20}$ (QY = 5%), respectively.[103,124]

The PL property of $Au_n(SR)_m$ NCs is promising for bioimaging and sensing applications. Although the QY is still lower than other fluorophores (*e.g.*, quantum dots or organic molecules), thiolate-protected Au NCs have suitable imaging properties including photo-stability, tunable emission energies and good biocompatibility.[125,126] The surface structure or ligand layer of Au NCs can be easily tailored to create targeting abilities inside a biological environment. The high emission and good biocompatibility enables Au NCs to be suitable nanomaterials as *in vivo* and *in vitro* imaging probes.[127,128] As will be discussed in Section 1.2.4, protein-stabilized Au NCs are a promising category of luminescent Au NCs for imaging and sensing applications with high QYs, good photo-physical properties and low toxicity.

1.2.3.4 Silver nanoclusters

Other noble metals have been used in combination with Au to form atomically-precise thiolate-protected metal NCs following the breakthroughs for $Au_n(SR)_m$ NCs. Metals such as Cu, Pt, Pd and Ag have all been used as dopants to modulate the electronic properties of $Au_n(SR)_m$ NCs.[129–132] However, only Ag has demonstrated the ability to form atomically-precise thiolate-protected metal NCs without the addition of Au or any other metal.[133,134] In fact, utilizing Ag over Au is becoming an increasingly active area of NC research, which may introduce another set of physical or optical properties distinct from $Au_n(SR)_m$ NCs.

Ag NPs have been investigated simultaneously with the rapid developments for Au NPs.[8,26,135] In many respects, Ag is similar to the electronic and structural properties of Au; for example, they share a similar valence electron structure configuration (*i.e.*, $d^{10}s^1$) and have almost identical bulk unit cells (*e.g.*, FCC and unit cell length of ~ 4.08 Å). Like Au NPs, Ag NPs can be synthesized with thiolate ligand protection and exhibit SPR.[136,137] However, the stability of Ag NPs is hampered by the poor resistance against tarnishing,[138] which limited their advancement alongside Au NPs.

With the rise in total structure elucidation reports for $Au_n(SR)_m$ NCs, there were very few successes in synthesizing highly stable $Ag_n(SR)_m$ NCs that could also be crystallized. This made information on structural and optoelectronic properties difficult to study. Only recently have synthetic advancements aided in discovering the first few crystal structures of atomically-precise thiolate-protected Ag NCs ($Ag_n(SR)_m$ NCs). Notable breakthroughs for $Ag_n(SR)_m$ NCs have been made with $Ag_{44}(SR)_{30}$,[133,139] $Ag_{62}S_{12}(SR)_{32}$[140] and $Ag_{25}(SR)_{18}$[134] NC systems. Though it is hard to summarize the overall structural and electronic properties of $Ag_n(SR)_m$ NCs at this point, they have general molecule-like characteristics, similar to $Au_n(SR)_m$ NCs, that distinguish them from larger Ag NPs. Single-electron transitions between HOMO-LUMO levels are evident from multiple absorption features in the UV-NIR region.[133,139] Enhanced PL, in comparison to larger Ag NPs, has also been reported.[134,141,142] There are also distinct surface capping structures that protect unique icosahedral-based and FCC-based Ag core structures. Unlike $Au_n(SR)_m$ NCs, a sulfide surface layer has been found for certain $Ag_n(SR)_m$ NCs[140] similar to larger thiolate-protect Ag NPs,[137] which may be linked to their enhanced stability. Chapter 9 investigates the coinciding research area of thiolate-protected Ag NCs by examining the $Ag_{44}(SR)_{30}$ NC system in a similar manner to $Au_n(SR)_m$ NCs.

1.2.4 Protein-protected gold nanoclusters

The crossover of biology and nanotechnology (aptly referred to as bionanotechnology) has inspired new ideas for creating nanoscale devices and sensors. Biomolecule-protected Au NPs were an early example of directly combining the properties of nanoscale metals with biological materials to create functional bionanomaterial hybrids.[6,143] Biomolecules such as oligonucleotides, peptides and proteins have demonstrated an ability to protect and stabilize relatively monodisperse Au NPs.[143,144] With certain combinations of biological molecule types and Au, and under the right experimental conditions, biomolecules can direct the self-assembly of Au NPs or Au NCs.

Peptides and other biopolymers are attractive for the synthesis of Au NPs because the amino acid or monomer unit sequence can be carefully selected or artificially created to tailor the resultant product. For instance, DNA-protected Au NPs are a prominent system for biodetection and biorecognition applications because of the programmability of DNA sequences and nucleobase pairing. For the synthesis of peptide-protected Au NPs, select amino acids have been identified as important reducing or metal-binding residues. Slocik *et al.*[145] used custom multifunctional peptides that could reduce Au^{3+} ions and assemble monodisperse Au NPs at room temperature with only mixing. A study by Tan *et al.*[146] uncovered more on the interplay between amino acid type and proximity to other neighbouring amino acids for the synthesis of Au NPs. In the case of protein-directed synthesis, there are several amino acid residue sites that can work together for particle nucleation and protection.

Unlike oligonucleotides and peptides, the tertiary structure of polypeptides or proteins can easily change conformation in response to pH or temperature, to tune the particle shape and size. Proteins such as apoferritin,[147] amylase,[148] bovine serum albumin (BSA)[149] and lysozyme[150] have been reported to protect and stabilize Au NPs. Au NP size around 2 to 3 nm in diameter was achieved for both BSA- and lysozyme-protected Au NPs, which demonstrated good control over the particle growth and adequate protection to prevent particle agglomeration. The protecting protein molecule may also have a desirable biological property that can be paired with the optical properties of the Au particle for sensing or imaging (*e.g.*, SPR or PL).

More recently, protein-protected Au NCs emerged from combined advancements of protein-protected Au NPs and $Au_n(SR)_m$ NCs. The small Au NC size of the metal component inside the protein is responsible for intense PL that is useful for imaging, sensing and drug delivery applications.[70,71,151] Importantly, QYs for protein-protected Au

NCs are 100 to 1000 times greater than some thiolate-protected Au NCs (*e.g.*, $Au_{25}(SR)_{18}$).[70,71] Additionally, the protecting protein molecule invites facile integration into biomedical applications and enhances biocompatibility. Despite the tremendous potential of protein-protected Au NCs, the formation, structure, luminescence and sensing properties of these materials still awaits deeper understanding.

Several advantages come from the biomolecular self-assembly or protein-directed synthesis of Au NCs. Unlike the two-phase synthesis for organothiolate-protected Au NPs and NCs, proteins can facilitate a facile aqueous-phase synthesis of Au NCs. The protein-directed synthesis involves mild reaction conditions with limited use of strong chemical reagents, rendering Au NPs or NCs more suitable for biological applications without harmful, or difficult to separate, by-products.

1.2.4.1 Characterization and structure

Xie *et al.*[152] were the first to publish the efficient protein-directed protocol for the synthesis of highly luminescent Au NCs. They had shown BSA could direct the formation of 1 to 2 nm diamater Au NCs (AuBSA NCs) using a green, one-pot approach. The resultant AuBSA NCs were stable over a broad pH range and for several months in solution or in lyophilized powder. The red luminescent Au NCs were first characterized using MS as $Au_{\sim 25}$ in size and possibly resembled Au_{25} metallic clusters protected by dendrimers[58] or $Au_{25}(SR)_{18}$. Soon after this seminal publication on highly luminescent AuBSA NCs, many other protein molecules were found to produce red luminescent Au NC, indicating the successful application of this approach.[70,71,153] The protein-directed synthesis has also been extended to Ag and Cu NCs,[154–156] although Au NCs are by far the most investigated system. The pH of the reaction mixture for BSA-directed and other protein-directed syntheses is typically alkaline, which allows for better metal binding and reducing potential from certain amino acid residues. Amino acid residues are able to reduce Au(III) to Au(I) and further to Au(0) if the pH conditions are adjusted to increase their reduction potential.[146,157–160] For proteins containing cysteine or cystine (two cysteine linked via disulfide), studies have indicated Au-S bonding as the crucial stabilizing interaction between protein and Au.[149,151,152,161]

In general, the structure of Au NCs inside the protecting protein is uncertain. Though some protein-protected Au NCs are expected to contain covalent Au-S interactions like the surface layer of $Au_n(SR)_m$ NCs, there is little experimental evidence that suggests Au NC structure resembles them at all. Using the size difference between pure protein and the protein-Au NC from MS measurements, reports have suggested Au NC sizes that range from Au_9 to Au_{38}.[152,161,162] X-ray photoelectron spectroscopy (XPS) analysis of the Au 4f core level have indicated the presence of both Au(0) and Au(I) with a higher relative amount of Au(0).[163,164] However, MS results suffer from noisy and broad size/charge peaks, and incident X-rays from XPS measurements or electron beams from TEM measurements have been known potentially to reduce metals or cause beam-induced damage.[165] TEM imaging capabilities are limited since the size of Au NC is below 2 nm and the electron beam can induce particle agglomeration. XRD is unhelpful for determining the structure of Au NCs inside the protein, similar to $Au_n(SR)_m$ NCs, and the growth of protein-protected Au NC single crystals is extremely unlikely. Despite limitations in these characterization techniques, Au NCs are expected to be small in size and bound to the protein molecule via Au-S interactions.

From the protein perspective, IR and circular dichroism spectroscopies have been utilized to monitor the change in protein structure or conformation after the formation of Au NCs. For larger proteins, such as BSA, human serum albumin and transferrin, small changes in the secondary conformation were observed using IR.[166–168] Circular dichroism measurements show a shift in absorption features in the UV region related to a decrease in α-helix content.[167,168] More significant changes to protein structure have been reported for smaller proteins, such as lysozyme and trypsin.[169,170] Overall, protein conformational changes have not revealed information on the Au NC structure in significant detail.

1.2.4.2 Optical properties and photoluminescence

Protein-protected Au NCs are expected to share electronic and optical properties with $Au_n(SR)_m$ NCs described in Section 1.2.3. While $Au_n(SR)_m$ NCs have multiple absorption features that span from UV to NIR depending on the structural composition, protein-protected Au NCs with red luminescence typically have a broad absorption band centred at 500 nm. This absorption feature is generally ascribed to HOMO-LUMO electronic transitions.[152] Protein-protected Au NCs with blue luminescence correspondingly have a blue-shifted absorption band, again from HOMO-LUMO transitions, that is likely related to the smaller Au NC size.[161] There are fewer reports of protein-protected Au NCs with blue luminescence compared to those with red luminescence.

The PL properties of protein-protected Au NCs are distinct from other luminescent Au NCs, such as those protected by small thiolates or dendrimers. In particular, PL decay lifetimes are shorter for thiolate-protected (10^{-8} s)[120] and dendrimer-protected (10^{-9} s)[59] Au NCs, which is related to the metallic Au core component with faster excited state relaxations. The slower excited state relaxation for protein-protected Au NCs is on the order of 10^{-6} to 10^{-7} s.[171] Protein-protected Au NCs are expected to have more covalent and molecular bonding between the Au and the protecting molecule, which could explain the difference in relaxation dynamics from stronger ligand bonding. With regard to QY, emission intensity of protein-protected Au NCs is modest, around 5 to 7 %.[70,71]

Protein-protected Au NCs have photo-physical properties suitable for imaging and sensing applications. In comparison to conventional fluorophores, such as organic molecules and lanthanide complexes, protein-protected Au NCs have a favourably large Stokes shift, good photochemical stability and resistance against photobleaching.[166,172] Protein-protected Au NCs may not be able to compete with the superior optical properties of quantum dots, but one main advantage is their biocompatibility.[127,166,173] Quantum dots may be composed of toxic metals or employ other hazardous chemicals for their synthesis, and have relatively unprotected particle surfaces that cause undesirable reactions with its surrounding environment.[174] Protein-protected Au NCs circumvent these problems with a protein-directed synthesis that involves minimal reagents and a large encapsulating protein molecule. Cytotoxicity is also lower per particle for protein-protected Au NCs having only tens of Au atoms, while quantum dots can contain several hundreds or thousands of metal atoms that have higher toxicity than Au.

Red luminescent protein-Au NCs have been shown to specifically interact with heavy transition metals like Hg and Pb, which are environmental concerns in water systems.[37,175] The interaction between protein-protected Au NCs and Hg or Pb ions is selective, occurring through metallophilic, closed-shell $5d^{10}$-$5d^{10}$ interactions (*e.g.*, Au(I)-

Hg(II)). The result of this interaction causes a luminescence quenching effect, which can be used as an analytical detection tool for certain metal ions on the nM concentration level.[176–179] The luminescence quenching property of protein-protected Au NCs has also been applied for the detection of other analytes including acetylcholine,[180] Cu(II) ions[181] and glutaraldehyde.[172]

Other potential applications for luminescent protein-protected Au NCs include biolabelling and bioimaging. An example is the combined biocompatibility, preservation of bioactivity, and luminescence of insulin-protected Au NCs for imaging purposes.[173] Insulin-protected Au NCs were successful with *in vivo* testing for regulating blood glucose levels in mice and were additionally found to be suitable agents for X-ray computed tomography. Human transferrin-protected Au NCs with red luminescence demonstrated that the protecting protein had preserved its bioactivity after the protein-directed synthesis.[166] Cell viability tests confirmed the low cytotoxicity of the human transferrin-protected Au NCs and successful cellular uptake was shown. For *in vivo* tumor targeting and imaging, BSA-protected Au NCs were reported to be an excellent candidate given the biocompatibility, imaging contrast, and enhanced permeability and retention effects.[125]

1.2.5 XAFS characterization of gold nanoclusters

The examination of structure and electronic properties for $Au_n(SR)_m$ NCs is experimentally challenging and limited. Common materials-science characterization techniques such as XRD and TEM are unsuitable due to the lack of long-range atomic order and the 1 to 2 nm particle size of Au NCs. Obtaining crystals of a $Au_n(SR)_m$ NC product and characterizing via single-crystal XRD is ideal, but often difficult to accomplish due to crystallization challenges. XPS has shown some success in characterizing the electronic properties,[182,183] however the insulating electric effect of the ligand-protected surface prevents reliable characterization.[184] X-ray absorption fine structure (XAFS) spectroscopy, on the other hand, is an invaluable tool for examining both the electronic and structural properties of metal NP and NC materials, including $Au_n(SR)_m$ NCs and related systems.[185] XAFS is unique from other characterization techniques because of the element-specific and site-specific details that can be afforded. Uniquely, structural and electronic properties can also be measured simultaneously in one spectrum. For characterizing $Au_n(SR)_m$ NCs of sufficiently small size, XAFS data can be analyzed to separately probe core, surface and metal-ligand bonding environments,[186] and can be used to monitor the structure with accurate bond distances and other structural parameters.

A few examples are presented to demonstrate the utility of XAFS spectroscopy for the study of Au NC structure and electronic properties. XAFS structural characterizations of Au NCs were reported for Au_{55} alongside its discovery.[187–189] Au L_3-edge XAFS data was used to support a cuboctahedron core over an icosahedron core for Au_{55}.[188,189] The local structure of Au_{55} was further probed by Marcus *et al.*[189] who supported the cuboctahedron core model and provided new quantitative information on Au-ligand interactions. A few years after the initial XAFS studies on Au_{55}, Menard *et al.*[190] combined high resolution TEM imaging with XAFS to confirm the low heterogeneity of $Au_{13}(PPh_3)_4(S(CH_2)_{11}CH_3)_2Cl_2$ NCs and to investigate the local structure of Au. In this study, results pointed to an icosahedral Au_{13} core and molecule-like electronic structure from the Au L_3-edge. Structural findings also determined bridging and on-top bonding modes for the protecting ligands on the surface of Au_{13}.

The experimental conditions for XAFS measurements can be modified and controlled since vacuum conditions are not required for hard X-ray XAFS experiments; this allows for the study of Au NC response to temperature, solvent and chemical additives. Au NC structural and electronic changes have been observed *in-situ* from solvent and chemical reactions.[191,192] XAFS can also be a useful tool to characterize the effects of heating and annealing, which is sometimes conduct for the preparation of Au NC catalysts.[193,194]

1.3 Motivation and Outline

1.3.1 Scientific motivation

This thesis was inspired by the structure-property relationships that are now attainable using XAFS spectroscopy in conjunction with recently elucidated $Au_n(SR)_m$ NC structures.[185,195] The combination of crystal structure information and XAFS measurements enables the structure and associated properties of $Au_n(SR)_m$ NCs (*e.g.*, electronic and optical properties) to be examined in response to protecting ligand type, core structure and/or varied experimental conditions. These structure-property relationships are of significant interest for nanotechnology and nanoscience given the potential Au NCs, and related metal NC materials, have for advancing technologies such as catalysis and biomedical imaging/sensing. Furthermore, developing an experimental approach to study the core and surface structure of $Au_n(SR)_m$ NCs would improve future investigations on monitoring chemical reactions with Au NC systems (*e.g.*, catalytic activity and ligand exchange) and aid in the structural characterization of Au NCs in complex environments (*e.g.*, protein-protected Au NCs).

Studies in this thesis were designed to uncover NC structure-specific electronic, physical and optical properties. To accomplish this, a series of atomically-precise Au NCs ($Au_{19}(SR)_{13}$, $Au_{25}(SR)_{18}$, $Au_{36}(SR)_{24}$, $Au_{28}(SR)_{20}$, $Au_{25}(SeR)_{18}$ and $Au_{18}(SR)_{14}$) and extended NC systems (BSA-protected Au NCs and $Ag_{44}(SR)_{30}$) were investigated using synchrotron-based XAFS measurements along with supporting techniques and calculations. These studies were organized into three projects. Projects I and II examined how core structure and ligand type influence the bonding, electronic and/or optical properties of $Au_n(SR)_m$ NCs, while project III employed experimental and investigative XAFS approaches utilized in the first two projects to study other NC systems. XAFS analysis methodologies for studying Au NCs of various size and structure are also developed in this thesis with the hope and intention that XAFS spectroscopy will provide future researchers with a powerful experimental tool for studying metal NC materials.

1.3.2 Thesis outline

Before presenting scientific results from each project, Chapter 2 covers the background and scientific principles behind experimental techniques and theoretical calculations used in the thesis. Experimental details more specific to each study, or from collaboration, are included in their associated chapter sections. Chapter 10 is the overall conclusion and the proposed future work related to this thesis. The following is an outline of each project and chapter:

Project I – Core Structure: Research in Chapters 3, 4, and 5 investigated the influence of core structure and core geometry on the bonding and electronic properties of

$Au_n(SR)_m$ NCs. Chapter 3 used experimental XAFS and XPS to compare the structure and electronic properties of two similar-sized $Au_n(SR)_m$ NCs with icosahedral-based core structures: $Au_{25}(SR)_{18}$ and $Au_{19}(SR)_{13}$. A multi-shell EXAFS fitting analysis previously developed for $Au_{25}(SR)_{18}$ NCs[196] was employed to probe the undetermined structure of Au_{19}, verifying theoretical structural predictions from other research.[197] This comparative X-ray spectroscopy study demonstrated how changing the $Au_n(SR)_m$ NC core structure or composition by only a few Au atoms can have a substantial effect on the structure and electronic properties of icosahedral-based $Au_n(SR)_m$ NCs.

Chapter 4 and Chapter 5 examined how the core geometry of FCC-ordered $Au_n(SR)_m$ NCs influences electronic and bonding properties. The first-ever discovered FCC-ordered $Au_n(SR)_m$ NC, $Au_{36}(SR)_{24}$, was studied in Chapter 4. Temperature-dependent XAFS revealed initial insights on how the FCC-ordered core structure directs the electronic and bonding properties in a different manner than icosahedral-based $Au_n(SR)_m$ NCs. In particular, pseudo Au_4 core structures were identified within the FCC-ordered core, which offered an explanation for their divergent bonding behaviour and electronic structure from $Au_n(SR)_m$ NCs similar in size, but with different core geometry. In Chapter 5, smaller FCC-ordered $Au_{28}(SR)_{20}$ NCs that share similar core and surface structural features with $Au_{36}(SR)_{24}$ were examined and followed-up on results from Chapter 4. $Au_{28}(SR)_{20}$ was examined with similar temperature-dependent XAFS experiments that consistently supported the role pseudo Au_4 core structures have in directing the electronic and bonding properties for FCC-ordered $Au_n(SR)_m$ NCs.

Project II – Ligand Type: In Chapter 6, the impact of ligand head group type was studied by comparing two Au_{25} NCs, one protected by phenylethanethiolate ligands

($Au_{25}(SC_2H_4Ph)_{18}$, same as in Chapter 3) and the other by benzeneselenolate ligands ($Au_{25}(SePh)_{18}$). Electronic properties and local structure of the selenolate-protected Au_{25} analog were investigated from XAFS studies at the Au L_3-edge and, for the first time, at the Se K-edge (*i.e.*, ligand's perspective). Au-Se metal-ligand bonding was shown to be more covalent than Au-S, which had a significant influence on the Au electronic structure and the Au-Au framework of Au_{25} NCs. Temperature-dependent XAFS measurements and supporting molecular dynamics (MD) simulations revealed a unique thermal contraction property that originated from the surface of $Au_{25}(SePh)_{18}$.

A subtler change in ligand type was examined by comparing cyclohexanethiolate-protected and glutathione-protected $Au_{18}(SR)_{14}$ NCs in Chapter 7. This comparison demonstrated how organo-soluble thiolate ligands and water-soluble thiolate ligands can alter the bonding properties in solid-phase and in solution-phase. The small size and high SR:Au ratio of $Au_{18}(SR)_{14}$ NCs provided an opportunity to capture solvent-ligand interactions that affect NC surface structure. The $Au_{18}(SR)_{14}$ system was also of interest as the two thiolate ligand types had different luminescence intensities despite having the same Au NC framework. A correlation of ligand-induced structural and electronic effects with the PL identified important structural conditions of glutathione-protected $Au_{18}(SR)_{14}$ that could account for its enhanced luminescence.

Project III – Extended Systems: Moving from studies on $Au_n(SR)_m$ NCs, Chapter 8 and Chapter 9 investigated two closely related Au and Ag NC systems. Chapter 8 investigated the unresolved structure of luminescent Au NCs protected by protein molecules. Bovine serum albumin-protected Au NCs were synthesized and studied with XAFS to understand their formation and Au structure inside a protein molecule. Using XAFS methodologies developed from previous studies in this thesis and additional experiments, the Au NCs were identified as interlocking gold-thiolate rings that resemble catenane molecules. This extended study highlighted the role of ligand type for directing the structure and properties of Au NCs, and provided the first report of an experimentally determined structure for protein-protected Au NCs in the known literature that also described the enhanced PL property for protein-protected Au NCs.

Chapter 9 examined the bonding properties of highly stable, thiolate-protected $Ag_{44}(SR)_{30}$ NCs. Being the first $Ag_n(SR)_m$ NC to have its core, surface and metal-ligand structure solved via single-crystal XRD, an XAFS study on $Ag_{44}(SR)_{30}$ NCs was conducted to develop some initial structure-property relationships. A fitting analysis was designed and applied to study $Ag_{44}(SR)_{30}$ NCs in solid-phase, solution-phase and in mixed solvents. The surface structure of $Ag_{44}(SR)_{30}$ was found to respond to coordinating solvents, suggesting the solvent plays a role in the unusually high stability of these thiolate-protected Ag NCs. A different mode of solvent-NC interaction was identified for coordinating solvents and $Ag_{44}(SR)_{30}$ NCs in comparison to that found in Chapter 7 for $Au_{18}(SR)_{14}$. Lastly, the stability and structural conversion of $Ag_{44}(SR)_{30}$ NCs at high temperature was investigated.

Chapter 2 - Experimental Methods

2.1 Ultraviolet-visible and Fluorescence Spectroscopy

Ultraviolet-visible (UV-Vis) spectroscopy is a useful tool for monitoring the progress of a reaction and characterizing final products. On the simplest level, a spectrophotometer detects the intensity of light before and after it has passed through a sample. The chemical species being measured will absorb light of a particular wavelength that corresponds to the energy required for an electronic transition from the ground state to an excited state. The absorbance (A) of the light for a certain chemical species is dependent on the path length (b), the molar absorptivity (ε) and the concentration (c). This relation to absorbance is known as Beer's law[198] and is shown in Eqn. 2.1.

$$A = \varepsilon bc \tag{2.1}$$

When a molecule absorbs a photon in the UV-Vis region, it undergoes an electronic transition to an excited state from the ground state. In order for the molecule to return to the ground state, the absorbed energy must dissipate through physical or electronic processes. One process is an internal conversion from the excited state back to the ground state where it will relax by transferring vibrational energy to the surroundings. This involves only vibrational relaxation with no emission of light.

Another possibility for returning to the ground state is through fluorescence or phosphorescence. Fluorescence emission is the result of a fast transition occurring from an excited state to a ground state where both states have the same spins. Phosphorescence is the result of an intersystem crossing between excited states having different spins (*i.e.* singlet to triplet). This latter process occurs on a longer time scale than fluorescence and its occurrence is relatively rare. The fluorescence or phosphorescence intensity can be calculated using Eqn. 2.2, where I is the luminescence intensity, k is a representative emission rate constant of the species being measured, P_0 is the radiant power of the excitation source, and c is the concentration of the fluorescent species.[199]

$$I = kP_0c \tag{2.2}$$

The emission efficiency of a luminescent molecule or material is sometimes needed for comparison to other systems. This value of efficiency is often calculated as the quantum yield (QY) in percent form. To calculate the QY of a sample, a comparison can be made with a fluorescent molecule standard with a known QY (*e.g.*, Rhodamine B, QY = ~95 % in ethanol). Typically, the integrated areas of the sample and standard reference emissions are calculated and compared. The absorption value at the excitation wavelength used for the sample and the standard should be equal for a valid estimate of QY for the sample.

Experimental set-ups for absorbance and fluorescence measurements are similar in nature, apart from the fact that fluorescence is detected 90° from the excitation source to collect only emission from the sample, whereas absorbance uses a linear transmission detection set-up. Figure 2.1 shows a general experimental set-up for each technique. For all UV-Vis absorption and fluorescence measurements, a suitable reference (*e.g.*, the solvent used to dissolve the sample of interest for subsequent measurement) was first measured to obtain a background signal. This signal was subtracted from the absorption or fluorescence spectrum of the sample to exclude effects from ambient light and/or imperfections in the quartz cuvette cell.

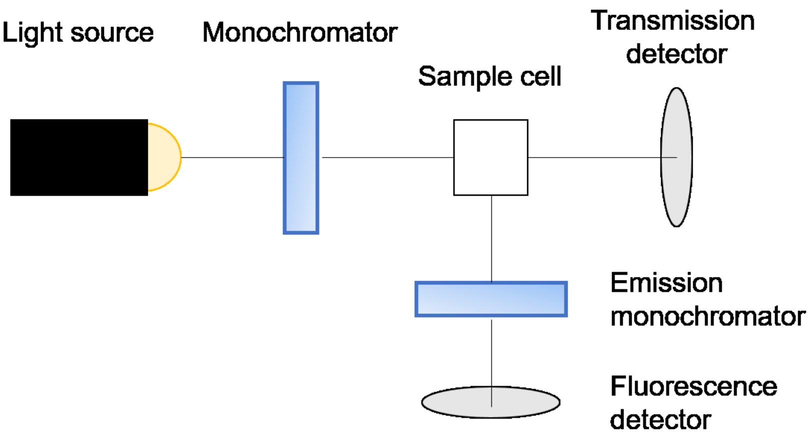

Figure 2.1 Experimental set-up for in-house UV-Vis absorption and fluorescence spectroscopy measurements.

2.2 X-ray Absorption Fine Structure (XAFS) Spectroscopy

XAFS spectroscopy is a versatile X-ray characterization technique used to investigate both the local structure and electronic properties of a material. Since XAFS is an element-specific technique, where multiple absorption edges can be measured in one sample, and even low concentrations (dopant concentration levels) can be detected and measured. With careful fitting analysis of spectra, XAFS has the ability to distinguish different bonding interactions at various distances from the absorbing atom.[200] Since XAFS is inherently a local structure characterization technique, materials that are structurally amorphous or non-crystalline can be examined. From the high energy nature of XAFS experiments, samples can be measured in experimental conditions at ambient pressure (without low-pressure conditions of a vacuum chamber), for example, in solution-phase. This versatility offers unique opportunities to study materials under application-relevant conditions.

The X-ray absorption process for obtaining XAFS spectra involves excitation, emission and scattering processes. X-ray absorption occurs when high energy incident photons excite specific core-level electrons of the desired absorbing atom, first to unoccupied valence energy levels, then into the continuum at higher excitation energies. The removal of a core-level electron leaves the system in an excited state with a time-limited core-hole.[201] Absorption edges from the excitation of 1s, 2s and 2p core levels are commonly referred to as K, L_1 and $L_{2,3}$ (two edges from spin-orbit coupling for 2p) edges, respectively. Excited core-level electrons leave the vacuum level of the absorbing atom in the form of photoelectron waves and backscatter from neighbouring atoms local to the absorbing atom. The lifetime of the photoelectron wave is limited, as is the core-hole excited state of the absorbing atom; therefore, backscattering from the nearest atoms predominates. Outgoing photoelectron waves and returning backscattered photoelectron waves interfere constructively and deconstructively over the course of the experiment. This creates modulations in the measured X-ray absorption coefficient ($\mu(E)$) over the change in incident photon energy.[202] As the incident X-ray photon energy increases during the experiment, the kinetic energy and the mean free path of the emitted photoelectron also increase, providing a greater proportion of scattering information from more distant neighbouring atoms to the absorbing atom. The X-ray absorption process is illustrated in Figure 2.2.

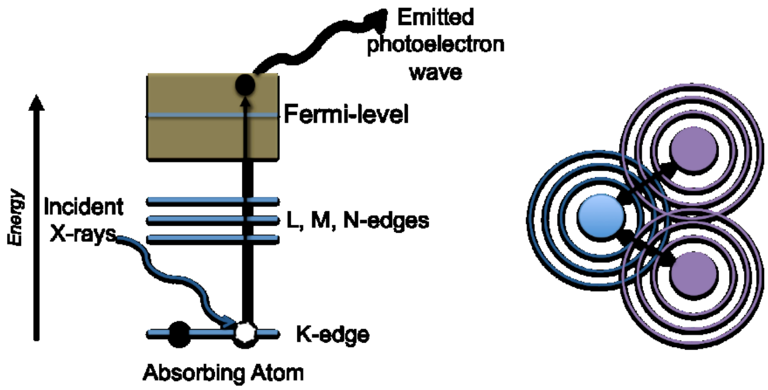

Figure 2.2 Absorption of incident X-rays above the edge energy will cause a core-level electron to be ejected (left, K-edge excitation shown for example) from the atom in the form of a photoelectron. Local surrounding atoms cause backscattering of the photoelectron wave (right) that leads to modulation in the measured X-ray absorption coefficient.

XAFS data can be collected using a variety of experimental set-ups. The general configuration for XAFS experiments conducted in this thesis is shown in Figure 2.3. In this work, transmission and fluorescence yield (FLY) detection modes were used. For transmission measurements, the following relation determines the modulation in the X-ray absorption coefficient with energy,

$$\mu(E) = \ln(\frac{I_0}{I_T}) \tag{2.3}$$

where I_0 is the incident X-ray intensity and I_T is the X-ray intensity transmitted through the sample.[202] The signal intensity before and after the sample is measured with gas ionization chambers with voltage readings for each energy point in the XAFS spectrum. A reference material (typically a metal foil) can be placed downstream from the sample, and XAFS data for this reference can be collected simultaneously using an additional ionization chamber. In a similar manner to the transmission data collection of the sample, the voltage readings before (I_T) and after (I_REF) the reference are used to plot the XAFS spectrum. Transmission measurements are typically used if the material has a high concentration of the element that is being measured. The sample thickness is important when considering transmission experiments for a concentrated sample to avoid self-absorption.

FLY detection mode is used when the concentration of the absorbing element is dilute in the bulk of the sample and if self-absorption effects are not significant. For FLY measurements, a multi-element fluorescence detector is positioned 90° to the sample. The sample is normally positioned 45° to the incident beam for FLY detection. Both X-ray fluorescence photons and Auger electrons are emitted from the sample as decay products of the core-hole, and both can be collected as a means for determining $\mu(E)$.[202] The following relationship describes the modulation of the X-ray absorption coefficient for FLY measurements,

$$\mu(E) = I_{\mathrm{FLY}}/I_0. \tag{2.4}$$

where I_{FLY} is the measured signal intensity from the multi-element fluorescence detector.[203]

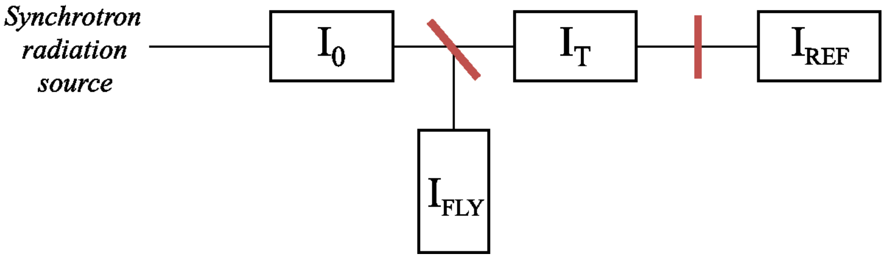

Figure 2.3 XAFS experimental set-up with sample oriented at 45° to the beam and positioned between I_0 and I_T ionization chambers. A reference sample is positioned between I_T and I_{Ref}.

2.2.1 Synchrotron and beamline facilities

Au L_3-edge (11.919 keV) and Ag K-edge (25.514 keV) XAFS data presented in this work were collected from the CLS@APS (Sector 20-BM) beamline at the Advanced Photon Source (APS), Argonne National Laboratory, IL, USA. The APS synchrotron is a third generation facility that accelerates electrons up to 7.0 GeV in energy with a beam current of 200 mA in the storage ring. Specifically, Au L_3-edge XAFS experiments were conducted at the bending magnet end-station (hence, Sector 20-BM). A Si(111) double-crystal monochromator and a Pt harmonic rejection mirror are used at Sector 20-BM to select the desired X-ray wavelengths from unfiltered synchrotron light. Ionization gases used in I_0, I_T and I_REF chambers were commonly a mix of N_2 and Ar. For X-ray fluorescence measurements, a liquid N_2-cooled 12-element detector was positioned 90° to the incident X-ray beam to collect X-ray fluorescence from the sample.

S K-edge (2.472 keV) XAFS data presented in this work was collected from the Soft X-ray Microcharacterization Beamline (SXRMB) at the Canadian Light Source (CLS), University of Saskatchewan, SK, Canada. The CLS is also a third generation synchrotron facility that can accelerate electrons up to 2.9 GeV with a maximum operating beam current of 250 mA in the storage ring. SXRMB is located at a bending magnet endstation and uses Si(111) and InSb(111) crystal monochromators to select the incident X-ray energy. For solid-phase measurements at SXRMB, samples are loaded into a vacuum chamber and pumped down to ~10^{-8} Torr. Vacuum conditions are necessary due to the lower energy of X-ray photons used for these experiments.

2.2.2 Sample preparation

NC samples were measured in either solid-phase or solution-phase. For solid-phase measurements, NCs in powdered form were either spread evenly onto kapton tape using a spatula or re-dispersed in solvent and drop-cast onto kapton film using a glass pipette. Kapton is a polyimide film that is transparent to X-rays and compatible with extreme cold and hot temperatures; thus, it is useful for preparing samples for XAFS measurements. In either case above, the NC sample must be concentrated into a small region to avoid empty space or pin holes within the sample, which would lead to noisy data. If the concentration of the absorbing element is too low for transmission data collection, the kapton film with deposited sample can be folded in order to increase X-ray absorption. For solid-phase measurements at the Au L_3-edge or Ag K-edge, prepared samples were mounted on a multi-cell sample holder and measured at ambient pressure. At lower X-ray energies, such as S K-edge, samples for solid-phase measurements were prepared by spreading the NC material onto carbon tape, which was then mounted on a Cu sample holder for measurement inside a vacuum chamber.

For solution-phase XAFS measurements, NC samples were dissolved in aqueous or organic solvents and pipetted into a teflon liquid cell with kapton film windows. Having kapton film on both sides of the cell allowed X-rays to pass through for transmission data collection, but could still be measured at 45° using a fluorescence detector positioned at 90° to the incident X-ray beam.

2.2.3 X-ray absorption near-edge structure (XANES)

There are two important regions of the XAFS spectrum to analyze: X-ray absorption near-edge structure (XANES) and extended X-ray absorption of fine structure (EXAFS). The XANES region is located around the core level absorption edge, from ~10 eV before to ~30 eV after the absorption edge, depending on the core-level transition. In this region, excited core-level electrons are promoted to low-lying valence levels, which allow for the examination of the absorbing element's valence electronic structure.[200,201,203]

A normalized XANES spectrum for a Au foil reference (bulk Au) is shown in Figure 2.4. Before the energy is high enough to excite core-level electrons from the absorbing element, there is absorption from the bulk of the material or the background that can be seen in the pre-edge region. For some K-edge XAFS spectra, pre-edge absorption features can be detected from forbidden, quadrupole transitions.[204,205] Following the pre-edge is the main absorption edge. The primary absorption peak following the absorption edge is known as the white-line. The intensity of this feature reflects the valence electron density of the allowed final state. Electronic transitions to this final state are governed by dipole-allowed transitions, which follow the selection rule,

$$\Delta l_i = \pm 1 l \tag{2.5}$$

where *l* values are angular momentum quantum numbers.[201] Taking the Au L_3-edge transition as an example, the white-line intensity is inversely proportional to the electron population of 5d orbitals and some 6s orbitals. This means high valence electron density or fully occupied valence level (*e.g.*, Au(0) in bulk Au) will yield a low white-line intensity. Near-edge features directly following the white-line are complicated by scattering of the emitted photoelectron, but can be considered in a qualitative sense to distinguish the coordination environment of the absorbing element (e.g., Au-S vs. Au-Au bonding).[203] For example, the feature at ~11.945 keV is typically seen for bulk Au or FCC-structured Au.

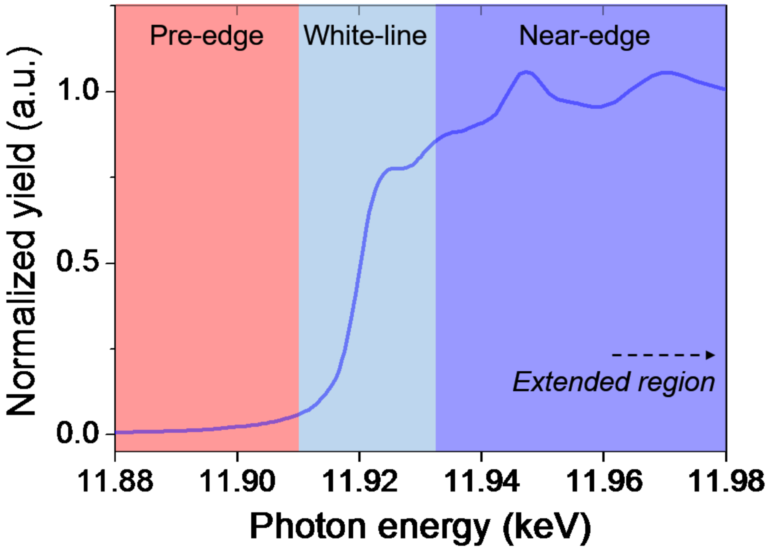

Figure 2.4 Au L_3-edge XANES of Au foil with labelled regions.

2.2.4 Extended X-ray absorption fine structure (EXAFS)

Following the XANES region, oscillations of the X-ray absorption coefficient that occur over an extended energy range can be examined to reveal fine structure information of the absorbing atom's local environment. The fine structure as a function of incident photon energy ($\chi(E)$) is determined by,

$$\chi(E) = \frac{\mu(E) - \mu_0(E)}{\Delta\mu_0(E)} \tag{2.6}$$

where $\mu(E)$ is the measured X-ray absorption coefficient of the material, $\mu_0(E)$ is the smooth background absorption of the absorbing atom in the material with no scattering effects and $\Delta\mu_0(E)$ is the absorption edge jump, where the former accounts for the difference in X-ray absorption before and after the absorption edge.[202] For EXAFS analysis, it is more appropriate to examine post-absorption edge modulations as a function of photoelectron wavenumber ($\chi(k)$). The conversion of photon energy to the photoelectron wavenumber (k) is obtained with,

$$k = \sqrt{\frac{2m(E-E_0)}{\hbar^2}} \tag{2.7}$$

where m is the electron mass, E is the incident X-ray energy, E_0 is the threshold energy or absorption edge energy and $\hbar$ is the reduced form of Planck's constant. The units of the photoelectron wavenumber are reciprocal distance (representing spatial frequency), typically expressed in inverse Angstroms (Å^{-1}). Post-edge oscillations ($\chi(k)$), presented as a function of k, make up what is known as a k-space plot.

Figure 2.5 illustrates the standard XAFS work-up procedure from raw data to k-space and R-space, the latter is also referred to as the Fourier transformed-EXAFS spectrum (FT-EXAFS). The raw data (Figure 2.5a) is first normalized by subtracting the background signal from the pre-edge and post-edge regions. The pre-edge region is typically fit with a linear polynomial and the post-edge region is fit with a linear or cubic polynomial. Once the XAFS data has been normalized (Figure 2.5b), the spectrum is energy calibrated by checking the E_0 value of a reference material (*e.g.*, Au L_3-edge of Au metal is 11.919 keV) and adjusting the energy of the data accordingly. The XAFS data is presented in Figure 2.5b as a normalized and calibrated energy spectrum, or XANES spectrum if the region around the E_0 was in focus. The next step involves conversion of energy to k-space (Figure 2.5c). From the energy spectrum or XANES, the E_0 value is found by determining the inflection point of the absorption edge, using its first or second derivative, and is assigned a value of 0 Å^{-1} in k-space. A higher degree polynomial (n^{7-9}) spline function is then used to fit through the median of the XAFS oscillations, as shown in Eqn. 2.6 as $\mu_0(E)$ (or $\mu_0(k)$ in k-space). Once an appropriate range for the $\mu_0(k)$ fit is found, XAFS oscillations are separated from pre-edge and near-edge regions. The data is now in the form of a normalized *k*-space spectrum, shown in Figure 2.5d. A *k*-weighting can be added to increase the intensity of high-*k* oscillations (Figure 2.5e), which is sometimes useful to closely examine the scattering contribution from heavier atoms or from longer-range scattering. The *k*-weighting is also important for the next transformation to *R*-space, where scattering features are directly observed. Lastly, a region of *k*-space (shown in Figure 2.5e) is Fourier transformed to yield the spectrum shown in Figure 2.5f, which is the *R*-space or FT-EXAFS. The *k*-space region selected should encompass enough fine structure or oscillations to accurately represent the local structure of the absorbing element while avoiding excessive experimental noise in the high-*k* region. The minimum *k*-range will vary depending on the sample and/or absorption edge, but a *k*-range of ~3 to 10 $Å^{-1}$ is typically required to discern two or three single scattering paths for Au L_3-edge EXAFS.

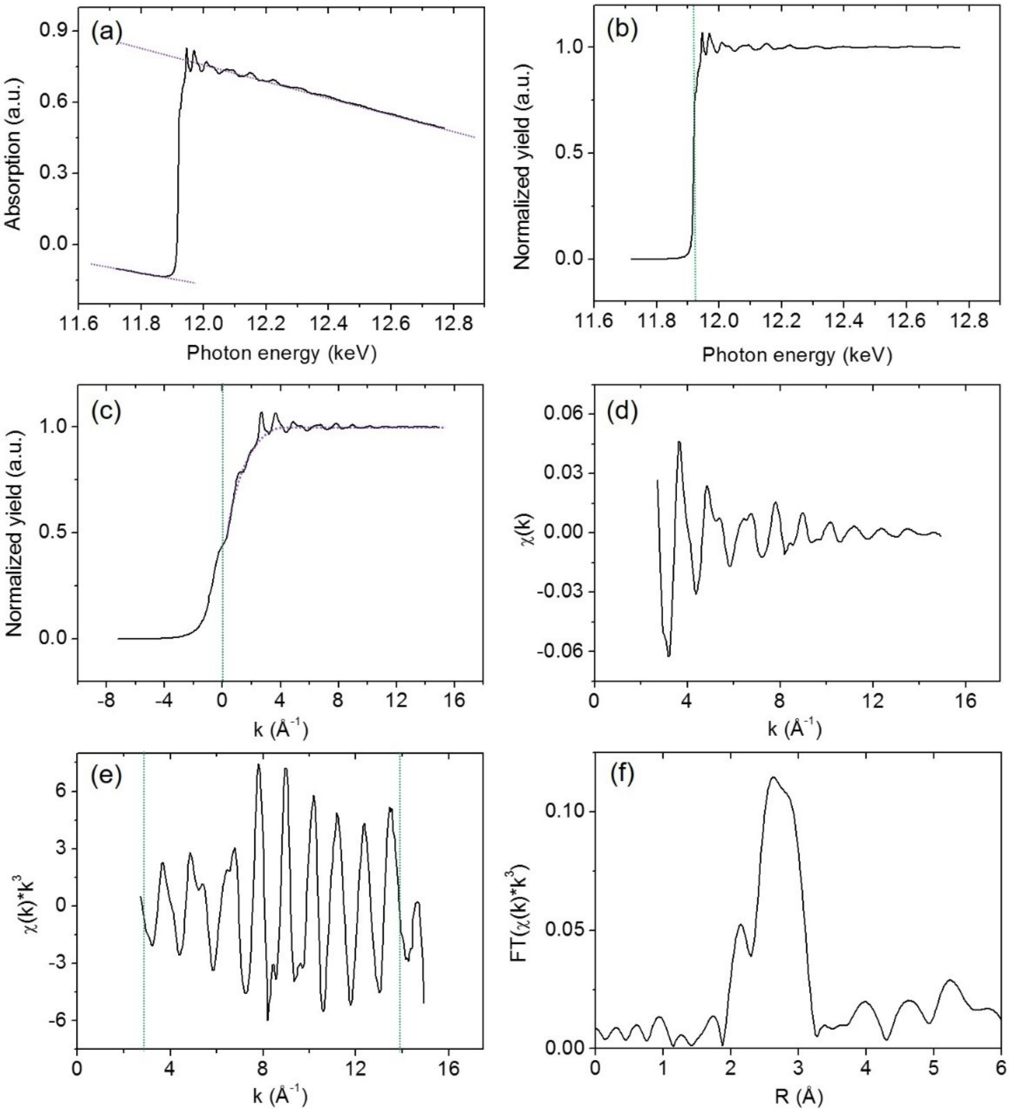

Figure 2.5 Au L$_3$-edge XAFS data work-up process for Au foil from (a) raw XAFS to (b) normalized XANES to (c,d,e) *k*-space to (f) *R*-space or FT-EXAFS. Purple dotted lines are background fitting functions and green dotted lines are for point or region selections.

To elucidate the contributions from different scattering neighbours in the measured $\chi(k)$, the *k*-space data is commonly converted to FT-EXAFS. The FT deconvolutes the measured signal to determine the scattering intensity from atoms located at various distances from the absorbing atom.[202,206,207] The resulting *R*-space plot or FT-EXAFS offers a visualization of the local structural environment. However, there are typically many single and multiple scattering paths in any given sample that complicate the features in the FT-EXAFS spectrum. Without further refinement, both k-space and R-space can offer qualitative information regarding structural properties of the sample. Another approach for understanding the structural information from XAFS was explored in Chapter 7 using wavelet-transformed EXAFS (WT-EXAFS).[208] WT-EXAFS is a two-dimensional (2-D) plot in both k-space and R-space, and is useful for separating overlapping contributions from different backscattering elements without quantitative analysis. This method helps resolve k-space features as they pertain to specific scattering features in the R-space.[209] Furthermore, this is particularly helpful for complicated systems with more than one backscattering atom type and with many single/multiple scattering features, such as $Au_n(SR)_m$ NCs.

For quantitative structural information, the EXAFS equation (described in the following section) is used to account for scattering effects and wave properties in order to refine local structural information such as bond lengths and coordination numbers.[210]

2.2.5 EXAFS fitting

To understand the origin of the EXAFS equation and how structural parameters are obtained from experimental EXAFS data, the following simple approximation is first considered,

$$\chi(k) = \frac{f(k)}{kR^2}\sin[2kR + \delta(k)] \tag{2.8}$$

where R is the radial distance to a single scattering atom, $f(k)$ is the scattering amplitude function of the scattering atom as a function of k, and $\delta(k)$ is the phase-shift function of the scattering atom as a function of k.[203] Both the scattering and phase-shift functions are specific to the scattering atom and can be determined empirically from known standard EXAFS spectra. However, *ab initio* methods are now capable of calculating these functions. The simplified approximation of the EXAFS equation assumes a spherical photoelectron wave and only one backscattering atom. Developing this approximation into a more representative EXAFS equation requires additional factors to be considered concerning the material and scattering effects.

One important factor to consider in the more complete EXAFS equation is multiple-scattering effects caused by the photoelectron wave being scattered by more than one neighbouring atom before returning to the absorbing atom. This can create problems when fitting the data in a region where multiple-scattering contributes significantly to the measured signal. Additional factors included in the EXAFS equation are the contribution from several single-scattering paths, inelastic scattering and a limited electron mean-free path. With these considerations in mind, the more complete EXAFS equation[200,202,203,206,210] can be formulated as follows:

$$\chi(k) = S_0^2 \sum_j^n CN_j \frac{e^{-2k^2\sigma_j^2} e^{-2R_j/\lambda(k)} f_j(k)}{kR_j^2} \sin[2kR_j + \delta_j(k)] \qquad (2.9)$$

where S_0^2 is the amplitude reduction factor to account for inelastic losses of the photoelectron, CN_j is the coordination number (CN) for particular scattering distance (j), σ_j^2 is the Debye-Waller factor, R_j is the scattering distance and $\lambda(k)$ is the mean-free path of the photoelectron wave. The S_0^2 parameter is determined by fitting a standard reference with known coordination, thereby allowing more accurate fitted CNs for unknown sample materials. The Debye-Waller factor accounts for the thermal and static disorder among atoms of a particular scattering shell. The Debye-Waller factor has units of Å^2, which represents the mean-squared variation in the scattering path.

It is nearly impossible to include all the possible scattering paths when fitting an EXAFS spectrum. Even if the structure of the material is known and all scattering paths can be assigned, the Nyquist criterion[211] limits the number of dependent fit parameters (CN, R, σ_j^2, and E_0 shift) that are introduced when a scattering path is incorporated into the fit. The maximum number of independent variables (N) in a given EXAFS spectrum is found with,

$$N = \frac{2\Delta k \Delta R}{\pi} \tag{2.10}$$

where Δk is the k-range used for the transformation to R-space and ΔR is the fitting window in R-space. It is desirable to have the number of dependent variables less than two-thirds the total number of independent data points. The number of independent data points can be maximized by increasing the k-range used for the Fourier transformation and by selecting a wide fitting window in the R-space. From this information, it is easy to understand that scattering paths have to be carefully selected in order to account for as much of the local structure as possible.

EXAFS fitting was conducted using the WinXAS software package. The program employs a least-squares minimization analysis (χ^2) to provide optimized EXAFS fitting parameters (CN, R, σ^2, ΔE_0) for each of the simulated scattering paths included in the fit. For Chapters 4 through 9, uncertainties in fitted EXAFS parameters were calculated using a combined approach from the Artemis EXAFS data fitting program and suggestions by Newville.[212–214] This method uses standard deviation values associated with each fit parameter from off-diagonal elements of the fit correlation matrix and weights them with a reduced χ^2 value from the EXAFS fit. The magnitude of experimental noise in the FT-EXAFS from 15 to 25 Å, and the number of independent (*N*) and dependent variables (each fitting parameter), are included in calculating the reduced χ^2 value.

2.2.6 EXAFS fitting of gold nanoclusters

EXAFS structural analysis of atomically-precise Au NCs has many advantages over other characterization techniques. This is mainly due to the fact that the EXAFS signal is averaged over all Au atoms in the NC and there are a consistent number of Au atoms in each particle, with a variety of distinct scattering or bonding environments. Unlike larger Au NPs which have the majority of seemingly identical Au bonding environments located in the bulk of the particle, Au NCs have Au environments somewhat equally distributed in the Au core, on the Au core surface and in surface protecting Au(I)-SR oligomer structures. This enables local structural information to be gained from the Au NC core, surface and the Au-ligand interface simultaneously, which is impossible to determine for larger Au NPs or with other characterization techniques since the signal from their relatively large cores obscures the signal from surface atoms.

The number of scattering shells that can be added to account for each Au bonding environment in Au NCs is still limited by the Nyquist criterion and the limited scattering range of the photoelectron wave. Nevertheless, just a few scattering shells can be employed in the EXAFS fit to account for each environment, given that there is not a substantial overlap in Au bonding distributions. This information can only be gained for Au NC structures elucidated from single-crystal XRD characterization. Inspection of each crystal structure and the spatially distinguishable bonding environments can provide the ideal CN and average bond distance for each scattering shell. Maximum resolution between EXAFS scattering shells of the same scattering neighbour type (*e.g.*, core Au-Au scattering and surface Au-Au scattering) is determined by Eqn. 2.11.

$$\Delta R = \frac{2\pi}{\Delta k} \tag{2.11}$$

CN parameters for each distinct scattering shell can be fixed to limit the number of dependent variables in the EXAFS fit. In general, given the abilities and limitations of EXAFS fitting for Au NCs, it is achievable to fit three to five scattering shells of various scattering element types and distances given that a sufficient *k*-range is collected and the experimental noise is minimized.

2.3 FEFF Calculations

The *ab initio* computational code FEFF was used to generate simulated XANES spectra and angular momentum-projected densities of states (*l*-DOS) to compare with experimental data, and to create output files of scattering functions that were used in conjunction with XAFS data analysis packages, such as WinXAS or Artemis,[212] to obtain quantitative EXAFS fitting results. In particular, the FEFF8.2 computational package was employed in this work.[200,215]

The FEFF computational code employs self-consistent energy calculations and real-space multiple-scattering Green's function calculations to simulate a variety of X-ray absorption and scattering spectra (*e.g.*, EXAFS and XANES), and to calculate electronic structure (*e.g.*, *l*-DOS).[216] FEFF calculations first determine the relativistic atomic potential of each isolated atom in a particular cluster (defined by Cartesian coordinates) by solving the Dirac-Fock equation.[217] Ground-state energy calculations include von Barth-Hedin exchange-correlation potentials.[218] Atomic potentials are then reconstructed for the cluster of atoms to yield the molecular potential by applying a muffin-tin approximation.[219] The muffin-tin approximation uses a spherically symmetric muffin-tin-like shape to account for the potential field around each atom, having a muffin-tin radius dependent on its potential. The framework of muffin-tin potentials will touch or slightly overlap, creating an interstitial region between atomic potentials. This interstitial region is approximated by a constant potential. With the molecular potential in place, a scattering potential for photoelectrons can be determined for a particular cluster of atoms. A core-hole calculation is also included to account for the change in energy levels following the excitation of a core electron in an absorption event. Green's function is used in the FEFF calculation of simulated EXAFS to handle multiple-scattering contributions, weeding out ineffective paths that do not significantly contribute to the calculation of $\mu(E)$.[216]

FEFF simulations are conducted from a site-specific approach. Instead of calculating the entire system, a sphere of neighbouring atoms around the specified atom (absorbing atom) is defined, which usually includes 30 to 50 atoms. To calculate the molecular potential of the given cluster of atoms, a self-consistent field loop is utilized to calculate the energy of the system. From here, EXAFS scattering paths and simulated XANES or *l*-DOS spectra are calculated. Using a complex plane of the Green's function, the imaginary component is related to the total electron DOS. This method of calculating the DOS avoids the costly calculation of wave functions or eigenstates. Although this approach to calculate electronic structure is not as robust as modern DFT methods, FEFF is used in this work to further inspect or interpret the electronic properties observed from XANES or XPS results. In particular, the site-specific electronic calculations using FEFF are useful to examine the contributions of various unique Au sites in $Au_n(SR)_m$ NCs.

Simulated *l*-DOS spectra from FEFF computations are used in this work to compare with experimental XPS of the valence region (Chapter 3) or with experimental XANES (Chapters 4 to 6). Although the calculated *l*-DOS spectra are more directly related to the XPS valence band data, it is useful for identifying relative contributions from orbitals or atom type to the valence electron density that may affect near-edge absorption/scattering features. FEFF simulated *l*-DOS enables the calculation of specific electron DOS contained in the valence region (*e.g.*, 5d for Au), which can aid in determining structural properties that affect valence band energy shift or narrowing.

2.4 X-ray Photoelectron Spectroscopy (XPS)

XPS is an X-ray technique widely used to study the electronic structure and atomic compositions of materials. Incident X-ray energy is used to excite both core and valence level electrons from various elements of a material into the continuum; this process is famously known as the photoelectric effect.[220] Photoelectrons emitted from a material can provide information regarding the electronic structure through determination of the original electron binding energy.

In a typical XPS experiment, the sample is placed under vacuum conditions and exposed to a monochromatic X-ray beam. When the energy of the incident X-rays is sufficient to liberate an electron from the core or valence energy levels of atoms in the sample, a photoelectron will be emitted. A detector positioned above the surface of the sample measures the kinetic energy of the emitted photoelectron. By knowing the energy of the incident X-rays ($h\nu$) and the kinetic energy (KE) of the emitted photoelectron, the binding energy (BE) from the original energy level where the electron resided can be determined. For accurate measurement and comparison with other samples, the addition of a work function term (ϕ) to the kinetic energy is required for the calculation of binding energy.[221] The work function accounts for the energy required to remove an electron from the Fermi level to the vacuum level.[221] The calculation for determining the electron binding energy is therefore,

$$BE = h\nu - (KE + \phi). \tag{2.12}$$

2.5 Gold Nanocluster Synthesis

2.5.1 Atomically-precise thiolate-protected Au NCs

The use of high-purity, single-sized Au and Ag NC products was crucial for detailed EXAFS analysis and reliable structure-property studies in this thesis. These samples were synthesized and provided by collaborators from the laboratories of Dr. Rongchao Jin (Carnegie Mellon University, Pittsburgh, PA, USA), Dr. Manzhou Zhu (Anhui University, Hefei, Anhui, P. R. China), Dr. Jiangping Xie (National University of Singapore, Singapore) and Dr. Terry Bigioni (University of Toledo, Toledo, OH, U.S.A.). These laboratories specialize in the synthesis, isolation and characterization of atomically-precise NCs using advanced chromatography and MS techniques. The characteristic UV-Vis absorption profile for each Au or Ag NC sample, which often have specific absorption features associated with core structure,[88] was measured and confirmed with previous measurements before conducting synchrotron X-ray experiments. General synthesis procedures for each Au NC studied in this thesis are briefly introduced below. Complete details on the synthesis and experimental characterization of the NC material can be found in the given references.

$Au_{19}(SR)_{13}$ (Chapter 3), $Au_{25}(SR)_{18}$ (Chapter 3, Chapter 5, Chapter 6) and $Au_{18}(SR)_{14}$ (Chapter 7) were synthesized using modified Brust-Schiffrin procedures.[81,83,222] Modified versions used careful control over the Au:SR ratio, stirring speeds, addition of reducing agent and temperature to generate $Au_n(SR)_m$ NC products of a select composition in high yield.[83] Controlling the initial aggregation conditions of Au(I)-SR intermediates was used to avoid the formation of larger particles.[81] A size-focusing or aging technique was employed to yield the most thermodynamically favoured Au NC size (*e.g.*, $Au_{19}(SR)_{13}$ in Chapter 3).[222]

$Au_n(SR)_m$ NCs can also be transformed to other compositions via ligand exchange. This procedure was used by collaborators to yield $Au_{36}(SR)_{24}$ from $Au_{38}(SR)_{24}$ (Chapter 4),[100] $Au_{28}(SR)_{20}$ from $Au_{25}(SR)_{18}$ (Chapter 5)[223] and $Au_{25}(SeR)_{18}$ from $Au_{25}(SR)_{18}$ (Chapter 6).[224] With this method, the ligand to be exchanged onto the Au NC surface was in high excess (>100 times than initial ligand) in solution. Typically, the reaction mixture was stirred for a few hours at higher temperatures (~80°C) to complete the ligand exchange. $Au_{36}(SR)_{24}$ and $Au_{28}(SR)_{20}$ NCs were formed from $Au_{38}(SR)_{24}$ and $Au_{25}(SR)_{18}$, respectively, by introducing *tert*-butylbenzenethiolate ligands, which have a more rigid molecular structure than phenylethanethiolate.[100,223] This caused reconstruction of the Au NC surface and affected the arrangement of Au atoms in the core, thereby changing the framework and composition of the $Au_n(SR)_m$ NC. $Au_{25}(SeR)_{18}$ NCs were formed using ligand exchange, but the composition and the framework were preserved.[224] This was likely due to the similar size and molecular structure of the benzeneselonolate ligand that was exchanged for phenylethanethiolate.

$Au_{18}(SG)_{14}$ (Chapter 7) and $Ag_{44}(SR)_{30}$ (Chapter 9) NCs were synthesized using aqueous and semi-aqueous methods, respectively. $Au_{18}(SG)_{14}$ NCs were synthesized in a methanol/water mixture where Au(I)-SG precursors were reduced by $NaBH_4$ at 0°C to avoid large Au particle growth.[80] No phase-transfer was needed. After the reaction was complete, the $Au_{18}(SG)_{14}$ fraction was separated with polyacrylamide gel electrophoresis, cut from the gel, further separated from the gel matrix, centrifuged and washed to obtain the final product. $Ag_{44}(SR)_{30}$ NCs were synthesized in a similar fashion using a water/dimethylsulfoxide mixture.[133] Ag(I)-SR precursors were formed in this mixture under alkaline conditions and were reduced by $NaBH_4$ with stirring. The reaction proceeded for one hour, followed by precipitation and purification.

2.5.2 Protein-protected gold nanoclusters

Protein-protected Au NCs studied in Chapter 8 were synthesized in the Zhang laboratory at Dalhousie University using a protein-directed one-pot synthesis.[71,152] The protein-directed synthesis of Au NCs involved three general steps. First, aqueous solutions of tetrachloroauric acid ($HAuCl_4$) and protein (BSA) were prepared separately and then added into the reaction vessel. Second, the reaction mixture was stirred under incubation conditions (sealed vessel at 37°C) for at least 2 min. Lastly, enough NaOH was added to the reaction mixture to produce an alkaline solution (pH 11 or 12) and then the mixture was left to react with vigourous stirring and incubation for several hours (~12 h). The final protein-stabilized Au NCs were typically luminescent in the red region of the Vis spectrum. Any small by-products such as excess metal salts were removed with dialysis. The resultant sample was stable in solution or in lyophilized powdered form for several months.

Chapter 3 - Sensitivity of Structural and Electronic Properties to the Atomic Composition: A Comparative Study of $Au_{19}(SR)_{13}$ and $Au_{25}(SR)_{18}$

Sections 3.3-3.6 are reproduced in part with permission from: Chevrier, D. M.; MacDonald, M. A.; Wu, Z.; Jin, R.; Chatt, A.; Zhang, P. Sensitivity of Structural and Electronic Properties of Gold-thiolate Nanoclusters to the Atomic Composition: A Comparative X-ray Study of $Au_{19}(SR)_{13}$ and $Au_{25}(SR)_{18}$. *J. Phys. Chem. C* **2012**, *116*, 25137-25142. Copyright 2012, American Chemical Society.

3.1 Contributions

M.A.M. conducted XAFS and XPS measurements. W. Z. synthesized and provided $Au_{19}(SR)_{13}$ and $Au_{25}(SR)_{18}$ samples. R.J. supervised W. Z.. D.M.C. analyzed XAFS and XPS data, conducted FEFF simulations and wrote the manuscript. A.C. and P.Z. supervised D.M.C. and helped revise the manuscript.

3.2 Foreword

Owing to the synthesis of truly monodisperse or single-sized Au NCs (e.g., $Au_{25}(SR)_{18}$), a meaningful understanding of structural and electronic properties can be attained for Au NCs as it relates to size and composition. This chapter utilizes XAFS and XPS techniques to investigate the change in structural and electronic properties when the $Au_n(SR)_m$ NC composition and core structure differ by only a few Au atoms and thiolate *ligands. This comparison of composition and core size was accomplished through a comparative study of* $Au_{19}(SR)_{13}$ *and* $Au_{25}(SR)_{18}$ *NCs, where SR was phenylethanethiolate for both NCs. The EXAFS fitting method used to account for multiple core and surface bonding environments was demonstrated in this first study for* $Au_n(SR)_m$ *NCs. FEFF calculations were also employed to support the interpretation of XPS valence band results. This initial investigation demonstrated the sensitivity of X-ray spectroscopy to the atomic composition, predicating its utility for proceeding chapters.*

3.3 Introduction

The isolation and purification of atomically-precise Au NCs has enabled fundamental studies that probe their unique electronic, optical and physical properties.[54,55,95,115] Uncovering the total structures of $Au_{102}(SR)_{44}$,[89] $Au_{38}(SR)_{24}$,[90] and $Au_{25}(SR)_{18}$[92,95,16] was a significant turning point when it comes to understanding the core-surface interface for Au NCs. The presence of surface staple or semi-ring units was an important insight into the distinctive surface environment of thiolate-protected Au NCs.[225,226] Being able to correlate the local structure of Au NCs with chemical and physical properties has opened up new opportunities in theoretical calculations, as well as for optical and catalysis applications.[227–229]

On the topic of uncovering the structure of newly isolated clusters, new approaches in computational chemistry have facilitated the understanding of structural evolution and structural determination of many Au NCs.[86,230,231] More recently, Jiang was able to predict the staple motif arrangement on the surface of $Au_{25}(SR)_{18}$ and $Au_{38}(SR)_{24}$ with a selection process termed “staple fitness”.[197] The only stipulation is that favourable core structures must be determined before you begin the “staple fitness” procedure. Jiang was able to use this method to predict two structural scenarios for the recently isolated $Au_{19}(SC_2H_4Ph)_{13}$ NC by Wu *et al.*[222]

Experimental determination of the local structure of Au NCs without available crystal structures can be a difficult and exhaustive process if the right characterization techniques are not available to the researcher. Alternatively, the X-ray spectroscopy approach, in association with *ab initio* calculations, has been found useful in uncovering the unique structural environment of many Au NCs.[68,182,186,190,232,233] This work aimed to use XPS and XAFS analyses to experimentally probe the structure and properties of $Au_{19}(SC_2H_4Ph)_{13}$ NCs in order to test the recently predicted structural model from Jiang[197] and to unveil the structure-electronic property relationships from a small change in Au NC composition.

3.4 Materials and Methods

The synthesis and isolation of anionic $[Au_{25}(SR)_{18}]^-$ ($Au_{25}(SR)_{18}$ is used throughout this work for simplicity) and $Au_{19}(SR)_{13}$ NCs have been reported earlier in the literature.[81,222,234]

Au L_3-edge XAFS measurements of solid-phase $Au_{19}(SR)_{13}$ and $Au_{25}(SR)_{18}$ NCs were collected in transmission mode at the Hard X-ray MicroAnalysis (HXMA) beamline of the CLS and the CLS@APS (Sector 20-BM) beamline of the APS.

XAFS data work-up, sample preparation and EXAFS fitting were conducted following the procedures outlined in Section 2.2. The $Au_{25}(SR)_{18}$ crystal structure model[92] was used to simulate scattering paths for fitting. FT-EXAFS fitting of $Au_{19}(SR)_{13}$

was performed following two separate procedures: two-shell fitting (one Au-S and one Au-Au) and multi-shell fitting (one Au-S and three Au-Au). For two-shell fitting, a short *k*-range (2.5 to 10 Å^{-1}) was found useful to minimize the contribution from long distance Au-Au bonds (*e.g.,* aurophilic bonding), thus providing more reliable information on the fitting results of the first-shell Au-Au bonding. Multi-shell fitting required a longer *k*-range of 2.5 to 11.5 Å^{-1} to incorporate the three Au-Au bonding environments. The amplitude reduction factor (S_0^2) was determined by fitting Au foil with a fixed CN of 12. A value of 0.9 was obtained and used for all EXAFS fitting. Error calculations were obtained using the double-χ^2 method.[235]

XPS measurements of the valence band were conducted at the Spherical Grating Monochromator beamline of the CLS. All samples were prepared by depositing a thin layer of NCs onto a Si(111) wafer. Samples were then loaded into the SGM vacuum chamber, operated using a 700 eV excitation energy, a base pressure of 7.5 x 10^{-10} Torr and a temperature of 85 K. Binding energy calibration was conducted using the C1s peak and Au foil reference.

l-DOS simulations of $Au_{19}(SR)_{13}$ and $Au_{25}(SR)_{18}$ were performed with the FEFF8.2 computational program. The coordinates of $Au_{19}(SR)_{13}$ were borrowed from recent literature[197] whereas coordinates for $Au_{25}(SR)_{18}$ were from its crystal structure.[95] For our simulation purposes, the thiolate molecule was simplified to a methanethiolate group instead of a phenylethanethiolate group.

3.5 Results and Discussion

3.5.1 The Au core composition of $Au_{19}(SR)_{13}$

From recent theoretical predictions of the $Au_{19}(SR)_{13}$ NC, the only two possible Au core compositions are Au_{11} or Au_{12} with a combination of single and double staple motifs on the surface (shown in Figure 3.1b and 3.1c). Scenario 1 consists of two single staples and three double staples on the Au_{11} core. Of the 13 S atoms, only 10 (4 from two single staples and 6 from three double staples) directly bind to the Au core surface, resulting in a Au_{11} core model with one Au atom in the centre and 10 Au on the surface. Scenario 2 consists of 5 single staples and one double staple on the Au_{12} core. Given that the predicted Au_{12} core model has all 12 Au atoms on the surface and no central Au site,[197] there should be 12 S atoms directly binding to the Au_{12} surface. From these structural predictions, theoretical CNs for $Au_{19}(SR)_{13}$ can be compared to our EXAFS fitting results.

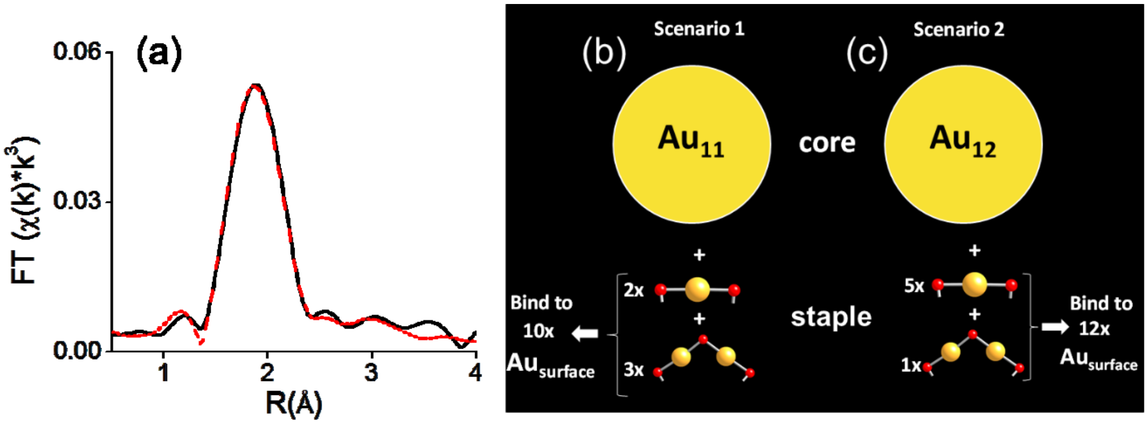

Figure 3.1 (a) Experimental FT-EXAFS of $Au_{19}(SR)_{13}$ (black line) with simulated two-shell fit (red dotted line) and structural compositions for Scenario 1 (b) and Scenario 2 (c).

The theoretical calculation for scenario 1 is as follows: Au-S CN is ((10 surface

Au atoms × one bond to S) + (8 staple Au atoms × two bonds to S)) / 19 total Au atoms = 1.37. For the first-shell Au-Au core CN, ((10 surface Au atoms × one bond to centre Au) + (one centre Au atom × 10 bonds to surface Au)) / 19 total Au atoms = 1.05. For scenario 2: Au-S CN is ((12 surface Au atoms × one bond to S) + (7 staple Au atoms × two bonds to S)) / 19 total Au atoms = 1.37, which is the same for scenario 1. For the Au-Au interaction in Au_{12}, without a centre Au the first Au-Au shell should come from the bonding between the nearest surface Au atoms. From theoretical results, the number of nearest neighbouring atoms for stable Au_{12} structures should be in the range of 4 to 5 (*i.e.* I_h, O_h, D_{5h} symmetry),[182,236] yielding a theoretical first-shell Au-Au CN = (12 surface Au atoms x 4 to 5 bonds to surface Au) / 19 = 2.5 to 3.2.

With the two proposed models for $Au_{19}(SR)_{13}$, a two-shell fitting procedure (Au-thiolate and Au-Au core bonding) was employed to determine which structural scenario was most prevalent in EXAFS fitting results (shown in Figure 3.1a). Since the calculated Au-S CN is identical for both scenarios, the resulting CN value for Au-Au core bonding was the deciding factor from two-shell fitting results. The experimental FT-EXAFS of $Au_{19}(SR)_{13}$ with simulated fit are shown in Figure 3.1a with results shown in Table 3.1. From standard two-shell fitting, a Au-S CN of 1.3(1) was obtained which corresponded with both scenarios. The Au-Au CN, however, was found to be 1.0(5) with a bond length of 2.84(6) Å. The low CN value for Au-Au indicated the presence of centre-surface bonding and supported the Au_{11} core model predicted in scenario 1. In contrast, the theoretical CN value (2.5 to 3.2) of first-shell Au-Au for scenario 2 (*i.e.*, Au_{12}) was significantly different from the experimental EXAFS results, making scenario 1 the best candidate for $Au_{19}(SR)_{13}$.

Table 3.1 Preliminary EXAFS fitting results from two-shell fitting of $Au_{19}(SR)_{13}$. Theoretical CNs are shown in bold for each scenario. Uncertainties in the fitted parameters are shown in parentheses.

Shells	CN	Scn.1	Scn.2	R (Å)	σ^2 (Å^2)	ΔE_0 (eV)
Au-S	1.3(1)	**1.37**	**1.37**	2.32(1)	0.0004(2)	-1(1)
Au-Au	1.0(5)	**1.05**	**2.5-3.2**	2.84(6)	0.012(9)	-1(1)

As can be seen from this standard two-shell fit, the difference in core composition for $Au_{19}(SR)_{13}$ can be determined from EXAFS fitting results, demonstrating the usefulness for identifying the Au core structure of thiolate-protected Au NCs. It should be noted that in Jiang's theoretical work, a total of 11 isomers were predicted for the Au_{11} scenario.[197] However, most isomers had the same number of surface (10) and centre (one) Au atoms, thus, they cannot be distinguished with EXAFS analysis, which is a limitation of EXAFS-based structural analysis on these Au NCs. To understand more on the Au-Au bonding structure of $Au_{19}(SR)_{13}$, a multi-shell fitting procedure was employed in the next section with in-depth structural comparisons with the well-known and previously studied $Au_{25}(SR)_{18}$ NC.[186] The best candidate structure for $Au_{19}(SR)_{13}$, as determined by Jiang (Figure 3.1b), is a defective icosahedral core (Au_{11}) with three double and two single staples on the surface. This model was further explored with multi-shell EXAFS fitting and discussion of the electronic properties.

3.5.2 Site-specific structural analysis of $Au_{19}(SR)_{13}$

Au L_3-edge XAFS was collected for Au foil, $Au_{25}(SR)_{18}$ and $Au_{19}(SR)_{13}$. XANES spectra are shown in Figure 3.2a, with all spectra normalized and overlapped for close comparison. There was a small difference in white-line intensity between Au NC samples. $Au_{19}(SR)_{13}$ and $Au_{25}(SR)_{18}$ both have higher white-line intensities than the bulk, indicating more d-band vacancies because of molecule-like interactions (Au(I)-SR) on the surface. Near-edge features after the absorption edge do not change significantly for both measured NCs, partly from a similar coordination environment on the NC surface.

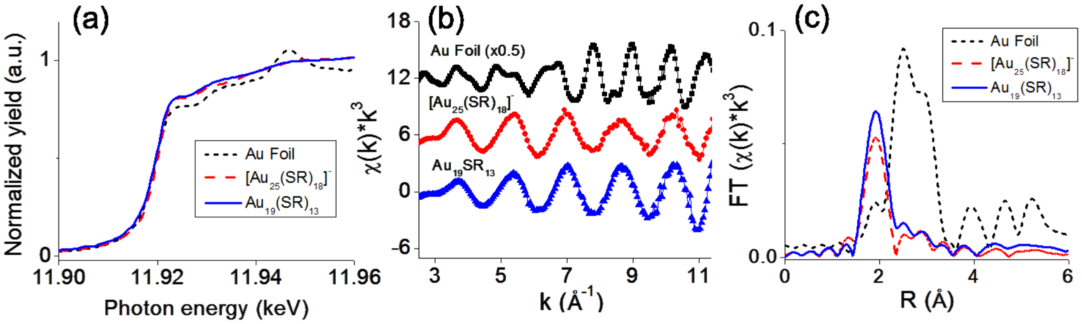

Figure 3.2 (a) XANES comparison of measured Au NCs and Au Foil reference at the Au L_3-edge. (b) *k*-space oscillations of measured Au NCs and Au Foil for reference. Spectra are vertically adjusted for comparison. (c) FT-EXAFS of Au NCs and Au Foil using a *k*-range of 2.5 to 11.5 Å^{-1}.

k-space oscillations of the measured samples are presented in Figure 3.2b with a k^3-weighting for each spectrum. Oscillations from $Au_{25}(SR)_{18}$ and $Au_{19}(SR)_{13}$ NCs were similar in frequency and position. Au foil *k*-space illustrated FCC oscillation patterns which are absent in Au NC samples due to their small core sizes. A *k*-range of 2.5 to 11.5 Å^{-1} was used for the FT-EXAFS of each sample as seen in Figure 3.2c. From a qualitative look at the FT-EXAFS spectra, $Au_{19}(SR)_{13}$ had scattering patterns similar to $Au_{25}(SR)_{18}$ with a large contribution from Au-S bonding and a multi-shell Au-Au environment.

To further probe the structure of $Au_{19}(SR)_{13}$, a Au-Au multi-shell EXAFS fitting procedure was conducted, as seen in Figure 3.3c. Fitting results from a previous study on $Au_{25}(SR)_{18}$ were included in Table 3.2 for a close comparison of Au-Au bonding with results for $Au_{19}(SR)_{13}$. The *k*-range was extended for multi-shell FT-EXAFS fitting to increase the number of total independent parameters to account for a good fit of all 4 shells. Fitting results are presented in Table 3.2, where Au-thiolate (Au-S), Au-Au centre-surface bonding (Au-Au$_1$), Au-Au surface-surface bonding (Au-Au$_2$) and long-range aurophilic bonding (Au-Au$_3$) make up the multi-shell fitting region.

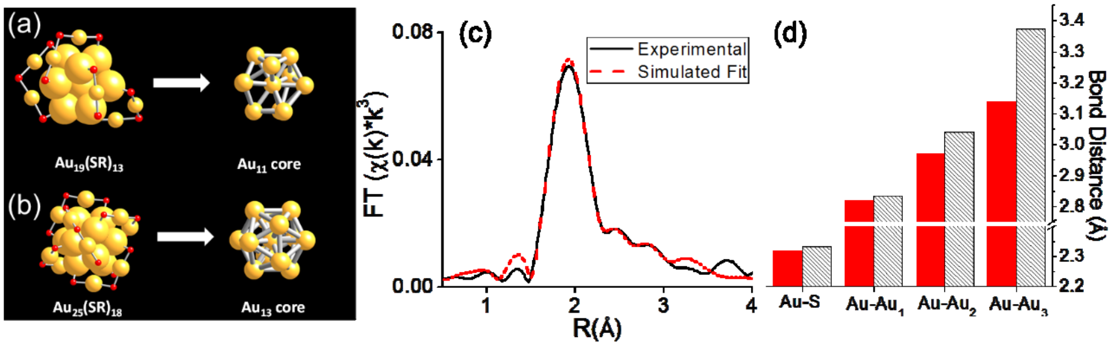

Figure 3.3 Comparison of (a) $Au_{19}(SR)_{13}$ and (b) $Au_{25}(SR)_{18}$ total structure and core structure. (c) Multi-shell EXAFS fitting of $Au_{19}(SR)_{13}$. (d) Bond distances are plotted in for close comparison between NCs, $Au_{25}(SR)_{18}$ (red) and $Au_{19}(SR)_{13}$ (black striped).

Closely comparing the bond lengths for each system in Figure 3.3d, there is little change in Au-S and centre-surface Au-Au bonding. However, it was observed that for the other two Au-Au shells, $Au_{19}(SR)_{13}$ has increasingly longer bond lengths from surface-surface to aurophilic interactions. Significantly longer Au-Au surface-surface and aurophilic bonding could be attributed to the defective icosahedral core where the structure is more relaxed and disordered than the highly symmetric icosahedral core in $Au_{25}(SR)_{18}$ NCs. From multi-shell fitting, scenario 2 was further excluded as a possible candidate since EXAFS fitting gave distinct scattering contributions to account for centre-surface and surface-surface bonding. The mixed variation of single and double staples could also promote longer aurophilic bond lengths due to vacancies on the cluster surface, affecting the capping interactions from staple units. Indeed, the determined

$Au_{19}(SR)_{13}$ NC structure (scenario 1, Figure 3.3a) is not as symmetric as its $Au_{25}(SR)_{18}$ relative, considering the defective icosahedral core and variety of surface staple units. This lack of structural symmetry could lead to variable site-specific electronic properties in $Au_{19}(SR)_{13}$.

Table 3.2 EXAFS fitting results from the multi-shell fitting procedure of $Au_{19}(SR)_{13}$ and $Au_{25}(SR)_{18}$. CNs are fixed using the theoretical values calculated from cluster models (shown in bold). E_0 shift for Au – Au shells are correlated. [a]EXAFS parameters for $Au_{25}(SR)_{18}$ were borrowed from literature.[186] Uncertainties in the fitted parameters are shown in parentheses.

		$Au_{19}(SR)_{13}$			$Au_{25}(SR)_{18}$	
Shells	CN	R (Å)	σ^2 (Å^2)	ΔE_0 (eV)	CN	R (Å)
Au – S	**1.37**	2.33(1)	0.0006(1)	1(1)	**1.44**[a]	2.32[a]
Au – Au_1	**1.05**	2.83(1)	0.004(1)	1(2)	**1.44**[a]	2.82[a]
Au – Au_2	**1.89**	3.04(2)	0.01(2)	1(2)	**1.92**[a]	2.97[a]
Au – Au_3	**1.89**	3.37(3)	0.03(1)	1(2)	**2.88**[a]	3.14[a]

3.5.3 Sensitivity of the electronic properties

Traditionally, XPS or UV photoelectron spectroscopy (UPS) valence band data have been useful to understand the size-dependent evolution of electronic properties of transition metal nanocrystals when investigating structure-property relationships. Interestingly, the two NC systems studied here, $Au_{19}(SR)_{13}$ and $Au_{25}(SR)_{18}$, have nearly the same size (~1 nm), but different composition; thus, providing an opportunity to evaluate the sensitivity of the core composition on the electronic properties of thiolate-protected Au NCs. In Figure 3.4, the valence band data is presented for $Au_{19}(SR)_{13}$ and $Au_{25}(SR)_{18}$. Elevated intensity at ~10 eV was due to background noise in both samples. A ~0.2 eV shift in higher energy is visible for d-band centroid of $Au_{19}(SR)_{13}$. This shift in higher energy is also consistent with XANES results, where $Au_{19}(SR)_{13}$ NCs have slightly higher white-line intensity (see Figure 3.2a). Negishi *et al.*[80] reported earlier that an "initial-state effect" was the main factor determining the relative band energy shift for different sizes of thiolate-protected Au NCs. In the case of $Au_{19}(SR)_{13}$, the smaller Au_{11} core could cause a slight energy shift through the "initial-state effect". Another possible explanation is the anionic form of $Au_{25}(SR)_{18}$ measured could be shifted to lower energy due to the additional negative charge resting on the cluster.

Interestingly, the valence band profile of $Au_{19}(SR)_{13}$ appears to be clearly different from that of $Au_{25}(SR)_{18}$. A sizeable d-band narrowing effect is apparent for $Au_{19}(SR)_{13}$ NCs. The smaller core of $Au_{19}(SR)_{13}$ (Au_{11} vs. Au_{13}) could explain the narrowing effect as it has been seen in previous gas phase studies of metal clusters.[48] The longer Au-Au bonding in $Au_{19}(SR)_{13}$ NCs could also contribute to this band narrowing effect. The same narrowing was also observed from d-DOS simulations of the $Au_{38}(SR)_{24}$ NC.[233] A closer inspection of the X-ray data further reveals a difference of the spectral shape, that is, the $Au_{25}(SR)_{18}$ NCs show an extra feature in the region of 2 to 3 eV, which is nearly absent in the spectrum of $Au_{19}(SR)_{13}$. Smalley *et al.*[48] has also observed a similar feature (2 to 3 eV range) for gas-phase clusters where the intensity of this feature is sensitive to the composition of the clusters such as Au_6^-, Au_8^- and Au_{20}^-. A small composition change for these gas-phase clusters can significantly change the valence band structure. These experimental findings point out that this feature is also sensitive to the core composition change of thiolate-protected Au NCs, similar to these previous observations.[48,237]

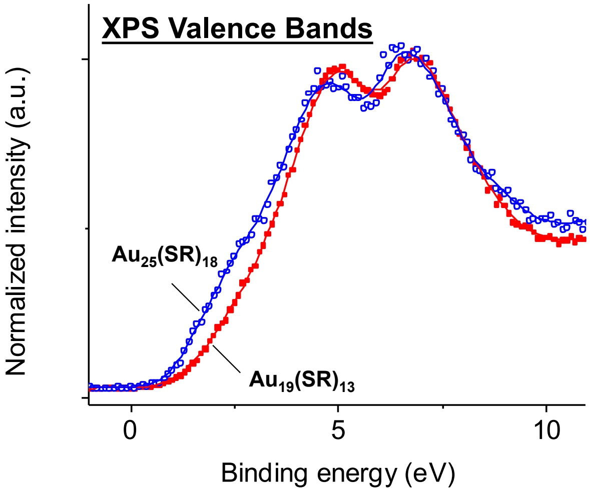

Figure 3.4 Experimental XPS valence band of $Au_{25}(SR)_{18}$ and $Au_{19}(SR)_{13}$ with lines of best fit.

To further elucidate the electronic properties of $Au_{19}(SR)_{13}$ NC from a site-specific perspective, *ab initio* calculations were performed to examine the Au 5d-projected density of states (d-DOS) from each representative atomic site. Figure 3.5a displays the calculated d-DOS from the breakdown of the $Au_{19}(SR)_{13}$ cluster into 5 unique Au sites: Au in double staple, Au in single staple, surface Au bonded to double staple, surface Au bonded to single staple and the centre Au.

A dramatic change in d-DOS was seen when comparing staple sites to other sites. The narrow d-DOS structure for surface staple sites reflects the expected molecule-like behaviour of the staple Au in the NCs. Interestingly, the surface site that bonds to double staples shows a narrower band than surface sites bonded to single staples. This observation could be reasoned by considering the arrangement of surface Au atoms on the cluster. From the predicted model, single staples are connected to surface sites adjacent to vacancies on the defective icosahedral core. From d-DOS calculations, the

$Au_{19}(SR)_{13}$ NC appears to have electronic properties that significantly change from site to site in the cluster, which could offer potential opportunities for catalytic application.

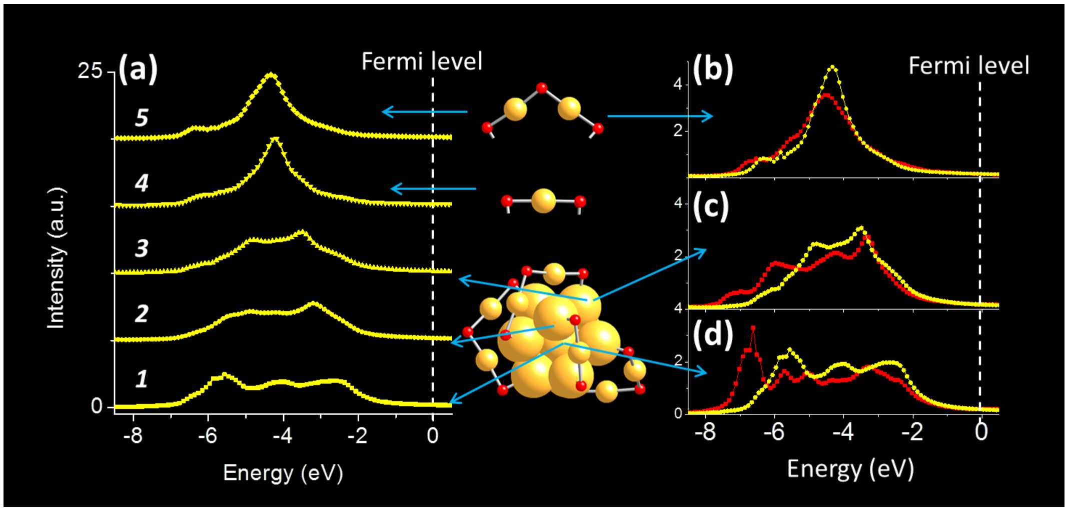

Figure 3.5 (a) FEFF simulated d-DOS of the $Au_{19}(SR)_{13}$ NC from a site-specific perspective. d-DOS simulations comparing identical sites on both $Au_{19}(SR)_{13}$ (yellow) and $Au_{25}(SR)_{18}$ (red) NCs for (b) double staple Au, (c) surface Au bonded to double staple and (d) centre Au. All spectra are calibrated to their own calculated Fermi energy.

Comparative results of the d-DOS shape of the double-staple Au, surface Au (binding to the double-staple) and the centre Au site from $Au_{19}(SR)_{13}$ and $Au_{25}(SR)_{18}$ are provided in Figure 3.5b, c and d, respectively. Simulated d-DOS of $Au_{25}(SR)_{18}$ were reproduced from previous work.[226] It is clear that the d-DOS of the surface and centre Au sites from $Au_{25}(SR)_{18}$ are broadened compared to the corresponding Au sites from $Au_{19}(SR)_{13}$. This observation can be interpreted by the difference in the defective Au_{11} core structure for $Au_{19}(SR)_{13}$, which has less Au-Au bonding interactions than the Au_{13} core in $Au_{25}(SR)_{18}$.

3.6 Conclusion

In conclusion, a series of findings have been presented on the unique structural and electronic properties of the thiolate-protected Au NC, $Au_{19}(SR)_{13}$, based on X-ray spectroscopy experiments and *ab initio* calculations. Important experimental results include (i) supporting evidence of the structural model of $Au_{19}(SR)_{13}$ predicted by the "staple fitness" method, (ii) increased bond length for surface-surface and aurophilic Au-Au bonds and (iii) sensitivity of Au 5d band structure of the two examined NCs to the atomic composition revealed by XPS and *ab initio* calculations. These findings highlight the sensitivity of the local structure and electronic behaviour of thiolate-protected Au NCs to even a small change of the metal core from Au_{13} to Au_{11}, and point out the significance of the "composition effect" in the regime of small thiolate-protected Au NCs instead of the "nano-size effect" widely used for regular nanoscale materials.

Chapter 4 - Electronic and Bonding Properties of Thiolate-protected Gold Nanoclusters with FCC Core: $Au_{36}(SR)_{24}$ (Part I)

Sections 4.3-4.6 are reproduced in part with permission from: Chevrier, D. M.; Chatt, A.; Zeng, C.; Jin, R.; Zhang, P. Unique Bonding Properties of the $Au_{36}(SR)_{24}$ Nanocluster with FCC-like Core. *J. Phys. Chem. Lett.* **2013**, *4*, 3186-3191. Copyright 2013, American Chemical Society.

4.1 Contributions

C.Z. synthesized and provided the $Au_{36}(SR)_{24}$ NC sample. R.J. supervised C.Z.. D.M.C. collected all XAFS data, conducted FEFF calculations, performed all data analyses and wrote the manuscript. P.Z. and A.C. supervised D.M.C. and helped revise the manuscript.

4.2 Foreword

The previous chapter examined how core size and composition alter the framework and electronic properties of icosahedral-based $Au_n(SR)_m$ NCs. The influence of core structure or core geometry on the electronic and bonding properties was then investigated for $Au_n(SR)_m$ NCs with FCC-ordered core structures. This chapter examines the $Au_{36}(SR)_{24}$ NC, which has a Au_{28} core with distinct FCC-ordered packing, using Au and S XAFS measurements in conjunction with ab initio simulations. Elucidated from this *study were the unique bonding properties of $Au_{36}(SR)_{24}$ to provide an understanding of how icosahedral- and FCC-based $Au_n(SR)_m$ NCs could be distinguished.*

4.3 Introduction

It was only recently shown that an FCC-ordered core and bridging thiolate structures could exist for $Au_n(SR)_m$ NCs when Zeng *et al.*[100,238] demonstrated that $Au_{38}(SR)_{24}$ NCs can be transformed into $Au_{36}(SR)_{24}$ NCs through a ligand-exchange process, with resultant successful single crystal growth of $Au_{36}(SR)_{24}$ NCs. The structure of $Au_{36}(SR)_{24}$ consists of an FCC-like Au_{28} core with 12 bridging thiolates (12 x -S(R)-) and 4 dimeric staple motifs (4 x (-S(R)-Au-S(R)-Au-S(R)-). The structural transformation dramatically changes the core:staple Au ratio, going from 23:15 for $Au_{38}(SR)_{24}$ to 28:8 for $Au_{36}(SR)_{24}$, via a disproportionation mechanism.[238] It was also demonstrated that $Au_{25}(SR)_{18}$ NCs could undergo a similar ligand-exchange induced transformation to form $Au_{28}(SR)_{20}$ NCs with an FCC-ordered core, also with a mixture of bridging and staple motifs.[239] A remarkable finding for $Au_{36}(SR)_{24}$ was the increase in the optical gap from 0.9 eV ($Au_{38}(SR)_{24}$) to 1.7 eV ($Au_{36}(SR)_{24}$). This difference in optical gap would also lead to the assumption that the electronic properties of $Au_{36}(SR)_{24}$ are more molecule-like than $Au_{38}(SR)_{24}$, despite having an FCC-ordered core. Therefore, these latest discoveries of an FCC-ordered core pose an interesting question about the effect of the core on the bonding properties and electronic structure of $Au_n(SR)_m$ NCs. In particular, how does the FCC-ordered core behave in relation to icosahedral-based core structures found for other $Au_n(SR)_m$ NCs such as $Au_{25}(SR)_{18}$ or $Au_{38}(SR)_{24}$?

The remarkable bonding and electronic properties of $Au_{36}(SR)_{24}$ were investigated using XAFS and *ab initio* calculations. Comparisons were drawn to $Au_{38}(SR)_{24}$ NCs as they have an almost identical composition to $Au_{36}(SR)_{24}$, but contrasting structural properties such as icosahedral versus FCC cores and staple versus bridging motifs. The Au_{28} FCC-ordered core is highlighted in this work as the structural and electronic properties are studied from a site-specific perspective. Results revealed smaller pseudo-Au_4 units within the core largely contribute to the molecule-like electronic properties of $Au_{36}(SR)_{24}$, which was consistent with the experimental findings from Au L_3-edge XANES and temperature-dependent EXAFS. The role of the Au-S bonding motif on the electronic properties was also examined from the S perspective using S K-edge XANES and *ab initio* calculations.

4.4 Materials and Methods

Synthetic procedures for the preparation of $Au_{38}(SC_2H_4Ph)_{24}$ (abbreviated here as Au_{38}) and $Au_{36}(SC_6H_4C(CH_3)_3)_{24}$ (abbreviated here as Au_{36}) NCs have been published elsewhere.[82,100] Both syntheses produced Au NCs in high purity suitable for detailed XAFS studies.

Au L_3-edge XAFS measurements were collected in transmission mode at the CLS@APS beamline (Sector 20-BM) of the APS. Au_{36} was measured at both low temperature (90 K) and room temperature (295 K) in the solid-phase. S K-edge XAFS measurements were collected for solid-phase Au_{36} in fluorescence mode at the soft X-ray micro-characterization beamline (SXRMB) of the CLS. XAFS data work-up, sample preparation, EXAFS fitting and error analysis were conducted following the procedures outlined in Section 2.2. High quality XAFS oscillations were collected up to 16 Å^{-1} in *k*-space for Au_{36} (Figure 4.1). A *k*-range of 3.0 to 13.7 Å^{-1} was used for FT-EXAFS spectra. EXAFS fitting of Au_{36} spectra required three shells (one Au-S and two Au-Au) to fit an *R*-window of 1.5 to 3.1 Å. Upon inspection of the $Au_{36}(SR)_{24}$ crystal structure,[100] two distributions of Au-Au bonding were visible with the first being a narrow distribution of short Au-Au bonds < 2.89 Å and the second a broader distribution of longer Au-Au bonds > 2.89 Å (Figure 4.2). It can be seen that the first Au-Au shell (Au-Au_1) accounts for short Au-Au cluster bonding in the core while the second Au-Au shell (Au-Au_2) is from Au-Au bonding closer to the surface.

Simulated XANES and *l*-DOS spectra were calculated using the FEFF8.2 computational program.[216] The hydrocarbon substituent of each thiolate ligand was simplified with a methyl group for simulation purposes.

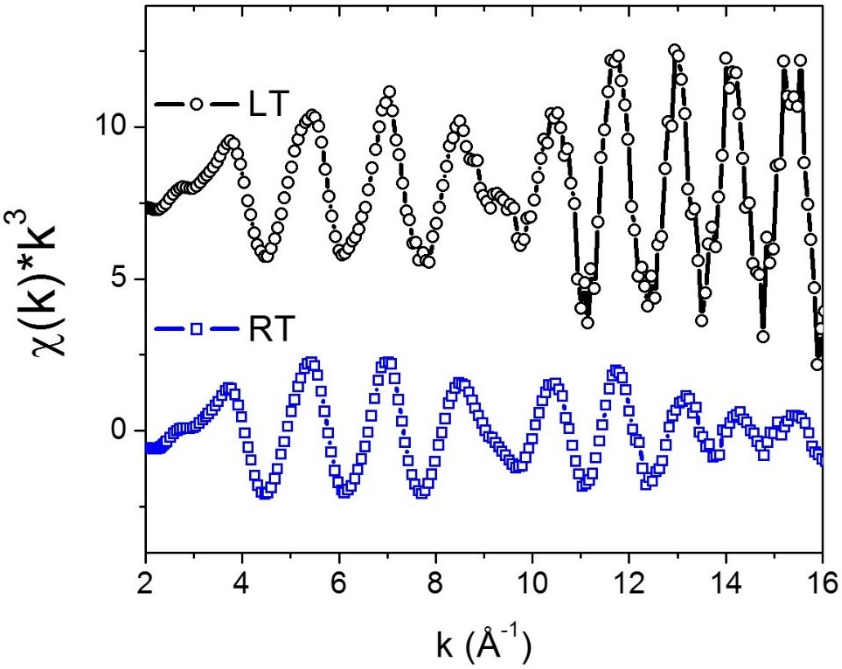

Figure 4.1 Experimental *k*-space spectra of Au_{36} at low temperature (LT, 90 K) and room temperature (RT, 295 K).

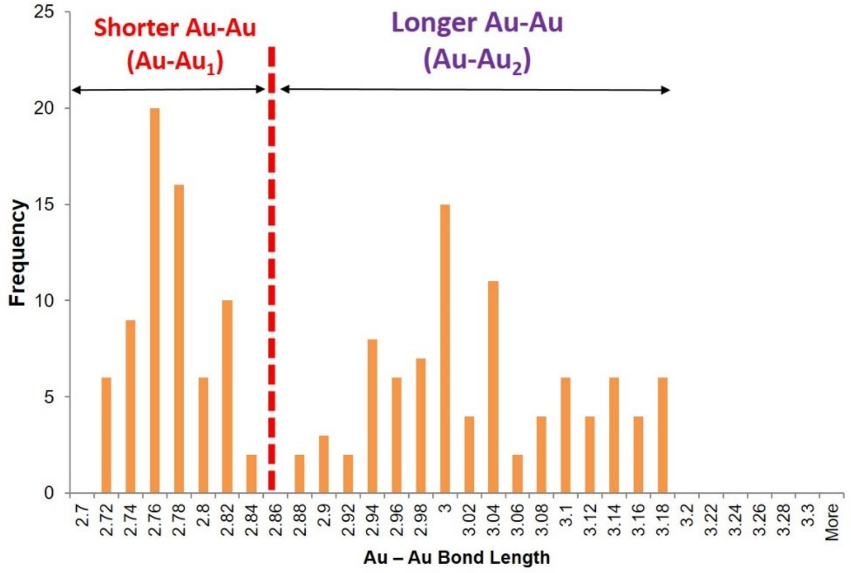

Figure 4.2 Distribution of Au-Au bond lengths from the Au_{36} crystal structure.

4.5 Results and Discussion

4.5.1 Local structure of $Au_{36}(SR)_{24}$

The analysis of $Au_{36}(SR)_{24}$ started with an investigation of the Au-Au bonding properties by Au L_3-edge EXAFS. The structure of Au_{36} is depicted in Figure 4.3a with isolated layers to clearly illustrate the FCC-ordered Au_{28} core (staple Au sites are removed) and its inner tetrahedral component. Two different Au-S bonding modes are also shown and are known as the staple and bridging motifs, where Au atoms are held in the core for bridging motifs. Figure 4.3b displays the FT-EXAFS of Au_{36} (*k*-range of 3.0 to 16.0 Å^{-1} used for transformation) at low temperature (90 K), with Au foil shown underneath to serve as bulk FCC Au. On an important side note, a deeper understanding of Au-Au bonding environment can be achieved with EXAFS when the sample is of high purity and is measured at low temperatures to obtain high quality oscillations up to the high *k*-region (*i.e.*, $k = 16.0$ Å^{-1}). This is evident in FT-EXAFS spectra when scattering shells are well resolved and the high-*R* shell intensities are enhanced. With this in mind, there are three distinct scattering peaks in the FT-EXAFS (indicated with asterisks in Figure 4.3b) from long distance neighbours that are similar in distance and intensity for Au_{36} and Au foil, indicating FCC EXAFS oscillations are prominent in Au_{36}.

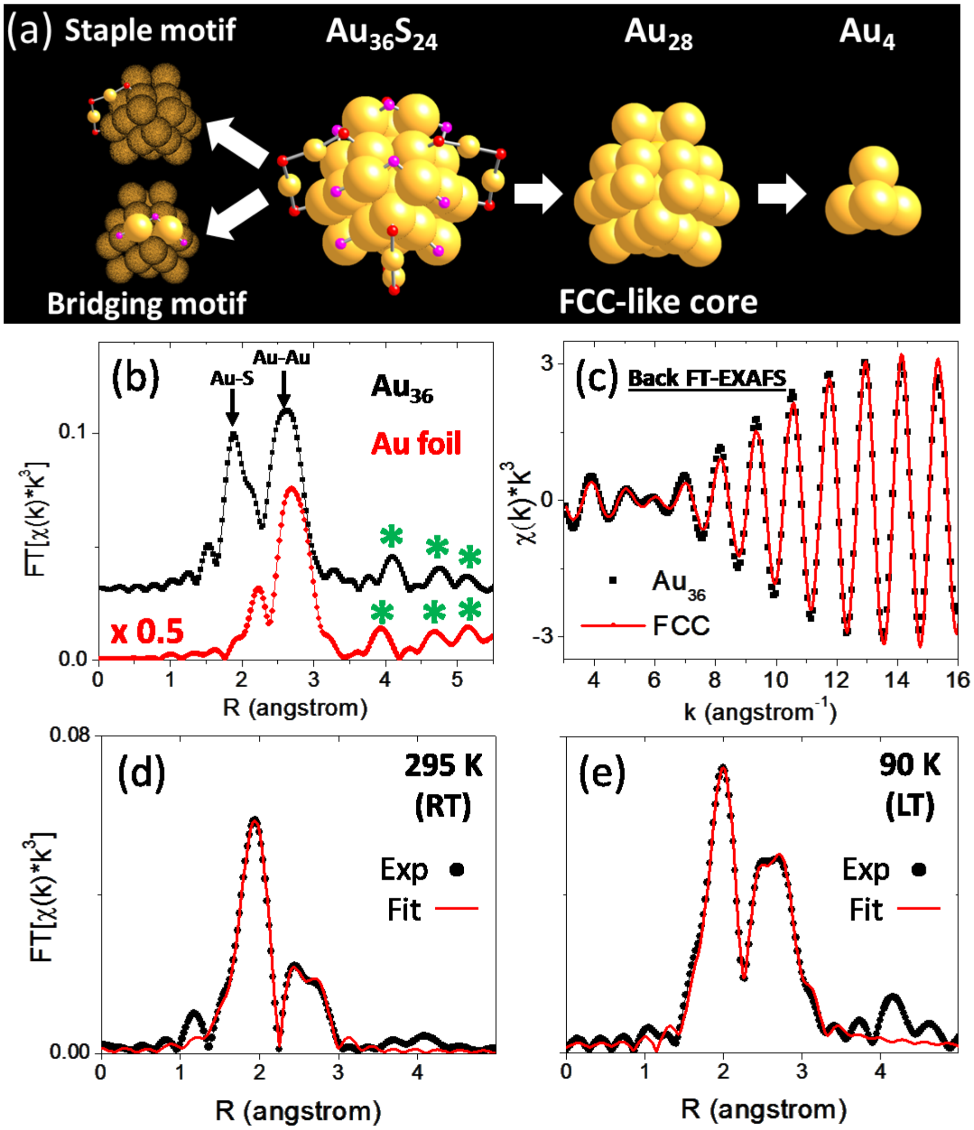

Figure 4.3 (a) Depiction of surface and internal structure for $Au_{36}S_{24}$ (Au atoms are gold, S atoms are red and magenta), (b) offset FT-EXAFS of Au_{36} and Au foil (*k*-range: 3 to 16 Å^{-1}), and (c) back-transformed FT-EXAFS (*R*-filter: 2.4 to 2.9 Å) of Au_{36} Au-Au core bonding with comparison to Au_{28} FCC-like core model (y-scale for EXAFS of the theoretical FCC model is re-scaled to account for the thermal vibration effect). Best fits for Au_{36} (d) room temperature and (e) low temperature FT-EXAFS spectra (*k*-range: 3 to 13.5 Å^{-1}).

Before quantitative EXAFS fitting results are shown, a qualitative approach to quickly identify FCC Au-Au bonding structure in $Au_n(SR)_m$ NCs was demonstrated. To do this, the back-FT-EXAFS signal (*i.e.*, region of *R*-space is selected and backward Fourier-transformed to *k*-space) from the Au-Au bonding environment of the Au core in Au_{36} was isolated and compared with simulated structural model of an FCC Au_{28} core, shown in Figure 4.3c. Overlapping back-FT-EXAFS oscillations produced an almost perfect match of phase and frequency between Au_{36} and the FCC Au_{28} core.

A three-shell EXAFS (Au-S, Au-Au_1 and Au-Au_2) fit was performed for the Au_{36} spectra at both room temperature (RT) and low temperature (LT) to obtain quantitative structural parameters for each shell's environment. FT-EXAFS spectra and their respective best fits are shown in Figure 4.3d and 4.3e with fitting results summarized in Table 4.1. Upon inspection of the $Au_{36}(SR)_{24}$ crystal structure, calculation of the ideal Au-S CN gave a value of 1.33 and was fixed for the three-shell fitting process. Due to the complex variety in Au-Au bonding environments, a multi-shell EXAFS fit accounting for each of these scattering paths was not obtainable. However, preliminary fitting of the Au-Au environment consistently lead to two distinct Au-Au scattering paths which provided an excellent fit from 1.5 to 3.2 Å, encompassing the strongest single scattering paths (including Au-S). Organizing all Au-Au bond length data into a histogram confirmed these two distributions of Au-Au bonding where ideal CN values could be calculated and used in the three-shell EXAFS fitting method (Figure 4.2). As a result, Au-Au$_1$ and Au-Au$_2$ shells account for Au-Au bonding between *ca.* 2.72 to 2.86 Å and *ca.* 2.86 to 3.10 Å, respectively.

Table 4.1 Au L$_3$-edge EXAFS fitting results for Au$_{36}$ measured at room temperature and low temperature. Uncertainties in fitted parameters are shown in parentheses.

T (K)	Shell	CN	R (Å)	σ^2 (Å^2)	ΔE_0 (eV)
295 (room)	Au-S	1.33	2.322(2)	0.0039(1)	0.0(5)
	Au-Au$_1$	2.06	2.732(4)	0.0080(3)	0.0(5)
	Au-Au$_2$	2.56	2.89(1)	0.018(2)	0.0(5)
90 (low)	Au-S	1.33	2.329(2)	0.0026(1)	2.0(5)
	Au-Au$_1$	2.06	2.746(3)	0.0037(9)	2.0(5)
	Au-Au$_2$	2.56	2.951(5)	0.0103(6)	2.0(5)

4.5.2 Au$_4$ core structures and temperature-dependent bonding properties

Previously reported EXAFS fitting of Au$_{38}$(SR)$_{24}$ and Au$_{25}$(SR)$_{24}$ NCs at RT showed short Au-Au bonding in the core at 2.789(7)[233] and 2.80(1)[186] Å, respectively; whereas the short Au-Au bond length for Au$_{36}$ (Au-Au$_1$) was much shorter at 2.732(4) Å. The shorter Au-Au bonding framework representing the Au-Au$_1$ shell for Au$_{36}$ is illustrated in Figure 4.4, with comparison to the biicosahedral Au$_{38}$ core. Interestingly, short Au-Au bonding ($R_{Au\text{-}Au} < 2.86$ Å) is more localized for Au$_{36}$ than for the Au$_{38}$ with smaller Au-Au bonding occurring within and nearby pseudo-Au$_4$ tetrahedral units. These pseudo-Au$_4$ units are highlighted with red bonds in Figure 4.4. Complete evolution of the Au$_4$ unit with Au-Au bond length is further shown in Figure 4.5. The fact that shorter metallic bonding occurs as separate small clusters in the FCC-ordered core can help account for the much shorter bond lengths found from EXAFS results at RT. Recently, the important role of Au_4 units in $Au_n(SR)_m$ NCs has been brought to attention by Jiang,[101] proposing that these tetrahedral units could be the smallest Au core structures for $Au_n(SR)_m$ NCs. Cheng *et al.*[102] also used Au_4 core units as the foundation for super-atom-networks to explain the stability of certain $Au_n(SR)_m$ NCs.

Another important finding from EXAFS analysis was the expansion of bond lengths for the two Au-Au shells at LT, with the Au-Au_2 shell having a more pronounced expansion of 2.1%. The expansion of metal-metal bonding with decreasing temperature is an uncommon property for bulk FCC-ordered metals although it has been observed in a few studies with larger Au NPs.[240,241] A previous temperature-dependent EXAFS study on $Au_{25}(SR)_{18}$ showed noticeable contraction of the first-shell Au-Au bond at LT, which illustrated the metallic bonding behaviour of the core for $Au_{25}(SR)_{18}$.[186]

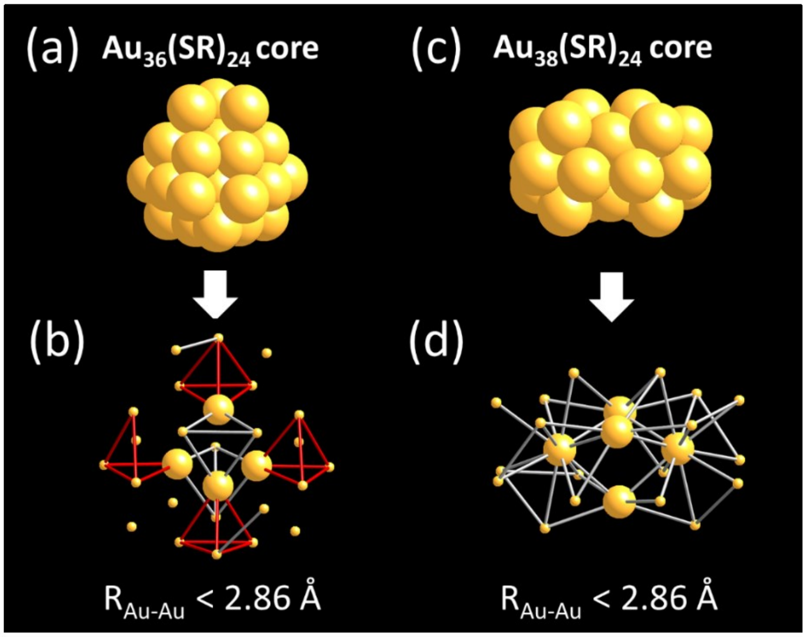

Figure 4.4 Representation of the (a) FCC-ordered core (in Au_{36}) and (c) biicosahedral core (in Au_{38}) with the shorter Au-Au bonding frameworks shown in (b) and (d), respectively. Central Au sites not bonded to thiolate ligands are shown as larger spheres in (b) and (d).

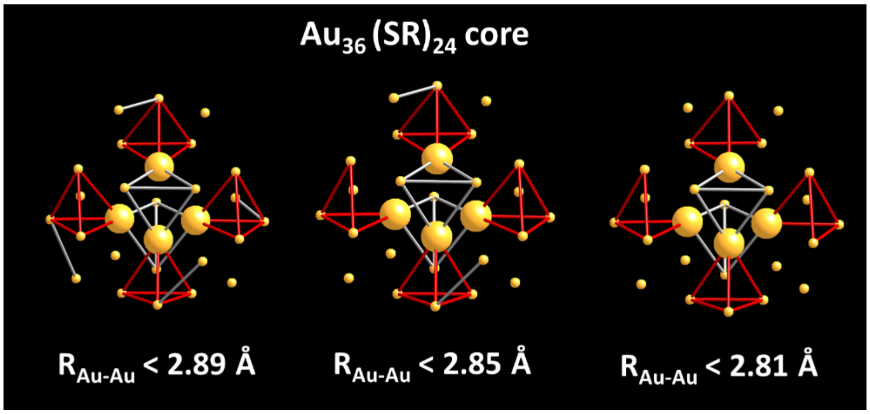

Figure 4.5 Schematic evolution of pseudo-Au_4 units (red bonding) in the Au_{36} core. Central Au sites not bonded to thiolate ligands are shown as larger spheres.

Returning to the EXAFS results on Au_{36}, structural parameters from the Au-Au_1 shell mainly correspond to the short Au-Au bonding found within and nearby the pseudo-Au_4 clusters mentioned above. It is interesting to note that there are 4 Au atoms located in the core also forming a tetrahedral shape (Figure 4.3a, right), which are the only Au atoms not bonded to any thiolate ligand. Nonetheless, these 4 central Au atoms are in fact are not tightly bonded to each other being, on average, 2.95 Å apart and are therefore represented by the longer Au-Au_2 shell. Furthermore, slight Au-Au expansion was seen within the small Au clusters at low temperature, 2.732(4) to 2.746(3) Å, while significantly more expansion was experienced between the clusters and on the surface of the core going from 2.89(1) to 2.951(5) Å. This physicochemical observation was an intriguing property for Au_{36}, exemplifying the more molecule-like behaviour of its FCC-ordered core. This property could also be considered useful for novel applications involving negative thermal expansion materials.

4.5.3 Electronic properties of $Au_{36}(SR)_{24}$

After identifying the unique pseudo-Au_4 environment in the Au_{36} core framework, the electronic structure was then investigated with XANES and *l*-DOS from both Au and S perspectives to probe the influence of such Au_4 clusters on the molecule-like behaviour of Au_{36}.

Au L_3-edge XANES for Au_{38}, Au_{36} and Au foil are presented in Figure 4.6a. Absorption edge positions (E_0) for Au_{36} and Au_{38} are both at higher energy than Au foil. This is generally caused by S-Au(I)-S interactions that occur on the surface of $Au_n(SR)_m$ NCs. Interestingly, a noticeable decrease in the white-line intensity (the first resonance feature following the edge jump, indicated by arrow) is seen for Au_{36} compared to Au_{38}. The significant difference between Au_{36} and Au_{38} white-line intensities indicated valence energy levels are more highly occupied in Au_{36} than Au_{38}. This was somewhat surprising since surface Au will lose d-electron density due to LMCT, and there are actually fewer Au atoms in the core of Au_{36} not bonded to S (4 for Au_{36} and 5 for Au_{38}, as seen in Figure 4.4).

The unexpected difference in electronic structure between the measured Au_{36} and Au_{38} could be due to the small pseudo-Au_4 units that comprise the Au_{36} core are approaching the limit of observable nano-size effects. As was reported in the literature, the net nano-size effect of Au (without contribution from LMCT) results in an increase of Au d-electron density due to the lesser extent of s-p-d rehybridization (*i.e.,* less intra-atomic electron flow from d to s/p state).[242] Therefore, this decrease in core size (*e.g.,* pseudo-Au_4 units vs. Au_{23} biicosahedral core) should cause the valence d-orbitals to become more highly occupied. To verify this, the Au L_3-edge XANES of the central Au site of Au_{36} and Au_{38} (*i.e.*, site not bonding to surface thiolate in order to exclude the metal-ligand charge transfer effect) were simulated. Simulated Au L_3-edge XANES (Figure 4.6b) shows the same trend of white line intensity as that in Figure 4.6a, which further confirmed the suggested hypothesis. This supports the idea that smaller Au clusters are governing the electronic properties to be more molecule-like for Au_{36}, more so than the thiolate ligand. To further probe the influence of the Au_{28} FCC core on the electronic properties from a site-specific perspective, *l*-DOS calculations were performed on all unique Au sites in Au_{36}.

Since the effect of the Au_{28} FCC-ordered core on the bonding and electronic properties of Au_{36} is the main interest, *l*-DOS calculations were calculated for the 5d level of Au (d-DOS). Figure 4.6c presents the site-specific d-DOS analysis of the Au_{36} structure. A gradual narrowing of the 5d level was apparent for Au atoms closer to the surface. This indicated the electronic structure of each Au site transitions from metal-like to molecule-like going from the central sites (band (i)) to staple sites (band (vi)). Besides this metallic-molecular band structure trend, also observed in studies for other $Au_n(SR)_m$ systems,[226,243] d-DOS illustrated the subtle difference between surface sites and bridging sites (bands (ii) to (v)) where the Au-S CN is one and two, respectively.

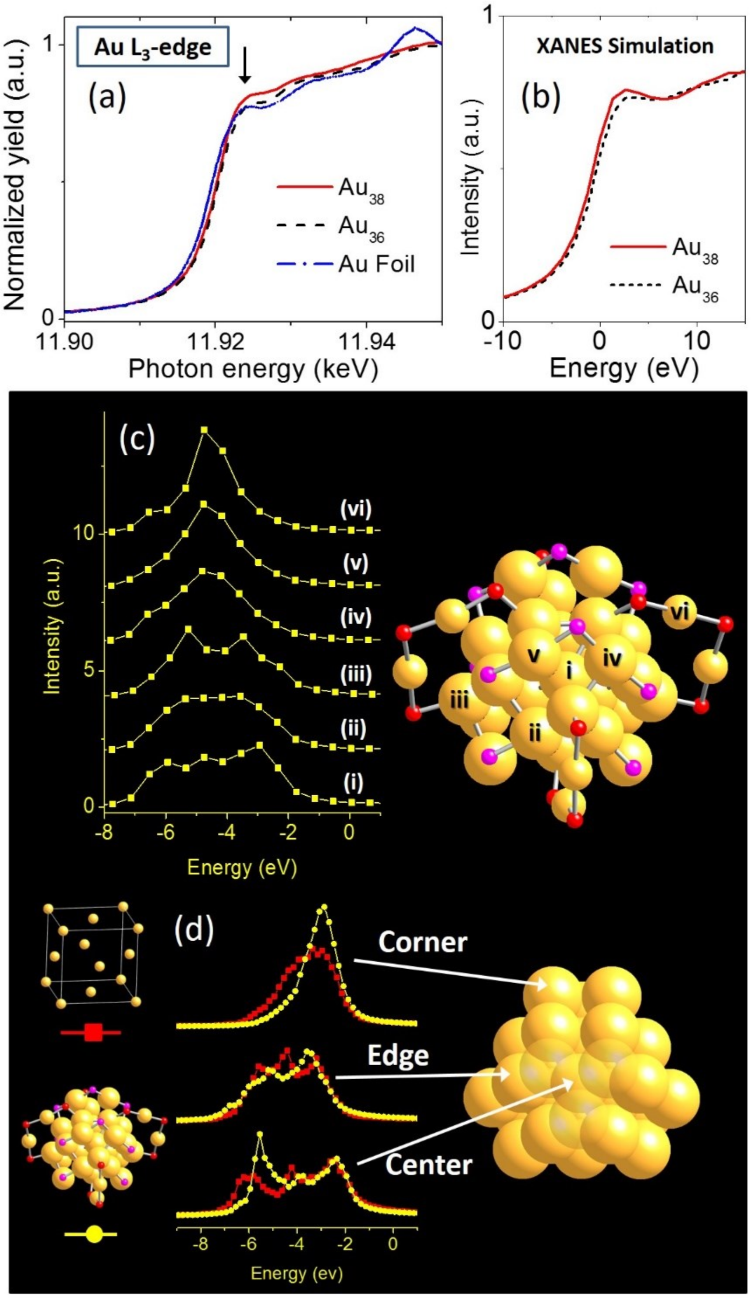

Figure 4.6 (a) Au L$_3$-edge XANES of Au$_{36}$, Au$_{38}$ and Au foil, (b) Au L$_3$-edge XANES simulation of central Au site in Au$_{36}$ and Au$_{38}$, (c) site-specific interpretation of d-DOS band structure for Au$_{36}$ including (i) central, (ii) bridging surface, (iii) double staple surface, (iv and v) bridging and (vi) double staple Au sites, (d) d-DOS comparison of an ideal Au$_{28}$ FCC-ordered cluster from bulk Au (Au-Au distance adjusted to match that of Au$_{36}$) with actual Au$_{28}$ FCC-like core from Au$_{36}$ with S atoms removed.

Bands (ii) and (iii) represented the two unique surface sites with slightly different environments, where site (ii) is bonded to a bridging motif and site (iii) is bonded to a double staple. Band (iii) appeared to have finer structure than band (ii) most likely originating from the nature of the corner position on the core's surface. There are other corner sites on the Au_{28} core but are involved in bridging thiolate bonding where the Au-S CN is two. These Au sites are represented by bands (iv) and (v). For bridging sites, Au atoms are displaced from the core more than corner sites in band (iii) due to stronger Au-S bonding, resulting in further narrowing of their 5*d* bands compared to other surface sites. The different distance of bridging Au to the surface may have caused the appearance of a shoulder in band (iv), since these particular Au sites are held more closely to the surface. The electronic nature of these bridging Au sites in conjunction with the smaller pseudo-Au_4 units in the core (which do not share similar Au sites) would strongly contribute to the molecule-like electronic structure of Au_{36}. Additional d-DOS simulations compare the bare Au_{28} core (*i.e.,* without Au(I)-SR bonding effect) from Au_{36} with an ideal Au_{28} core from bulk gold, shown in Figure 4.6d. Simulated d-DOS bands were overlapped for similar sites on both models. Clearly, the bridging thiolates have a dramatic effect on the corner Au sites since the band was significantly narrower (*i.e.,* more molecule-like) than the ideal structure (Figure 4.6d, top). In addition, the central Au site in the NC showed a narrower d-DOS than that in the ideal structure.

In the above discussions, the electronic structure of Au_{36} was probed from the Au perspective. S K-edge XANES spectra of Au_{36} and Au_{38} were then examined to investigate the effect of the thiolate-bonding motif on the electronic structure. Experimental S K-edge XANES in Figure 4.7a shows the overlap of Au_{36} and Au_{38}. The most important finding from this comparison was the distinct broadening of the first near-edge feature for Au_{36}. In fact, previous S K-edge XANES studies on Au_{25}, Au_{38} and Au_{144} NCs showed no broadening of this feature, only an increase in the pre-edge feature at 2.471 keV.[182] To understand the origin of this broadening, XANES simulations (Figure 4.7b) were performed for each S site on Au_{36} and Au_{38}. The structure of staple and bridging motifs both have two different S sites (-S^e(R)-Au-S^a(R)-Au-S^e(R)-), referred to as edge S (S^e) and apical S (S^a). For bridging motifs, it is clear that Au sites are still apart of the FCC-ordered core.

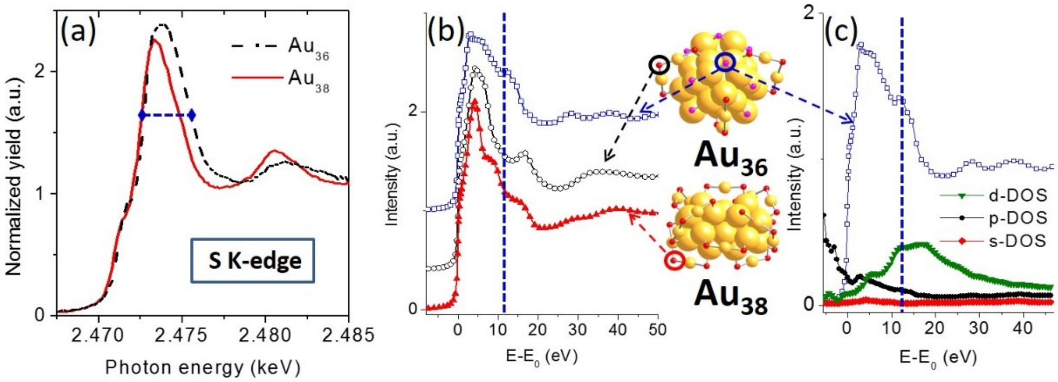

Figure 4.7 (a) S K-edge XANES of Au_{36} and Au_{38}, (b) simulated S K-edge XANES for apical bridging and staple S, and (c) simulated S K-edge XANES of apical bridging site with corresponding calculated DOS band structure.

Simulated S K-edge XANES for thiolate ligands on the edge of each motif, shown in Figure 4.8, had almost identical spectra for either bridging or staple motif on either NC. The apical S atom in the double staple motif for both Au_{36} and Au_{38} are also similar in structure although the spectrum for Au_{36} is slightly broader, as shown in Figure 4.7b. More significantly, the apical S atom in the bridging motif was much broader than any other S site due to an additional near-edge feature higher in energy from the absorption edge (shown with dotted line), which could contribute to the broader near-edge feature seen from the experimental XANES.

To understand the origin of the S K-edge XANES line-broadening of Au_{36}, the *l*-DOS components that influence the post-edge features in XANES spectra are presented for the apical bridging S in Figure 4.7c. It was observed that S d-DOS resonance for the apical bridging S is positioned in the same region where the additional near-edge feature appears for the apical bridging S, suggesting the line-broadening of S K-edge XANES (Figure 4.7a) could be related to the Au-S bonding associated with the unoccupied S d-state. This observation implied that the Au-S bonding related to the S d-state is sensitive to the local structural difference between the apical S in the bridging and the staple motif. Moreover, this finding of near-edge broadening for Au_{36} could be a method to detect the presence of bridging motifs or perhaps FCC-ordered core structures for $Au_n(SR)_m$ NCs without known structures.

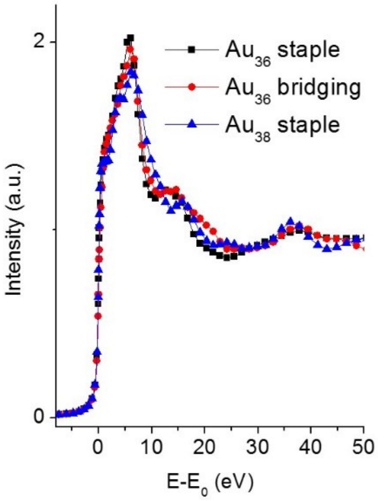

Figure 4.8 Simulated S K-edge XANES spectra of the edge S position for Au_{36} dimeric staple, Au_{36} bridging and Au_{38} dimeric staple.

4.6 Conclusion

In summary, XAFS measurements in conjunction with *ab initio* calculations and comparisons with icosahedral-based Au NCs of similar composition demonstrated the unique bonding properties for FCC-ordered $Au_{36}(SR)_{24}$ from both the Au core and Au(I)-SR surface motif perspectives. Findings indicated that the molecule-like Au-Au bonding properties of $Au_{36}(SR)_{24}$ were largely influenced by tightly bonded pseudo-Au_4 units within the FCC-ordered Au_{28} core, and that the bonding of its Au(I)-SR bridging motif differs from that of the staple-like motif. This work strongly suggested that the FCC-ordered Au-Au packing structure in small thiolate-protected Au NCs should be treated differently from its bulk counterpart and possibly larger thiolate-protected Au NPs.

Chapter 5 - Electronic and Bonding Properties of Thiolate-protected Gold Nanoclusters with FCC Core: $Au_{28}(SR)_{20}$ (Part II)

Sections 5.3-5.6 are reproduced in part with permission from: Chevrier, D. M.; Zeng, C.; Jin, R.; Chatt, A.; Zhang, P. Role of Au_4 Units on the Electronic and Bonding Properties of $Au_{28}(SR)_{20}$ Nanoclusters from X-ray Spectroscopy. *J. Phys. Chem. C* **2015**, *119*, 1217-1223. Copyright 2015, American Chemical Society.

5.1 Contributions

C.Z. synthesized and provided the $Au_{28}(SR)_{20}$ NC sample. R.J. supervised C.Z.. D.M.C. collected all XAFS data, conducted ab initio calculations, performed all data analysis and wrote the manuscript. P.Z. and A.C. supervised D.M.C. and helped revise the manuscript.

5.2 Foreword

With a similar surface composition of bridging thiolates, dimeric staple structures, and FCC packing arrangement of Au atoms in the core, $Au_{28}(SR)_{20}$ NCs share many structural characteristics with $Au_{36}(SR)_{24}$ NCs studied in the previous chapter. This chapter continues with examining how FCC-ordered core structures influence the electronic and bonding properties of $Au_n(SR)_m$ NCs, but now with a clearer focus on the role of Au_4 core structures that comprise the Au core.

5.3 Introduction

The synthesis and total structure elucidation of $Au_{36}(SR)_{24}$ and $Au_{28}(SR)_{20}$ NCs (where R = $C_6H_4C(CH_3)_3$) introduced the possibility of $Au_n(SR)_m$ NCs accommodating core structures with FCC-ordered geometry similar to larger Au NPs (diameter > 2 nm) and the bulk.[100,239] The appearance of bridging thiolate motifs on the FCC-ordered core was also a first for $Au_n(SR)_m$ NCs, which were originally predicted as the thiolate bonding motif for larger Au NPs and Au(111) surfaces.[73,94] Shortly after, $Au_{44}(SR)_{28}$ and $Au_{20}(SR)_{16}$ NCs were isolated forming a "magic series" of 4 $Au_n(SR)_m$ NCs, differentiating by $Au_8(SR)_4$ units.[104,244] It is interesting to note that the total structure of $Au_{30}S(SR)_{18}$ NCs has revealed a core structure almost identical to $Au_{28}(SR)_{20}$ NCs synthesized with a *tert*-butyl thiolate ligand instead of *tert*-butyl benzene thiolate.[245] Aside from the unexpected FCC arrangement of Au atoms in the core, attention has been shifted to smaller tetrahedral Au_4 or vertex-sharing bitetrahedral Au_7 clusters within the core in order to identify the implication these fundamental core units have on the nucleation/formation and composition-dependent bonding/electronic properties of $Au_n(SR)_m$ NCs.[101,246,247] Furthermore, Au_4 and Au_7 clusters within $Au_{28}(SR)_{20}$ NCs have been described and interpreted with the divide-and-protect model and the noble gas superatom theory as basic $2e^-$ and $4e^-$ superatoms, respectively.[248]

In continuation from the previous study on $Au_{36}(SR)_{24}$ NCs, $Au_{28}(SR)_{20}$ NCs were examined with temperature-dependent XAFS experiments and *ab initio* simulations of valence electronic structure. The findings demonstrated the valence electronic structure was fundamentally different from its similar-sized, icosahedral-based counterpart $Au_{25}(SR)_{18}$ because of the unique local structure of smaller Au_4 units in the core of

$Au_{28}(SR)_{20}$. A multi-shell EXAFS fitting analysis was then conducted on $Au_{28}(SR)_{20}$ to examine the local structure of short Au-Au within Au_4 units and longer Au-Au bonding in the core. By measuring the $Au_{28}(SR)_{20}$ NC at both low (90 K) and room temperature (300 K), thermal contraction of longer Au-Au bonding was detected, which was consistent with previous experiments on $Au_{36}(SR)_{24}$ NCs. Overall, results suggested Au_4 units play an important role in understanding the electronic properties and the bonding properties of FCC-ordered Au NCs.

5.4 Materials and Methods

$Au_{28}(SC_6H_4C(CH_3)_3)_{20}$ NCs were synthesized via ligand-exchange induced transformation using $Au_{25}(SC_2H_4Ph)_{18}^-$ NCs (counterion: $^+N(C_8H_{17})_4$) as the precursor material. Briefly, $Au_{25}(SC_2H_4Ph)_{18}$ NCs were reacted with excess amounts of *tert*-butyl benzene thiol in toluene at 80˚C. After ~2 h of mixing, a high yield of transformed $Au_{28}(SC_6H_4C(CH_3)_3)_{20}$ NCs was collected. Synthesis details and complete characterization of the reaction product have been published elsewhere.[239]

Au L_3-edge XAFS measurements were collected in transmission mode at the CLS@APS beamline (Sector 20-BM) of the APS. Solid-phase measurements were conducted at 300 K under ambient conditions and at 90 K using a helium-cooled cryostat chamber. XAFS data work-up, sample preparation, EXAFS fitting and error analysis were conducted following the procedures outlined in Section 2.2. The amplitude reduction factor (S_0^2) was fixed at 0.90 for Au L_3-edge EXAFS fitting, which was determined by fitting the Au-Au scattering of a Au foil reference with a fixed Au-Au CN of 12. For multi-shell EXAFS fitting, CNs were fixed according to the $Au_{25}(SR)_{18}$ and

$Au_{28}(SR)_{20}$ crystal structures.[92,95,239] A *k*-range of 3 to 11.25 Å^{-1} was used for the Fourier-transformation of all *k*-space data to *R*-space. A fitting window of 1.5 to 2.9 Å and 1.5 to 3.2 Å was used for two-shell and three-shell fits, respectively.

l-DOS calculations for each Au site in $Au_{25}(SR)_{18}$ and $Au_{28}(SR)_{20}$ NCs (the R group was simplified to one C atom for calculation purposes) were conducted using the FEFF8.2 computation package,[216] with only the d-DOS results presented herein.

5.5 Results and Discussion

5.5.1 Local structure and comparison of $Au_n(SR)_m$ NC core structures

As mentioned in the previous section, $Au_{28}(SR)_{20}$ NCs were synthesized from $Au_{25}(SR)_{18}$ NCs using a ligand-exchange protocol that dramatically reconstructed the icosahedral Au_{13} core and surface structure of $Au_{25}(SR)_{18}$. The resulting structure of $Au_{28}(SR)_{20}$, as determined by X-ray crystallography, consists of an FCC-ordered core composed of 20 Au atoms and 8 Au atoms (smaller atoms) located in four double staple motifs (Figure 5.1a, top).[239] The remainder of the thiolate ligands bond with three Au atoms on each end of the 20 Au atom core (Figure 5.1a, centre). As a result, these 6 Au atoms are pulled away from the two central Au sites (shown as purple), leaving a 14 Au atom alternative core structure (Figure 5.1a, bottom). Additionally, considering Au-Au bond lengths shorter than 2.88 Å, 4 Au_4 or two Au_7 units are revealed as the core constituents (connected with red bonds).

A preliminary investigation of the local structure was conducted to confirm consistency with the total structure of $Au_{28}(SR)_{20}$ NCs and to compare with the $Au_{25}(SR)_{18}$ precursor. First, Au L_3-edge EXAFS simulations were conducted on the

$Au_{28}(SR)_{20}$ NC by simulating the scattering environment of each Au site in order to create an average EXAFS signal. Site-specific scattering environments and the average simulated R-space EXAFS spectrum are depicted in Figure 5.1b and Figure 5.1c, respectively. From these spectra, the origin of the most dominant EXAFS scattering peaks (1.5 to 3.5 Å) can be identified. The first feature for surface, bridge and staple sites is from Au-S scattering (Figure 5.1b). The second scattering feature is from the shortest Au-Au bonding that occurs within the Au_{20} core. This scattering feature is seen for centre and surface Au sites. The last scattering feature that will be examined herein is a longer Au-Au bonding type that can be found for centre, surface, bridge and some staple sites.

Between the average simulation and the experimental EXAFS (90 K) there was good agreement with the position of the Au-S (1.9 Å, not phase-corrected) and Au-Au (2.45 and 2.75 Å, not phase-corrected) scattering peaks. The relative intensities of Au-S and Au-Au peaks were also comparable. These similarities in the EXAFS reassured the measured $Au_{28}(SR)_{20}$ NC contains Au local structural features expected from the crystal structure. Longer-range Au-Au scattering features were more intense for the simulated EXAFS since the simulation is effectively conducted at 0 K without thermal dampening of the EXAFS signal or the same limited mean free path for the scattered photoelectron.[200] A k^1-weighting was used for the simulated and experimental EXAFS for this reason. The theoretical CNs for each of the scattering paths identified above were then calculated from the bond distance distribution, shown in Figure 5.2. From the two distinct Au-Au bonding distributions (2.7 to 2.8 Å and 2.9 to 3.15 Å), two Au-Au scattering shells were confidently assigned in the EXAFS fit. Depictions of Au_{28} in Figure 5.2 indicated the first Au-Au scattering shell ($Au\text{-}Au_1$) accounted for Au-Au bonding in Au_4 or Au_7 core structures, exclusively. The second Au-Au scattering shell ($Au-Au_2$) encompassed a variety of Au-Au bonding environments throughout the Au NC including surface-surface, bridge-bridge, bridge-surface, centre-centre, surface-centre and staple-surface.

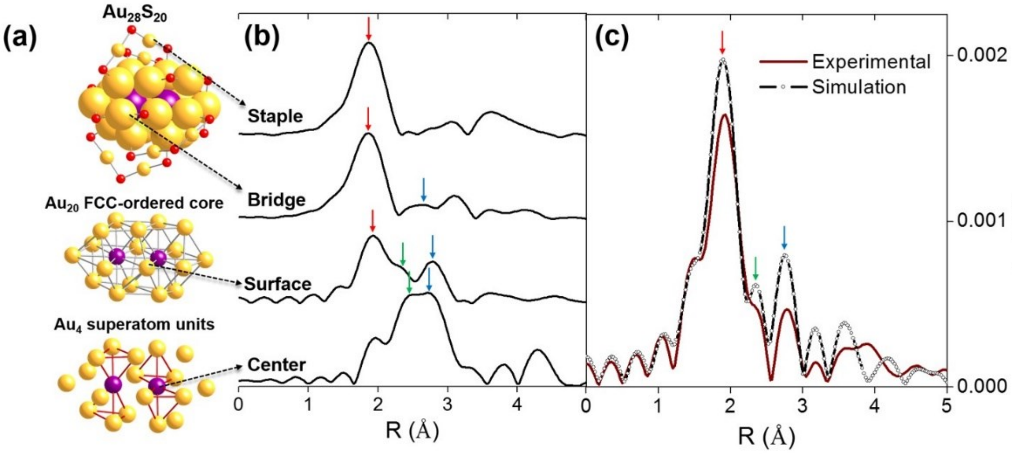

Figure 5.1 (a) Representation of the $Au_{28}(SR)_{20}$ NC with core structures, (b) simulated Au L_3-edge EXAFS spectra of each unique Au site and (c) comparison of the average simulated and experimental (measured at 90K) Au L_3-edge EXAFS.

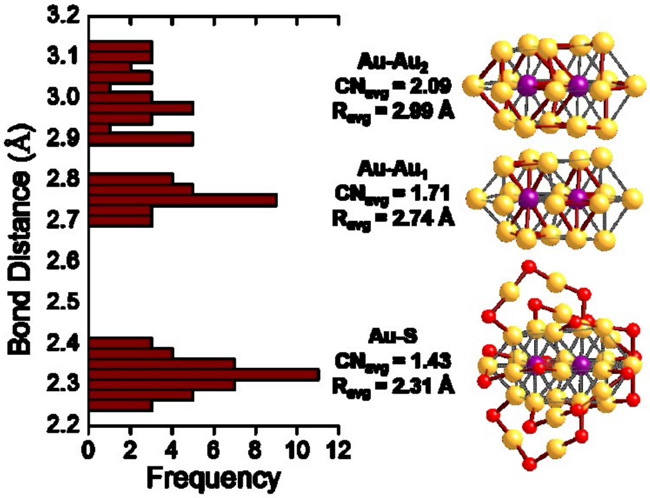

Figure 5.2 Bond length distribution for $Au_{28}(SR)_{20}$ and representative EXAFS scattering shells.

The *k*-space spectra of $Au_{28}(SR)_{20}$ and $Au_{25}(SR)_{18}$ NC samples measured at 300 K are shown in Figure 5.3a. The spectra were comparable in oscillation pattern and intensity but with noticeable changes in oscillation frequency. Identical *k*-ranges of 3.0 to 11.25 $Å^{-1}$ were used to acquire FT-EXAFS for each Au NC sample shown in Figure 5.3b. Au-S scattering peaks were similar in position and intensity for both Au NCs, which is consistent with the average CN for Au-S bonding being 1.44 for $Au_{25}(SR)_{18}$ and 1.43 (((14 Au each bonded to 2 S) + (12 Au each bonded to 1 S)) / 28 Au) for $Au_{28}(SR)_{20}$ (Figure 5.2). Although $Au_{28}(SR)_{20}$ contains double staple motifs (planar semi-rings) and bridging motifs (which can also be thought of as bent semi-rings), fitting results from a two-shell refinement (shown in Figure 5.3c and Table 5.1) revealed the Au-S bonding distance and structural disorder (Debye-Waller factor, σ^2) are close to $Au_{25}(SR)_{18}$, which only contains double staple units on its surface.

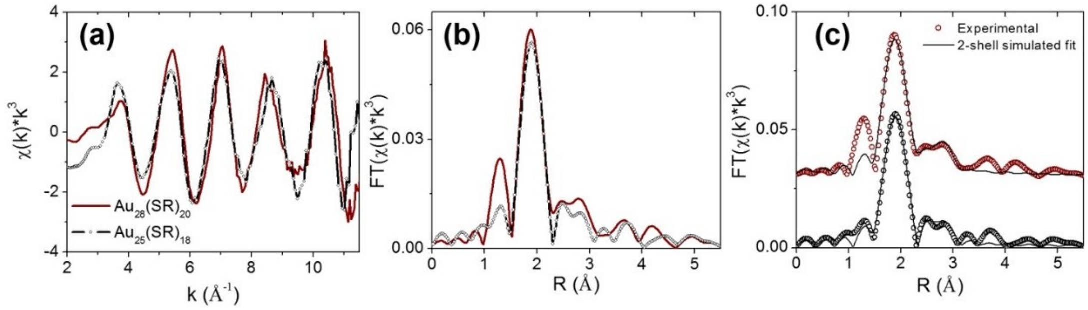

Figure 5.3 Au L_3-edge (a) *k*-space, (b) FT-EXAFS and (c) fitted EXAFS spectra of $Au_{25}(SR)_{18}$ and $Au_{28}(SR)_{20}$.

Structural deviations of the $Au_{28}(SR)_{20}$ from $Au_{25}(SR)_{18}$ were more noticeable with the Au-Au scattering shell from the two-shell fit in Figure 5.3c. Using a similar Au-Au scattering path for the EXAFS fit of each Au core,[243] the shortest Au-Au bonding for Au_{28} was on average 2.73(2) Å in length compared to 2.80(1) Å for the icosahedral core of $Au_{25}(SR)_{18}$. The determined Au-Au bond length is very close to what Zeng *et al.*[239] had reported as the shortest Au-Au bond type (2.74(3) Å). This short Au-Au bond length is a common signature of small FCC-ordered Au cores or smaller Au_4 tetrahedral units.[100,103,104,249] The structural disorder from the Debye-Waller factor for the shortest Au-Au scattering path was also less for $Au_{28}(SR)_{20}$ than $Au_{25}(SR)_{18}$, suggesting lower structural disorder of Au-Au bonding within the FCC-ordered core of $Au_{28}(SR)_{20}$. This is another indication that the shortest Au-Au scattering shell ($Au\text{-}Au_1$) originates from the two staggered bitetrahedrons (Au_7 core units), which contain tightly bonded Au_4 tetrahedral units.

Table 5.1 Two-shell EXAFS fitting results for $Au_{28}(SR)_{20}$ and $Au_{25}(SR)_{18}$ NCs at room temperature (300 K). CNs were fixed according to the expected value determined from the total structure of $Au_{25}(SR)_{18}$ and $Au_{28}(SR)_{20}$ NCs.[92,95,239] Uncertainties in fitted parameters are shown in parentheses.

	$Au_{25}(SR)_{18}$				$Au_{28}(SR)_{20}$			
Shell	CN	R (Å)	σ^2 (Å^2)	ΔE_0 (eV)	CN	R (Å)	σ^2 (Å^2)	ΔE_0 (eV)
Au-S	1.44	2.321(5)	0.0033(2)	-1(1)	1.43	2.314(9)	0.0035(4)	-1(2)
$Au\text{-}Au_1$	1.44	2.80(1)	0.009(1)	-1(1)	1.71	2.73(2)	0.007(1)	-1(2)

The relative S/Au ratio is similar for each Au NC: 0.71 for $Au_{28}(SR)_{20}$ and 0.72 $Au_{25}(SR)_{18}$. Thus, only considering the electron withdrawal from the thiolate ligands in Au-S bonding from π-electron backdonation (Au 5d to S 3p), it is expected that the Au 5d electron occupancy would be similar for each Au NC. Moreover, the ratio of theoretical Au(I)/Au(0) (using the general rule that Au atoms bonding to two thiolate molecules are expected to have a Au(I) oxidation state)[98,250] is similar for each Au NC system (0.50 for

$Au_{28}(SR)_{20}$ and 0.48 for $Au_{25}(SR)_{18}$). In this regard, $Au_{25}(SR)_{18}$ and $Au_{28}(SR)_{20}$ NCs were expected have a similar Au valence electronic structure. Presented in Figure 5.4 are Au L_3-edge XANES spectra of $Au_{28}(SR)_{20}$, $Au_{25}(SR)_{18}$ and Au foil. It was immediately evident that the white-line feature (promotion of Au 2p electrons to vacant Au 5d valence levels) for $Au_{28}(SR)_{20}$ was much lower than $Au_{25}(SR)_{18}$, despite the almost identical S/Au and Au(I)/Au(0) criteria mentioned above. Instead, the white-line intensity was more similar to Au foil with a shift in the E_0 position to lower energy (inset). Both results indicate $Au_{28}(SR)_{20}$ had a substantially higher 5d electron density than $Au_{25}(SR)_{18}$. On the NP or NC size regime, however, higher occupation of Au 5d valence orbitals can originate from under-coordinated Au sites or smaller clusters of Au, decreasing the amount of s-p-d hybridization and approaching a more atomic-like Au electronic structure ($5d^{\sim 10}$) instead of bulk Au ($5d^{\sim 9.6}$).[242] From initial inspection of the $Au_{28}(SR)_{20}$ local structure from EXAFS fitting, the Au-S bonding on the surface was similar on average for both Au NCs while each Au core had contrasting bonding properties likely related to the different core structures (Au_{13} icosahedral core versus FCC-ordered core containing smaller Au_4 core structures). To examine the influence of the core structures on the valence electronic properties, namely the bound electronic states in d-DOS, *ab initio* simulations were conducted from a site-specific perspective to elucidate differences in valence electronic structure for each Au NC system.

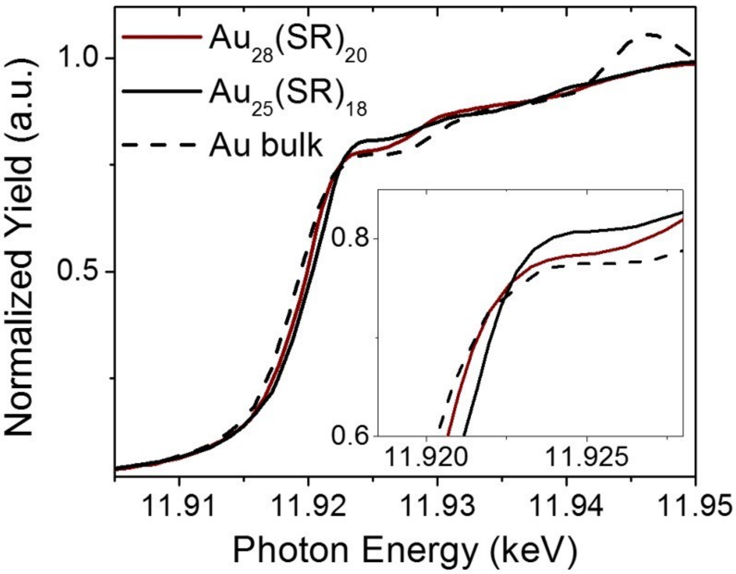

Figure 5.4 Au L_3-edge XANES of $Au_{28}(SR)_{20}$, $Au_{25}(SR)_{18}$ and Au bulk (inset, white-line region).

The simulated d-DOS spectrum for the centre Au (centre of Au_7 core unit (purple atoms), Figure 5.1a), surface Au (surface of Au_7 core unit), bridge Au and staple Au are displayed in Figure 5.5. Simulations were also performed for $Au_{25}(SR)_{18}$, which has three unique Au sites instead of 4 for $Au_{28}(SR)_{20}$. Stacked plots of the simulated d-DOS are presented for each specific site in Figure 5.5 with all spectra corrected to their respective calculated Fermi energy (dotted line). Starting from the outermost staple Au sites for both systems, the 5d bands of bound electronic states were comparable in overall width and fine structure features. The narrow and sharp 5d band was understandably from the localization of 5d electrons from molecular SR-Au(I)-SR staple-like motifs on the surface of each Au NC.[226,243] The $Au_{28}(SR)_{20}$ NC contains a special bridging Au site that has, so far, only been identified in Au NCs with FCC-ordered cores. In the previous study on $Au_{36}(SR)_{24}$ NCs, which contain FCC-ordered core of 28 Au atoms, the bridging Au site resembled the molecule-like electronic character of staple Au sites, despite having short Au-Au bonding with the rest of the FCC-ordered core.[251] Once again, the d-DOS simulation of the bridging site for Au_{28} (compared with both staple and surface sites in Figure 5.5) had a band width and structure comparable to staple Au sites. A Bader-charge analysis by Knoppe *et al.*[248] also classified these bridging Au sites as more similar to the electronic structure of staple Au sites.

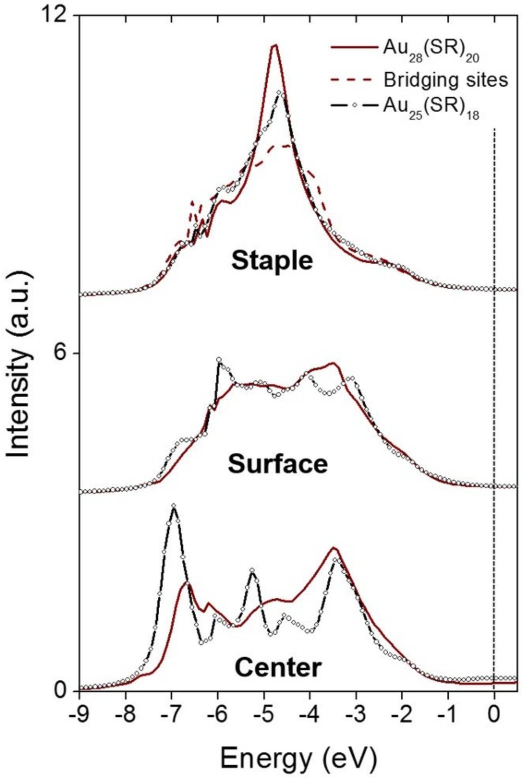

Figure 5.5 Site-specific *d*-DOS simulations of $Au_{25}(SR)_{18}$ and $Au_{28}(SR)_{20}$ NCs. Each spectrum is corrected to their own calculated Fermi energy (dotted line).

Examining the surface of each Au core structure (icosahedron surface vs. Au_7 core unit surface), the surface Au sites for $Au_{28}(SR)_{20}$ were slightly narrower with some change in the fine structure of the 5d band. The most significant difference in the d-DOS is evident for the central Au sites of $Au_{28}(SR)_{20}$ where the valence electron density is more localized into a narrower 5d band. A narrower 5d band for a larger $Au_n(SR)_m$ NC and Au core is unexpected, which suggested the local environment of the tightly bonded Au_4 units can modify the electronic properties considerably. From both the unbound (XANES) and bound (d-DOS) electronic perspectives, the unique core structure of Au_{28} has a prominent influence on the electronic properties; namely, XANES results indicated higher 5d electron occupancy and d-DOS simulations showed more localized 5d energy levels for $Au_{28}(SR)_{20}$ compared to $Au_{25}(SR)_{18}$. This was consistent with $Au_{36}(SR)_{24}$, where the combination of bridging Au sites (which are similar in valence electronic structure to staple Au sites) and Au_4 core units lead to more localized 5d electron density when compared to a Au NC of similar size and icosahedral core.

5.5.2 Effect of composition on the bonding properties of $Au_n(SR)_m$ NCs with FCC-ordered core structures

The presence of Au_4 units within the FCC-ordered core of $Au_{36}(SR)_{24}$ offered an explanation for the molecule-like temperature-dependent bonding behaviour, which exhibited thermal contraction of the longer Au-Au metallic bonding in the FCC-like core. This section further investigated the role of Au_4 units in directing the bonding properties of $Au_{28}(SR)_{20}$ with comparisons drawn to $Au_{36}(SR)_{24}$ in order to examine the effect of composition and size on Au NCs with FCC-ordered cores.

The local structure of $Au_{28}(SR)_{20}$ was further analyzed by including a second Au-Au scattering shell ($Au-Au_2$) that accounted for longer Au-Au bonding between Au_4 units and between Au atoms on the surface of the Au core (see Figure 5.2). Longer aurophilic bonding, between staple Au and surface Au, was not detected due to the low average CN (~0.5). Correlating the total structure and the Au-Au bond distance distributions, the

EXAFS fitting analysis then examined the bonding properties of $Au_{28}(SR)_{20}$ with temperature and were compared with previous EXAFS fitting results on $Au_{36}(SR)_{24}$ NCs.

The three-shell EXAFS fitting results of $Au_{28}(SR)_{20}$ at 90 K (low temperature, LT) (Figure 5.6a) were first examined to check for consistency with the average bond distances expected for each scattering environment. Figure 5.6b presents the EXAFS spectrum of Au_{28} at 90 K with simulated three-shell fit, and fitting results in Table 5.2. Consistent with the structure determined by X-ray crystallography, bond distances determined from EXAFS fitting (2.328(6) Å, 2.73(1) Å and 2.99(3) Å) were within experimental or statistical error from the total structure. After confirming the validity of the three-shell EXAFS fitting procedure, the same fit was conducted for the EXAFS spectrum of $Au_{28}(SR)_{20}$ collected at 300 K (room temperature, RT) (Figure 5.6c) to examine the effect of temperature on the bonding properties of the FCC-ordered core. Comparing the fitting results of $Au_{28}(SR)_{20}$ at 90 and 300 K, there was a striking consistency with $Au_{36}(SR)_{24}$. A direct comparison of $Au_{28}(SR)_{20}$ and $Au_{36}(SR)_{24}$ bond distances from EXAFS results is shown Figure 5.6d. The shorter Au-Au bonding of Au_4 units again appeared to be impervious to the temperature change, remaining around 2.73(2) Å in average distance for $Au_{28}(SR)_{20}$. The longer Au-Au bonding, however, is sensitive to a change in temperature displaying thermal contraction from 2.99(3) Å to 2.93(3) Å. The shift in Au-Au scattering with temperature was also evident when directly comparing the FT-EXAFS in Figure 5.6a.

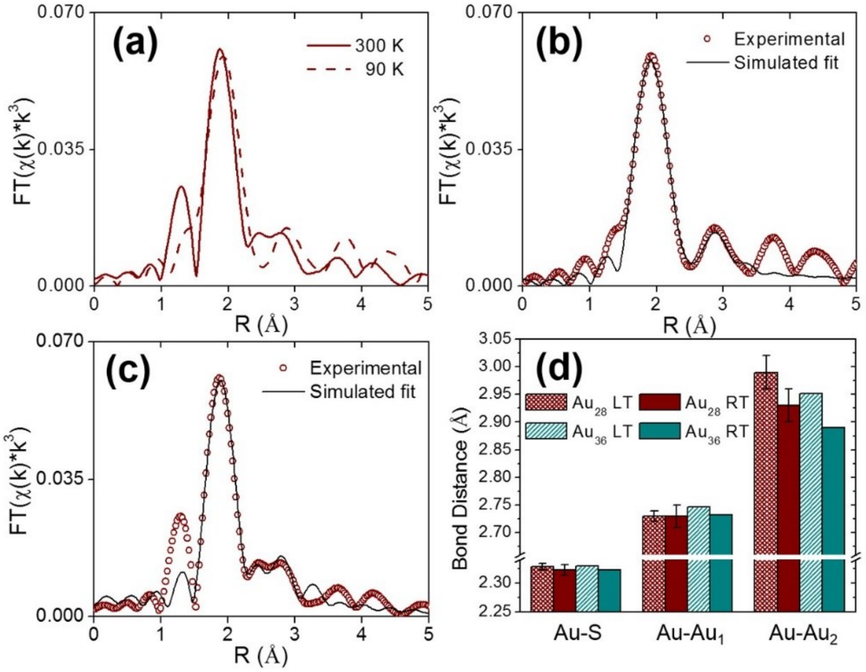

Figure 5.6 (a) Au L$_3$-edge FT-EXAFS of Au$_{28}$(SR)$_{20}$ collected at 90 and 300 K. Simulated EXAFS three-shell fit of Au$_{28}$(SR)$_{20}$ at (b) 90 K and (c) 300 K with (d) comparison of temperature-dependent EXAFS fitting results between Au$_{28}$(SR)$_{20}$ and Au$_{36}$(SR)$_{24}$.[251]

The magnitude of the thermal contraction was slightly less than that found for the Au$_{36}$(SR)$_{24}$ core (1.7% versus 2.1%) but still significant in comparison to the thermal expansion of larger Au NPs and bulk Au.[241] The thermal contraction of Au$_{28}$(SR)$_{20}$ is proposed to occur through a similar mechanism to Au$_{36}$(SR)$_{24}$ where Au-Au bonds within Au$_4$ units are more rigid than Au-Au bonds on the surface of the NC core and between Au$_4$ units. As a result, these short Au-Au bonds are resistant to temperature-induced structural changes and longer Au-Au bonds contract with temperature, possibly to conserve stability of the Au NC by counteracting the high surface energy (*i.e.,* large curvature and many unique Au sites) and/or thermal vibrations of the thiolate ligands. Specifically, there are three potential locations through which Au-Au contraction could occur: i) between Au_7 (or Au_4) core units, ii) bridging Au atoms and/or iii) staple Au atoms. Further experiments and theoretical studies should be pursued for FCC-ordered Au NCs in order to determine the structural changes that occur from a site-specific perspective with response to varied temperature conditions.

Table 5.2 EXAFS fitting results of $Au_{28}(SR)_{20}$ at various temperatures using three scattering shells. CNs were fixed according to the expected value determined from the total structure of $Au_{28}(SR)_{20}$ NCs. Uncertainties in the fitted parameters are shown in parentheses.

Temperature (K)	Shell	CN	R (Å)	σ^2 (Å^2)	ΔE_0 (eV)
90 (LT)	Au-S	1.43	2.328(6)	0.0028(3)	2(1)
	Au-Au_1	1.71	2.73(1)	0.006(1)	2(1)
	Au-Au_2	2.09	2.99(3)	0.015(4)	2(1)
300 (RT)	Au-S	1.43	2.322(9)	0.0033(4)	1(2)
	Au-Au_1	1.71	2.73(2)	0.005(1)	1(2)
	Au-Au_2	2.09	2.93(3)	0.011(4)	1(2)

5.6 Conclusion

In summary, XAFS experiments and *ab initio* calculations were utilized to examine the bonding and electronic properties of $Au_{28}(SR)_{20}$ NCs, with FCC-ordered core structure, in comparison with its icosahedral counterpart $Au_{25}(SR)_{18}$ (similar composition) and its FCC-ordered core relative $Au_{36}(SR)_{24}$ (considerably different composition). It was found that the Au_4 unit within $Au_{28}(SR)_{20}$ controls its electronic and bonding properties in these studies, which consistently accounts for its differing electronic behaviour from $Au_{25}(SR)_{18}$ and identical temperature-dependent bonding properties with $Au_{36}(SR)_{24}$. These findings are useful towards better understanding the structure-property relations of thiolate-protected Au NCs with regards to the cluster composition and core geometry perspectives. In particular, $Au_n(SR)_m$ NCs with FCC-ordered core structures may represent a special category of nanomaterials whose bonding properties are not sensitive to cluster size/composition change, differing from the size-dependent behaviour commonly observed for nanoscale materials.

Chapter 6 - Impact of Selenium-based Ligands on the Electronic and Structural Properties of Au_{25} Nanoclusters

Sections 6.3-6.6 are reproduced in part with permission from: Chevrier, D. M.; Meng, X.; Tang, Q.; Jiang, D.-e.; Zhu, M.; Chatt, A.; Zhang, P. Impact of the Selenolate Ligand on the Bonding Behavior of Au_{25} Nanoclusters. *J. Phys. Chem. C* **2014**, *118*, 21730-21737. Copyright 2014, American Chemical Society.

6.1 Contributions

X.M. synthesized $Au_{25}(SeR)_{18}$ NCs and was supervised by M.Z.. Q.T. conducted MD-DFT simulations and was supervised by D.-e.J.. D.M.C. performed all XAFS experiments, fitting analyses, ab initio simulations of XANES and l-DOS spectra, and wrote the manuscript. A.C. and P.Z. supervised D.M.C. and helped revise the manuscript.

6.2 Foreword

This chapter is the first of two studies in Project II. Here, the influence of a heavier chalcogen-based ligand, selenolate, is inspected with the $Au_{25}(SR)_{18}$ system as reference. Compared with $Au_{25}(SR)_{18}$, the selenolate-protected analog ($Au_{25}(SeR)_{18}$) demonstrates noticeable changes in the Au electronic properties and the bonding properties of the Au NC on the surface and core. Examining the heavier selenolate-protected Au_{25} analog also enabled the electronic and structural properties to be probed from the ligand perspective through Se K-edge XANES and EXAFS. Comparing thiolate-

and selenolate-protected Au_{25} NCs provided a better understanding on how the ligand head group can influence electronic and physical properties of Au NCs. This study was also motivated by the fact that selenolate-protected Au NCs have been shown to be more stable than thiolate-protected Au NCs.

6.3 Introduction

Atomically-precise selenolate-protected gold nanoclusters ($Au_n(SeR)_m$ NCs) have recently surfaced in the field of Au NC research. Earlier studies have pursued selenium-based ligands for the protection of larger Au NPs to improve the stability or to investigate the surface structure of selenolate-Au nanomaterials.[252–254] In particular, the Au-Se bond is expected to be more covalent in nature than the Au-S bond because of the larger covalent radius of Se and the almost identical electronegativity values of Se and Au. Exchanging the thiolate ligands for selenolate ligands could, therefore, enhance the stability of Au NCs.

The first record of $Au_n(SeR)_m$ NCs was published by Negishi *et al.,*[255] who reported the synthesis of $Au_{25}(SeC_8H_{17})_{18}$ NCs, which had an identical composition to the well-characterized $Au_{25}(SR)_{18}$ NC.[92,95] Although the total structure of $Au_{25}(SeC_8H_{17})_{18}$ was not elucidated, experimental evidence (later supported with a DFT-optimized structure[256]) strongly suggested the framework of the selenolate-stabilized Au_{25} NC is equivalent to that of $Au_{25}(SR)_{18}$ NCs. Following this, Meng *et al.*[224] performed a ligand-exchange reaction to replace the phenylethanethiolate ligand (SC_2H_4Ph) on $Au_{25}(SC_2H_4Ph)_{18}$ NCs with benzeneselenol (HSePh). This resulted in complete conversion to $Au_{25}(SePh)_{18}$ NCs. The same study also reported $Au_{25}(SePh)_{18}$ NCs were more stable than $Au_{25}(SC_2H_4Ph)_{18}$ against degradation when exposed to air. Kurashige *et al.*[256] went on to examine the ligand-induced stability of selenolate-protected Au NCs with a comparison of $Au_{25}(SC_8H_{17})_{18}$ and $Au_{25}(SeC_8H_{17})_{18}$, rationalizing that the more covalent Au-Se bonding (compared to Au-S bonding) accounted for the increased stability of selenolate-protected Au NCs by preventing surface Au-ligand degradation. A follow-up study by Kurashige *et al.*[257] demonstrated that the increased stability from the alkylselenolate ligand allowed for incorporation of Cu atom dopants into the Au_{25} framework. Although the increased stability has been proposed to originate from the covalent Au-Se bonding on the surface, the influence of the selenolate ligand on the Au local structure and electronic properties was not well understood.

In addition to $Au_{25}(SeR)_{18}$ NCs, other selenolate-Au NCs such as $Au_{18}(SeR)_{14}$,[258] $Au_{38}(SeR)_{24}$ [259] and $Au_{24}(SeR)_{20}$ [249] NCs have now been synthesized. It is worthwhile to note that the crystal structures of $Au_{24}(SR)_{20}$ and $Au_{24}(SeR)_{20}$ NCs (the organic constituent, R, is different for each Au NCs) were recently discovered.[103,249] Although the core and surface oligomer compositions are similar (having a Au_8 core with long interlocking oligomer units), there are a few conformational differences between thiolate- and selenolate-protected Au_{24} NCs, such as 4 tetramer Au-SR units (in $Au_{24}(SR)_{20}$) versus two trimeric/two pentameric Au-SeR units (in $Au_{24}(SeR)_{20}$) and anti-prismatically-joined Au_4 tetrahedrons (in $Au_{24}(SR)_{20}$) versus cross-joined Au_4 tetrahedrons (in $Au_{24}(SeR)_{20}$) in the Au_8 core. It is still uncertain whether or not such conformational variations exist for other thiolate-/selenolate-Au NCs of identical composition (*i.e.,* $Au_{25}(SR)_{18}$ and $Au_{25}(SeR)_{18}$).

Synchrotron-based XAFS experiments were conducted to investigate the influence of the selenolate ligand (benzeneselenolate) on the Au_{25} NC framework through the Au/Se local structure and electronic properties. Multi-shell EXAFS fitting results revealed that, at a lower temperature (50 K), the Au_{13} core had similar Au-Au bonding to $Au_{25}(SR)_{18}$ NCs, but with markedly longer aurophilic interactions from the staple Au to surface Au sites. When $Au_{25}(SeR)_{18}$ NCs were measured at a higher temperature, Au-Au interactions in the core and on the surface of the NC were found to contract from EXAFS fitting results, which suggested negative thermal expansion behaviour. A mechanism to account for the thermal contraction was proposed and supported with DFT-MD simulations. Such temperature-dependent structural changes were also observed with the electronic properties of $Au_{25}(SeR)_{18}$ NCs. Se K-edge XANES was further interpreted with simulated XANES and *l*-DOS to identify near-edge features related to Se-Au and Se-C bonding. This work highlighted the sensitivity of Au_{25} NC structure and properties to the selenolate protecting ligand and the relatively unexplored realm of Au NC temperature-dependent behaviour.

6.4 Materials and Methods

Phenylethanethiolate-protected Au_{25} ($Au_{25}(SC_2H_4Ph)_{18}$) and benzeneselenolate-protected Au_{25} ($Au_{25}(SePh)_{18}$) NCs studied herein were synthesized according to a modified Brust-Schiffrin two-phase method and a previously published ligand-exchange protocol, respectively.[224] Both $Au_{25}(SeR)_{18}$ and $Au_{25}(SR)_{18}$ were synthesized in the anionic state (counterion: $^{+}N(C_8H_{17})_4$) and were thoroughly characterized to confirm their chemical composition.[224]

Au L_3- and Se K-edge XAFS measurements were collected in transmission mode at the CLS@APS beamline (Sector 20-BM) of the APS. Measurements were conducted at 300 K under ambient conditions and at 50 K using a helium-cooled cryostat chamber. XAFS data work-up, sample preparation, EXAFS fitting and error analysis were conducted following the procedures outlined in Section 2.2. The S_0^2 was fixed at 0.90 for Au L_3-edge EXAFS fitting, which was determined using a Au foil reference and fixing the Au-Au CN at 12. A S_0^2 value of 0.99 was determined for Se K-edge EXAFS fitting by measuring a Se mesh reference and fixing the Se-Se CN at 2. For EXAFS fitting of each Au_{25} NC sample, E_0 shifts were correlated for all fits and CNs were fixed according to the theoretical value from the $Au_{25}(SR)_{18}$ crystal structure.[92,95]

Valence electron count analyses, simulated XANES and *l*-DOS were calculated using the FEFF8.2 computation package.[216]

The DFT computations of the $Au_{25}(SePh)_{18}^-$ cluster were performed using the VASP code (version 5.3.5).[260] The Perdew, Burke and Ernzerhof (PBE) form[261] of the generalized-gradient approximation (GGA) was used for electron exchange-correlation. The $Au_{25}(SePh)_{18}^-$ cluster was placed in a 28 Å × 28 Å × 28 Å cubic box, large enough to avoid the interactions between periodically repeated clusters. The negative charge of the cluster was balanced by a uniform positive background. Standard projector-augmented wave potentials[262] were used for Au, Se and H, while a soft version was used for C, so a lower kinetic energy cutoff of 274 eV could be used to save the computational cost while maintaining accuracy. Only the Gamma-point was used for k-point sampling. The convergence threshold for geometry optimization was set to be 10^{-2} eV/Å in force, to obtain the 0 K structure. For MD simulations, the $Au_{25}(SePh)_{18}^-$ cluster was heated up to 300 K with a time step of 1 fs in 300 fs to obtain the 300 K structure.

6.5 Results and Discussion

6.5.1 Local structure of $Au_{25}(SeR)_{18}$

Kurashige *et al.*[259] have investigated the local structure of alkylselenolate-protected Au_{25} NCs with EXAFS using two scattering shells to represent Au-Se bonding and the shortest Au-Au interactions from Au_{13} core bonding. This study on Au_{25}(benzeneselenolate)$_{18}$ (abbreviated as $Au_{25}(SeR)_{18}$) further developed an understanding of how the selenolate ligand influences bonding properties of the Au_{25} NC framework with an extended, multi-element XAFS analysis. Importantly, probing the Se K-edge (instead of S K-edge) with a hard energy X-ray source (~12 to 13 keV) provided stronger post-edge EXAFS oscillations that were analyzed in addition to the Au L_3-edge data. Thus, the combination of Se and Au XAFS data presented a unique opportunity for a more complete characterization of selenolate-protected Au NC materials by investigating the local structure of the metal core, surface and ligand environments.

Figure 6.1a displays the Au L_3-edge EXAFS oscillations at 50 K in *k*-space (using a k^3-weighting) for $Au_{25}(SeR)_{18}$ along with $Au_{25}(SC_2H_4Ph)_{18}$ ($Au_{25}(SR)_{18}$) for direct comparison of the Au local structure. By comparing the *k*-space spectra, it was evident that exchanging the thiolate for the selenolate ligand dramatically changed fine structure oscillations in the early *k*-space region (2 to 6 $Å^{-1}$) due to Au-Se bonding. The late *k*-space oscillations (8 to 13 $Å^{-1}$) also increased in intensity, possibly from more tightly ordered Au-Au bonding. For FT-EXAFS (shown in Figure 6.1b), a *k*-space region from 3 to 13 Å^{-1} was used for both samples to allow the incorporation of additional scattering shells with enough spatial resolution to distinguish different Au-Au scattering paths (ΔR = ~0.2 Å, the approximate difference between core and surface Au-Au bond lengths). The most intense feature observed in the FT-EXAFS for both Au_{25} NCs was due to either Au-S or Au-Se interactions, with the broader scattering peak from Au-Se shifted to a longer distance, causing an overlap with a Au-Au scattering peak that typically appears around 2.5 Å (not phase-corrected) for $Au_{25}(SR)_{18}$ NCs.[186] Au L_3-edge EXAFS spectra of $Au_{25}(SeC_{12}H_{25})_{18}$ NCs from Kurashige *et al.*[259] showed a similar broadening of the Au-Se scattering peak.

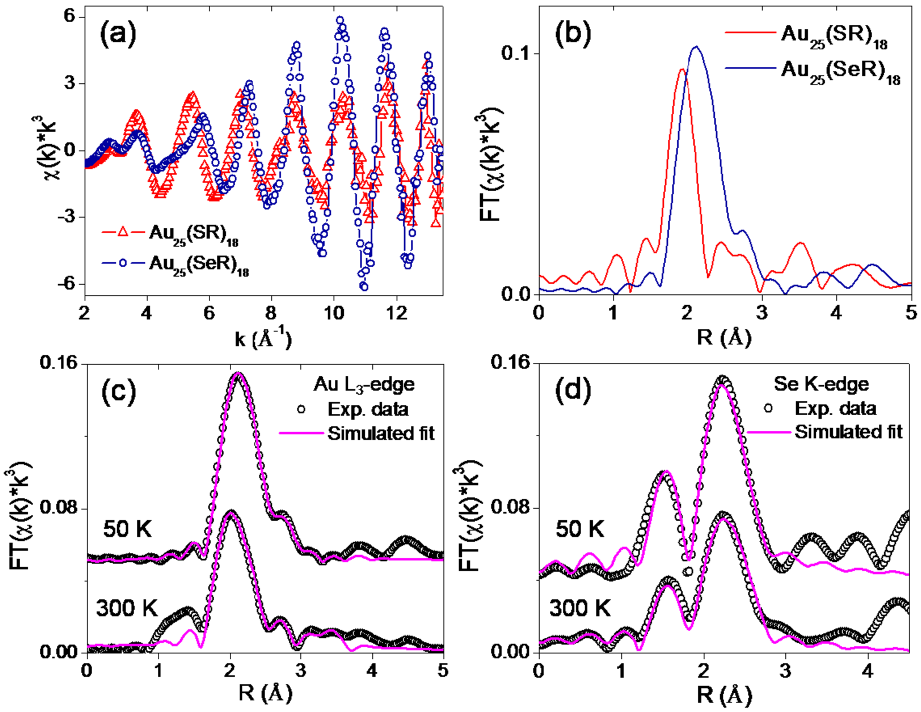

Figure 6.1 Au L_3-edge (a) *k*-space spectra and (b) FT-EXAFS of $Au_{25}(SR)_{18}$ and $Au_{25}(SeR)_{18}$ NCs measured at 50 K. (c) Au L_3-edge and (d) Se K-edge multi-shell EXAFS fit of $Au_{25}(SeR)_{18}$ NCs at different temperatures.

A detailed multi-shell Au L_3-edge EXAFS fitting analysis was conducted following a similar data treatment protocol to previous work on phenylethanethiolate-protected $Au_{19}(SR)_{13}$[243] (Chapter 3) and $Au_{25}(SR)_{18}$ NCs.[186] Four scattering shells were used to fit Au L_3-edge EXAFS, along with two shells to fit the Se K-edge EXAFS. Together, this offered a site-specific investigation of Se-C, Au-Se (from both edges), Au-Au core (Au-Au_1), Au-Au surface (Au-Au_2) and Au-Au aurophilic (Au-Au_3) environments. All *k*-space data are presented in Figure 6.2. Before fitting the Au L_3-edge EXAFS data for the $Au_{25}(SeR)_{18}$ sample, $Au_{25}(SR)_{18}$ FT-EXAFS spectra in Figure 6.3 were fit to check for consistency. The determined bond distances for each scattering path (Table 6.1) were indeed comparable to those reported earlier,[186] with only a small discrepancy between fitted parameters, likely from the different experimental temperature and longer *k*-range used in this work for the transformation to FT-EXAFS.

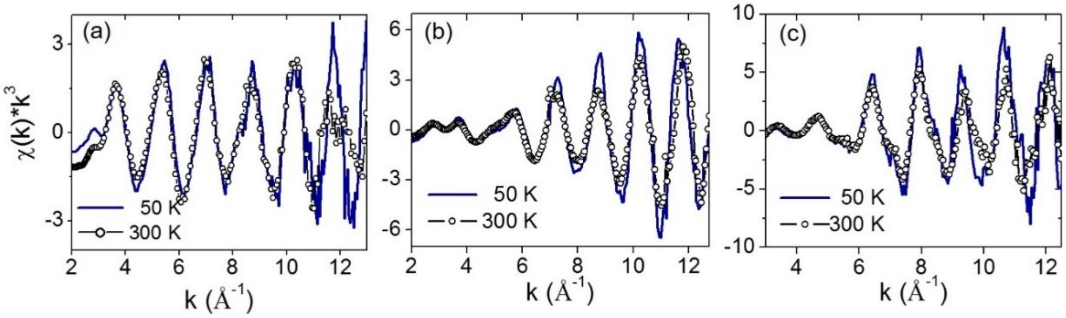

Figure 6.2 k^3-space spectra for (a) $Au_{25}(SR)_{18}$ NCs at the Au L_3-edge and $Au_{25}(SeR)_{18}$ NCs at the (b) Au L_3-edge and (c) Se K-edge.

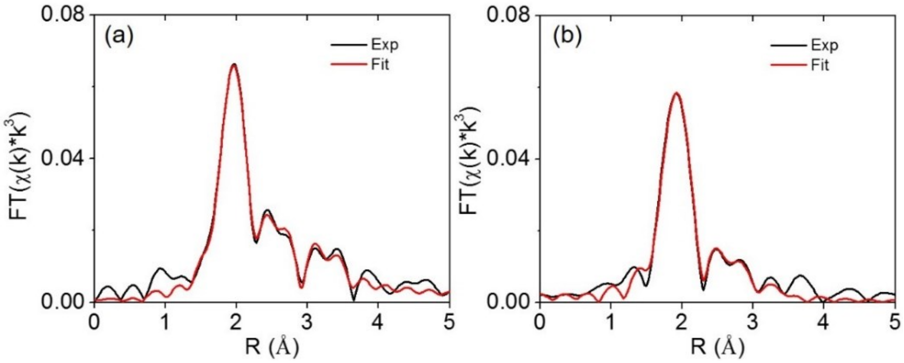

Figure 6.3 Multi-shell EXAFS fitting of $Au_{25}(SR)_{18}$ NCs at (a) 50 K and (b) 300 K.

Figure 6.1c displays the fitted Au L_3-edge R-space spectrum of $Au_{25}(SeR)_{18}$ (1.6 to 3.5 Å fitting window, not phase corrected) at 50 K with EXAFS results tabulated in Table 6.1. A good fit of the spectrum was achieved using the 4 aforementioned scattering paths. A Au-Se bond distance of 2.428(4) Å was determined from the fit, which is comparable to the 2.433 Å distance obtained with EXAFS for $Au_{25}(SeC_{12}H_{25})_{18}$ NCs[259] and shorter than the 2.50 Å predicted from a DFT-optimized $Au_{25}(SeCH_3)_{18}$ structure.[256] Although longer than Au-S bonding, the Au-Se bond is more covalent than Au-S bonding because of the smaller difference in electronegativity ($\chi_{Se} = 2.55$ versus $\chi_{Au} = 2.54$) and larger covalent radius for the Se atom. The local structure of the ligand shell was examined from the Se K-edge perspective using Se-C and Se-Au scattering paths to fit the Se K-edge EXAFS spectrum at 50 K, shown in Figure 6.1d with the results tabulated in Table 6.1. The Se-Au bond length was shorter than the Au L_3-edge length by only *ca.* 0.02 Å, which is almost within the range of reported uncertainties. The bond distance from Se to the C of the benzene ring was determined to be 1.87(3) Å. This is slightly shorter than Se-C bonding in diphenyl diselenide.[263]

Table 6.1 Multi-shell EXAFS fitting results for $Au_{25}(SR)_{18}$ and $Au_{25}(SeR)_{18}$ NCs measured at 50 K. CNs for each scattering shell were fixed based on the theoretical weighted average of nearest neighbours in the $Au_{25}(SR)_{18}$ crystal structure.[92] **Uncertainties in the fitted parameters are shown in parentheses.**

		$Au_{25}(SR)_{18}$		$Au_{25}(SeR)_{18}$	
Shell	CN	R (Å)	σ^2 (Å^2)	R (Å)	σ^2 (Å^2)
Se-C	1.0	-	-	1.87(3)	0.0028(3)
Se-Au	2.0	-	-	2.41(1)	0.0028(3)
Au-S/Se	1.44	2.327(3)	0.0028(1)	2.428(4)	0.00218(9)
$Au-Au_1$	1.44	2.784(6)	0.0044(4)	2.775(9)	0.0054(7)
$Au-Au_2$	1.92	2.955(8)	0.0061(5)	2.98(1)	0.009(1)
$Au-Au_3$	2.88	3.16(1)	0.017(1)	3.60(3)	0.016(3)

Returning to the Au L_3-edge EXAFS, the core Au-Au bonding ($Au-Au_1$) was determined to be, on average, 2.775(9) Å in distance with surface Au-Au bonding ($Au-Au_2$) at 2.98(1) Å. The Au-Au core bonding is considerably shorter than the DFT-predicted distance of 2.85 Å while the Au-Au surface bonding is more similar at 2.99 Å.[256] Compared to thiolate-protected Au_{25} NCs measured under identical experimental conditions (Table 6.1), the Au_{13} core component was relatively unchanged despite the lengthening of Au-ligand bonding (Au-Se). On the other hand, interactions occurring from staple Au sites to surface Au sites ($Au-Au_3$) were found to be much longer at 3.60(3) Å compared to 3.16(1) Å for $Au_{25}(SR)_{18}$ NCs. It is noted that aurophilic interactions on the surface at this distance are much weaker than $Au_{25}(SR)_{18}$ NCs and are approaching the sum of two Au van der Waals radii.[264] This could be understood by considering the longer Au-Se bond distance separates the dimeric staple units further from the core in comparison to $Au_{25}(SR)_{18}$.

6.5.2 Temperature-dependent bonding properties of $Au_{25}(SeR)_{18}$

From the initial local structural study of $Au_{25}(SeR)_{18}$ NCs at 50 K, the most significant and intriguing difference between selenolate- and thiolate-protected Au_{25} NCs was the absence of strong aurophilic interactions on the surface between Au in the dimeric staple units and the Au_{13} core. The role of aurophilic-like interactions in directing the temperature-dependent structural behaviour has been reported for other materials with closed-shell d^{10}-d^{10} interactions.[265–267] Such studies have shown that materials with aurophilic or argentophilic (Ag(I)-Ag(I)) contacts can induce a monumental increase in the linear thermal expansion coefficient or direct specific structural conformational changes when these closed-shell interactions become stronger (closer contact between metal centres) with increasing temperature. To explore the potential temperature-dependent behaviour of aurophilic interactions for $Au_{25}(SeR)_{18}$ NCs, site-specific and multi-element XAFS analyses further probed the local structure and electronic properties by varying the experimental temperature.

The effect of temperature on the ligand shell of $Au_{25}(SeR)_{18}$ NCs was first investigated from the Se K-edge perspective. EXAFS fitting (Figure 6.1d, with results in Table 6.2) indicated the Se-Au bonding at 300 K was almost identical to 50 K. Se-C bonding, on the other hand, increased in length by *ca.* 0.08 Å, from 1.87(3) to 1.95(2) Å, when the temperature was 300 K (depicted in Figure 6.4a). Lengthening of the Se-C bond at higher temperature could be related to a previous stability study on $Au_{25}(SeR)_{18}$ NCs that found Se-C bonds to be weaker than S-C bonds under high temperature treatment.[256]

Table 6.2 Se K-edge EXAFS fitting of $Au_{25}(SeR)_{18}$ NCs at 50 and 300 K. Uncertainties in the fitted parameters are shown in parentheses.

	Se-C			Se-Au		
T (K)	CN	R(Å)	σ^2(Å^2)	CN	R(Å)	σ^2(Å^2)
50	1	1.87(3)	0.0028(3)	2	2.40(1)	0.0028(3)
300	1	1.95(2)	0.0048(3)	2	2.408(9)	0.0048(3)

Multi-shell EXAFS fitting of the Au L_3-edge spectrum at 300 K (Figure 6.1(c) and Table 6.3) indicated a very small decrease in Au-Se bonding (similar to Se K-edge results) and a dramatic contraction of all three Au-Au shells (plotted in Figure 6.4a) where Au-Au_1 decreases from 2.775(9) Å to 2.70(1) Å, Au-Au_2 from 2.98(1) Å to 2.87(2) Å and Au-Au_3 from 3.60(3) Å to 3.45(4) Å. This is contrary to a previous EXAFS temperature-dependent study on $Au_{25}(SR)_{18}$ NCs[186] (and reproduced with the $Au_{25}(SR)_{18}$ sample in this work (Table 6.1 and Table 6.3)), where Au-SR and Au-Au core interactions slightly increased with temperature and aurophilic interactions remained similar in average distance. Trends of the Debye-Waller factor (σ^2) from EXAFS fitting (accounts for both the thermal and static disorder of the particular scattering shell) are plotted in Figure 6.4b and 6.4c for each temperature and each Au NC system to compare the temperature-dependent EXAFS results. $Au_{25}(SR)_{18}$ NCs display the anticipated trend of higher σ^2 values at 300 K for each Au-Au shell as a result of increased thermal disorder since the Au-Au framework does not significantly change in the measured temperature range (where 'Core' is Au-Au_1, 'Surface' is Au-Au_2 and 'Auro' is Au-Au_3). On the other hand, σ^2 values at 300 K for $Au_{25}(SeR)_{18}$ NCs were not significantly higher than at 50 K and follow a similar trend. This unexpected trend of Debye-Waller factors is consistent with the thermal contraction of the Au-Au framework shown in the bond distance analysis.

Table 6.3 Multi-shell EXAFS fitting results for $Au_{25}(SR)_{18}$ and $Au_{25}(SeR)_{18}$ NCs measured at 300 K. CNs for each scattering shell were fixed based on the theoretical weighted average of nearest neighbours in the $Au_{25}(SR)_{18}$ crystal structure.[92] Uncertainties in the fitted parameters are shown in parentheses.

		$Au_{25}(SR)_{18}$		$Au_{25}(SeR)_{18}$	
Shell	CN	R (Å)	σ^2 (Å^2)	R (Å)	σ^2 (Å^2)
Au-S/Se	1.44	2.333(2)	0.0029(1)	2.417(9)	0.0036(2)
$Au-Au_1$	1.44	2.790(5)	0.0048(4)	2.70(1)	0.005(1)
$Au-Au_2$	1.92	2.97(1)	0.009(1)	2.87(2)	0.008(2)
$Au-Au_3$	2.88	3.22(6)	0.04(1)	3.46(4)	0.014(4)

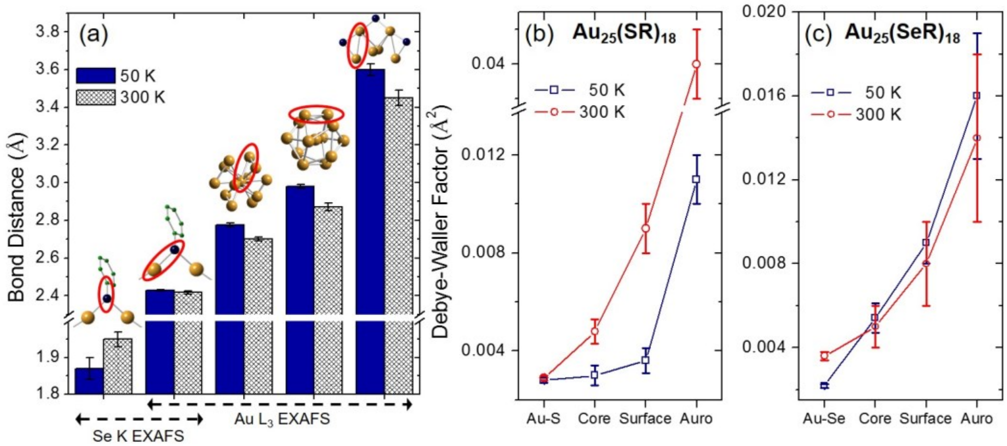

Figure 6.4 Temperature-dependent plots of (a) $Au_{25}(SeR)_{18}$ site-specific bond distances (models and circled regions correspond to the bond type), (b) $Au_{25}(SR)_{18}$ Debye-Waller factors and (c) $Au_{25}(SeR)_{18}$ Debye-Waller factors from EXAFS results.

Since the average Au-Se bond length does not decrease at the higher measured temperature, contraction of aurophilic bonding on the surface must originate from a change in the $Au_{surface}$-Se-Au_{staple} bond angle to bring staple and surface Au atoms closer together accounting for the decrease found in the Au-Au_3 distance. Similar influence of long-range metal-metal interactions has been identified for negative thermal expansion materials such as $Ag_3[Co(CN)_6]$,[265] where closed-shell interactions between Ag atoms (d^{10}-d^{10}), like aurophilic interactions, become shorter at higher temperatures, causing the material to contract along a particular lattice direction. Based on this, $Au_{25}(SR)_{18}$ NCs are not expected to exhibit this significant thermal contraction behaviour since the aurophilic bond distance is much shorter, making it less sensitive to the change in temperature. To confirm this hypothesis of aurophilic-induced thermal contraction, simulations were performed using first-principles MD based on DFT. Starting with the DFT-optimized structure of the $Au_{25}(SePh)_{18}$ NC (that is at 0 K) shown in Figure 6.5, the cluster was heated up to 300 K in the MD simulation to investigate the proposed mechanism of negative thermal expansion. Figure 6.5 displays the isolated dimeric staple unit and surface environment of $Au_{25}(SePh)_{18}$ from optimized DFT structures at each temperature along with the average bond angles for each structure. Consistent with the proposed mechanism, the angle between $Au_{surface}$-Se-Au_{staple} (indicated as (i)) became more acute at 300 K by *ca.* 7° and is as small as 70.4° (smallest angle for 0 K was found to be 78.1°). Along with this, the Au_{staple}-Se-Au_{staple} angle (indicated as (ii)) became more obtuse at 300 K by *ca.* 2°, bringing the staple Au closer to the Au_{13} surface. The simulation results also indicated that increase of the Au_{staple}-Se-Au_{staple} angle was more localized to three of the 6 dimeric staple units with the largest angle for the 300 K structure being 104.7° compared to 95.7° for the 0 K structure.

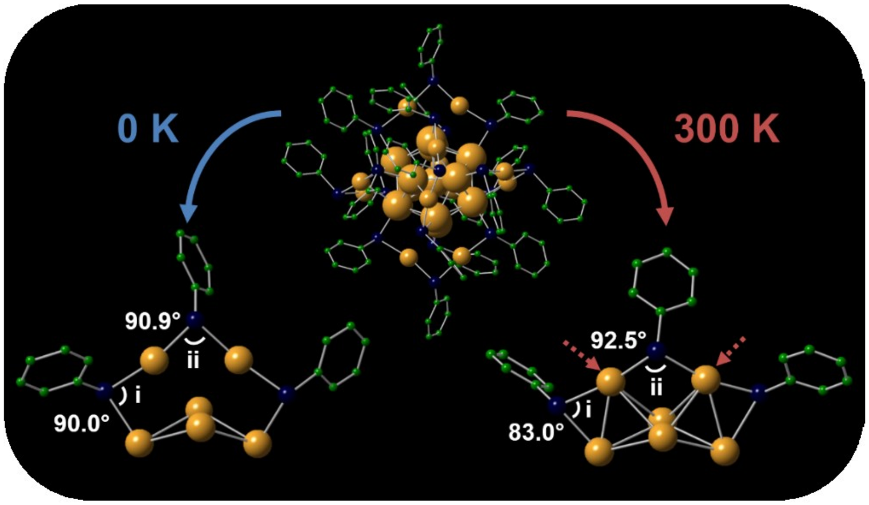

Figure 6.5 MD-DFT simulated structure of the $Au_{25}(SePh)_{18}$ NC. A typical structural change of the dimeric motif in the $Au_{25}(SePh)_{18}$ NC from 0 K (after DFT geometry optimization) (bottom left) to 300 K (after heating up in DFT-based MD simulation) (bottom right) with average bond angles.

Although the decrease in average aurophilic bonding distance would produce stronger Au-Au interactions on the surface, a change in dimeric staple conformation (-Se-Au-Se-Au-Se-) could result in a strained interface between the ligand shell and the metal core. Therefore, the contraction of the Au_{13} core (Au-Au_1 and Au-Au_2) could counteract this created surface tension or higher surface energy. Due to the extremely high curvature of small Au cluster surfaces (*i.e.*, Au_{13} core), very short Au-Au distances (< 2.78 Å) are commonly observed to increase the stability of the system.[268,269] Considering the contraction of the Au_{13} core between 50 and 300 K, an approximate calculation of the coefficient of thermal expansion (α) is very large at *ca.* -3×10^{-4} K^{-1}. Sanchez *et al.*[270] also observed a negative thermal expansion for supported-Pt clusters around ~0.9 to 1.1 nm in diameter. It is noted that the estimated α for $Au_{25}(SeR)_{18}$ is an order of magnitude larger than the Pt clusters of similar size, which could indicate the unique role of the staple-like motif in the negative thermal expansion behaviour of $Au_{25}(SeR)_{18}$.

6.5.3 Electronic properties of $Au_{25}(SeR)_{18}$

Thus far, an extended and multi-element EXAFS analysis of $Au_{25}(SeR)_{18}$ has unveiled the local structure from both the Au core and ligand shell perspectives. It is expected that both the selenolate ligand and the unique Au-Au bonding properties will have a significant influence on the electronic properties of Au_{25} NCs. To verify this, XANES spectra for $Au_{25}(SR)_{18}$, $Au_{25}(SeR)_{18}$ and relevant reference materials were examined from both Au and Se perspectives. The unusual temperature-dependent behaviour of $Au_{25}(SeR)_{18}$ is also revisited through the electronic properties.

Figure 6.6a shows the overlapped Au L_3-edge XANES region of $Au_{25}(SeR)_{18}$, $Au_{25}(SR)_{18}$ and Au foil. An important distinction between each spectrum is seen with the first feature in the near-edge region historically known as the white-line. The intensity of the white-line reflects the vacancies in the absorbing atom’s valence states (mainly the Au 5d level for Au L_3-edge XANES). $Au_{25}(SR)_{18}$ NCs have the highest white-line intensity, compared to Au foil and $Au_{25}(SeR)_{18}$ NCs, due to the electron withdrawing nature of the thiolate ligand, which will remove 5d electron density from mainly surface and staple Au atoms. $Au_{25}(SeR)_{18}$ NCs, on the other hand, have a white-line intensity lower than Au foil, indicating valence electrons are more localized in the 5d level than $Au_{25}(SR)_{18}$ NCs. The higher occupation of 5d electronic states for $Au_{25}(SeR)_{18}$ can be attributed to highly covalent Au-selenolate bonding, meaning less electron density is removed from valence states of surface and staple Au atoms. *Ab initio* calculations were performed on $Au_{25}(SCH_3)_{18}$, $Au_{25}(SeCH_3)_{18}$ and bulk FCC Au models to compare the electron occupation of 6s, 6p and 5d valence levels of Au, and the charge transfer from Au. Calculation results in Table 6.4 show that $Au_{25}(SeCH_3)_{18}$ indeed has a higher 5d electron count with less charge transfer for all Au sites (core, surface and staple sites), compared to $Au_{25}(SCH_3)_{18}$ NCs. Furthermore, surface Au sites on $Au_{25}(SeR)_{18}$ have an even higher 5d electron occupancy than bulk Au.

Table 6.4 Electron occupation and charge transfer calculations for (A) $Au_{25}(SCH_3)_{18}$, (B) bulk Au and (C) $Au_{25}(SeCH_3)_{18}$.

	Au centre				**Au surface**				**Au-Au staple**			
	Electronic configuration			CT	Electronic configuration			CT	Electronic configuration			CT
A	$s^{0.770}$	$p^{0.674}$	$d^{9.253}$	0.303	$s^{0.842}$	$p^{0.689}$	$d^{9.288}$	0.181	$s^{0.926}$	$p^{0.664}$	$d^{9.203}$	0.207
B	$s^{0.819}$	$p^{0.652}$	$d^{9.368}$	0.167								
C	$s^{0.784}$	$p^{0.632}$	$d^{9.316}$	0.268	$s^{0.878}$	$p^{0.642}$	$d^{9.373}$	0.107	$s^{0.966}$	$p^{0.596}$	$d^{9.311}$	0.128

Temperature-dependent bonding behaviour of $Au_{25}(SeR)_{18}$ was evident from Au L_3-edge XANES spectra, as shown in Figure 6.6b. Comparing the 50 K and 300 K measurements (both calibrated using the same Au reference material), the E_0 for 300 K shifted *ca.* 0.2 eV lower in energy, which was possibly due to the contraction of the Au-Au framework, effectively lowering the energy levels relative to the core levels. Simulated Au d-DOS spectra (Au 5d states) of surface Au (Figure 6.6c) and staple Au (Figure 6.6d) sites (these sites account for 24/25 of the total Au sites) reproduced this shift of occupied states to lower energy (0.3 eV shift in the Au 5d) when the $Au_{25}(SeCH_3)_{18}$ model was subjected to 3% contraction (to replicate the temperature-dependent bonding found from EXAFS results).

As an aside, an even lower white-line intensity was observed for benzeneselenolate-protected Au_{25} NCs (studied here) than alkylselenolate-protected Au_{25}

NCs (studied by Kurashige *et al.*),[259] where the latter shows a similar white-line intensity to Au foil. This difference in valence band occupation between Au$_{25}$(SePh)$_{18}$ and Au$_{25}$(SeC$_8$H$_{17}$)$_{18}$ NCs could be due to the proximity of the electron-rich aromatic group from the benzeneselenol ligand to Au atoms in staple and surface sites, compared to the long-chain alkylselenol ligand with less electron density donation to Au atoms. This observation implies the sensitivity of Au NC electronic properties to the selenol ligand type (aromatic versus alkyl), which could further influence the stability or the physicochemical properties of the Au NC.

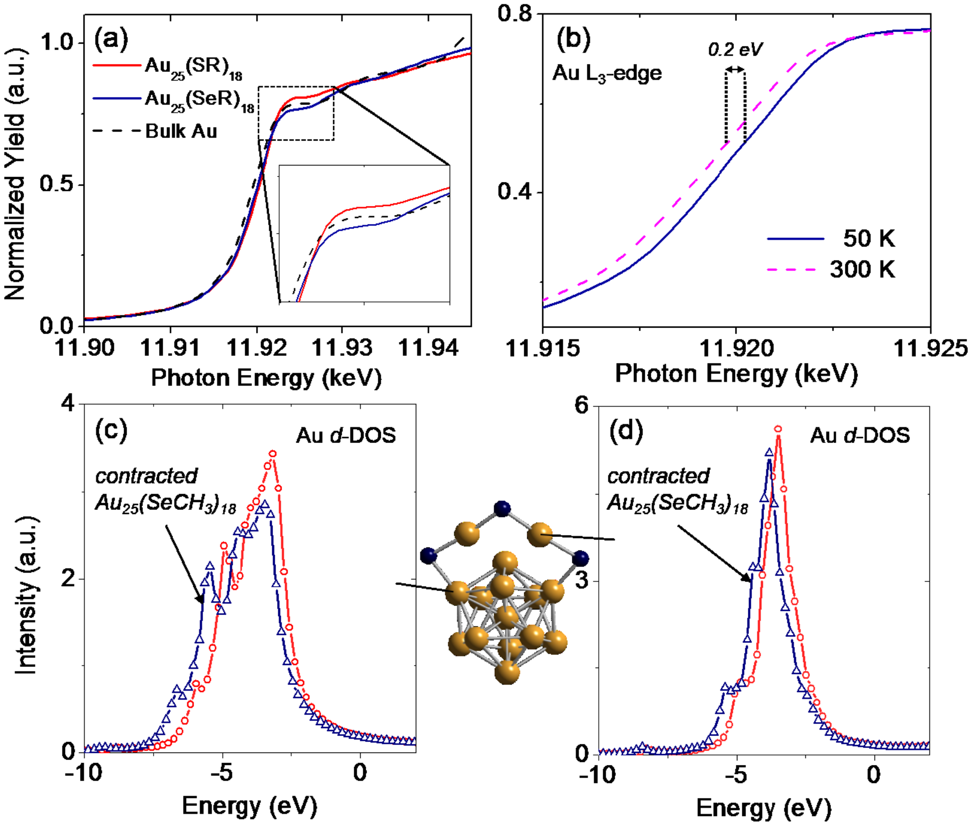

Figure 6.6 (a) Au L$_3$-edge XANES analysis of Au$_{25}$(SeR)$_{18}$ with closer inspection of the white-line intensity (inset) and (b) the absorption edge energy position with respect to temperature. *Ab initio* simulation of Au d-DOS for Au$_{25}$(SeR)$_{18}$ (original model and 3% contracted model) at (c) surface Au sites and (d) staple Au sites.

The Se K-edge XANES spectrum of $Au_{25}(SeR)_{18}$ NCs is shown in Figure 6.7a with free benzeneselenol ligand (HSePh) to illustrate the change in Se electronic properties with, and without, Se-Au bonding. Both the white-line intensity and the E_0 increase for $Au_{25}(SeR)_{18}$ NCs, indicating significant electron density from 4p levels is being shared with proximal Au atoms (staple and surface sites), and possibly being withdrawn by the benzene group. Residual evidence of $Au_{25}(SeR)_{18}$ temperature-dependent bonding behaviour was also observable from Se K-edge XANES, shown in Figure 6.7b. At 300 K, the absorption edge shifted *ca.* 0.6 eV to lower energy along with a decrease in the white-line intensity. Such changes in the electronic properties could be related to the longer Se-C bonding found from the temperature-dependent EXAFS fitting. Since the C atom has a higher electronegativity than the Se atom, Se will lose partial charge to C and a longer Se-C bond will weaken such charge transfer, resulting in a negative shift of E_0 for the 300 K XANES spectrum. In order to identify the origin and significance of each near-edge feature, the Se K-edge XANES and *l*-DOS were simulated for the $Au_{25}(SeCH_3)_{18}$ model and compared with experimental data, as shown in Figure 6.7c. A good agreement was achieved between the simulation and experimental XANES, with 4 consistent near-edge features at similar energies relative to the E_0 (normalized to 0 eV). With this agreement between the model and the measured sample, each feature was interpreted with the unoccupied regions of the C, Se and Au *l*-DOS spectra.

As shown above, protecting the Au NC with a heavier Se-based ligand allows for collection of complementary EXAFS data, enabling a further exploration of the ligand local structure. The Se K-edge XANES spectrum could provide important information on the Se-Au bonding mode for selenolate-protected Au NCs, especially if the total structure is unknown. Figure 6.7d presents the simulated Se K-edge XANES (near-edge features of interest are indicated with dotted lines) and corresponding *l*-DOS spectra (Se d,p-DOS, Au d-DOS and C p-DOS). Feature (*i*), or the white-line, arises from the dipole-allowed transition of Se 1s electrons to empty 4p states. Nevertheless, there appears to be some contribution from C p-DOS in addition to Se d-DOS, indicating the selenolate ligand variety could influence the intensity of the white-line. Indeed, the position of the C p-DOS suggests the change in Se-C bond length identified from EXAFS could influence the first feature in the XANES. Resonance features from Se d-DOS appear to coincide with the near-edge feature following the white-line (*ii*), with some smaller contributions from Se p-DOS and possibly Au d-DOS. Depending on the bonding environment of Se on the surface of Au NCs, this near-edge feature could serve as an indication of the Au-Se bonding mode (*e.g.*, dimeric staple, trimeric staple or bridging motif). Feature (*iii*) also appears to be influenced by Se p-DOS and Au d-DOS empty states. However, features (*iii*) and (*iv*) will be more difficult to interpret experimentally due to spectral broadening and potential overlap with EXAFS oscillations.

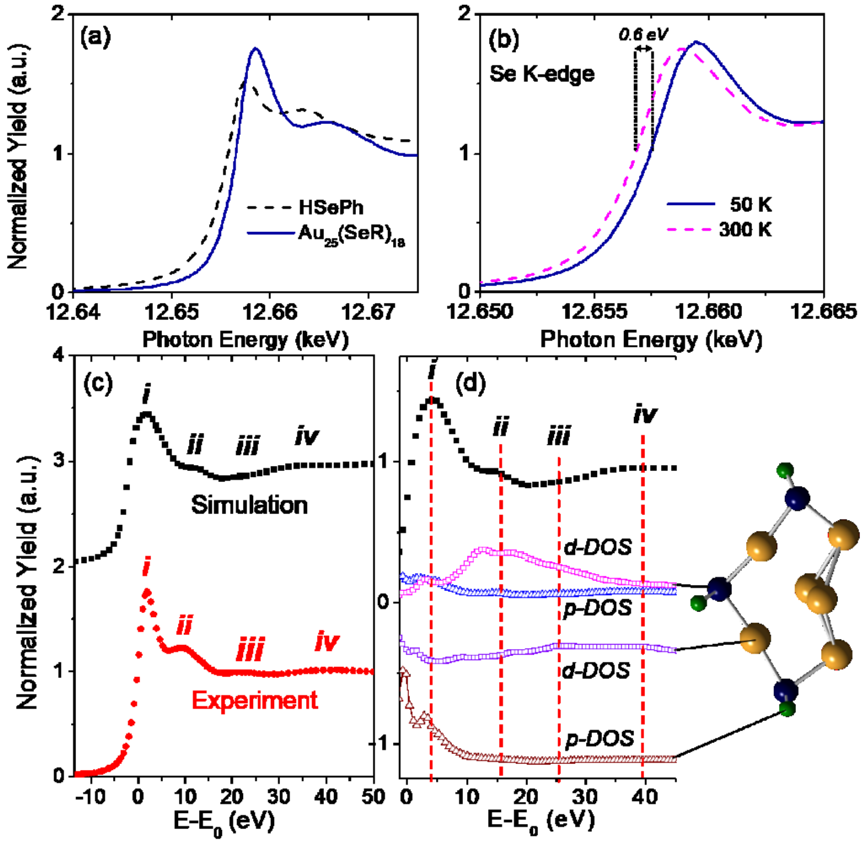

Figure 6.7 (a) Se K-edge XANES analysis of Au$_{25}$(SeR)$_{18}$ and (b) comparison of XANES with temperature. *Ab initio* simulation of (c) Se K-edge XANES (offset) for Au$_{25}$(SeR)$_{18}$ and (d) interpretation of simulated Se K-edge XANES spectrum with unoccupied regions of simulated site-specific *l*-DOS spectra (as indicated with model).

6.6 Conclusion

Selenolate-protected Au$_{25}$ NCs were studied with a detailed site-specific, multi-shell EXAFS analysis from both Au and Se perspectives, at varied temperatures. Significantly longer aurophilic interactions from staple Au to surface Au sites were identified for Au$_{25}$(SeR)$_{18}$, which became shorter with increasing temperature, inducing a contraction of the Au-Au framework in Au$_{25}$. Temperature-dependent structural changes were also observable from Au and Se electronic properties, providing further evidence of the Au-Au framework contraction. These experimental findings were consistent with results from MD-DFT structural modeling and *ab initio* simulations of X-ray spectra. This work brings to light the remarkable bonding behaviour of Au_{25} nanoclusters induced by the selenolate ligand and implies that the selenolate-protected Au NCs behave differently from their thiolate-protected counterparts in the context of aurophilic bonding.

Chapter 7 - Structure and Luminescence Properties of Cyclohexanethiolate- and Glutathione-protected $Au_{18}(SR)_{14}$ Nanoclusters

Manuscript in preparation for submission

Daniel M. Chevrier, Anindita Das, Yao Qiaofeng, Zhentao Luo, Jianping Xie, Rongchao Jin, Víctor Rojas-Cervellera, Carme Rovira, Jaakko Akola, Amares Chatt, Peng Zhang*

7.1 Contributions

D.M.C. conducted all XAFS measurements, analyzed XAFS data, measured UV-Vis absorption and preliminary photoluminescence spectra, and wrote the manuscript. A. D. synthesized and provided the $Au_{18}(SC_6H_{11})_{14}$ *sample. R.J. supervised A.D.. Z.L. synthesized and provided the* $Au_{18}(SG)_{14}$ *sample. Y.Q. conducted photoluminescence measurements for the* $Au_{18}(SC_6H_{11})_{14}$ *sample. J.X. supervised Z.L. and Y.Q.. V.R.-C. and C.R. conducted simulations on the* $Au_{18}(SR)_{14}$ *clusters and were supervised by J.A.. A.C. and P.Z. supervised D.M.C. and helped revise the manuscript.*

7.2 Foreword

The previous chapter demonstrated how changing the head group of the ligand from S to Se had profound effects on the structure and electronic properties of Au NCs. This second study in Project II examines a subtler ligand effect by comparing two thiolate ligands on $Au_{18}(SR)_{14}$ *NCs: cyclohexane and glutathione. In this work, organo-soluble (cyclohexane) and water-soluble (glutathione) thiolate protecting ligands are studied* *with XAFS to reveal the effect of ligand type and solvent-ligand interactions for each $Au_{18}(SR)_{14}$ NC. The difference in Au local structure and ligand are considered to account for the enhanced luminescence property of glutathione-protected $Au_{18}(SR)_{14}$ NCs. This chapter also serves as a transition leading into Chapter 8, where highly luminescent Au NCs protected by biomolecules larger than glutathione are studied.*

7.3 Introduction

The type of thiolate ligand that protects the surface of Au NCs can modulate the electronic and optical properties.[119,271,272] Therefore, the choice of protecting ligand type can be an important consideration, especially for Au NCs intended for catalysis or bioimaging applications. Glutathione (SG) is a tripeptide, composed of glycine, cysteine and glutamate, that is a useful anti-oxidant for living systems. SG protection can improve the biocompatibility of Au NCs, and are widely-studied as water-soluble $Au_n(SR)_m$ NCs.[80,126] SG protection also enables surface functionality for biologically-related applications, though it is uncertain how water-soluble SG ligands modify the structure of Au NCs, which can in turn affect the stability, solubility and electronic properties.

SG-protected Au NCs ($Au_n(SG)_m$) have compositions identical to those found for some organothiolate-protected Au NCs, such as $Au_{15}(SR)_{13}$, $Au_{18}(SR)_{14}$ and $Au_{25}(SR)_{18}$,[80,273] and, hypothetically, have similar Au NC structures. One recurring difference between ligand types is the higher emission yield from $Au_n(SG)_m$ NCs over organothiolate-protected Au NCs of the same composition.[119,274] However, a unified mechanism behind $Au_n(SR)_m$ NC luminescence has not been ascertained, making it difficult to account for the enhancement exhibited by certain types of thiolate ligands.

Current studies have reported intense luminescence from Au NCs is related to surface Au(I)-SR oligomers being in an aggregated state or rigid conformation.[103,123,124,275] Regarding the higher emission from SG specifically, Wu *et al.*[119] suggested that charge is donated from amino acid residues adjacent to cysteine to the Au core. Regardless, their biocompatible surface functionality and luminescence property make $Au_n(SG)_m$ NCs promising nanomaterials for biological imaging and sensing applications.

So far, crystal structures of $Au_n(SG)_m$ NCs have not been determined, which limits an understanding of how the SG ligand influences the local structure and PL property. In this study, XAFS was utilized to compare the local structure and electronic properties of organo-soluble $Au_{18}(SC_6H_{11})_{14}$ NCs and water-soluble $Au_{18}(SG)_{14}$ NCs. Experiments were conducted in the solid-phase and in solution-phase. The small size of $Au_{18}(SR)_{14}$ NCs, and the high SR:Au ratio, was ideal for identifying ligand effects on the Au NC local structure and electronic properties. The PL of each Au_{18} NC was also examined and discussed based on the structural and electronic properties ascertained from XAFS results.

7.4 Materials and Methods

$Au_{18}(SC_6H_{11})_{14}$ NCs were synthesized according to a one-pot protocol by Das *et al.*[276] See the primary reference for further details on the characterization of $Au_{18}(SC_6H_{11})_{14}$ NCs. $Au_{18}(SG)_{14}$ NCs were synthesized according to the protocol by Negishi *et al.*[80]

Au L_3-edge XAFS data was collected for all $Au_{18}(SR)_{14}$ NC samples from the CLS@APS beamline (Sector 20-BM) at the APS. Solid- and solution-phase measurements were conducted at 300 K and atmospheric pressure. XAFS data work-up, sample preparation, EXAFS fitting and error analysis were conducted following the procedures outlined in Section 2.2. The amplitude reduction factor (S_0^2) was fixed at 0.90 for Au L_3-edge EXAFS fitting, as determined by fitting the Au-Au scattering of a Au foil reference with a fixed Au-Au CN of 12. For multi-shell EXAFS fitting, CNs were fixed according to the $Au_{18}(SR)_{14}$ crystal structures. A *k*-range of 3 to 12 Å^{-1} was used for the Fourier transformation of all *k*-space data to *R*-space. A fitting window of 1.5 to 3.5 Å was used for fits. WT-EXAFS plots[208] were generated using Cauchy-type wavelets (order of 100) and a *k*-range of 3 to 12 Å^{-1}.

Quantum mechanics (QM) geometry optimization and molecular mechanics (MM) simulations (together, QM/MM) of $Au_{18}(SC_6H_{11})_{14}$ and $Au_{18}(SG)_{14}$ (gas-phase and solution-phase for each cluster) were conducted in a similar manner to previous work by Rojas-Cervellera *et al.*[277] on $Au_{25}(SR)_{18}$. To briefly summarize, *ab initio* MD simulations were performed using the Car-Parrinello approach,[278] which is based on DFT. The exchange-correlation functional employed the parametrization by Perdew-Burke-Ernzerhoff (PBE),[261] which has been widely used to describe Au NCs. Au atoms were represented by a Goedecker type pseudopotential ($5d^{10}6s^1$ valence structure),[279,280] C, S and O atoms by a Troullier-Martins type[281] and H atoms by a Car-von Barth type.[282] For geometry optimization, an annealing factor was introduced for MD, and its value was gradually incremented from 0.9 to 0.999 to remove kinetic energy from the ionic degrees of freedom. Convergence was reached when the largest nuclear gradient was lower than 5.0×10^{-4} atomic units.

MM simulations with classical potentials were performed using the NAMD software,[283] prior to QM/MM simulations. Ligands and solvent molecules were modelled with the FF99SB and TIP3P force fields, respectively. $Au_{18}(SC_6H_{11})_{14}$ and $Au_{18}(SG)_{14}$ were surrounded by 2000-3000 solvent molecules, with 14 Na^+ ions added to $Au_{18}(SG)_{14}$ to balance the monovalent charge on each SG. Classical MM simulations of 2 to 8 ns was performed to equilibrate the solvent and ligands. The QM/MM interface was modelled by using monovalent carbon pseudopotentials, which saturates the valence of atoms treated with QM at the border (linking atoms).[284] The electrostatic interactions in the interface of QM and MM regions are described by Laio *et al.*[285] The average structure over 7.5 ps of QM/MM simulations at 300 K in gas-phase, or in solvent-phase, was considered for bond distance analysis.

Absorption and PL spectra were measured using CaryBio 100 UV-Vis and PerkinElmer LS-55 fluorescence spectrometers, respectively. Solutions were measured in a standard quartz cuvette (path length of 1 cm) at room temperature. The concentration of each $Au_{18}(SR)_{14}$ NC was adjusted to yield the same peak absorption at the excitation wavelength used for PL measurements (365 nm).

7.5 Results and Discussion

7.5.1 Multi-shell fitting of $Au_{18}(SR)_{14}$

The crystal structure of $Au_{18}(SC_6H_{11})_{14}$, one of the smallest thiolate-protected Au NCs, was reported simultaneously by two research groups.[276,286] Both studies elucidated the same unprecedented HCP Au_9 core (consisting of three staggered Au_3 core units) and combination of Au(I)-SR oligomers, or “staple-like” motifs, protecting the Au_9 core (shown in Figure 7.1). Aliphatic cyclohexanethiol molecules (abbreviated as SC_6H_{11}) were used as the protecting ligand in both studies.

The crystal structure and the Au L_3-edge FT-EXAFS spectrum of $Au_{18}(SC_6H_{11})_{14}$ (Figure 7.1a and b) were first examined to determine a reliable fitting method to account for distinct core and surface bonding environments. EXAFS scattering shells for Au-S bonding, Au-Au core bonding "$Au\text{-}Au_{core}$" (mainly within Au_3 core units, 2.65 to 2.85 Å), Au-Au surface bonding "$Au\text{-}Au_{surf}$" (between Au_3 core units and on Au_9 core surface, 2.85 to 3.05 Å) and Au-Au aurophilic bonding "$Au\text{-}Au_{auro}$" (between staple Au and the Au core, 3.05 to 3.50 Å) were assigned from inspection of the Au-Au bonding distribution, displayed in Figure 7.2. In the FT-EXAFS range of 1.5 to 3.5 Å, these shells account for core, surface and metal-ligand bonding environments. There is a smaller amount of separation between the bonding distributions of $Au\text{-}Au_{core}$ and $Au\text{-}Au_{surf}$ shells, in comparison to $Au\text{-}Au_{surf}$ and $Au\text{-}Au_{auro}$; nevertheless, these shells both represent Au-Au bonding in the Au_9 core and can be considered together as Au core bonding. Viewing the $Au_{18}(SR)_{14}$ structure from the end-on perspective (Figure 7.1c, right), $Au\text{-}Au_{core}$ and $Au\text{-}Au_{surf}$ bonding occur in the middle of the cluster, mostly related to the Au_9 core. The $Au\text{-}Au_{auro}$ shell can be seen to account for the surface interface between Au core and Au(I) in the ligand shell in a pseudo-symmetric six-pointed star configuration.

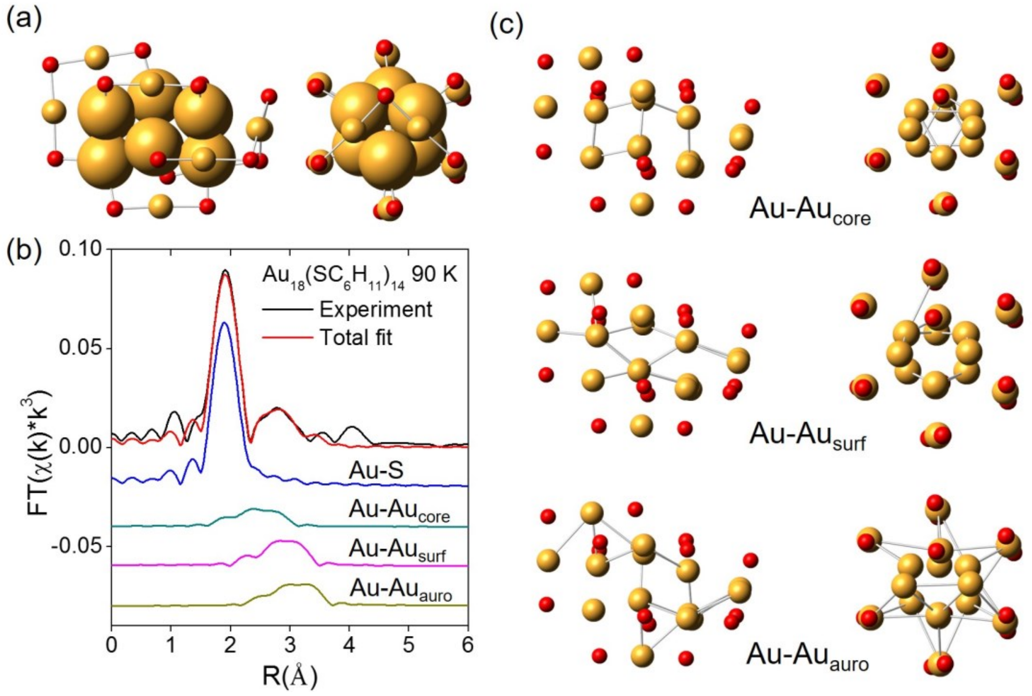

Figure 7.1 (a) Side-on (left) and end-on (right) view of the $Au_{18}(SR)_{14}$ crystal structure (Au atoms in Au_9 core (large yellow), Au atoms in staple units (yellow), and S atoms (red) (C and H atoms omitted)). (b) Au L_3-edge FT-EXAFS spectrum of solid-phase $Au_{18}(SC_6H_{11})_{14}$ at 90 K with EXAFS multi-shell fit and individual contributions from each scattering shell. (c) Distinct Au-Au scattering shells employed for $Au_{18}(SR)_{14}$ EXAFS multi-shell fit.

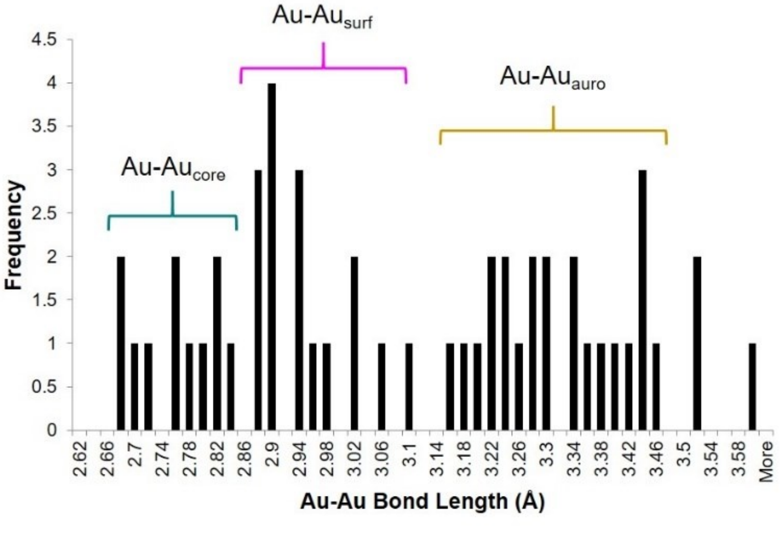

Figure 7.2 Distribution of Au-Au bond lengths from the crystal structure of $Au_{18}(SC_6H_{11})_{14}$.

Multi-shell Au L_3-edge EXAFS fitting was initially conducted for $Au_{18}(SC_6H_{11})_{14}$ NCs in the solid-phase at 90 K to verify the assignment of each bonding environment. The fitted EXAFS spectrum and individual scattering paths are shown in Figure 7.1b with EXAFS parameters for each shell in Table 7.1. The distances refined from the EXAFS fit corresponded well with the average bond distances calculated from the crystal structure, indicating the suitability of the designated scattering shells to account for each distinct bonding environment. Debye-Waller factors were within the expected range for small $Au_n(SR)_m$ NCs from short Au-S bonding (~0.002 Å^2) to longer Au-Au interactions (~0.01 Å^2) based on previous EXAFS studies (Chapters 3 to 6).

Table 7.1 EXAFS multi-shell fitting results for $Au_{18}(SC_6H_{11})_{14}$ in solid-phase at 90 K. CNs were fixed according to the theoretical value determined by inspection of the crystal structure. The average bond distance for each shell from the $Au_{18}(SC_6H_{11})_{14}$ crystal structure*.[276] Uncertainties in fitted parameters are shown in parentheses.

Shell	CN	R (Å)	σ^2 (Å^2)	ΔE_0 (eV)
Au-S	1.56	2.299(7) (2.326*)	0.0013(2)	-1(2)
Au-Au_{core}	1.33	2.69(3) (2.743*)	0.009(3)	-1(2)
Au-Au_{surf}	1.78	3.07(4) (2.940*)	0.008(3)	-1(2)
Au-Au_{auro}	2.44	3.29(5) (3.330*)	0.010(3)	-1(2)

7.5.2 Ligand effect on $Au_{18}(SR)_{14}$

After a multi-shell EXAFS fitting method was established for $Au_{18}(SR)_{14}$ NCs, the same approach was applied to EXAFS data collected at room temperature (300 K) in solid-phase for $Au_{18}(SC_6H_{11})_{14}$ and the SG-protected analog, $Au_{18}(SG)_{14}$. *k*-space spectra for $Au_{18}(SC_6H_{11})_{14}$ and $Au_{18}(SG)_{14}$ in solid-phase at 300 K are shown in Figure 7.3. FT-EXAFS spectra for $Au_{18}(SC_6H_{11})_{14}$ and $Au_{18}(SG)_{14}$ in the solid-phase at 300 K, are shown in Figure 7.4a and 7.4b, respectively. EXAFS fitting results for each ligand type are presented in Table 7.2 and 7.3, respectively. Although there were deviations in the average distances between the same Au-Au shell of each $Au_{18}(SR)_{14}$ NC, the resulting fits generally confirm the core and surface environments have the same bonding arrangement and configuration despite their different ligand types. This finding was further substantiated by similar characteristic absorption features observed for both NCs (shown below in Figure 7.8a). Debye-Waller factors of each shell were also similar in magnitude for both ligand types supporting the similar structural framework in the solid-phase.

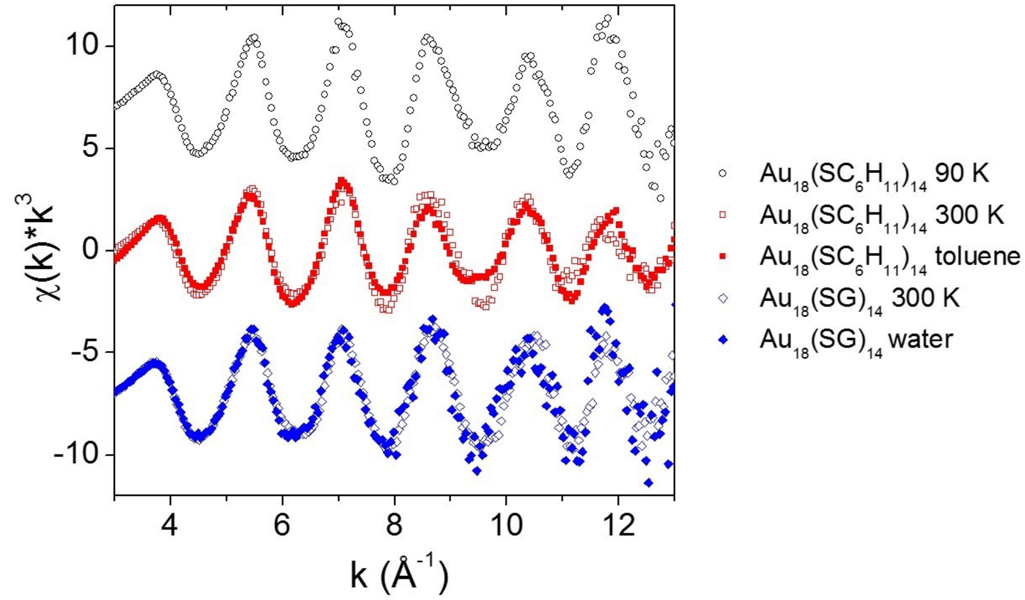

Figure 7.3 *k*-space spectra of $Au_{18}(SC_6H_{11})_{14}$ and $Au_{18}(SG)_{14}$ NCs in solid-phase and solution-phase.

Distances for $Au\text{-}Au_{core}$ and $Au\text{-}Au_{surf}$, representing the Au_9 HCP core structure, were closer together in distance for $Au_{18}(SG)_{14}$. Additionally, the $Au\text{-}Au_{auro}$ distance for $Au_{18}(SG)_{14}$ was shorter than for $Au_{18}(SC_6H_{11})_{14}$. The shortening of Au-Au bonds on the surface (> 2.85 Å) could occur from the higher spatial demand of SG ligands on the surface of the Au NC. This result implied that the Au-Au framework of $Au_{18}(SR)_{14}$ is responsive and adaptive to the ligand size while Au-S bonding does not change significantly in distance or disorder. In order for the aurophilic interactions between staple Au and surface Au to decrease by the observed *ca*. 0.1 to 0.2 Å, Au(I)-SR surface oligomer structures are predicted to undergo a conformational change by twisting or bending, possibly similar to dimeric staple contraction in Chapter 6.

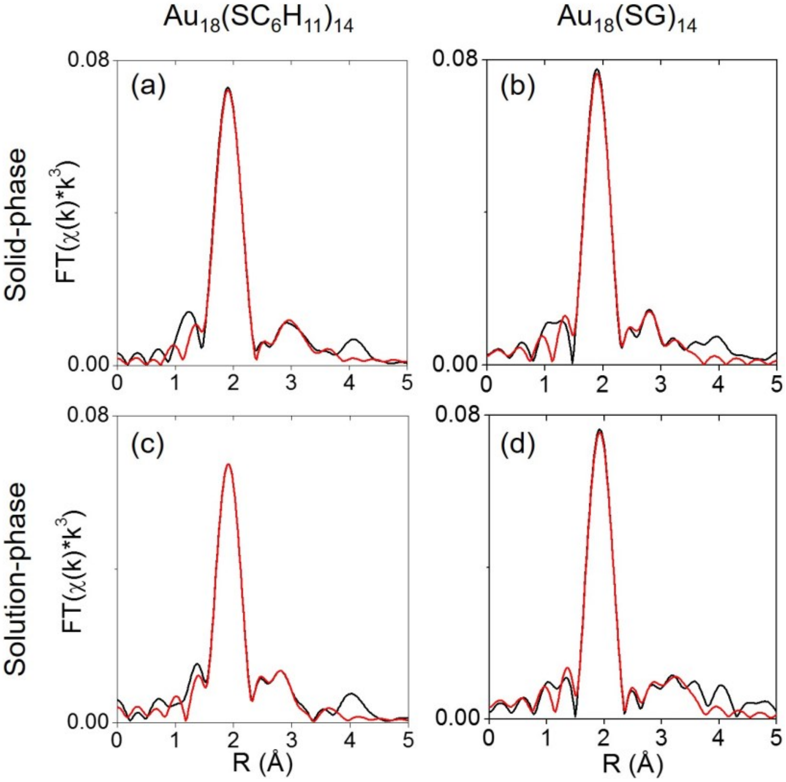

Figure 7.4 Au L_3-edge FT-EXAFS spectra of $Au_{18}(SC_6H_{11})_{14}$ and $Au_{18}(SG)_{14}$ in solid-phase (a and b, respectively) and in solution-phase (c and d, respectively) (black line) with EXAFS multi-shell fitting (red line).

The thiolate ligand type is anticipated to affect electron density in Au valence levels for $Au_{18}(SR)_{14}$ based on the covalent nature of the Au-S bond and the high SR:Au ratio (every Au atoms bonds to at least one S). Au L_3-edge XANES spectra are presented in Figure 7.5, showing a lower white-line intensity for $Au_{18}(SG)_{14}$ in the solid-phase, which is indicative of a more highly occupied 5d level. It is possible that cysteine, and adjacent amino acid residues, could donate additional electron density to surface Au atoms. This was previously proposed by Wu *et al.*[119] to explain the higher emission from $Au_{25}(SG)_{18}$. The electronic properties are revisited in the following section.

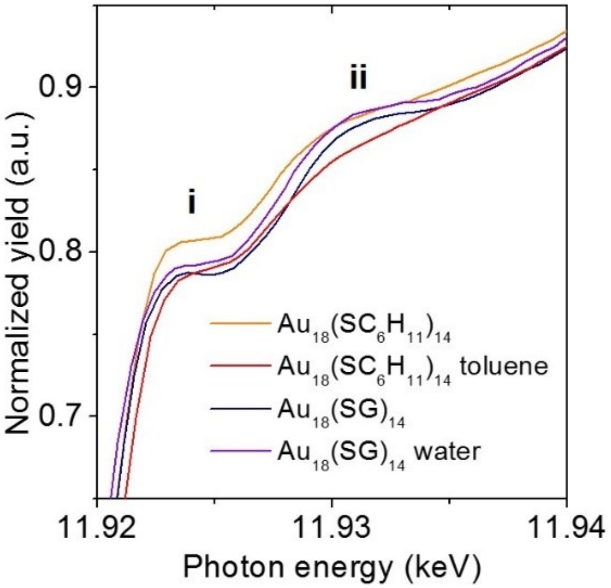

Figure 7.5 Au L_3-edge XANES of $Au_{18}(SC_6H_{11})_{14}$ and $Au_{18}(SG)_{14}$ in solid-phase and in solution-phases.

Table 7.2 Au L_3-edge EXAFS fitting results for $Au_{18}(SC_6H_{11})_{14}$. CNs were fixed according to the theoretical value determined by inspection of the crystal structure. Uncertainties in fitted parameters are shown in parentheses.

Shell	CN	R (Å) (300 K / toluene)	σ^2 (Å^2) (300 K / toluene)	ΔE_0 (eV)
Au-S	1.56	2.303(8)/2.318(3)	0.0024(3)/0.0034(1)	-2(2)/1.0(6)
Au-Au$_{core}$	1.33	2.65(5)/2.717(7)	0.014(6)/0.0073(5)	-2(2)/1.0(6)
Au-Au$_{surf}$	1.78	3.11(3)/2.94(6)	0.008(3)/0.03(1)	-2(2)/1.0(6)
Au-Au$_{auro}$	2.44	3.34(4)/3.39(3)	0.012(4)/0.021(5)	-2(2)/1.0(6)

Table 7.3 Au L_3-edge EXAFS fitting results for $Au_{18}(SG)_{14}$. CNs were fixed according to the theoretical value determined by inspection of the crystal structure. Uncertainties in fitted parameters are shown in parentheses.

Shell	CN	R (Å) (300 K / water)	σ^2 (Å^2) (300 K / water)	ΔE_0 (eV)
Au-S	1.56	2.298(5)/2.319(6)	0.0019(2)/0.0019(2)	-1(1)/0(1)
Au-Au_{core}	1.33	2.74(3)/2.73(4)	0.011(4)/0.012(4)	-1(1)/0(1)
Au-Au_{surf}	1.78	3.00(4)/2.99(4)	0.009(3)/0.010(4)	-1(1)/0(1)
Au-Au_{auro}	2.44	3.23(5)/3.24(3)	0.015(6)/0.010(2)	-1(1)/0(1)

7.5.3 Solvent effect on $Au_{18}(SR)_{14}$

Previous XAFS studies have demonstrated $Au_n(SR)_m$ NC local structure can change in response to temperature (Chapter 4 and Chapter 5), ligand head group[256,287] (Chapter 6) and solvation conditions.[191,196,233] Owing to the versatility of XAFS measurements and the sensitivity of fitting analyses, probing the solution-phase of $Au_n(SR)_m$ NCs with XAFS may offer new insights on solvation-induced structural changes. In order to assess the response of each ligand type to solvation, XAFS measurements for $Au_{18}(SC_6H_{11})_{14}$ in toluene and $Au_{18}(SG)_{14}$ in water were conducted.

EXAFS fitting results for $Au_{18}(SC_6H_{11})_{14}$ NCs in toluene indicated a structural change in both Au core and Au-ligand bonding environments (Figure 7.4 and Table 7.2). Au-S bond length increased by 0.015 Å, along with an increase in the Debye-Waller factor. A similar solvation-induced increase in the Au-S bond length and disorder was observed for $Au_{25}(SR)_{18}$ and $Au_{38}(SR)_{24}$ (SR = phenylethanethiolate for both NCs) when dissolved in toluene.[196,233] Compared to the solid-phase, Au-Au interactions within the Au_9 core were slightly longer at 2.72(1) Å and the surface Au-Au interactions on the Au_9

core had contracted significantly, by ~0.2 Å. Aurophilic interactions slightly increased in distance upon solvation, which could be coupled with the increase of Au-S bonding distance, moving the Au staple sites away from the Au core. Similarly, but not as prominently, $Au_{25}(SR)_{18}$ NCs in toluene saw a small contraction of Au-Au bonding related to the Au core and an increase in aurophilic interaction distance.[196] Results for $Au_{18}(SC_6H_{11})_{14}$ suggest toluene molecules could be gaining access to space between ligands and interacting with cyclohexane substituents, pushing the S and Au staple sites away from the Au core. Such solvent-ligand interactions could also be the cause of the enhanced surface disorder reflected by the increase in Debye-Waller factors for scattering shells representing the surface of the $Au_{18}(SR)_{14}$ (Au-S, $Au\text{-}Au_{surf}$ and $Au\text{-}Au_{auro}$).

Interestingly, $Au_{18}(SG)_{14}$ NCs in water had virtually no change of surface or core Au-Au bonding in comparison to the solid-phase. Au-Au distances and Debye-Waller factors were similar for both measurements. The one consistent structural change observed for both ligand types, however, was the lengthening of Au-S bonding upon solvation. Unlike $Au_{18}(SC_6H_{11})_{14}$, there was no increase in disorder for Au-S in $Au_{18}(SG)_{14}$. From this solid- to solution-phase comparison, SG ligands appeared to efficiently encapsulate the $Au_{18}(SR)_{14}$ NC, preventing ligand-solvent interactions closer to the Au core.

QM/MM simulations were conducted to provide support of solvation-induced structural changes for $Au_{18}(SR)_{14}$ NCs. Weak interactions between toluene molecules and a $Au_{18}(SC_6H_{11})_{14}$ cluster were evident from the simulation by the modulated arrangement of cyclohexanethiolate ligands on the surface compared to the gas-phase simulation of $Au_{18}(SC_6H_{11})_{14}$ (no toluene molecules). This can be observed by inspection of the end-on view of $Au_{18}(SC_6H_{11})_{14}$ in Figure 7.6, where cyclohexane substituents in staple structures were in more of an eclipsed conformation for the toluene-phase simulation of $Au_{18}(SC_6H_{11})_{14}$. The ligand rearrangement resulted from toluene molecules that occupied space between staple structures, perpendicularly interacting with cyclohexane rings where the aromatic ring edge is pointed toward the middle of the cyclohexane ring. Furthermore, Figure 7.6 presents the averaged distribution of bond lengths for simulated gas-phase and toluene-phase of $Au_{18}(SC_6H_{11})_{14}$. The Au-Au bonding distribution is narrower for toluene-phase $Au_{18}(SC_6H_{11})_{14}$, with Au-Au bond lengths range from 2.6 to 3.0 Å, instead of 2.6 to 3.2 Å for the gas-phase. This narrower distribution is in agreement with the contraction of Au-Au initially identified from EXAFS fitting of $Au_{18}(SC_6H_{11})_{14}$ in toluene.

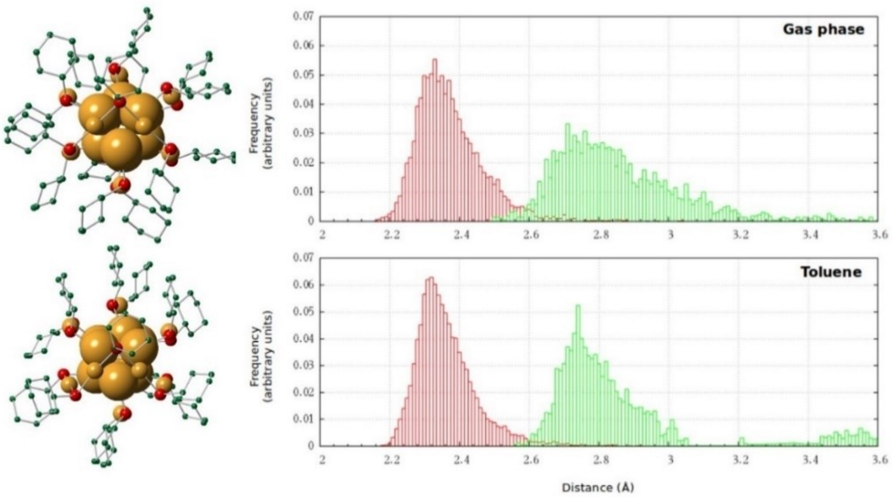

Figure 7.6 Simulated structures of $Au_{18}(SC_6H_{11})_{14}$ in gas-phase and in toluene-phase with average Au-S (red) and Au-Au (green) bonding distributions.

QM/MM simulations were performed in a similar manner for the $Au_{18}(SG)_{14}$ system, except with water molecules simulating the solvent. Figure 7.7 displays the bonding distribution for the gas-phase and aqueous-phase calculation of $Au_{18}(SG)_{14}$. The

SG ligand is removed from each model shown in this case, since it is difficult to understand subtle ligand changes without three-dimensional (3-D) inspection. Nevertheless, the bonding distribution shows a similar spread for the Au-Au distances between the gas-phase and the aqueous-phase, with the majority of Au-Au bond lengths occurring between 2.6 to 3.3 Å. Additional calculations of HOMO-LUMO transitions using DFT are currently underway for each ligand system.

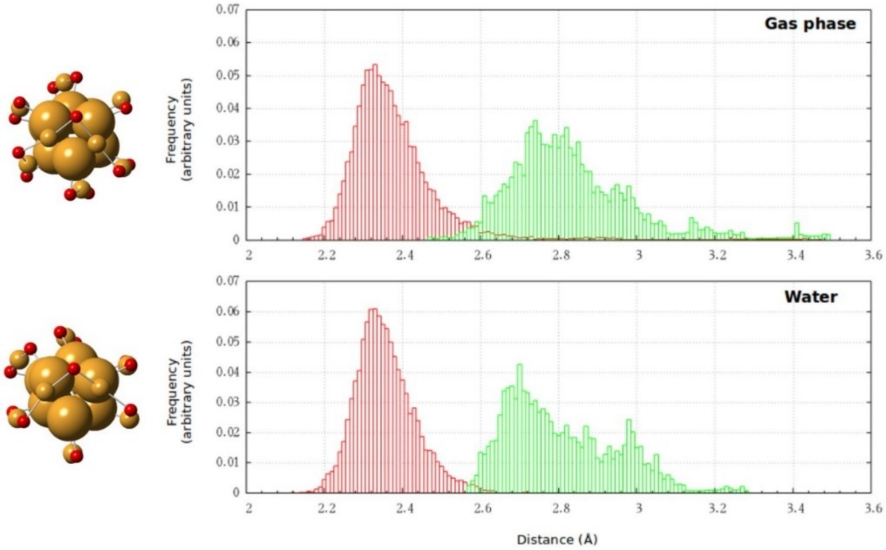

Figure 7.7 Simulated structures of $Au_{18}(SG)_{14}$ in gas-phase and in aqueous-phase with average Au-S (red) and Au-Au (green) bonding distributions.

The electronic properties were revisited after EXAFS and simulation results to consider the effect of solvation. A decrease in the Au L_3-edge white-line intensity (i) and the following near-edge feature (ii) is evident for toluene-phase $Au_{18}(SC_6H_{11})_{14}$ NCs in Figure 7.5. $Au_{38}(SR)_{24}$ NCs in toluene also showed a small decrease in the white-line intensity in comparison to the solid-phase.[233] For $Au_{18}(SG)_{14}$ in water, there is only a slight increase in the labeled XANES features in comparison to the solid-phase. Therefore, the expansion in Au-S bond length (as observed for both ligand types in solution) is unlikely to account for the marked white-line intensity decrease for $Au_{18}(SC_6H_{11})_{14}$ in toluene. The localization of 5d electron density could then potentially originate from the Au core structural response to toluene, as seen with the surface Au-Au bond contraction (from 3.1 to 2.9 Å) and decrease in core Au-Au disorder (from 0.014 to 0.007 Å^2, suggesting more rigid Au-Au bonding).

7.5.4 Photoluminescence properties and structural rigidity

The structural response from ligand type and solution-phase revealed significant differences between $Au_{18}(SC_6H_{11})_{14}$ and $Au_{18}(SG)_{14}$. In particular, Au-Au bonding associated with the Au NC surface, and the Au-SR interface, was more rigid for the larger SG ligands and was not significantly perturbed in water. On the other hand, toluene molecules were shown to disturb cyclohexanethiolate ligands, which caused a contraction of the Au core and increased structural disorder on the surface of $Au_{18}(SR)_{14}$ NCs. From these results, a correlation of solution-phase local structure and optical properties was made to examine the role of ligand and Au-Au framework on the PL of $Au_{18}(SR)_{14}$ NCs.

Absorption spectra for both clusters in Figure 7.8a have features at similar energies, which confirmed the same composition and structure of $Au_{18}(SR)_{14}$ NCs for both thiolate ligand types. In order to closely compare the PL intensity and energy, the concentration of each NC was adjusted to yield identical absorption at 365 nm, which was the excitation wavelength used for measuring the PL. With photo-excitation at 365 nm, both NCs had emission in the red to NIR region (650 to 850 nm) with the maximum peak slightly red-shifted for $Au_{18}(SG)_{14}$ (Figure 7.8b and 7.8c). The emission intensity was almost two times higher for $Au_{18}(SG)_{14}$.

A large Stoke's shift (> 400 nm) is seen here for $Au_{18}(SR)_{14}$ NCs. This has been attributed to LMCT-type PL for other Au(I)-SR complexes and polymers.[288,289] $Au_{25}(SR)_{18}$ NCs have a similar emission energy around 700 to 800 nm for both phenylethanethiolate and SG ligands, with stronger emission from $Au_{25}(SG)_{18}$.[119,271] In fact, many of the $Au_n(SG)_m$ NCs isolated by Negishi *et al.*[80] exhibited emission in the range of 730 to 885 nm (1.7 to 1.4 eV).

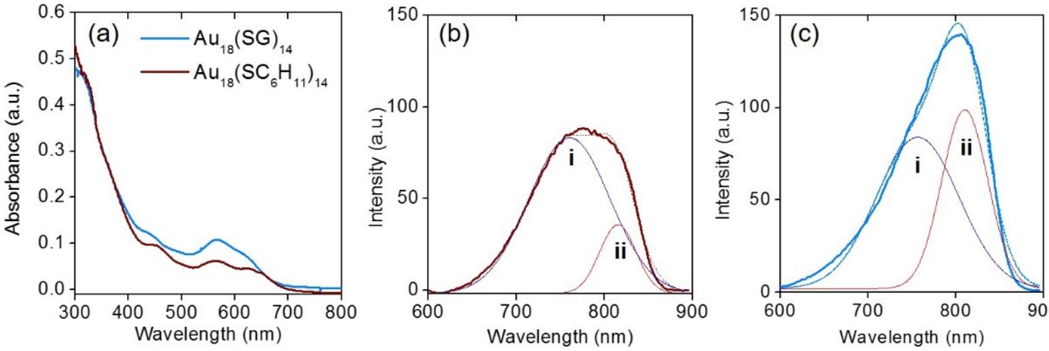

Figure 7.8 (a) UV-Vis absorption spectra and PL spectra (excitation @ 365 nm) of (b) $Au_{18}(SC_6H_{11})_{14}$ and (c) $Au_{18}(SG)_{14}$.

Two components contribute to each PL spectrum, centred around 755 nm and 810 nm. Interestingly, the higher energy component (i) was comparable in shape and intensity for both ligands and the lower energy component (ii) was significantly more intense for $Au_{18}(SG)_{14}$, causing a change in the overall emission shape. Considering the similar intensity of the first higher energy emission peak (i), it must originate from a shared electronic and structural characteristic between the two clusters. From EXAFS results, the Au-S bonding environment and the general $Au_{18}(SR)_{14}$ framework appeared to be consistent, and if the luminescence is governed by LMCT from S to Au, this would explain the similar PL band shape and intensity.

The lower energy component of the PL spectrum (ii), on the other hand, increased by three times for $Au_{18}(SG)_{14}$. Aurophilic interactions between Au(I)-SR complexes have been known to cause splitting in HOMO-LUMO electronic levels causing the emission to red-shift.[288,290] Moreover, enhanced emission from aggregated or rigidified Au(I)-SR surface oligomers has been attributed to ligand to metal-metal charge transfer (LMMCT).[121,123,275] Thus, the enhancement of the lower energy emission (ii) contribution could originate from stronger aurophilic interactions on the surface of $Au_{18}(SG)_{14}$, where Au(I)-Au(I) interactions ($Au\text{-}Au_{auro}$) were shorter by ~0.15 Å and Debye-Waller factors for surface Au-Au shells ($Au\text{-}Au_{surf}$ and $Au\text{-}Au_{auro}$) were considerably lower, in comparison to $Au_{18}(SC_6H_{11})_{14}$.

Since the findings of Au-Au surface rigidity for $Au_{18}(SG)_{14}$ NCs rely on the EXAFS fitting process where a degree of uncertainty is inevitable in each fitted parameter, an alternative approach for determining the origin and relative intensity of EXAFS scattering features was demonstrated using a wavelet-transformed EXAFS (WT-EXAFS) analysis.[208] Comparing the Au-Au scattering peaks between FT-EXAFS spectra for ultra-small Au NCs is challenging since Au-Au bonding can range from ~2.7 to 3.5 Å in distance, and the intensity of these scattering features can be relatively weak compared to Au-S scattering. WT-EXAFS improves on conventional FT-EXAFS spectra by adding resolution from *k*-space contributions, providing a means to discern scattering features according to backscattering element type, and to separate multiple scattering features that coincide with single scattering. In this case, analysis of WT-EXAFS spectra was used to distinguish the intensity of different Au-Au scattering environments.

Figure 7.9 presents the WT-EXAFS for both ligand types in their respective solvents to revisit the structural rigidity determined from EXAFS fitting results. The strongest feature (i) comes from Au-S scattering, which also dominates the FT-EXAFS in Figure 7.1b. With the WT-EXAFS method, Au-S multiple scattering (iii) can be seen more clearly in both spectra at a distance of 3.8 Å (not phase corrected) and centred at 6 Å^{-1}. The multiple scattering feature was more intense for $Au_{18}(SG)_{14}$, which indicated less structural disorder in the Au(I)-SR layer. Comparing the Au-Au scattering region (ii) for both ligand types, the strongest Au-Au scattering peaks are located around 2.8 Å for $Au_{18}(SC_6H_{11})_{14}$ and at 3.2 Å for $Au_{18}(SG)_{14}$. This supported the contracted Au core for $Au_{18}(SC_6H_{11})_{14}$ in toluene and the more rigid aurophilic interactions for $Au_{18}(SG)_{14}$ in water. Together, the more intense Au-S multiple scattering and Au-Au scattering related to aurophilic interactions for $Au_{18}(SG)_{14}$ support a more rigid surface Au(I)-SR layer when SG is the protecting ligand. Revisiting the PL properties of $Au_{18}(SG)_{14}$, this offers an explanation for the enhanced emission based on rigidified Au(I)-SR surface oligomers.

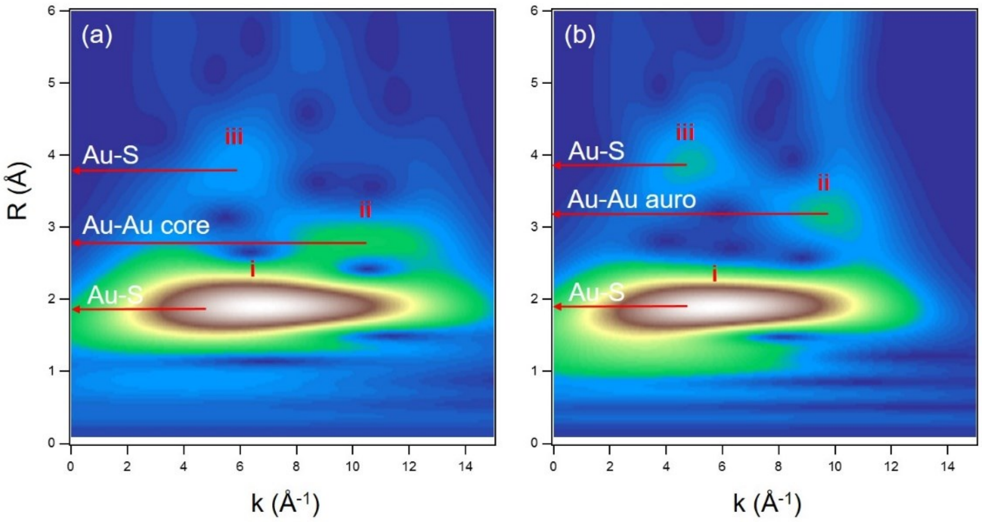

Figure 7.9 WT-EXAFS plots of (a) $Au_{18}(SC_6H_{11})_{14}$ in toluene and (b) $Au_{18}(SG)_{14}$ in water.

7.6 Conclusion

The local structure and PL properties of $Au_{18}(SC_6H_{11})_{14}$ and $Au_{18}(SG)_{14}$ were studied with XAFS and fluorescence spectroscopy to uncover the effect of thiolate ligand type and solvation on $Au_{18}(SR)_{14}$ NCs. A multi-shell EXAFS fitting method was established for $Au_{18}(SR)_{14}$ NCs to account for Au core, Au surface and Au(I)-SR interactions. When the ligand type was compared in the solid-phase, $Au_{18}(SG)_{14}$ NCs had shorter surface Au-Au bonding and higher Au 5d electron density. In solution, Au-S bonding lengthened by ~0.02 Å for both ligand types, but only $Au_{18}(SC_6H_{11})_{14}$ had a substantial change in the Au-Au NC framework, which was identified as a contraction of the Au core. Solvent-ligand interactions were further investigated using QM/MM simulations to explore structural changes in the solution-phase. Lastly, it was revealed that the SG ligand rigidifies Au(I)-Au(I) interactions within the Au(I)-SR surface layer of $Au_{18}(SG)_{14}$ NCs, which could help account for the enhanced luminescence property.

Chapter 8 - Structure of Highly Luminescent Protein-protected Gold Nanoclusters

Manuscript submitted

Daniel M. Chevrier, Viraj Dhanushka Thanthirige, Zhentao Luo, Steve Driscoll, Peter Cho, Mark A. MacDonald, Ramakrishna Guda, Jiangping Xie, Erin R. Johnson, Nanfeng Zheng, Amares Chatt, Peng Zhang*

8.1 Contributions

D.M.C. prepared protein-protected Au NC samples, conducted XAFS experiments, analyzed XAFS data, and wrote the manuscript. V.D.T. performed temperature-dependent and time-resolved photoluminescence measurements. R.G. supervised V.D.T.. Z.L. synthesized $Au_{10}(SG)_{10}$ *NCs. J.X. supervised Z.L.. S.D. performed DFT calculations. E.J. supervised S.D.. P.C. and M.A.M. contributed to preliminary preparation of protein-protected Au NC samples. A.C. and P.Z. supervised D.M.C. and helped revise the manuscript. N.F. helped revise the manuscript.*

8.2 Foreword

Au NCs studied in previous chapters were protected by small, organo-soluble thiolate ligands (aside from benzeneselenol in Chapter 6). In Chapter 7, water-soluble glutathione-protected Au NCs with moderate photoluminescence were found to have a more rigid Au(I)-SR surface layer than organothiolate-protected Au NCs. In the same direction of highly luminescent and water-soluble Au NCs, protein-protected Au NCs are *another category of ligand-protected Au NC materials that exhibit remarkable stability and excellent photo-physical properties. This first study in Project III continues on from the effect of protecting ligand in Project II to investigate the structure, photoluminescence and formation of bovine serum albumin (BSA)-protected Au NCs using XAFS and supporting techniques. From the high number of cysteine residues per BSA protein, it was anticipated that Au NCs would be completely thiolate-protected based on the chemical affinity of Au for S. EXAFS fitting methodologies employed in previous chapters were utilized to uncover the local structure of Au NCs inside the BSA protein. This extended study identifies a specific Au(I)-SR structural unit for highly luminescent Au NCs inside the BSA protein that is in a rigidified state (similar to Chapter 7). Overall, an EXAFS approach for identifying the structure of small Au clusters encapsulated by a large globular protein is demonstrated in this work.*

8.3 Introduction

Composed of only tens or hundreds of Au atoms, Au NCs are highly stable 1 to 2 nm diameter particles with distinctive core/surface structures and molecule-like optical properties.[89,291–293] Due to the high surface area and quantum confinement effects of Au NCs, stabilizing ligands play an important role in directing their structure and properties. Besides small thiolate ligands, large and more complex ligand types such as proteins and other biomolecules have been implemented to stabilize various sizes of Au particles, which further improves their integration into biomedical-related applications.[143,294] Concurrently with the development of these new bionanomaterials, the biomolecular self-assembly process that controls the formation of Au nanostructures has intrigued researchers for years.[144,295,296]

Protein-protected Au NCs are a unique class of bionanomaterials with intense luminescence and highly specific chemical recognition properties suitable for biological imaging and chemical sensing applications.[71,151,166,173,176] Conveniently, and rather remarkably, protein molecules can act as both the stabilizing ligand and the structure-directing agent to facilitate the formation of ultra-small Au NCs. This was successfully shown recently where highly luminescent Au NCs (QY = ~6 %, over 10^8 times higher than bulk Au) were stabilized by bovine serum albumin (BSA) using a facile one-pot, protein-directed synthesis.[152] This approach reduces the number of steps in Au NC synthesis and avoids the use of harsh chemical reagents, making it greener than general Au NC syntheses.

Despite the promising luminescence property of BSA-protected and other protein-protected Au NCs,[178,297] little is known about the biomolecular self-assembly and atomic structure of Au NCs inside the protein. Complicating this unresolved puzzle are the reported inconsistencies on the relative Au(0)/Au(I) composition measured from XPS and the disparity between Au_nBSA compositions proposed from MS.[70,71] To further complicate the problem, the Au NC structure inside the BSA protein has been hypothesized to be $Au_{25}(SR)_{18}$,[92,95] even though they do not share similar PL properties.

In order to advance this new class of bionanomaterials, identifying the atomic-level structure and self-assembled formation of Au NCs in the protein molecule would help determine the origin of protein-protected Au NC luminescence and lead to better-guided developments in sensing and imaging technologies. Experimental and investigative techniques beyond standard laboratory methods (*e.g.,* FT-IR, XPS, MS) were applied in order to reveal more informative and reliable details on Au NC structure and properties. Synchrotron-based XAFS spectroscopy was critical in this regard, as it provided the ability to resolve interactions between few-atom Au NCs and stabilizing protein residues from an element-specific perspective. In conjunction with other experimental techniques and in-depth analyses, the atomic structure of Au NCs in BSA was surprisingly found to resemble interlocked gold-thiolate (Au-SR) ring structures, which slowly develop over the course of the protein-directed synthesis. Additional experiments and quantum calculations are presented that consistently support the atomic structure of Au NCs in BSA. The distinctive red luminescence property, as it relates to the newly identified structure, is also examined.

8.4 Materials and Methods

AuBSA NCs were synthesized following a procedure from Xie *et al.*[152] A 5 mL aqueous solution of bovine serum albumin (50 mg/mL) was incubated at 37°C with vigorous mixing. Once BSA dissolved (5 min), a 5 mL aqueous solution of $HAuCl_4$ (10 mM) was added to the reaction vessel containing BSA. 500 μL of a 1 M NaOH solution was added to the reaction 2 min later, raising the pH of solution to ~11 to 12. The reaction proceeded with incubation and stirring for at least 12 h to obtain the final product with maximum luminescence. Nanopure water (18.2 MΩ-cm) was used to make up all solutions for the synthesis. For the time-dependent study, samples were taken at 0, 1, 2, 3, 6, 12 and 36 h from the reaction, immediately frozen and then lyophilized for further studies (0 h sample was taken as soon as NaOH was added to the reaction).

Luminescence was preserved after the lyophilisation (see Figure 8.1). Samples measured for multi-shell EXAFS fitting were dialyzed against nanopure water (18.2 MΩ-cm) for 24 h with fresh nanopure water changed every 8 h. For destabilizing AuBSA NCs via enzymatic digestion, 0.5 mL of a freshly prepared 0.1 mg/mL trypsin solution was added to 1 mL of the purified AuBSA NCs. This solution was mixed and incubated for 24 h at 37°C.

Chemicals used include $HAuCl_4 \cdot 3H_2O$ (Alfa Aesar, 99.99% metal basis), bovine serum albumin (BSA) (Sigma Aldrich, ≥96% purity), NaOH (ACP Chemicals, ≥97.0% purity), tetraoctylammonium bromide (TOABr, 98%), Nanopure water (Barnstead millipore system, 18.2 MΩ-cm), dialysis tubing (Fisherbrand, 12000-14000 MWCO). All chemicals were used without further purification.

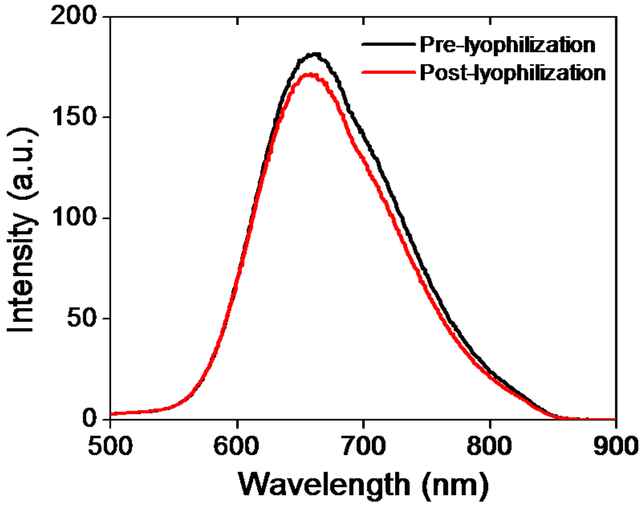

Figure 8.1 Photoluminescence of AuBSA NCs (12 h sample) before and after lyophilization.

The synthesis of $[Au(I)\text{-}SC_{12}H_{25}]_n$ (Au(I)-SR polymer reference) closely followed a protocol by Cha *et al.*[289] Briefly, a 0.1 M tetrahydrofuran (THF) solution of *n*-dodecanethiol was added to a 0.02 M THF solution of $HAuCl_4 \cdot 3H_2O$ of equal volume.

The mixture was stirred for 1 day and a white precipitate was formed. This was collected as the product, which was washed with methanol and dried under vacuum before XAFS measurement.

For a typical synthesis of $Au_{10}(SG)_{10}$ NCs, GSH (0.1 M, 0.20 mL) was mixed with 4.30 mL of nanopure water, followed by the addition of $HAuCl_4 \cdot 3H_2O$ (0.02 M, 0.50 mL) under gentle stirring (500 rpm) at 25 °C for 5 min. A precipitate was formed, which was then dissolved by adjusting pH to ~7 with NaOH (0.5 M). The solution was aged for 2 h at 40 °C, and the resultant solution of oligomeric Au(I)−thiolate complexes was then lyophilized for further characterizations.[123]

For rigidifying studies, 10 mg of $Au_{10}(SG)_{10}$ dissolved in 10 mL of nanopure water and 10 mg of TOABr dissolved in 5 mL of toluene were added together into a 20 mL scintillation vial. The pH of aqueous solution was then adjusted to pH 9.0 by adding NaOH to ensure carboxyl groups of SG were in the anionic form. The electrostatic interaction between the carboxylate anions of the SG ligand and the hydrophobic TOA cations in the toluene phase is strong, therefore the TOA^+-paired $Au_{10}(SG)_{10}$ clusters can be readily transferred to the toluene phase (referred to as the "rigidified" state) by stirring the two solutions. The toluene phase was then separated and washed with copious amounts of water to wash away all the water soluble impurities.

UV-Vis and fluorescence spectroscopy measurements for the time-dependent study another supporting measurements besides the rigidifying experiments were collected with the Cary 100 Bio and the Cary Eclipse spectrophotometers, respectively. Solutions were measured using a quartz cuvette sample holder.

Au L_3-edge XAFS data was collected from the CLS@APS (Sector 20-BM) beamline at the APS. Au L_3-edge EXAFS spectra for $Au_{25}(SR)_{18}$ and $Au_{38}(SR)_{24}$ NCs (both were measured at room temperature in powdered form) were borrowed from previous studies.[186,233] XAFS data work-up, sample preparation, EXAFS fitting and error analysis were conducted following the procedures outlined in Section 2.2. The amplitude reduction factor (S_0^2) used for EXAFS fitting was determined using a Au(I)-SR polymer material. The Au-S CN was fixed at 2 to obtain a value of 0.93 which was used for all Au L_3-edge EXAFS fitting. All measurements were collected at room temperature and atmospheric pressure. A k-range of 3.0 to 12.0 $Å^{-1}$ was used for all FT-EXAFS spectra. For time-dependent samples of AuBSA NCs taken at 0, 1, 2, 3, 6, 12 and 36 h, two or three scattering paths were fitted to the experimental EXAFS spectrum. For these EXAFS fits, the E_0 shift values were correlated for each shell with all other parameters running free. This was done to help meet the Nyquist criterion for number of dependent and independent parameters when conducting EXAFS fitting.[298] The $Au_{10}(SR)_{10}$ catenane model was used to generate simulated scattering paths to fit the AuBSA NCs sample and the $Au_{10}(SG)_{10}$ sample with more Au scattering environments. Unlike the two-/three-shell fit, CNs for each scattering path were fixed to their ideal values according to the $Au_{10}(SR)_{10}$ model. Bond lengths (R) and Debye-Waller (σ^2) parameters ran free for the fit with all E_0 shift values correlated, again to help satisfy the Nyquist criterion. A total of 4 single scattering paths were used and fitted over a R-range of 1.5 to 4.0 Å.

Simulated EXAFS spectra of Au(I)-SR clusters were calculated using the FEFF8.2 program with coordinates from crystal structure files or DFT-optimized structures. The L_3-edge EXAFS spectrum for each Au site was calculated using a self-consistent field radius set at 4.5 Å to encompass enough atoms in the cluster for full multiple scattering calculations. The averaged FT-EXAFS spectrum was Fourier-transformed using an identical k-space region to AuBSA NCs (3.0 to 12.0 Å^{-1}) for the pre-screening process. FT-EXAFS for simulated Au(I)-SR clusters were k^1-weighted.

Steady-state PL and temperature-dependent PL measurements were carried out with an Edinburgh spectrofluorimeter (F900S). PL QYs were measured using Rhodamine B in ethanol as a standard.[299] For temperature-dependent PL measurements, the fluorimeter was coupled with Optistat DN cryostat (Oxford instruments) and ITC temperature controller. The measurements were carried out from 77 to 303 K. The vacuum in the cryostat was maintained with a Leybold turbo molecular pump. Spectra were taken at different temperatures after a wait period of 10 min. The error in temperature setting was ±0.5 K. The $Au_{10}(SG)_{10}$ sample was dissolved in a 65:35 glycerol/water mixture for temperature-dependent PL measurements. All the samples were purged with N_2 to get rid of dissolved oxygen to omit problems in solvent freezing temperatures as well as the effect of oxygen on phosphorescence lifetimes. Optical absorption measurements before and after temperature-dependent PL measurements have shown no change suggesting the samples did not change during the measurements.

Time-resolved PL decay lifetime measurements were measured using a time-correlated single photon counting technique after excitation at 373 nm with a diode laser excitation and the measurements were carried out with an Edinburgh F900S spectrofluorimeter. The PL lifetimes were measured at their respective PL maxima with an emission slit width of 10 nm. Cooled Hamamatsu R-921P PMT was used as the detector.

Geometry optimization was performed on all species using the LC-ωPBE functional[300–302] and the XDM[303,304] dispersion correction, with the Couty-Hall modified LANL2DZ basis set for Au,[305] 6-31G* for C and H, and 6-31+G* for S. Single-point energy calculations on the optimized geometries were carried out using the same LC-ωPBE-XDM method with the aug-cc-pVDZ-PP[306] basis set for Au and aug-cc-pVDZ[307,308] for C, H, and S. The XDM damping parameters were a_1=0.8134, a_2=1.3736 for the geometry optimizations and a_1=1.1800, a_2=0.4179 for the single-point energy calculations, as in previous work that demonstrated the excellent performance of LC-ωPBE-XDM for modeling of aurophilic effects in gold complexes.[309] All calculations were performed using the Gaussian 09 software package,[310] along with the postg program (freely available at http://schooner.chem.dal.ca) for the dispersion energies. The EMSL Basis Set library was used to obtain all basis set and ECP input parameters.[311]

8.5 Results and Discussion

8.5.1 Local structure of Au NCs

The synthesis of red luminescent BSA-protected Au NCs (AuBSA NCs) is schematically shown in Figure 8.2a. The initial investigation utilized FT-EXAFS to determine whether Au structures in AuBSA NCs are related to the core/shell structures of atomically-precise NCs, such as $Au_{25}(SR)_{18}$ NCs, which reports on protein-protected Au NCs have suggested.[70,71] Figure 8.2b directly compares the FT-EXAFS of luminescent AuBSA NCs with $Au_{25}(SR)_{18}$ and $Au_{38}(SR)_{24}$. The spectral regions corresponding to Au-S and Au-Au bonding are highlighted in blue and orange, respectively. The overlap of each reference FT-EXAFS spectrum with AuBSA NCs clearly shows there is no significant Au core structure, as evidenced by the absence of metallic Au-Au scattering in the 2.5 to 3.0 Å region for AuBSA NCs. Fitting the Au-S region of AuBSA NCs EXAFS (Table 8.1, Figure 8.2b) yielded a CN of 2.1(1) and a bond length of 2.31(2) Å. Thus, the majority of Au atoms likely exist in RS-Au-SR structures (CN = 2 and SR - cysteine from BSA) with no Au core structure, meaning an oxidation state of Au(I) is expected for Au atoms in AuBSA NCs. This was substantiated by inspection of the XANES region of AuBSA NCs with Au(I) and Au(0) reference materials (Figure 8.3).

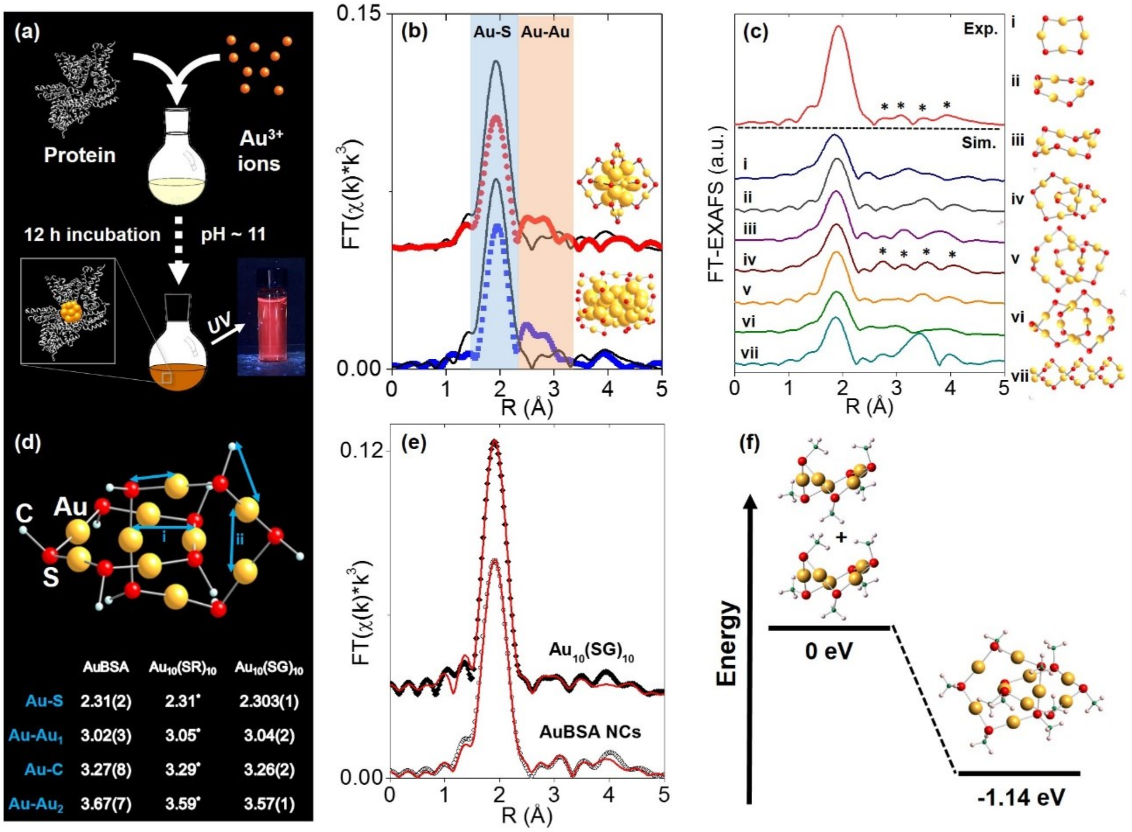

	AuBSA	$Au_{10}(SR)_{10}$	$Au_{10}(SG)_{10}$
Au-S	2.31(2)	2.31*	2.303(1)
$Au\text{-}Au_1$	3.02(3)	3.05*	3.04(2)
Au-C	3.27(8)	3.29*	3.26(2)
$Au\text{-}Au_2$	3.67(7)	3.59*	3.57(1)

Figure 8.2 The structural elucidation process of AuBSA NCs. (a) Protein-directed synthesis of luminescent Au NCs. (b) Au L_3-edge FT-EXAFS of luminescent AuBSA NCs (black line) with $Au_{25}(SR)_{18}$ (red dot) and $Au_{38}(SR)_{24}$ (blue dot) (inset, respective models with Au (yellow) and S (red) atoms). (c) Simulated Au L_3-edge FT-EXAFS of Au(I)-SR structures including (i) Au_4S_4 ring, (ii) Au_5S_5 ring, (iii) Au_6S_6 ring, (iv) $Au_{10}S_{10}$ catenane, (v) $Au_{11}S_{11}$ catenane, (vi) $Au_{12}S_{12}$ catenane and (vii) Au-S double helix (methyl substituents were omitted from all structures for

clarity). (d) 4 representative EXAFS scattering paths from the $Au_{10}(SR)_{10}$ catenane model used for fitting with determined scattering distances and literature values*.[312] **(e) Au L_3-edge FT-EXAFS of $Au_{10}(SG)_{10}$ (SG – glutathione) and AuBSA NCs. (f) DFT-optimized geometries of $Au_5(SMe)_5$ and $Au_{10}(SMe)_{10}$ with relative energy difference.**

Although Au-Au scattering representing Au core structures was not found in the EXAFS fitting of AuBSA NCs, longer-range Au-Au scattering related to aurophilic interactions (*i.e.*, Au(I)-Au(I) interactions of longer distance than a metallic bond) was identified. EXAFS fitting yielded a CN parameter of 0.8(5) and a distance of 3.02(2) Å (Table 8.1) for these Au(I)-Au(I) interactions. This bond distance is indeed much longer than bulk Au-Au bonding (~2.88 Å) and Au-Au bonding from atomically-precise Au NC core structures (~ 2.78-2.82 Å) (*e.g.*, $Au_{25}(SR)_{18}$).[192,195] This part of the structural study suggested that there are inter-molecular aurophilic interactions between SR-Au(I)-SR structures.

Table 8.1 Au L_3-edge EXAFS fitting results for AuBSA NCs. Uncertainties in fitted parameters are shown in parentheses.

Parameters	Au-S	Au-Au
CN	2.2(1)	0.8(5)
R (Å)	2.321(8)	3.02(2)
σ^2 (Å^2)	0.0036(3)	0.011(4)
ΔE_0 (eV)	1.1(3)	1.1(3)

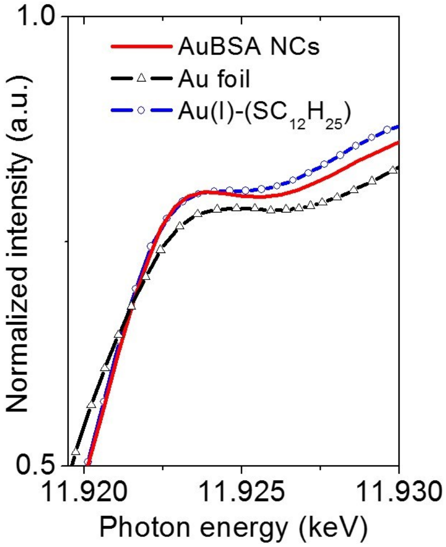

Figure 8.3 White-line region of Au L$_3$-edge XANES for AuBSA NCs with Au(I)-SR polymer and Au foil (Au(0)) references.

In search of a structural model to obtain more quantitative information from EXAFS fitting (additional scattering paths and corresponding structural parameters), a pre-screening step was first implemented by comparing the experimental FT-EXAFS of AuBSA NCs with simulated spectra of all the available Au(I)-SR cluster references (Figure 8.2c).[108,312–316] Such references are distinct Au(I)-SR structures known from X-ray crystallography or predicted from theory (rings ($Au_4(SR)_4$, $Au_5(SR)_5$, $Au_6(SR)_6$), interlocked rings or catenanes ($Au_{10}(SR)_{10}$, $Au_{11}(SR)_{11}$, $Au_{12}(SR)_{12}$) and polymer ($[Au(SR)]_x$)). Screening the simulated EXAFS spectra of several different Au(I)-SR clusters allowed a close comparison of scattering features that follow the dominant Au-S peak in order to narrow down the specific conformation of Au(I)-SR structures in AuBSA NCs. The $Au_{10}(SR)_{10}$ catenane structure (two interlocked $Au_5(SR)_5$ rings) had the closest resemblance with four similarly positioned scattering features following the Au-S peak. Importantly, the average inter-ring Au-Au distance from the $Au_{10}(SC_6H_4C(CH_3)_3)_{10}$ structure[312] is 3.05 Å and is the most similar to the aurophilic interaction distance found in AuBSA NCs (3.02 Å), whereas $Au_{11}(SR)_{11}$ and $Au_{12}(SR)_{12}$ catenanes have significantly longer average distances of 3.28 and 3.35 Å, respectively.[312,316] Interlocking Au(I)-SR ring structures have also been identified for larger Au NCs such as $Au_{22}(SR)_{18}$ and $Au_{24}(SR)_{20}$ NCs.[103,124] Consistent with this work, both Au NCs have red luminescence and QYs similar to AuBSA NCs.

Table 8.2 Multi-shell Au L_3-edge EXAFS fitting results for AuBSA NCs and $Au_{10}(SG)_{10}$ NCs. Uncertainties in fitted parameters are shown in parentheses.

	Parameters	Au-S	Au-Au	Au-C	Au-Au
AuBSA NCs	CN	2	1.8	2	2
	R (Å)	2.31(2)	3.02(3)	3.27(8)	3.67(7)
	σ^2 (Å^2)	0.0035(3)	0.016(3)	0.02(1)	0.019(9)
	ΔE_0 (eV)	2.4(4)	2.4(4)	2.4(4)	2.4(4)
$Au_{10}(SG)_{10}$	CN	2	1.8	2	2
	R (Å)	2.303(1)	3.04(2)	3.26(2)	3.57(1)
	σ^2 (Å^2)	0.00263(6)	0.016(2)	0.006(2)	0.0122(9)
	ΔE_0 (eV)	2.2(3)	2.2(3)	2.2(3)	2.2(3)

After identifying the $Au_{10}(SR)_{10}$ catenane as the best structural match to AuBSA NCs, EXAFS scattering paths that specifically describe the $Au_{10}(SR)_{10}$ model (Figure 8.2d) were used to fit AuBSA NCs in more detail. In addition to Au-S and intermolecular aurophilic interactions, Au-C scattering (between Au and C adjacent to S) and longer Au-Au scattering (between Au-Au in the same ring) were included. The multi-shell EXAFS fit of these four scattering environments for AuBSA NCs is shown in Figure 8.2e along with fitting results in Table 8.2. Bond distances obtained from the multi-shell EXAFS fit were perfectly in line with the average distances from the $Au_{10}(SR)_{10}$ crystal structure (Figure 8.2d, inset table), thereby reinforcing the structural identification of interlocking Au(I)-SR rings for AuBSA NCs.

Free-standing (*i.e.*, without protein host) $Au_{10}(SR)_{10}$ NCs protected by SG ligands ($Au_{10}(SG)_{10}$) were also synthesized to provide additional verification of the interlocked ring structures from an experimental perspective. Figure 8.2e compares the experimental FT-EXAFS spectrum of $Au_{10}(SG)_{10}$ with AuBSA NCs, which clearly demonstrated the identical position and pattern of all scattering features previously identified with simulated FT-EXAFS of $Au_{10}(SR)_{10}$. Furthermore, detailed EXAFS fitting analysis using the $Au_{10}(SR)_{10}$ model was performed for $Au_{10}(SG)_{10}$ NCs and yielded consistent structural parameters to AuBSA NCs (Table 8.2 and Figure 8.2d, inset). As a final confirmation, DFT was applied[309] to optimize the structures of $Au_5(SR)_5$ and $Au_{10}(SR)_{10}$ (where SR is SCH_3 for computational efficiency, details in SI) and the resulting energies support the favourable formation of interlocked ring structures over individual isolated ring structures. Figure 8.2f depicts the large stabilization energy of -1.14 eV calculated for interlocking two $Au_5(SR)_5$ rings to form a $Au_{10}(SR)_{10}$ catenane, offering a valid explanation for the high stability of AuBSA NCs experimentally reported.[152] Additionally, the distinct inter-ring and intra-ring Au-Au bonding distributions of optimized $Au_{10}(SR)_{10}$ (Figure 8.4) corresponded well with the crystal structure and EXAFS fitting results for AuBSA NCs and $Au_{10}(SG)_{10}$.

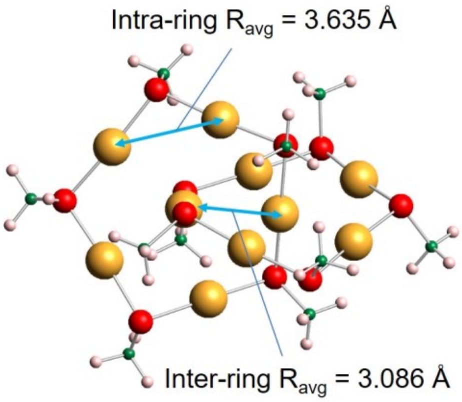

Figure 8.4 DFT-optimized structure of $Au_{10}(SMe)_{10}$ with average inter- and intra-ring Au-Au bond distances.

8.5.2 Photoluminescence properties and rigidification studies

The PL properties were next examined to understand how protein-protected Au NCs could be related to SG-protected Au NCs, besides their structure, and to further elucidate the PL mechanism of AuBSA NCs. AuBSA NCs have PL centred at 650 nm when excited at 365 nm (Figure 8.5). The excitation spectrum shows that two peaks, one at 365 nm and another at 475 nm, are responsible for the observed luminescence. The QY was determined to be 6.8 % (photo-physical results are shown in Table 8.3). The large stokes shift (285 nm) and long PL decay lifetime measured (1.065 µs, Table 8.3) further suggested the emission from AuBSA NCs was characteristic of phosphorescence, similar to other known Au(I)-SR structures.[288,317] Overall, the observed luminescence of AuBSA NCs matched well with what has been reported previously.[70,71,152] Although a virtually-identical Au local structure was determined from our EXAFS analysis, $Au_{10}(SG)_{10}$ NCs showed a modest difference in luminescence energy, centred at 620 nm (excitation at 365 nm) instead of 650 nm, but with a significantly weaker emission intensity, with a QY of only 0.48 %.

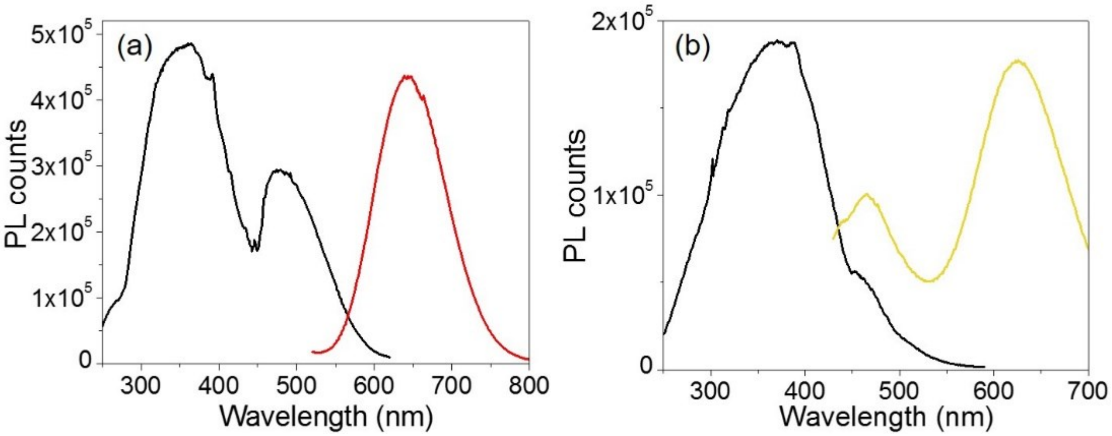

Figure 8.5 Photoluminescence (colour line) (excitation @ 365 nm) and excitation spectra (black line) of (a) AuBSA NCs and (b) $Au_{10}(SG)_{10}$ NCs.

Table 8.3 Excited-state photoluminescence decay lifetime components and quantum yield (Rhodamine B in EtOH as reference) measurements.

	t_1(ns)	t_2(ns)	t_3(ns)	t_{avg}(ns)	QY(%)
$Au_{10}(SG)_{10}$	15 ± 5 (74.3 %)	150 ± 30 (16.4 %)	890 ± 80 (9.3 %)	120	0.48
$Au_{10}(SG)_{10}$ -rigidified	35 ± 8 (54.6 %)	150 ± 40 (28.5 %)	880 ± 90 (16.9 %)	210	5.0
AuBSA NCs	30 ± 6 (22.4 %)	350 ± 50 (21.7 %)	1760 ± 120 (55.8 %)	1065	6.8

It can be understood that the small discrepancy in emission energy between AuBSA NCs and $Au_{10}(SG)_{10}$ (~0.09 eV) is from the difference in ligand type (cysteine residue in BSA versus SG).[119] With regards to the large difference in QY, however, it is hypothesized that the high emission yield of AuBSA NCs might have its origins from the structural rigidity of Au(I)-SR clusters within the BSA molecule. It was reported in recent work on the PL of $Au_{22}(SG)_{18}$ clusters that the rigidity of the Au(I)-SG surface structures plays a major role on the enhanced QY from Au NCs.[124] Cysteine residues that bond with Au in BSA are fixed to the protein backbone, providing the aforementioned structural rigidity. The large globular structure of BSA can also shield Au(I)-SR clusters from the solvent, preventing excited-state energy transfer to surroundings and further enhancing the emission yield. Together, the rigid and solvent-isolated protein environment surrounding Au(I)-SR clusters would enable stronger aurophilic interactions that induce LMMCT, an effect known to enhance luminescence for Au(I) oligomers and complexes.[123,275,317–319] Therefore, although $Au_{10}(SG)_{10}$ has the same Au NC structure as AuBSA NCs, the lower QY is potentially a result of non-radiative energy transfer to the solvent or surroundings via vibrational and/or rotational processes of the SG ligand.

The structural rigidity hypothesis was first tested by performing a phase-transfer experiment, previously reported by Negishi *et al.*[320] and Pyo *et al.*[275]*,* with $Au_{10}(SG)_{10}$ NCs (See Appendix A, Figure A.1). Tetraoctylammonium (TOA^+) ions interact with the carboxylic end groups (COO^-) of SG ligands so that the octyl chains of TOA^+ protect $Au_{10}(SG)_{10}$ NCs from solvent interactions and restrict molecular vibrations or rotations (schematically shown in Figure 8.6a), thereby creating a “rigidified” state that prevents non-radiative emission processes. This phase-transferred or rigidified state also effectively simulates a protein-stabilized environment for Au(I)-SR clusters. The luminescence of rigidified $Au_{10}(SG)_{10}$ was enhanced by 10.4 times (QY = 5.0 %) with a blue-shift of 15 nm (620 nm to 605 nm, see Figure 8.6b). The average PL decay lifetime for rigidified $Au_{10}(SG)_{10}$ had also nearly doubled (from 0.120 to 0.210 μs, Figure 8.6c). Increased lifetime and enhanced QY point to a rigidified state of $Au_{10}(SG)_{10}$ NCs. It is interesting to note that a luminescence enhancement greater than 10 times for $Au_{10}(SG)_{10}$ was observed with the phase-transfer rigidifying experiment, which is higher than similar experiments on $Au_{22}(SG)_{18}$ (~9 times) and $Au_{25}(SG)_{18}$ (~6 times).[275] This is possibly due to the higher number of aurophilic interactions per Au atom. Further supporting the rigidified property, decreasing the temperature condition from room temperature to 77 K induced an even greater enhancement in emission yield (~35 times) and a larger blue shift in the emission energy (60 nm) (Figure A.2).

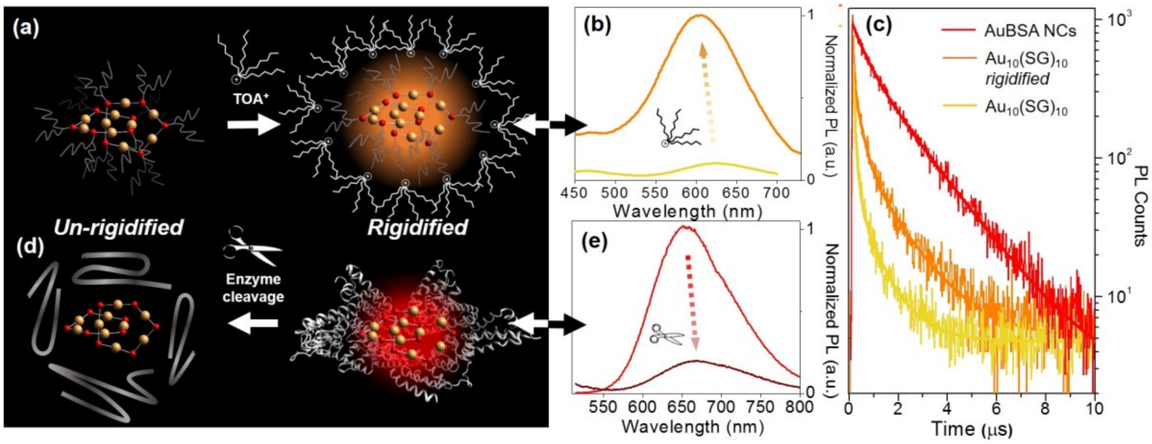

Figure 8.6 Photoluminescence properties of $Au_{10}(SG)_{10}$ and AuBSA NCs in rigidified and un-rigidified states. (a) Scheme of rigidifying $Au_{10}(SG)_{10}$ clusters with TOA^+/toluene phase-transfer and (b) luminescence enhancement of $Au_{10}(SG)_{10}$ clusters (rigidified, orange line). (c) Photoluminescence decay lifetime traces of AuBSA NCs (red), rigidified $Au_{10}(SG)_{10}$ clusters (orange) and original $Au_{10}(SG)_{10}$ clusters (yellow). (d) Scheme of un-rigidifying AuBSA NCs with enzyme digestion and (e) resultant decrease in luminescence (un-rigidified, dark red line).

Lastly, the importance of Au(I)-SR cluster rigidity was demonstrated from the alternative perspective, using protein-protected Au NCs already in their rigidified state. The protecting BSA protein was disrupted via enzymatic digestion to “un-rigidify” Au(I)-SR clusters (schematically shown in Figure 8.6d). After cleaving BSA molecules, luminescence of AuBSA NCs decreased by ~5 times (Figure 8.6e) and emission maximum had red-shifted by 15 nm (same magnitude of emission energy shift for $Au_{10}(SG)_{10}$ when rigidified) while all Au-S interactions remained intact (Figure A.3). Together, rigidifying $Au_{10}(SG)_{10}$ and un-rigidifying Au(I)-SR clusters in BSA validate the similar PL property that exists between these two systems, further linking the luminescence of small thiolate-stabilized Au NCs with the new category of protein-protected Au NCs.

8.5.3 Protein-directed synthesis of Au NCs

Following the identification of interlocked Au(I)-SR ring structures, the biomolecular self-assembly process guided by BSA could then be further understood by monitoring the protein-directed synthesis with a time-dependent XAFS study. Samples at 0, 1, 2, 3, 6, and 12 h were extracted from the synthesis to capture two distinct stages of the protein-directed synthesis. Absorbance (Figure A.4), photoluminescence (Figure 8.7a) and Au L_3-edge XAFS (Figure 8.7b, Figure 8.7c and Figure A.4) were collected for samples at each time point. Luminescence increased steadily over the course of the protein-directed synthesis until 12 h. Even after 36 h, the PL intensity did not increase further (Figure A.5). Au L_3-edge XANES spectra in Figure 8.7b show the white-line intensity (*i.e.*, first feature that follows the absorption edge, and the intensity of this feature reflects the valence electron occupancy, which is mainly the 5d level for Au at the L_3-edge) decreased over the course of the synthesis, which signified a reduction of Au(III) precursor ions to Au(I)-SR clusters. A white-line valence state integration analysis (inset, Figure 8.7b) reveals no further reduction of Au(I) after 6 h into the synthesis.

Using Au-X EXAFS scattering paths (where X is Cl, O, S or Au), quantitative structural parameters were determined by fitting the time-dependent Au L_3-edge EXAFS spectra (Figure 8.7c and Table A.1). A time plot of Au-X CN parameters is shown in Figure 8.7d to convey the two-stage process (0 to 3 h and 3 to 12 h). The first scattering path at ~1.7 Å (spectra not phase corrected) for the 0 h spectrum in Figure 8.7c was determined from EXAFS fitting to be Au–O bonding at 2.02(1) Å and surprisingly not Au-Cl bonding from the Au precursor ($HAuCl_4$). A comparison with $HAuCl_4$ (starting material) and $Au(OH)_3$ reference compounds is shown above the 0 h sample in Figure 8.7c to further demonstrate the similarity to the latter reference. EXAFS fitting of Au-O scattering for $Au(OH)_3$ gave a bond length of 2.005(4) Å (Figure A.6), similar to the 0 h sample. DFT calculations support the transformation of gold chloride to gold hydroxide in the presence of excess OH^- ions (Table A.2, Table A.3 and Table A.4). The formation energy was calculated for each step of the ligand exchange reaction with each intermediate chlorohydroxoaurate complex (Figure 8.7e). It was found that the formation of $Au(OH)_3$ from $AuCl_3$ has a total formation energy of -5.65 eV with the energies of the ligand-exchange steps ranging from -1.82 to -1.96 eV. With excess NaOH present, elevated temperatures and vigorous mixing in the protein-directed synthesis of AuBSA NCs, the initial formation of $Au(OH)_3$ is highly favourable.

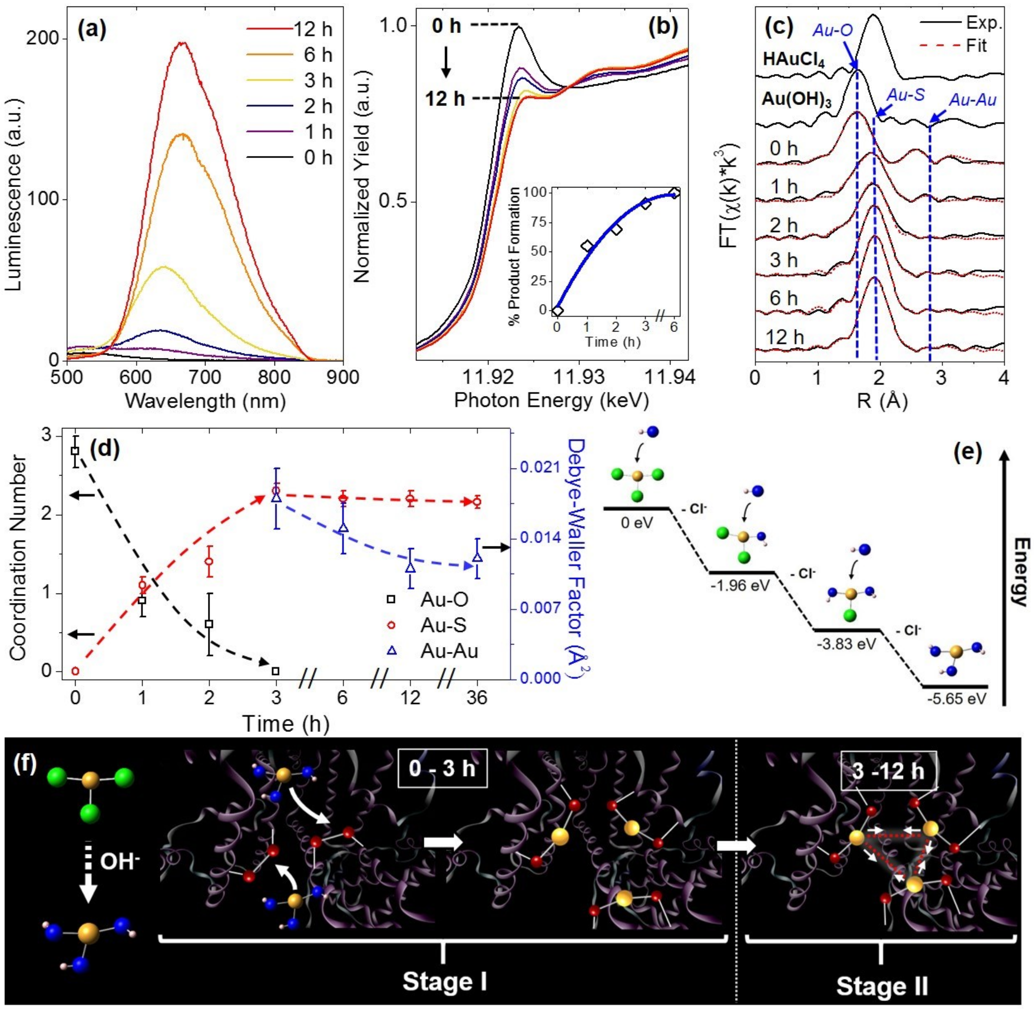

Figure 8.7 Time-dependent study of the protein-directed synthesis monitored with (a) photoluminescence spectra (excitation λ = 470 nm), (b) Au L_3-edge XANES (inset, white-line integration analysis for Au(III) to Au(I) formation), (c) Au L_3-edge FT-EXAFS with fitted spectra and reference materials and (d) quantitative plot for EXAFS fitting results. (e) Relative DFT energies of $AuCl_3$ (set to 0 eV), $Au(OH)_3$, and intermediate products of the ligand-exchange process. (f) Scheme depicting distinct stages of the AuBSA NC protein-directed synthesis.

After 1 h into the synthesis, Au-S bonding appears (feature at ~2 Å, not phase corrected) with an EXAFS fitted distance of 2.31(1) Å. At this point in the synthesis, Au atoms begin to form strong covalent bonds with cysteine residues in BSA, which were originally bonded to other cysteine residues via disulfide bonds. The nature of the Au–S bonding does not change from 3 h until the end of the synthesis, with an average bond distance of 2.32(1) Å and a CN of 2.1(1). Notably, appreciable luminescence is first observed around 3 h (Figure 8.7a), which is the point where SR-Au(I)-SR structures have mainly formed with no remaining Au-O interactions. The complete ligand exchange and formation of SR-Au(I)-SR structures from 0 to 3 h can be regarded as Stage I of the protein-directed synthesis (Figure 8.7f).

Stage II of the protein-directed synthesis is the optimization or final assembly of SR-Au(I)-SR structures, which is illustrated in Figure 8.7f. Au-Au interactions were resolvable from EXAFS spectra for samples 3 to 12 h with a consistent scattering distance around 3.02 Å and CN parameters decreasing from *ca.* 2 to 1 (Table A.1), which was suggestive of inter-ring Au-Au interactions early on in Stage II. From 3 to 12 h, the Debye-Waller factor (σ^2, accounts for thermal and positional disorder of neighbouring atoms in a particular scattering shell) and associated error value decreases for aurophilic interactions (plotted in Figure 8.7d), indicating that Au(I)-SR clusters are becoming more ordered inside of the protein as incubation and mixing continues. Since the change in atomic structure is minimal from 3 to 12 h, the increase in luminescence during this stage should be due to the structural optimization of BSA to accommodate the formed Au(I)-SR interlocking ring structures within the protein. No further change in Au local structure was observed even after 36 h of incubation and mixing (Figure A.6 and Table A.1).

8.6 Conclusion

Overall, this work has resolved the structure of highly luminescent Au NCs protected by BSA. Using a multi-step procedure that included screening of Au(I)-SR model structures, X-ray spectroscopy fitting, DFT simulations, analogous free-standing Au NC synthesis and rigidifying/un-rigidifying experiments, the structure of these unique bioinorganic NCs was revealed along with their luminescence property and biomolecular self-assembly mechanism. These findings accentuate the remarkable capability of a protein nano-reactor for producing bioinorganic clusters with intriguing structures and optical properties, and should be of importance for future preparation and application of luminescent protein-Au bionanomaterials. The investigative approach demonstrated in this work could also be extended to other biomolecule-metal materials where a large biological system interferes with characterization of the encapsulated metal component.

Chapter 9 - Atomically-precise $Ag_{44}(SR)_{30}$ Nanoclusters: Structural Response to Solvent and Thermal Decomposition

Manuscript in preparation for submission

Daniel M. Chevrier, Brian E. Conn, Scott R. J. Oliver, Terry Bigioni, Amares Chatt, Peng Zhang*

9.1 Contributions

D.M.C. prepared solution-phase and annealed samples for XAFS measurement, conducted all XAFS experiments, analyzed XAFS data and wrote the manuscript. B.E.C. synthesized and provided the $Ag_{44}(S(p\text{-}MBA))_{30}$ *sample. S.R.J.O. conducted the TGA of the* $Ag_{44}(S(p\text{-}MBA))_{30}$ *sample. T.B. supervised B.E.C. and S.O.. A.C. and P.Z. supervised D.M.C. and helped revise the manuscript.*

9.2 Foreword

In projects I and II, atomically-precise thiolate-protected Au NCs of various size and composition were investigated with EXAFS to reveal the effects of core structure, ligand type and solvation on the structure and electronic properties. This chapter extends from Au NCs to examine the structural response of thiolate-protected Ag NCs under similar experimental variables as tested for thiolate-protected Au NCs, such as phase, solvent type and temperature. This study utilizes structural information gained from the recent crystallization of $Ag_{44}(SR)_{30}$ *NCs to selectively monitor the response of core,* *surface and metal-ligand environments of thiolate-protected Ag NCs. The unique stability of* $Ag_{44}(SR)_{30}$ *NCs is discussed with respect to coordinating solvent interactions and high temperatures.*

9.3 Introduction

Thiolate-protected Ag NPs have been investigated for several years alongside the progress made with thiolate-protected Au NPs.[8,136,321,322] Similar to Au NPs, Ag NPs can be synthesized using the Brust-Schiffrin approach and exhibit optoelectronic properties, such as SPR.[26,136] Ag-based NPs are an enticing alternative to Au-based NPs since Ag has certain advantages and other properties employable for application. For example, the antibacterial properties of Ag can be utilized for biomedical applications of Ag NPs.[135] Ag-based NPs have also shown potential as advanced light harvesting materials.[323] Importantly, the lower cost of Ag is beneficial for scaling up NP syntheses. Despite these advantages, Ag NPs suffer from tarnishing,[138] which affects Ag NP stability and long-term usage of these materials in application stages. This also interferes with the fundamental understanding of optical and electronic properties as they relate to size and structure. That being said, structure-property information has been especially limited for smaller thiolate-protected Ag NC counterparts due to their low stability.

In recent years, advances in NC synthesis techniques have enabled the isolation and crystallization of a few $Ag_n(SR)_m$ NCs. The structural elucidation of atomically-precise $Ag_{44}(SR)_{30}$ NCs was a significant discovery for $Ag_n(SR)_m$ NC research.[133,139] The crystal structure revealed a distinctive metal core and discrete Ag-SR surface structural units much like the general construction of thiolate-protected Au NCs. The incredible stability of $Ag_{44}(SR)_{30}$ is an unprecedented property for Ag NCs. The $Ag_{44}(SR)_{30}$ structure is so greatly favoured over other Ag NC frameworks that quantitative yields are attainable, and the reaction can be scaled up to produce over 100 g of $Ag_{44}(SR)_{30}$ NCs per batch.[133,324] Other impressive properties of $Ag_{44}(SR)_{30}$ NCs include multiple absorption peaks in the UV-Vis spectrum, moderate PL emission and catalytic activity.[324,325] $Ag_n(SR)_m$ NCs appear to have molecule-like electronic and optical properties on this size-regime, much like $Au_n(SR)_m$ NCs.

The remarkable stability of $Ag_{44}(SR)_{30}$ is a breakthrough for $Ag_n(SR)_m$ NCs. The origin of this stability has been predicted to originate from the closed shell structure of the Ag core (Ag_{12} icosahedron inside Ag_{20} dodecahedron) and the relative ratio of Ag to SR, which mimic a closed shell electronic structure ($1S^2$, $1P^6$, $1D^{10}$) following the Aufbau rule.[133] Besides geometric and superatom properties, the role of core and surface structures, and their interactions with solvent molecules or response to temperature, may hold more information on the stability of $Ag_{44}(SR)_{30}$ NCs. Toward this end, the local structure of $Ag_{44}(SR)_{30}$ NCs was examined using Ag K-edge XAFS to understand the effect of temperature, solid-solution phase changes, coordinating solvents and solvent mixtures on the bonding properties. An annealing study coupled with Ag K-edge XAFS provided evidence of high temperature stability and an interesting structural change from $Ag_{44}(SR)_{30}$ to Ag_2S-structured particles.

9.4 Materials and Methods

$Ag_{44}(p\text{-MBA})_{30}$ NCs (*p*-MBA = *para*-mercaptobenzoic acid) were synthesized according to the protocol published by Desireddy *et al.*[133] Pertaining to this study, the reaction mixture used a water-DMSO co-solvent and the final product was precipitated using DMF.

Thermogravimetric analysis (TGA) was recorded using an SDT Q600 thermogravimetric analyzer from TA instruments. Powdered sample was placed on a Pt pan under N_2 gas for subsequent heating up to 1000°C.

Ag K-edge XAFS data was collected for $Ag_{44}(S(p\text{-MBA}))_{30}$ NC samples from the CLS@APS beamline (Sector 20-BM) at the APS. Both solid- and solution-phase measurements were conducted at 300 K and atmospheric pressure. The powdered sample collected at 90 K for the initial multi-shell fitting analysis was loaded into a helium-cooled cryostat chamber for measurement.

XAFS data work-up, sample preparation, EXAFS fitting and error analysis were conducted following the procedures outlined in Section 2.2. The amplitude reduction factor (S_0^2) was fixed at 0.90 for Ag K-edge EXAFS fitting, which was determined by fitting the Ag-Ag scattering of a Ag foil reference with a fixed Ag-Ag CN of 12. For multi-shell EXAFS fitting, CNs were fixed according to the $Ag_{44}(p\text{-MBA})_{30}$ crystal structure. Theoretical phase and scattering amplitudes for Ag-S and Ag-Ag scattering paths were calculated using the $Ag_{44}(p\text{-MBA})_{30}$ crystal structure model. A k-range of 3 to 12 $Å^{-1}$ was used for the Fourier transformation to R-space. A fitting window of 1.5 to 3.5 Å was used for fits.

Annealing was conducted at the high temperature laboratory (Andy George) in the Department of Physics, Dalhousie University. Samples for the annealing study were prepared by adding 10 mg of powdered $Ag_{44}(p\text{-MBA})_{30}$ into 5 quartz tubes each for annealing at 100, 230, 350, 390 and 600°C. The tubes were purged with Ar gas and then sealed under partial vacuum. Each tube was slowly heated to its target temperature and held for 10 min. The tubes remained sealed until they were prepared for solid-phase XAFS measurements.

9.5 Results and Discussion

9.5.1 Multi-shell EXAFS fitting

The crystal structure of $Ag_{44}(SR)_{30}$ (Figure 9.1a) has a Ag_{32} core composed of a hollow Ag_{12} icosahedron inside a Ag_{20} dodecahedron cage. Protecting the surface are six $Ag_2(SR)_5$ capping units known as “mount-like” motifs (or mount structures), which are positioned in an octahedral symmetry around the Ag_{32} core. From inspection of Ag-Ag bond distributions in Figure 9.1b, three distinct environments (including Ag-S) were identified that could serve as EXAFS scattering shells. Ag-Ag bonding environments are depicted in Figure 9.1c. Clearly, the Ag-S shell corresponds to covalent bonding between thiolate ligands and Ag sites in the Ag_{20} cage and in mount structures (Figure 9.1a, right). The shorter Ag-Ag shell ($Ag\text{-}Ag_1$) corresponds to metallic bonding within the hollow Ag_{12} icosahedron, and between Ag_{12} and the Ag_{20} cage. The last shell represents Ag-Ag bonding at a longer distance between Ag sites in mount structures, within the Ag_{20} cage, and also between mount and cage sites ($Ag\text{-}Ag_2$).

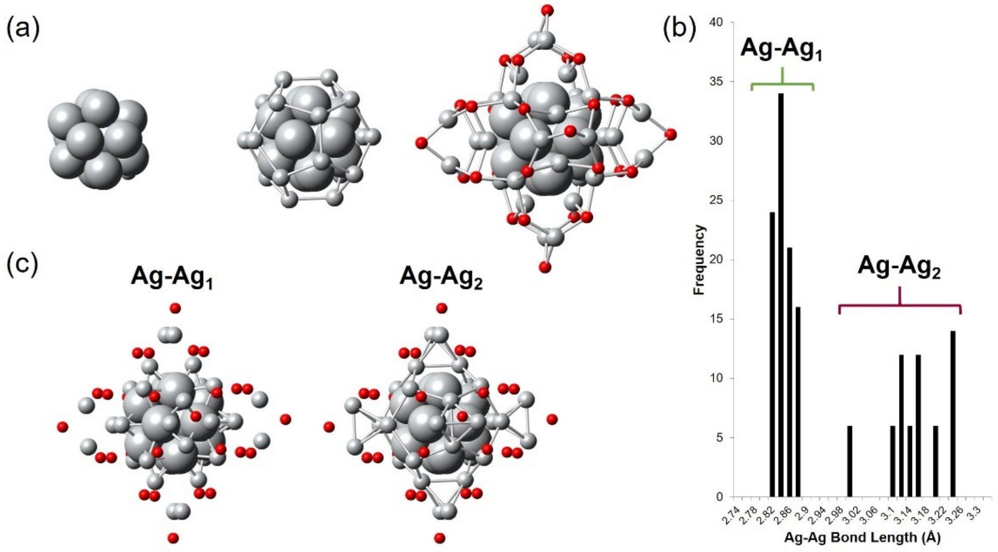

Figure 9.1 (a) Breakdown of the $Ag_{44}(SR)_{30}$ core and surface structure (Ag atoms in grey and S atoms in red, all other ligand atoms omitted for clarity). (b) Ag-Ag bond distribution from the $Ag_{44}(SR)_{30}$ crystal structure and (c) two types of Ag-Ag bonding environments to be represented by distinct Ag-Ag scattering shells in the EXAFS analysis of $Ag_{44}(SR)_{30}$ NCs.

Ag K-edge EXAFS spectrum of $Ag_{44}(SR)_{30}$ in the solid-phase at 90 K was first analyzed using the scattering paths discussed above. The multi-shell EXAFS fit is shown in Figure 9.2 with fitted parameters in Table 9.1. Using these three shells to fit the EXAFS spectrum from 1.5 to 3.5 Å, Ag-S and Ag-Ag distances matched well with the average bond lengths calculated from the crystal structure ($R_{Ag\text{-}S}$ = 2.55 Å, $R_{Ag\text{-}Ag1}$ = 2.84 Å, $R_{Ag\text{-}Ag2}$ = 3.14 Å), verifying the reliability of the EXAFS fitting method to account for core and surface interactions. Debye-Waller factors were as expected for Ag-Ag interactions, being larger for the Ag-Ag_2 shell that accounts for Ag-Ag interactions close to the Ag NC surface. A similar multi-shell EXAFS fitting analysis was then conducted to uncover the effect of temperature and the role of solvents on the core and surface structure of $Ag_{44}(SR)_{30}$ NCs.

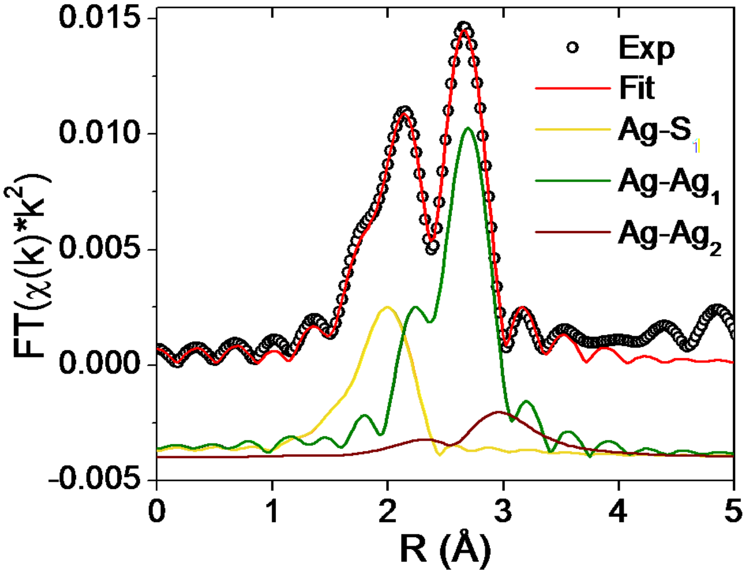

Figure 9.2 Ag K-edge FT-EXAFS of $Ag_{44}(SR)_{30}$ NCs at 90 K in the solid-phase.

Table 9.1 Multi-shell EXAFS fitting results for $Ag_{44}(SR)_{30}$ at 90 K in the solid-phase. Uncertainties in fitted parameters are shown in parentheses.

Shell	CN	R (Å)	σ^2 (Å^2)	ΔE_0 (eV)
Ag-S	1.9	2.501(7)	0.0066(4)	1(1)
$Ag\text{-}Ag_1$	4.1	2.876(3)	0.0051(1)	2.0(4)
$Ag\text{-}Ag_2$	3.3	3.08(1)	0.021(3)	2.0(4)

9.5.2 Solution-phase and semi-aqueous solvents

Solid- and solution-phase XAFS measurements were conducted at 300 K for $Ag_{44}(SR)_{30}$ NCs. All *k*-space spectra for solid-phase and solution-phases are shown in Figure 9.3. Dampening of late-*k* oscillations from stronger thermal vibrations is seen for the solid-phase sample at 300 K. *k*-space spectra for solution-phase samples are similar in oscillation pattern to the solid-phase spectrum, but with varying oscillation intensities. Fitted EXAFS spectra are shown in Figure 9.4 with associated fitting results in Table 9.2. Ag K-edge EXAFS fitting results for $Ag_{44}(SR)_{30}$ at 300 K in the solid-phase were consistent with results from 90 K, but with small variations in average bond distances and as expected higher Debye-Waller factors from thermal disorder. Notably, Ag-S and surface Ag-Ag (Ag-Ag_2) bond distances did not change significantly with temperature. Surprisingly, Ag-Ag bonds related to the Ag_{32} core decreased in length. Since the Ag-Ag_2 bonding does not shorten, contraction of Ag-Ag_1 could occur from Ag atoms in Ag_{12} icosahedral moving closer to the Ag_{20} cage for stronger bonding within the Ag_{32} core. The solid-phase temperature comparison may demonstrate the strong Ag_2S-like surface layer while the hollow Ag_{12} core is more sensitive to thermal vibrations.

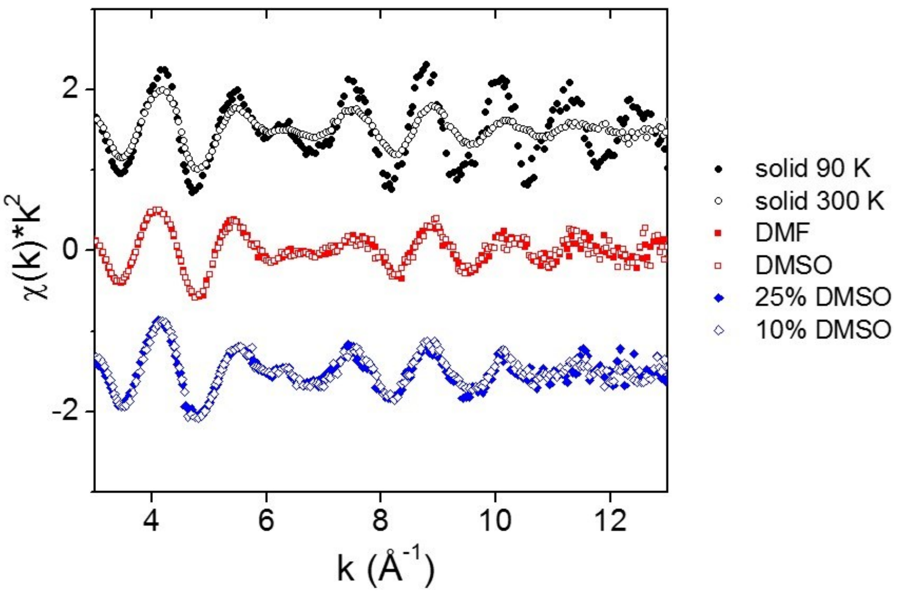

Figure 9.3 Ag K-edge *k*-space spectra of Ag_{44}(*p*-MBA)$_{30}$ NCs at various temperatures in the solid-phase and under solution-phase conditions.

The solvents chosen for examining the effects of solvation (*e.g.*, DMSO, DMF and water) were based on the documented preparation of Ag_{44}(*p*-MBA)$_{30}$ NCs.[133] Solution-phase studies were first conducted with pure DMSO and DMF, which are both coordinating and polar aprotic solvents. Ag K-edge EXAFS of $Ag_{44}(SR)_{30}$ in either solvent showed a similar structural response in comparison to the solid-phase EXAFS. Average Ag-S bonding lengthened by ~0.02 Å and the associated Debye-Waller factor remained constant when $Ag_{44}(SR)_{30}$ NCs were dissolved in each solvent. Ag-Ag interactions on the surface decreased in average distance for $Ag_{44}(SR)_{30}$ in solution, while the Ag-Ag bonding within the Ag_{32} core (Ag-Ag_1) only slightly changed in distance and disorder. This is contrary to observations of increased Au-S and Au-Au structural disorder on the surface of $Au_{18}(SC_6H_{11})_{14}$ NCs when dissolved in toluene (see Chapter 7). However, based on the difference between toluene and the solvents used here, another mode of solvation interactions is anticipated for *p*-MBA ligands with coordinating solvents.

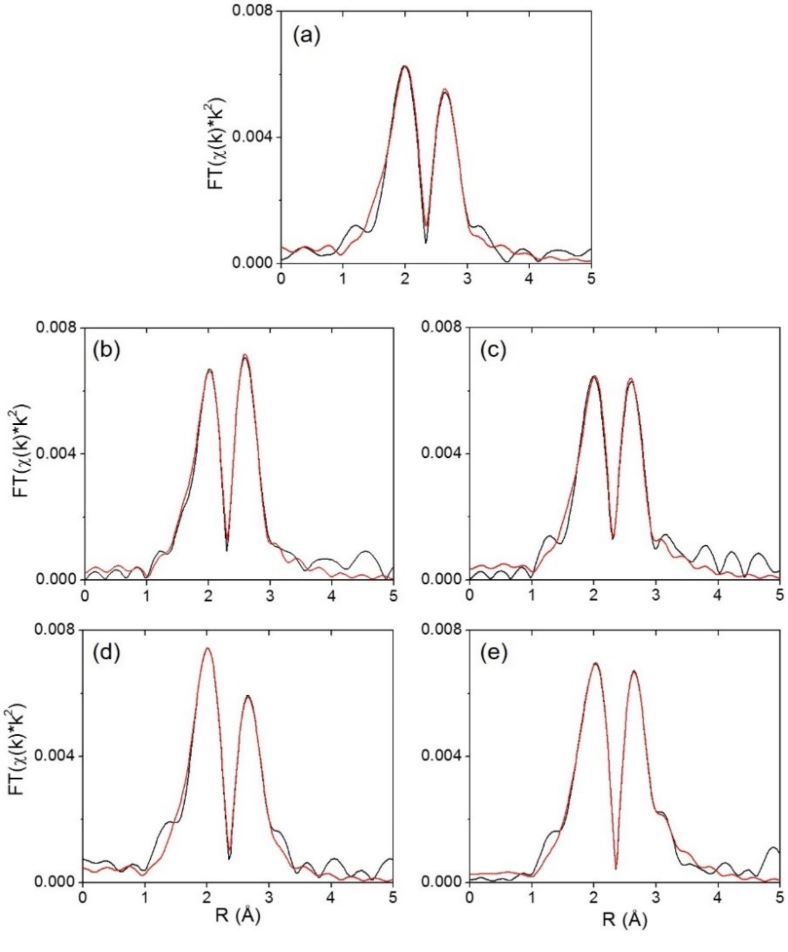

Figure 9.4 Ag K-edge EXAFS (black line) and multi-shell fit (red line) of $Ag_{44}(SR)_{30}$ NCs in (a) solid-phase (300 K), (b) DMF, (c) DMSO, (d) 25% vol. DMSO and (e) 10% DMSO.

Table 9.2 Multi-shell EXAFS fitting results for $Ag_{44}(SR)_{30}$ NCs in solid-phase and in various solution conditions at 300 K. Uncertainties in fitted parameter are shown in parentheses.

Condition	Shell	R (Å)	σ^2 (Å^2)	ΔE_0 (eV)
Solid	Ag-S	2.50(1)	0.011(1)	0(1)
	Ag-Ag_1	2.83(1)	0.013(1)	0(1)
	Ag-Ag_2	3.09(5)	0.03(1)	0(1)
DMF	Ag-S	2.525(7)	0.010(6)	-2.0(6)
	Ag-Ag_1	2.816(5)	0.011(4)	-2.0(6)
	Ag-Ag_2	3.02(2)	0.031(6)	-2.0(6)
DMSO	Ag-S	2.52(1)	0.010(9)	-1.4(8)
	Ag-Ag_1	2.818(8)	0.012(7)	-1.4(8)
	Ag-Ag_2	3.04(3)	0.025(6)	-1.4(8)
25% DMSO	Ag-S	2.49(1)	0.0083(6)	-3(1)
	Ag-Ag_1	2.863(8)	0.0123(7)	1.7(9)
	Ag-Ag_2	3.07(2)	0.023(4)	1.7(9)
10% DMSO	Ag-S	2.479(9)	0.0097(4)	-2(1)
	Ag-Ag_1	2.854(5)	0.0114(4)	2.1(5)
	Ag-Ag_2	3.05(1)	0.020(2)	2.1(5)

The observation of ligand bundling on the Ag_{44}(*p*-MBA)$_{30}$ surface from the crystal structure suggests ligand-ligand interactions could create opportunities for solvent molecules to interact directly with the Ag NC surface. Figure 9.5 shows an isolated mount structure with *p*-MBA ligands bundling together through apparent π- π interactions between benzene rings (oxygen atoms in the carboxylate groups are omitted due to poor spatial resolution of these groups from the crystal structure). This shows relatively unprotected areas that would be exposed to the solvent. The carboxylate groups at the terminus of the ligand (not shown) could also play a role in ligand-ligand interactions. In fact, carboxylate groups have already been shown to influence structural and mechanical properties of 3-D assemblies of $Ag_{44}(SR)_{30}$ NCs through cluster-cluster interactions.[326] The carboxylate groups may also interact with water molecules through hydrogen bonding since water was used as a co-solvent in the synthesis. From the solution-induced changes of Ag-S/Ag-Ag surface interactions detected from EXAFS, *p*-MBA ligand arrangement in mount-like structures and the unique semi-aqueous synthesis of $Ag_{44}(SR)_{30}$ NCs, DMSO and DMF solvents are hypothesized to play an important role in the overall stability of the NC and could possibly lead to insights on the formation of highly stable $Ag_{44}(SR)_{30}$ NCs.

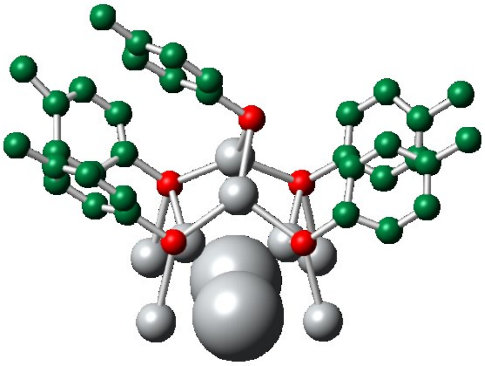

Figure 9.5 Ligand bundling from π- π interactions between benzene rings in a surface mount structure (Ag_2(*p*-MBA)$_5$) with eight Ag sites from the core (large grey atom from Ag_{12} core, small grey atom from Ag_{20} cage, carbon atoms from *p*-MBA in green).

The structural response of $Ag_{44}(SR)_{30}$ NCs was further tested in semi-aqueous solution conditions, similar to the solvent mixture used in the synthesis. Two solvent mixtures of DMSO (coordinating with the Ag NC surface) and water (interacting with carboxylate groups) were tested: 25% (v/v) DMSO/H_2O and 10% (v/v) DMSO/H_2O.

Beyond 10% (v/v) DMSO, $Ag_{44}(SR)_{30}$ NCs were no longer miscible and could not be measured. Interestingly, both solvent mixtures had similar EXAFS fitting results that differed from Ag core and surface local structure in the solid-phase and pure solution-phase. Ag-S bonding shortened by ~0.03 Å and metallic Ag-Ag in the Ag_{32} core expanded to be longer than both solid-phase and pure solution-phase. Here, the Ag atoms in Ag_{12} could be retreating towards the centre of the core, although it is difficult to discern any significant change in Ag-Ag surface interactions based on the average distance being between solution- and solid-phase.

Overall, the addition of water allowed for Ag-S bonds to shorten and the Ag_{32} core to expand. No increase in surface or core bond disorder was detected based on the Debye-Waller factors. The addition of water seems to allow the Ag core to relax from pure solvent conditions. We speculate that there could be a second mode of solvation under semi-aqueous conditions where water molecules interact with carboxylate groups of *p*-MBA through hydrogen bonding. These interactions at the tail of the ligand could change the ligand conformation and disrupt ligand-ligand bundling on the surface, further affecting the coordinating ability of DMSO. The influence of water-carboxylate interactions on the Ag_{32} core and the Ag-S surface framework is significant and could be highly dependent on the pH conditions. Future work should further examine this second mode of solvent-ligand interaction for semi-aqueous conditions by adjusting the pH from basic to acidic conditions while monitoring the structural change with solution-phase EXAFS.

9.5.3 Thermal decomposition

The high stability of $Ag_{44}(SR)_{30}$ NCs is an outstanding achievement for thiolate-protected Ag NCs as their stability against degradation in solution even matches, if not surpasses, $Au_{25}(SR)_{18}$ NCs.[133] From a structural point of view, the surface of $Ag_{44}(SR)_{30}$ NCs is well-protected with 6 mount structures that create an incomplete Ag_2S layer around the Ag_{32} core. The transformation of $Ag_{44}(SR)_{30}$ NCs to oxidized Ag_2S particles or sintered metallic Ag NPs is therefore of interest.

Another stability concern is how increased temperatures affect $Ag_{44}(SR)_{30}$ NCs. This is an important consideration since many of the promising materials science applications related to Ag NPs include conductive ink materials[327] and solar cell dye-NP sensitizers,[328,329] where temperature will affect their long term performance. Urushizaki *et al.*[325] used high temperature calcination conditions to convert $Ag_{44}(SR)_{30}$ NCs to small sulfur-free Ag NCs for dehydrogenation catalysis. For their high temperature conversion, however, $Ag_{44}(SR)_{30}$ NCs were first deposited on mesoporous carbon, and 4-(fluorophenyl)thiolate was used as the protecting ligand. The supporting material and ambient oxygen would have a significant effect on the thermal decomposition of $Ag_{44}(SR)_{30}$ NCs. Toward this end, $Ag_{44}(SR)_{30}$ NCs were sealed in quartz tubes under inert atmosphere with a small vacuum for annealing. Annealed samples were kept in sealed quartz tubes until XAFS measurements were conducted. EXAFS fitting results were used to monitor the structural change of $Ag_{44}(SR)_{30}$ NCs when annealed at various critical temperatures, which were determined from the TGA shown in Figure 9.6.

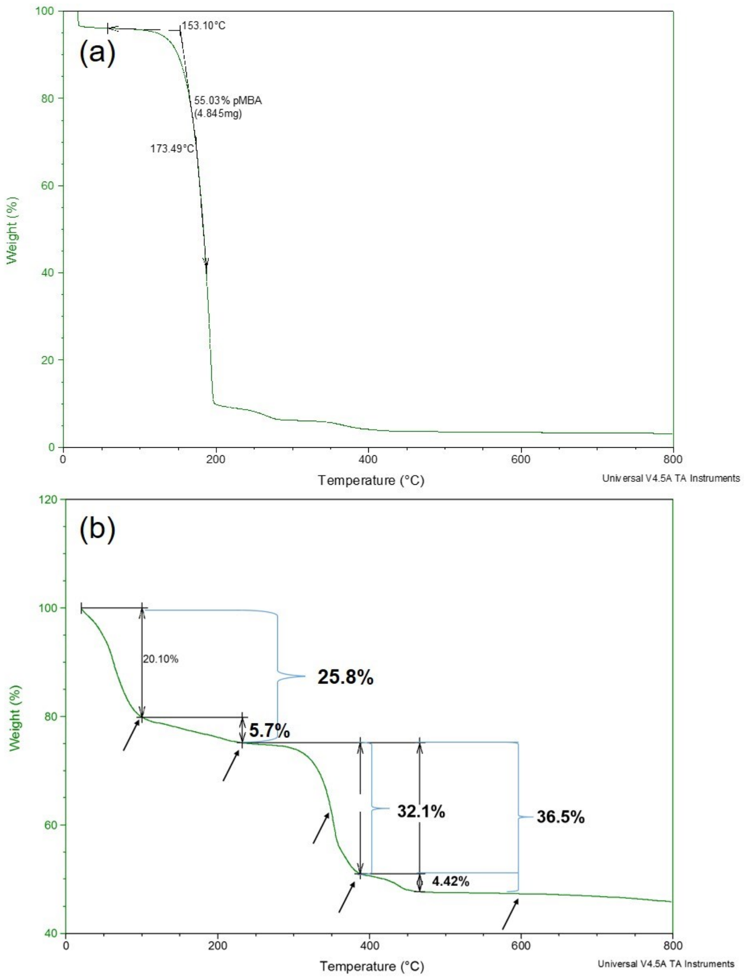

Figure 9.6 TGA of (a) *p*-MBA and (b) $Ag_{44}(p\text{-MBA})_{30}$ NCs. Arrows indicate temperatures that were selected for annealing $Ag_{44}(p\text{-MBA})_{30}$ NC samples. Solvent boiling points: water = 100°C, DMF = 153°C, DMSO = 189°C.

TGA of *p*-MBA is shown in Figure 9.6a. From this preliminary analysis, the thiol molecule began to degrade around 150°C and almost completely degraded around 200°C, with some residual mass remaining after 400°C. Although this is an important reference for the TGA of $Ag_{44}(p\text{-MBA})_{30}$ in Figure 9.6b, the degradation of *p*-MBA (in thiol form) may be different as it is bound to the Ag NC (in thiolate form). The first mass loss in the TGA of $Ag_{44}(p\text{-MBA})_{30}$ (Figure 9.6b) occurred from 25°C to 100°C and was likely due to evaporation of water. The next mass loss from 100°C to 230°C should include the evaporation of DMF (boiling point ~ 153°C) and DMSO (boiling point ~ 189°C). From

230°C to 390°C and onward, there are two mass loss events that could be attributed to degradation of ligand and/or some Ag atoms from the NC. Ag K-edge XAFS was collected for samples annealed around the aforementioned mass loss events to examine structural changes to the $Ag_{44}(SR)_{30}$ NC. The *k*-space spectra are displayed in Figure 9.7 for each annealing temperature. More significant changes to the EXAFS oscillation pattern became apparent between 350°C and 390°C.

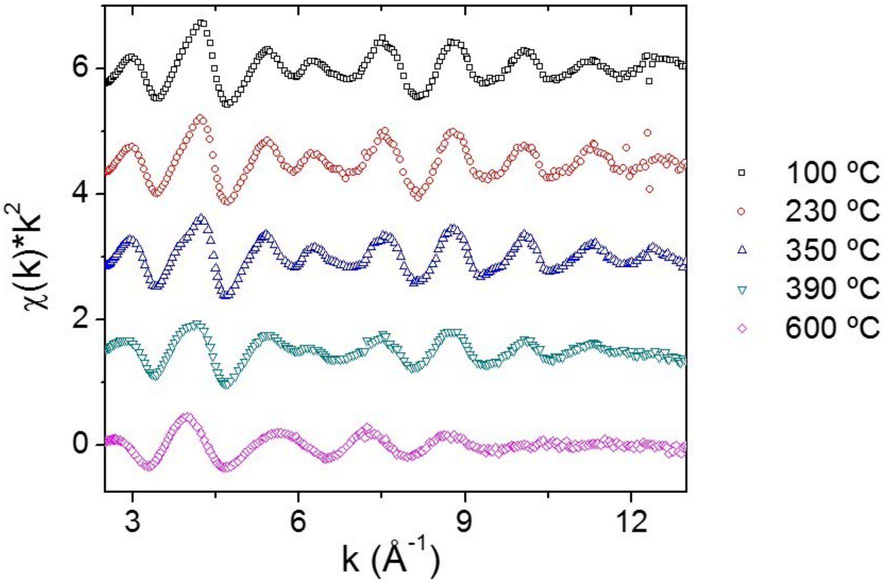

Figure 9.7 Ag K-edge *k*-space spectra of Ag_{44}(*p*-MBA)$_{30}$ NCs after being annealed at the indicated temperatures (*k*-space for 25°C is shown in Figure 9.3).

Figure 9.8 displays the overlap of FT-EXAFS spectra for annealed $Ag_{44}(SR)_{30}$ NC samples and Table 9.3 presents the structural parameters for fitted Ag-S and Ag-Ag paths. Only two scattering shells are employed for EXAFS fitting of annealed samples because the CN parameters are not fixed and the Ag-Ag framework was anticipated to change from $Ag_{44}(SR)_{30}$. From 25°C to 100°C, Ag-Ag scattering increased, which is evident in Figure 9.8 (increase in feature at 2.7 Å) and from the fitting result where the CN increased to 5.0 and the average Ag-Ag bond length changed from 2.826(6) Å to 2.865(2) Å. Although the Ag-Ag bond length is similar to that of bulk Ag-Ag (2.88 Å), the CN parameters still reflect particles on the NC size regime. The CN parameter from fitting Ag-S decreased to 1.5(2) from 1.9(2), indicating initial loss of thiolate ligands. From 100°C to 230°C, there was hardly any change in structure. From these results, evaporation of residual solvent and partial loss of thiolate ligands lead to an increase in Ag-Ag coordination and a longer average Ag-Ag bond length in the core.

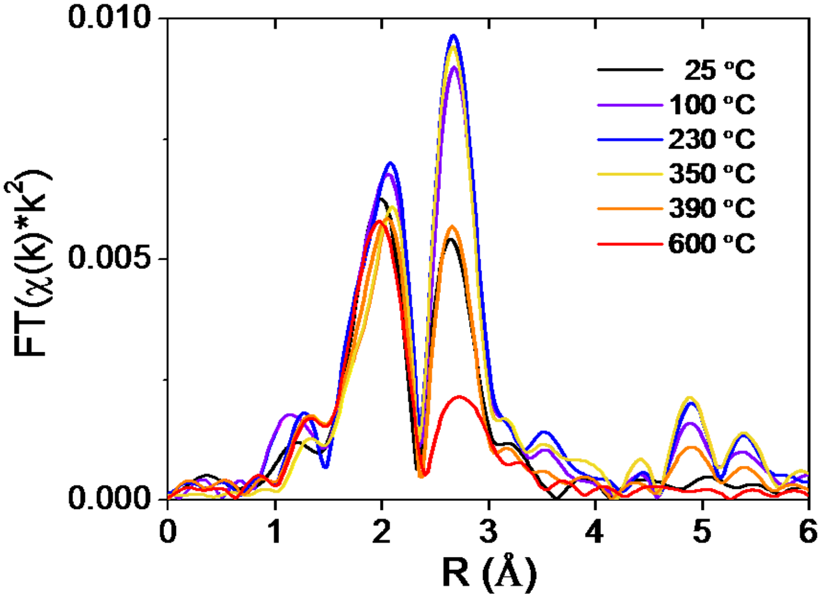

Figure 9.8 Ag K-edge FT-EXAFS of $Ag_{44}(SR)_{30}$ NCs after annealing at various temperatures.

The EXAFS fitting results and the mass loss indicated by TGA at 230°C suggested a small structural change had occurred for $Ag_{44}(SR)_{30}$ NCs. Considering the Ag-S CN of 1.3(2) and Ag-Ag CN of 5.4(4), the removal of Ag_2(*p*-MBA) from each of the 6 mount structures (Ag_2(*p*-MBA)$_5$) in $Ag_{44}(SR)_{30}$ creates agreeable theoretical CNs of 1.5 and 5.6, respectively. The proposed thermal decomposition to $Ag_{32}(SR)_{24}$ is presented in Figure 9.9. Interestingly, if the evaporation of residual solvent is ignored from 25°C to 230°C, the 25.8 % mass loss recorded from TGA in this range corresponds well with the mass loss when Ag_{44}(*p*-MBA)$_{30}$ is transformed to Ag_{32}(*p*-MBA)$_{24}$, which is calculated to be 23.7 %. Although $Ag_{32}(SR)_{24}$ NCs have not been found based on the current literature, a similar sized $Ag_{32}(SR)_{19}$ NC has been synthesized and isolated.[330]

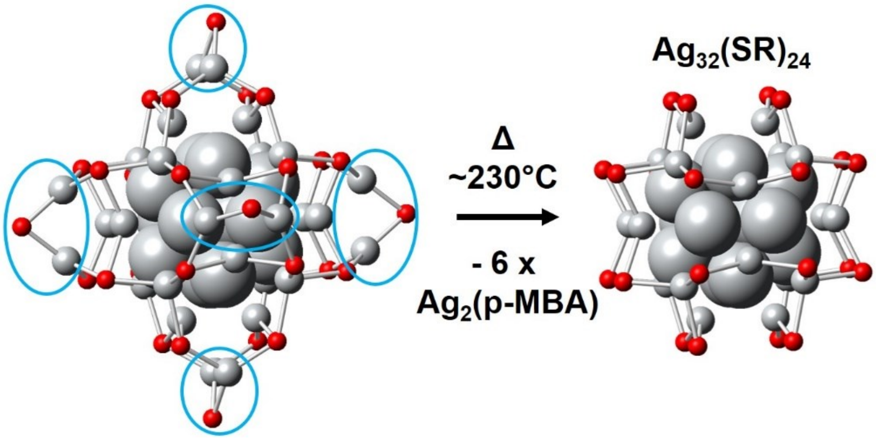

Figure 9.9 Proposed thermal decomposition pathway for $Ag_{44}(SR)_{30}$ NCs. *p*-MBA ligands are not shown.

There is a substantial mass loss of 36.5 % in the TGA between 230°C and 600°C (Figure 9.6b), giving rise to a total mass loss of 62.3 %. Based on the TGA-EXAFS analysis, it was expected that between 230°C and 600°C at least the organic substituent component of *p*-MBA ($-C_6H_4COOH$) would degrade from the sample, potentially leaving only S atoms in the Ag NC framework. EXAFS fitting of the 350°C sample indicated a decreased Ag-S CN from loss of thiolate ligand. Upon opening the quartz tube after annealing at 350°C, a strong sulfur smell was noticeable in comparison to quartz tubes annealed at lower temperatures. Ag-Ag scattering steadily decreased from 230°C (CN = 5.4(4)) to 390°C (3.4(5)). The Ag-S CN increased slightly at 390°C though the Ag-S scattering feature did not change in intensity from 350°C. This is likely a result from the loss of Ag atoms that were initially interacting with several other Ag atoms (therefore, Ag will have more interactions with S on average). Scattering in the *R*-space region around 4.5 to 5.5 Å decreased from 350°C to 600°C, which signified an absence of long-range ordering after annealing at these higher temperatures.

Table 9.3 Two-shell EXAFS fitting results (unfixed CN parameters) for $Ag_{44}(SR)_{30}$ NCs at various annealing temperatures. Uncertainties in fitted parameters are shown in parnetheses.

	Ag-S			Ag-Ag		
T (°C)	CN	R (Å)	σ^2 (Å^2)	CN	R (Å)	σ^2 (Å^2)
25	1.9(2)	2.481(7)	0.006(1)	4.1(4)	2.826(6)	0.014(1)
100	1.5(2)	2.490(5)	0.009(1)	5.0(2)	2.865(2)	0.0106(4)
230	1.3(2)	2.492(9)	0.008(2)	5.4(4)	2.865(4)	0.011(8)
350	1.2(2)	2.517(9)	0.010(2)	4.8(3)	2.864(3)	0.0098(4)
390	1.4(3)	2.51(1)	0.0085(3)	3.4(5)	2.870(6)	0.011(1)
600	1.6(1)	2.503(4)	0.007(1)	3.4(8)	2.95(1)	0.024(3)

The last sample in this study was annealed at 600°C, which was well beyond the degradation temperature of *p*-MBA ligands. At this temperature, the Ag-Ag scattering feature decreased significantly and became longer, with an average Ag-Ag distance of 2.95(1) Å. A higher Debye-Waller factor accompanied this change in Ag-Ag scattering. The combination of Ag-Ag bond length increase and higher structural disorder was indicative of a Ag_2S local structure.[331]

Considering the total mass loss of 62.3 %, the Ag_2S-like structure from EXAFS fitting results and the proposed structural change above in Figure 9.9, the removal of the benzoic acid constituent from *p*-MBA ligands could leave a $Ag_{32}S_{24}$ NC. For example, this species is ~45 % the original mass of Ag_{44}(*p*-MBA)$_{30}$, which is not far from the ~37.7 % indicated by TGA. It is difficult to propose a structure for $Ag_{32}S_{24}$ since the Ag-Ag framework has been significantly changed. However, the Ag-S CN of 1.6 is still around the theoretical CN for the proposed $Ag_{32}(SR)_{24}$ NC. Further TGA-MS studies of this annealing experiment, and possibly DFT-optimized structures of reduced $Ag_{44}(SR)_{30}$ structures, should be further investigated to reveal more on the thermal decomposition, which surprisingly leads to Ag_2S-like NCs and not sintered metallic Ag NPs.

9.6 Conclusion

The bonding properties of atomically-precise thiolate-protected $Ag_{44}(SR)_{30}$ NCs were investigated with Ag K-edge EXAFS under solid-phase and solution-phase conditions. For these experiments, core and surface bonding environments were individually monitored with a multi-shell EXAFS fitting analysis. The Ag_{32} core was found to contract at room temperature compared to low temperature, and when strong coordinating solvents (DMSO and DMF) were used for solution-phase measurements. Based on the change in $Ag_{44}(SR)_{30}$ NC bonding properties from EXAFS and the ligand bundling of *p*-MBA, coordinating solvents may interact directly with the Ag NC core. Semi-aqueous solutions induced another change in the Ag NC core and surface bonding, suggested through water-*p*-MBA interactions. Another specific mode of solvent-cluster interactions for water and $Ag_{44}(SR)_{30}$ awaits further investigation. Finally, $Ag_{44}(SR)_{30}$ NCs were annealed at various temperatures up to 600°C. It was shown that the majority of the cluster remains intact until about 350°C, where some thiolate ligands were lost. At 600°C, only Ag_2S-structured, NC-sized particles remained.

Chapter 10 - Conclusion

Studies in this thesis have demonstrated the unique electronic and bonding properties of various Au and Ag NCs using X-ray spectroscopies (mainly X-ray absorption spectroscopy) in conjunction with optical spectroscopy and computational calculations. Importantly, element-specific XAFS measurements and site-specific EXAFS fitting revealed several insights into the sensitive nature of Au and Ag NC structure and properties to the core structure, protecting ligand type and experimental factors, such as temperature and solvation effects. Quantum confinement of valence electrons was evident in several studies when the electronic properties were investigated, which supports the molecule-like properties of NCs.

Atomically-precise thiolate-protected Au NCs, and related NC systems, served as excellent models to examine site-specific bonding properties. Distinct local structural environments for Au and Ag NCs were identified using the available crystal structure information and assigning predominate scattering paths for EXAFS fitting. Local bonding environments, such as core, surface, metal-ligand interface and ligand, were monitored under varied experimental conditions or compared across a series of related NCs. This provided an experimental approach for correlating the bonding properties or the optical properties with NC local structure, which revealed important findings such as the thermal contraction property of FCC-based Au NCs and selenolate-protected Au NCs, and also the unique Au structural environments of highly luminescent glutathione- and protein-protected Au NCs. Scientific contributions from this research will hopefully benefit the future characterization and understanding of metal NC (*e.g.*, Au, Ag, Pt, Cu, *etc.*) structure and properties through X-ray absorption spectroscopy.

10.2 Proposed Future Work

$Au_{36}(SR)_{24}$ and $Au_{28}(SR)_{20}$ NCs studied in Chapters 4 and 5 exhibited an unexpected thermal contraction property as a result of their FCC-ordered core with Au_4 core substructures. Other studies have identified Au NPs of slightly larger size than Au NCs studied here (~2 nm in diameter) that appear to have a thermal contraction property or have very minimal thermal expansion in comparison to the bulk.[240,241] These previous studies have not employed a characterization technique that differentiates surface and core bonding environments, which is possible for small to medium sizes (~Au_{25}-Au_{50}) of atomically precise Au NCs (as shown in Chapters 4 and 5). Future work on FCC-ordered Au NCs should explore a finer temperature gradient to revisit the site-specific changes in Au-Au bonding properties (*i.e.*, surface and core). Moreover, total structures of FCC-ordered Au NCs larger than those studied in this work have been elucidated ($Au_{44}(SR)_{28}$ and $Au_{52}(SR)_{32}$).[332] Thus, a temperature-dependent Au L_3-edge EXAFS study on the extended series of FCC-ordered Au NCs would help to understand the thermal contraction property as it relates to Au core size.

Chapters 6 and 7 revealed the impact of selenolate and glutathione ligands on the structure and electronic properties of $Au_n(SR)_m$ NCs. Each of these ligand types offers a means to modulate or tailor the properties of thiolate-protected Au NCs, where selenolate ligands can improve stability and SG ligands can enhance luminescence or provide surface functionalization for biomedical application. However, it is still uncertain how each of these ligand types will modify the structure and electronic properties as the Au NC framework or composition changes. Future XAFS studies could expand on what was found in Chapter 6 to probe the structure and properties of $Au_{18}(SeR)_{14}$, $Au_{24}(SeR)_{20}$ and $Au_{38}(SeR)_{24}$ NCs.[249,258,259] In a similar manner, the SG-protected Au NC series (*e.g.*, $Au_{15}(SG)_{13}$, $Au_{18}(SG)_{14}$, $Au_{22}(SG)_{16-18}$, and $Au_{25}(SG)_{18}$) could be further compared with analogous compositions protected by simple organothiolate ligands to learn more on the role of structural rigidity and the PL mechanism for $Au_n(SR)_m$ NCs. There will be some limitations in the $Au_n(SR)_m$ NC series due to the large size of SG ligands, which may prevent the formation or hamper the stability of certain Au NC sizes or frameworks (*e.g.,* $Au_{38}(SG)_{24}$).

The experimental and analytical approach used in Chapter 8 afforded a wealth of information on BSA-protected Au NCs. Utilizing similar synchrotron-based XAFS techniques with supporting calculations and optical spectroscopies, other studies on protein-protected Au NCs should be pursued in order to elucidate more on the Au local structure and biomolecular self-assembly process. Other protein molecules have been identified for the synthesis of highly luminescent Au NCs including insulin, lysozyme, and transferrin.[173,178,297] Besides characterizing the final Au NC structure within each protein, pH-/temperature-dependent XAFS studies on each protein-directed synthesis of Au NCs would uncover more information regarding protein-specific Au local structural features that lead to the attractive highly luminescent property. Moreover, protein-stabilized Au NCs could be synthesized *in-situ* while XAFS measurements are conducted or synthesized *ex-situ*, lyophilized, and then measured at time of XAFS experiments, given that the Au NCs are stable after removal of water.

A more sophisticated XAFS approach for studying the formation mechanism of protein-protected Au NCs would be to take advantage of recent upgrades at the APS and CLS synchrotron facilities. At the Sector-9 beamline (APS) it will soon be possible to collect a complete Au L_3-edge EXAFS spectrum (up to ~15 k) of good quality in as little as 1 min or 1 s (compared to 15-20 min at Sector 20-BM). This technique, aptly known as quick-EXAFS, enables researchers to closely monitor and capture chemical reactions or physical changes to the system in more detail.[192,333] Other hardware advancements have been made at the CLS, as well. Scientists at the SXRMB beamline (CLS) have recently constructed an environmental chamber capable of collecting S K-edge XAFS spectra without a vacuum. This allows for solution-phase measurements and a more versatile soft X-ray experimental set-up. The combination of these two upgrades would offer more detailed insights on the formation of protein-protected Au NCs by conducting *in-situ* Au L_3-edge EXAFS to monitor the growth of Au NCs within the protein and solution-phase S K-edge measurements of sulfur-containing proteins to follow the protein's local perspective during the biomolecular self-assembly. These beamline upgrades would also be pertinent for the in-depth study of ligand exchange processes and for the catalytic activity of Au and Ag NCs. Capturing the detailed thiolate replacement, NC core restructuring, or chemical reactions that occur during catalytic reactions with these XAFS experiments would undoubtedly advance our understanding of thiolate-protected Au and Ag NCs.

Bibliography

(1) Grzelczak, M.; Pérez-Juste, J.; Mulvaney, P.; Liz-Marzán, L. M. *Chem. Soc. Rev.* **2008**, *37*, 1783.

(2) Sun, Y.; Xia, Y. *Science* **2002**, *298*, 2176.

(3) Kango, S.; Kalia, S.; Celli, A.; Njuguna, J.; Habibi, Y.; Kumar, R. *Prog. Polym. Sci.* **2013**, *38*, 1232.

(4) Liong, M.; Lu, J.; Kovochich, M.; Xia, T.; Ruehm, S. G.; Nel, A. E.; Tamanoi, F.; Zink, J. I. *ACS Nano* **2008**, *2*, 889.

(5) Niemeyer, C. M. *Angew. Chem. Int. Ed.* **2001**, *40*, 4128.

(6) Katz, E.; Willner, I. *Angew. Chemie Int. Ed.* **2004**, *43*, 6042.

(7) Salata, O. V. *J. Nanobiotechnology* **2004**, *2*, 1.

(8) Jain, P. K.; Huang, X.; El-Sayed, I. H.; El-Sayed, M. A. *Acc. Chem. Res.* **2008**, *41*, 1578.

(9) Stockman, M. I. *Phys. Today* **2011**, *64*, 39.

(10) Sanvicens, N.; Marco, M. P. *Trends Biotechnol.* **2008**, *26*, 425.

(11) Arico, A. S.; Bruce, P.; Scrosati, B.; Tarascon, J.-M.; Schalkwijk, W. Van. *Nat. Mater.* **2005**, *4*, 366.

(12) Kumari, A.; Yadav, S. K.; Yadav, S. C. *Colloids Surfaces B Biointerfaces* **2010**, *75*, 1.

(13) Kamat, P. V. *J. Phys. Chem. C* **2008**, *112*, 18737.

(14) Yin, Y.; Alivisatos, a P. *Nature* **2005**, *437*, 664.

(15) Crooks, R. M.; Zhao, M.; Sun, L.; Chechik, V.; Yeung, L. K. *Acc. Chem. Res.* **2001**, *34*, 181.

(16) Narayanan, R.; El-Sayed, M. A. *J. Phys. Chem. B* **2005**, *109*, 12663.

(17) Bell, A. T.; Bond, G. C.; Thompson, D. T.; Valden, M.; Lai, X.; Goodman, D. W.; Blasko, T.; Nieto, J. M. L.; Chen, K.; Bell, A. T.; Iglesia, E.; Koyama, T.; Komaya, T.; Gai, P. L.; Weyland, M.; Durscher, G.; Browning, N. D.; Pennycook, S. J.; Besenbacker, F.; Thune, P. C.; Loss, J.; Wonter, D.; Leustra, P. J.; Niemantsverdriet, J. W.; Corker, J.; Vidal, V.; Theolier, A.; Thivolle-Cazat, J.;

Basset, J.-M.; Nozkaki, C.; Lugmair, C. G.; Bell, A. T.; Tilley, T. D.; Kolb, D.; Jong, K. P. De; Geus, J. W. *Science* **2003**, *299*, 1688.

(18) Astruc, D.; Lu, F.; Aranzaes, J. R. *Angew. Chemie - Int. Ed.* **2005**, *44*, 7852.

(19) Cuenya, B. R. *Thin Solid Films* **2010**, *518*, 3127.

(20) Ozbay, E. *Science* **2006**, *311*, 189.

(21) Gao, X.; Cui, Y.; Levenson, R. M.; Chung, L. W. K.; Nie, S. *Nat. Biotechnol.* **2004**, *22*, 969.

(22) Erathodiyil, N.; Ying, J. Y. *Acc. Chem. Res.* **2011**, *44*, 925.

(23) Giljohann, D. A.; Seferos, D. S.; Daniel, W. L.; Massich, M. D.; Patel, P. C.; Mirkin, C. A. *Angew. Chemie Int. Ed.* **2010**, *49*, 3280.

(24) Dykman, L.; Khlebtsov, N. *Chem. Soc. Rev.* **2012**, *41*, 2256.

(25) Roduner, E. *Chem. Soc. Rev.* **2006**, *35*, 583.

(26) Kelly, K. L.; Coronado, E.; Zhao, L. L.; Schatz, G. C. *J. Phys. Chem. B* **2003**, *107*, 668.

(27) El-Sayed, M. A. *Acc. Chem. Res.* **2001**, *34*, 257.

(28) Daniel, M.-C.; Astruc, D. *Chem. Rev.* **2004**, *104*, 293.

(29) Katz, E.; Willner, I.; Wang, J. *Electroanalysis* **2004**, *16*, 19.

(30) Shan, J.; Tenhu, H. *Chem. Commun. (Camb).* **2007**, 4580.

(31) Zeng, S.; Yong, K.-T.; Roy, I.; Dinh, X.-Q.; Yu, X.; Luan, F. *Plasmonics* **2011**, *6*, 491.

(32) Faraday, M. *Trans. Faraday Soc.* **1857**, 145.

(33) Turkevich, J.; Stevenson, P. C.; Hillier, J. *Discuss. Faraday Soc.* **1951**, *11*, 55.

(34) Brust, M.; Walker, M.; Bethell, D.; Schiffrin, D. J.; Whyman, R. *J. Chem. Soc. Chem. Commun.* **1994**, 801.

(35) Sardar, R.; Funston, A. M.; Mulvaney, P.; Murray, R. W. *Langmuir* **2009**, *25*, 13840.

(36) Zhao, W.; Brook, M. A.; Li, Y. *Chembiochem* **2008**, *9*, 2363.

(37) Pradeep, T. *Thin Solid Films* **2009**, *517*, 6441.

(38) Baptista, P.; Pereira, E.; Eaton, P.; Doria, G.; Miranda, A.; Gomes, I.; Quaresma, P.; Franco, R. *Anal. Bioanal. Chem.* **2008**, *391*, 943.

(39) Tsuzuki, T.; McCormick, P. *J. Mater. Sci.* **2004**, *9*, 5143.

(40) Weare, W. W.; Reed, S. M.; Warner, M. G.; Hutchison, J. E. *J. Am. Chem. Soc.* **2000**, *122*, 12890.

(41) Leff, D. V; Brandt, L.; Heath, J. R. *Langmuir* **1996**, *12*, 4723.

(42) Link, S.; El-Sayed, M. A. *J. Phys. Chem. B* **1999**, *103*, 4212.

(43) Saha, K.; Agasti, S. S.; Kim, C.; Li, X.; Rotello, V. M. *Chem. Rev.* **2012**, *112*, 2739.

(44) Cao, J.; Sun, T.; Grattan, K. T. V. *Sensors Actuators, B Chem.* **2014**, *195*, 332.

(45) Joshi, G. K.; McClory, P. J.; Muhoberac, B. B.; Kumbhar, A.; Smith, K. A.; Sardar, R. *J. Phys. Chem. C* **2012**, *116*, 20990.

(46) Erathodiyil, N.; Ying, J. Y. *Acc. Chem. Res.* **2011**, *44*, 925.

(47) Alvarez, M. M.; Khoury, J. T.; Schaaff, T. G.; Shafigullin, M. N.; Whetten, R. L.; Vezmar, I. *J. Phys. Chem. B* **1997**, *101*, 3706.

(48) Taylor, K. J.; Pettiette-Hall, C. L.; Cheshnovsky, O.; Smalley, R. E. *J. Chem. Phys.* **1992**, *96*, 3319.

(49) de Heer, W. A. *Rev. Mod. Phys.* **1993**, *65*, 611.

(50) Valden, M.; Lai, X.; Goodman, D. W. *Science (80-.).* **1998**, *281*, 1647.

(51) Li, G.; Jin, R. *Acc. Chem. Res.* **2013**, *46*, 1749.

(52) Aiken, J. D.; Finke, R. G. *J. Mol. Catal. A Chem.* **1999**, *145*, 1.

(53) Schaff, T. G.; Shafigullin, M. N.; Khoury, J. T.; Whetten, R. L.; Cullen, W. G.; First, P.; Guitierrez-Wing, C.; Ascensio, J.; Jose-Yacaman, M. J. *J. Phys. Chem. B* **1997**, *101*, 7885.

(54) Parker, J. F.; Fields-Zinna, C. A.; Murray, R. W. *Acc. Chem. Res.* **2010**, *43*, 1289.

(55) Jin, R. *Nanoscale* **2010**, *2*, 343.

(56) Kubo, R.; Kawabata, A.; Kobayashi, S. *Annu. Rev. Mater. Sci.* **1984**, *14*, 49.

(57) Qian, H.; Zhu, M.; Wu, Z.; Jin, R. *Acc. Chem. Res.* **2012**, *45*, 1470.

(58) Zheng, J.; Zhang, C.; Dickson, R. *Phys. Rev. Lett.* **2004**, *93*, 5.

(59) Dickson, R. M.; Nicovich, P. R.; Zheng, J. *Annu. Rev. Phys. Chem.* **2007**, *58*, 409.

(60) Zheng, J.; Petty, J. T.; Dickson, R. M. *J. Am. Chem. Soc.* **2003**, *125*, 7780.

(61) Teo, B. K.; Shi, X.; Zhang, H. *J. Am. Chem. Soc.* **1992**, *114*, 2743.

(62) Schmid, G.; Pfeil, R.; Boese, R.; Bandermann, F.; Meyer, S.; Calis, G. H. M.; Velden, J. W. A. van der. *Chem. Ber.* **1981**, *114*, 3634.

(63) Schmid, G. *Chem. Soc. Rev.* **2008**, *37*, 1909.

(64) Boyen, H.-G.; Kastle, G.; Weigl, F.; Koslowski, B.; Dietrich, C.; Ziemann, P.; Spatz, J. P.; Riethmüller, S.; Hartmann, C.; Moller, M.; Schmid, G.; Garnier, M. G.; Oelhafen, P. *Science (80-.).* **2002**, *297*, 1533.

(65) Fauth, K.; Kreibig, U.; Schmid, G. *Zeitschrift für Phys. D - Atoms, Mol. Clust.* **1991**, *20*, 297.

(66) Zhang, H.; Schmid, G.; Hartmann, U. *Nano Lett.* **2003**, *3*, 305.

(67) Menard, L. D.; Gao, S. P.; Xu, H.; Twesten, R. D.; Harper, A. S.; Song, Y.; Wang, G.; Douglas, A. D.; Yang, J. C.; Frenkel, A. I.; Nuzzo, R. G.; Murray, R. W. *J. Phys. Chem. B* **2006**, *110*, 12874.

(68) Guliamov, O.; Frenkel, A. I.; Menard, L. D.; Nuzzo, R. G.; Kronik, L. *J. Am. Chem. Soc.* **2007**, *129*, 10978.

(69) Shichibu, Y.; Negishi, Y.; Watanabe, T.; Chaki, N. K.; Kawaguchi, H.; Tsukuda, T. *J. Phys. Chem. C* **2007**, *111*, 7845.

(70) Xavier, P. L.; Chaudhari, K.; Baksi, A.; Pradeep, T. *Nano Rev.* **2012**, *3*, 1.

(71) Chevrier, D. M. D. M.; Chatt, A.; Zhang, P.; Chatt, A. *J. Nanophotonics* **2012**, *6*, 64504.

(72) Lu, Y.; Chen, W. In *Gold Clusters, Colloids and Nanoparticles I*; Springer International Publishing, 2013; pp 117–153.

(73) Pensa, E.; Cortés, E.; Corthey, G.; Carro, P.; Vericat, C.; Fonticelli, M. H.; Benítez, G.; Rubert, A. A.; Salvarezza, R. C. *Acc. Chem. Res.* **2012**, *45*, 1183.

(74) Bourg, M.-C.; Badia, A.; Lennox, R. B. *J. Phys. Chem. B* **2000**, *104*, 6562.

(75) Love, J. C.; Estroff, L. A.; Kriebel, J. K.; Nuzzo, R. G.; Whitesides, G. M. *Chem. Rev.* **2005**, *105*, 1103.

(76) Hostetler, M. J.; Green, S. J.; Stokes, J. J.; Murray, R. W. *J. Am. Chem. Soc.* **1996**, *118*, 4212.

(77) Alvarez, M. M.; Khoury, J. T.; Schaaff, T. G.; Shafigullin, M.; Vezmar, I.; Whetten, R. L. *Chem. Phys. Lett.* **1997**, *266*, 91.

(78) Chaki, N. K.; Negishi, Y.; Tsunoyama, H.; Shichibu, Y.; Tsukuda, T. *J. Am. Chem. Soc.* **2008**, *130*, 8608.

(79) Negishi, Y.; Takasugi, Y.; Sato, S.; Yao, H.; Kimura, K.; Tsukuda, T. *J. Am. Chem. Soc.* **2004**, *126*, 6518.

(80) Negishi, Y.; Nobusada, K.; Tsukuda, T. *J. Am. Chem. Soc.* **2005**, *127*, 5262.

(81) Zhu, M.; Lanni, E.; Garg, N.; Bier, M. E.; Jin, R. *J. Am. Chem. Soc.* **2008**, *130*, 1138.

(82) Qian, H.; Zhu, Y.; Jin, R. *ACS Nano* **2009**, *3*, 3795.

(83) Qian, H.; Jin, R. *Nano Lett.* **2009**, *9*, 4083.

(84) Angel, L.; Majors, L.; Dharmaratne, A.; Dass, A. *ACS Nano* **2010**, *4*, 4691.

(85) Harkness, K. M.; Cliffel, D. E.; McLean, J. A. *Analyst* **2010**, *135*, 868.

(86) Pei, Y.; Zeng, X. C. *Nanoscale* **2012**, *4*, 4054.

(87) Jiang, D. *Nanoscale* **2013**, *5*, 7149.

(88) Jin, R. *Nanoscale* **2015**, *7*, 1549.

(89) Jadzinsky, P. D.; Calero, G.; Ackerson, C. J.; Bushnell, D. A.; Kornberg, R. D. *Science* **2007**, *318*, 430.

(90) Qian, H.; Eckenhoff, W. T.; Zhu, Y.; Pintauer, T.; Jin, R. *J. Am. Chem. Soc.* **2010**, *132*, 8280.

(91) Zhu, M.; Eckenhoff, W. T.; Pintauer, T.; Jin, R. *J. Phys. Chem. Lett.* **2008**, *112*, 14221.

(92) Heaven, M. W.; Dass, A.; White, P. S.; Holt, K. M.; Murray, R. W. *J. Am. Chem. Soc.* **2008**, *130*, 3754.

(93) Yourdshahyan, Y.; Zhang, H. K.; Rappe, A. M. *Phys. Rev. B* **2000**, *63*, 81405.

(94) Häkkinen, H. *Nat. Chem.* **2012**, *4*, 443.

(95) Zhu, M.; Aikens, C. M.; Hollander, F. J.; Schatz, G. C.; Jin, R. *J. Am. Chem. Soc.* **2008**, *130*, 5883.

(96) Tofanelli, M. a; Ackerson, C. J. *J. Am. Chem. Soc.* **2012**, *134*, 16937.

(97) Garci, D.; Maduen, R.; Bla, M.; Pineda, T. **2009**, 8756.

(98) Walter, M.; Akola, J.; Lopez-Acevedo, O.; Jadzinsky, P. D.; Calero, G.; Ackerson, C. J.; Whetten, R. L.; Grönbeck, H.; Häkkinen, H. *Proc. Natl. Acad. Sci. U. S. A.*

2008, *105*, 9157.

(99) Luo, Z.; Nachammai, V.; Zhang, B.; Yan, N.; Leong, D. T.; Jiang, D.; Xie, J. *J. Am. Chem. Soc.* **2014**, *136*, 10577.

(100) Zeng, C.; Qian, H.; Li, T.; Li, G.; Rosi, N. L.; Yoon, B.; Barnett, R. N.; Whetten, R. L.; Landman, U.; Jin, R. *Angew. Chemie Int. Ed.* **2012**, *51*, 13114.

(101) Jiang, D.-E.; Overbury, S. H.; Dai, S. *J. Am. Chem. Soc.* **2013**, *135*, 8786.

(102) Cheng, L.; Yuan, Y.; Zhang, X.; Yang, J. *Angew. Chemie Int. Ed.* **2013**, *52*, 9035.

(103) Das, A.; Li, T.; Li, G.; Nobusada, K.; Zeng, C.; Rosi, N. L.; Jin, R. *Nanoscale* **2014**, *6*, 6458.

(104) Zeng, C.; Liu, C.; Chen, Y.; Rosi, N. L.; Jin, R. *J. Am. Chem. Soc.* **2014**, *20*, 16.

(105) Yu, Y.; Luo, Z.; Chevrier, D. M.; Leong, D. T.; Zhang, P.; Jiang, D.; Xie, J. *J. Am. Chem. Soc.* **2014**, *136*, 1246.

(106) Hutchings, G. J.; Brust, M.; Schmidbaur, H. *Chem. Soc. Rev.* **2008**, *37*, 1759.

(107) Pyykko, P. *Chem. Rev.* **1988**, *88*, 563.

(108) Grönbeck, H.; Walter, M.; Häkkinen, H. *J. Am. Chem. Soc.* **2006**, *128*, 10268.

(109) Sellers, H.; Ulman, A.; Shnidman, Y.; Eilers, J. E. *J. Am. Chem. Soc.* **1993**, *115*, 9389.

(110) Schmidbaur, H.; Schier, A. *Chem. Soc. Rev.* **2012**, *41*, 370.

(111) Demuynck, J.; Rohmer, M.-M.; Strich, A.; Veillard, A. *J. Chem. Phys.* **1981**, *75*, 3443.

(112) Wertheim, G. K. In *Small Particles and Inorganic Clusters: Proceedings of the Fourth International Meeting on Small Particles and Inorganic Clusters University Aix-Marseille III Aix-en-Provence, France, 5--9 July 1988*; Chapon, C., Gillet, M. F., Henry, C. R., Eds.; Springer Berlin Heidelberg: Berlin, Heidelberg, 1989; pp 319–326.

(113) Weissker, H.-C.; Escobar, H. B.; Thanthirige, V. D.; Kwak, K.; Lee, D.; Ramakrishna, G.; Whetten, R. L.; López-Lozano, X. *Nat. Commun.* **2014**, *5*, 3785.

(114) Zeng, C.; Liu, C.; Pei, Y.; Jin, R. *ACS Nano* **2013**, *7*, 6138.

(115) Lopez-Acevedo, O.; Tsunoyama, H.; Tsukuda, T.; Häkkinen, H.; Aikens, C. M. *J. Am. Chem. Soc.* **2010**, *132*, 8210.

(116) Bigioni, T. P.; Whetten, R. L.; Dag, Ö. *J. Phys. Chem. B* **2000**, *104*, 6983.

(117) Wilcoxon, J. P.; Martin, J. E.; Parsapour, F.; Wiedenman, B.; Kelley, D. F. *J. Chem. Phys.* **1998**, *108*, 9137.

(118) Wang, G.; Huang, T.; Murray, R. W.; Menard, L.; Nuzzo, R. G. *J. Am. Chem. Soc.* **2005**, *127*, 812.

(119) Wu, Z.; Jin, R. *Nano Lett.* **2010**, *10*, 2568.

(120) Devadas, M. S.; Kim, J.; Sinn, E.; Lee, D.; Iii, T. G.; Ramakrishna, G. *J. Phys. Chem. C* **2010**, *114*, 22417.

(121) Liang, J.; Chen, Z.; Yin, J.; Yu, G.-A.; Liu, S. H. *Chem. Commun. (Camb).* **2013**, *49*, 3567.

(122) Goswami, N.; Yao, Q.; Luo, Z.; Li, J.; Chen, T.; Xie, J. *J. Phys. Chem. Lett.* **2016**, *7*, 962.

(123) Luo, Z.; Yuan, X.; Yu, Y.; Zhang, Q.; Leong, D. T.; Lee, J. Y.; Xie, J. *J. Am. Chem. Soc.* **2012**, *134*, 16662.

(124) Yu, Y.; Luo, Z.; Chevrier, D. M. D. M.; Leong, D. T. D. T.; Zhang, P.; Jiang, D.; Xie, J. *J. Am. Chem. Soc.* **2014**, *136*, 1246.

(125) Wu, X.; He, X.; Wang, K.; Xie, C.; Zhou, B.; Qing, Z. *Nanoscale* **2010**, *2*, 2244.

(126) Luo, Z.; Zheng, K.; Xie, J. *Chem. Commun. (Camb).* **2014**, *50*, 5143.

(127) Sun, C.; Yang, H.; Yuan, Y.; Tian, X.; Wang, L.; Guo, Y.; Xu, L.; Lei, J.; Gao, N.; Anderson, G. J.; Liang, X.-J.; Chen, C.; Zhao, Y.; Nie, G. *J. Am. Chem. Soc.* **2011**, *133*, 8617.

(128) Zhang, X.-D.; Wu, D.; Shen, X.; Liu, P.-X.; Fan, F.-Y.; Fan, S.-J. *Biomaterials* **2012**, *33*, 4628.

(129) Christensen, S. L.; Macdonald, M. A.; Chatt, A.; Zhang, P. *J. Phys. Chem. C* **2012**, *116*, 26932.

(130) Yamazoe, S.; Kurashige, W.; Nobusada, K.; Negishi, Y.; Tsukuda, T. *J. Phys. Chem. C* **2014**, *118*, 25284.

(131) Hartmann, M. J.; Häkkinen, H.; Millstone, J. E.; Lambrecht, D. S. *J. Phys. Chem. C* **2015**, *119*, 8290.

(132) Negishi, Y.; Kurashige, W.; Kobayashi, Y.; Yamazoe, S.; Kojima, N.; Seto, M.;

Tsukuda, T. *J. Phys. Chem. Lett.* **2013**, *4*, 3579.

(133) Desireddy, A.; Conn, B. E.; Guo, J.; Yoon, B.; Barnett, R. N.; Monahan, B. M.; Kirschbaum, K.; Griffith, W. P.; Whetten, R. L.; Landman, U.; Bigioni, T. P. *Nature* **2013**, *501*, 399.

(134) Joshi, C. P.; Bootharaju, M. S.; Alhilaly, M. J.; Bakr, O. M. *J. Am. Chem. Soc.* **2015**, *137*, 11578.

(135) Rai, M.; Yadav, A.; Gade, A. *Biotechnol. Adv.* **2009**, *27*, 76.

(136) Kang, S. Y.; Kim, K. *Langmuir* **1998**, *14*, 226.

(137) Padmos, J. D.; Zhang, P. *J. Phys. Chem. C* **2012**, *116*, 23094.

(138) Mcmahon, M. D.; Lopez, R.; Meyer, H. M.; Feldman, L. C.; Haglund, R. F. *Appl. Phys. B Lasers Opt.* **2005**, *80*, 915.

(139) Yang, H.; Wang, Y.; Huang, H.; Gell, L.; Lehtovaara, L.; Malola, S.; Häkkinen, H.; Zheng, N. *Nat. Commun.* **2013**, *4*, 2422.

(140) Jin, S.; Wang, S.; Song, Y.; Zhou, M.; Zhong, J.; Zhang, J.; Xia, A.; Pei, Y.; Chen, M.; Li, P.; Zhu, M. *J. Am. Chem. Soc.* **2014**, *136*, 15559.

(141) Yuan, X.; Yao, Q.; Yu, Y.; Luo, Z.; Dou, X.; Xie, J. *J. Phys. Chem. Lett.* **2013**, *4*, 1811.

(142) Yang, H.; Lei, J.; Wu, B.; Wang, Y.; Zhou, M.; Xia, A.; Zheng, L.; Zheng, N. *Chem. Commun. (Camb).* **2013**, *49*, 300.

(143) Dickerson, M. B.; Sandhage, K. H.; Naik, R. R. *Chem. Rev.* **2008**, *108*, 4935.

(144) Crookes-Goodson, W. J.; Slocik, J. M.; Naik, R. R. *Chem. Soc. Rev.* **2008**, *37*, 2403.

(145) Slocik, J. M.; Stone, M. O.; Naik, R. R. *Small* **2005**, *1*, 1048.

(146) Tan, Y. N.; Lee, J. Y.; Wang, D. I. C. *J. Am. Chem. Soc.* **2010**, *132*, 5677.

(147) Zhang, L.; Swift, J.; Butts, C. A.; Yerubandi, V.; Dmochowski, I. J. *J. Inorg. Biochem.* **2007**, *101*, 1719.

(148) Rangnekar, A.; Sarma, T. K.; Singh, A. K.; Deka, J. *Langmuir* **2007**, *23*, 5700.

(149) Burt, J. L.; Gutiérrez-Wing, C.; Miki-Yoshida, M.; José-Yacamán, M. *Langmuir* **2004**, *20*, 11778.

(150) Yang, T.; Li, Z.; Wang, L.; Guo, C.; Sun, Y. *Langmuir* **2007**, *23*, 10533.

(151) Shang, L.; Dong, S.; Nienhaus, G. U. *Nano Today* **2011**, *6*, 401.

(152) Xie, J.; Zheng, Y.; Ying, J. Y. *J. Am. Chem. Soc.* **2009**, *131*, 888.

(153) Zhang, L.; Wang, E. *Nano Today* **2014**, *9*, 132.

(154) Guo, C.; Irudayaraj, J. *Anal. Chem.* **2011**, *83*, 2883.

(155) Mathew, A.; Sajanlal, P. R.; Pradeep, T. *J. Mater. Chem.* **2011**, *21*, 11205.

(156) Goswami, N.; Giri, A.; Bootharaju, M. S.; Xavier, P. L.; Pradeep, T.; Pal, S. K. *Anal. Chem.* **2011**, *83*, 9676.

(157) Willett, R. L.; Baldwin, K. W.; West, K. W.; Pfeiffer, L. N. *Proc. Natl. Acad. Sci. U. S. A.* **2005**, *102*, 7817.

(158) Toroz, D.; Corni, S. *Nano Lett.* **2011**, *11*, 1313.

(159) Chen, C.-L.; Rosi, N. L. *Angew. Chemie Int. Ed.* **2010**, *49*, 1924.

(160) Zhong, Z.; Patskovskyy, S.; Bouvrette, P.; Luong, J. H. T.; Gedanken, A. *J. Phys. Chem. B* **2004**, *108*, 4046.

(161) Le Guevel, X.; Hotzer, B.; Jung, G.; Hollemeyer, K.; Trouillet, V.; Schneider, M. *J. Phys. Chem. C* **2011**, *115*, 10955.

(162) Chaudhari, K.; Xavier, P. L.; Pradeep, T. *ACS Nano* **2011**, *5*, 8816.

(163) Habeeb Muhammed, M. A.; Verma, P. K.; Pal, S. K.; Retnakumari, A.; Koyakutty, M.; Nair, S.; Pradeep, T. *Chem. Eur. J.* **2010**, *16*, 10103.

(164) Liu, Y.; Ai, K.; Cheng, X.; Huo, L.; Lu, L. *Adv. Funct. Mater.* **2010**, *20*, 951.

(165) Chen, Y.; Palmer, R. E.; Wilcoxon, J. P. *Langmuir* **2006**, *22*, 2851.

(166) Le Guével, X.; Daum, N.; Schneider, M. *Nanotechnology* **2011**, *22*, 275103.

(167) Zhang, M.; Dang, Y.-Q.; Liu, T.-Y.; Li, H.-W.; Wu, Y.; Li, Q.; Wang, K.; Zou, B. *J. Phys. Chem. C* **2013**, *117*, 639.

(168) Cao, X.; Li, H.; Yue, Y.; Wu, Y. *Vib. Spectrosc.* **2013**, *65*, 186.

(169) Kawasaki, H.; Yoshimura, K.; Hamaguchi, K.; Arakawa, R. *Anal. Sci.* **2011**, *27*, 591.

(170) Baksi, A.; Xavier, P. L.; Chaudhari, K.; Goswami, N.; Pal, S. K.; Pradeep, T. *Nanoscale* **2013**, *5*, 2009.

(171) Raut, S.; Chib, R.; Rich, R.; Shumilov, D.; Gryczynski, Z.; Gryczynski, I. *Nanoscale* **2013**, *5*, 3441.

(172) Wang, X.; Wu, P.; Lv, Y.; Hou, X. *Microchem. J.* **2011**, *99*, 327.

(173) Liu, C.-L.; Wu, H.-T.; Hsiao, Y.-H.; Lai, C.-W.; Shih, C.-W.; Peng, Y.-K.; Tang, K.-C.; Chang, H.-W.; Chien, Y.-C.; Hsiao, J.-K.; Cheng, J.-T.; Chou, P.-T. *Angew. Chemie Int. Ed.* **2011**, *50*, 7056.

(174) Hardman, R. *Environ. Health Perspect.* **2006**, *114*, 165.

(175) Lin, Y.-W.; Huang, C.-C.; Chang, H.-T. *Analyst* **2011**, *136*, 863.

(176) Xie, J.; Zheng, Y.; Ying, J. Y. *Chem. Commun. (Camb).* **2010**, *46*, 961.

(177) Lin, Y.-H.; Tseng, W.-L. *Anal. Chem.* **2010**, *82*, 9194.

(178) Wei, H.; Wang, Z.; Yang, L.; Tian, S.; Hou, C.; Lu, Y. *Analyst* **2010**, *135*, 1406.

(179) Hu, D.; Sheng, Z.; Gong, P.; Zhang, P.; Cai, L. *Analyst* **2010**, *135*, 1411.

(180) Mathew, M. S.; Baksi, A.; Pradeep, T.; Joseph, K. *Biosens. Bioelectron.* **2016**, *81*, 68.

(181) Lin, Z.; Luo, F.; Dong, T.; Zheng, L.; Wang, Y.; Chi, Y.; Chen, G. *Analyst* **2012**, *137*, 2394.

(182) MacDonald, M. A.; Zhang, P.; Qian, H.; Jin, R. *J. Phys. Chem. Lett.* **2010**, *1*, 1821.

(183) Ohta, T.; Shibuta, M.; Tsunoyama, H.; Negishi, Y.; Eguchi, T.; Nakajima, A. *J. Phys. Chem. C* **2013**, *25*, 3674.

(184) Losovyj, Y. B.; Li, S.; Lozova, N.; Katsiev, K.; Stellwagen, D.; Diebold, U.; Kong, L.; Kumar, C. S. S. R. *J. Phys. Chem. C* **2012**, *116*, 5857.

(185) Chevrier, D. M.; Yang, R.; Chatt, A.; Zhang, P. *Nanotechnol. Rev.* **2015**, *4*, 193.

(186) Macdonald, M. A.; Chevrier, D. M.; Zhang, P.; Qian, H.; Jin, R. *J. Phys. Chem. C* **2011**, *115*, 15282.

(187) Cluskey, P. D.; Newport, R. J.; Benfield, R. E.; Gurman, S. J.; Schmid, G. In *Atoms, Molecules and Clusters*; 1993; Vol. 11, pp S8–S11.

(188) Fairbanks, M. C.; Benfield, R. E.; Newport, R. J.; Schmid, G. *Solid State Commun.* **1990**, *73*, 431.

(189) Marcus, M. A.; Andrews, M. P.; Zegenhagen, J.; Laboratories, T. B.; Hill, M.; Montano, P. *Phys. Rev. B* **1990**, *42*, 3312.

(190) Menard, L. D.; Xu, H.; Gao, S.-P.; Twesten, R. D.; Harper, A. S.; Song, Y.; Wang, G.; Douglas, A. D.; Yang, J. C.; Frenkel, A. I.; Murray, R. W.; Nuzzo, R. G. *J.*

Phys. Chem. B **2006**, *110*, 14564.

(191) Li, Y.; Cheng, H.; Yao, T.; Sun, Z.; Yan, W.; Jiang, Y.; Xie, Y.; Sun, Y.; Huang, Y.; Liu, S.; Zhang, J.; Xie, Y.; Hu, T.; Yang, L.; Wu, Z.; Wei, S. *J. Am. Chem. Soc.* **2012**, *134*, 17997.

(192) Yao, T.; Sun, Z.; Li, Y.; Pan, Z.; Wei, H.; Xie, Y.; Nomura, M.; Niwa, Y.; Yan, W.; Wu, Z.; Jiang, Y.; Liu, Q.; Wei, S. *J. Am. Chem. Soc.* **2010**, *132*, 7696.

(193) Liu, J.; Krishna, K. S.; Losovyj, Y. B.; Chattopadhyay, S.; Lozova, N.; Miller, J. T.; Spivey, J. J.; Kumar, C. S. S. R. *Chem. Eur. J.* **2013**, *19*, 10201.

(194) Shivhare, A.; Chevrier, D. M.; Purves, R. W.; Scott, R. W. J. *J. Phys. Chem. C* **2013**, *117*, 20007.

(195) Zhang, P. *J. Phys. Chem. C* **2014**, *118*, 25291.

(196) Macdonald, M. A.; Chevrier, D. M.; Zhang, P.; Qian, H.; Jin, R.; Chevrier, D. M.; Zhang, P.; Qian, H.; Jin, R. *J. Phys. Chem. C* **2011**, *115*, 15282.

(197) Jiang, D. *Chem. Eur. J.* **2011**, *17*, 12289.

(198) Swinehart, D. F. *J. Chem. Educ.* **1962**, *39*, 333.

(199) Harris, D. C. *Exploring Chemical Analysis*, Fourth Edi.; W. H. Freeman and Company: New York, 2009.

(200) Rehr, J. J.; Albers, R. C. *Rev. Mod. Phys.* **2000**, *72*, 621.

(201) Stöhr, J. *NEXAFS Spectroscopy*; Springer: Verlag, Berlin, Heidelberg, 1992.

(202) Bunker, G. *A Practical Guide to X-ray Absorption Fine Structure Spectroscopy*; Cambridge University Press: Cambridge, New York, Melbourne, Madrid, Cape Town, Singapore, 2010.

(203) Newville, M. In *Consortium for Advanced Radiation Sources*; University of Chicago, Chicago, IL, 2004.

(204) Glaser, T.; Hedman, B.; Hodgson, K. O.; Solomon, E. I. *Acc. Chem. Res.* **2000**, *33*, 859.

(205) Tomson, N. C.; Williams, K. D.; Dai, X.; Sproules, S.; DeBeer, S.; Warren, T. H.; Wieghardt, K. *Chem. Sci.* **2015**, *6*, 2474.

(206) Stern, E. A. *Phys. Rev. B* **1974**, *10*, 3027.

(207) Sayers, D. E.; Stern, E. A.; Lytle, F. W. *Phys. Rev. Lett.* **1971**, *27*, 1204.

(208) Funke, H.; Scheinost, A. C.; Chukalina, M. *Phys. Rev. B* **2005**, *71*, 941107.

(209) Penfold, T. J.; Tavernelli, I.; Milne, C. J.; Reinhard, M.; Nahhas, A. El; Abela, R.; Rothlisberger, U.; Chergui, M. *J. Chem. Phys.* **2013**, *138*, 14104.

(210) Stern, E. A.; Sayers, D. E.; Lytle, F. W. *Phys. Rev. B* **1975**, *11*, 4836.

(211) Koningsberger, D. C.; Mojet, B. L.; Dorssen, G. E. Van; Ramaker, D. E. *Top. Catal.* **2000**, *10*, 143.

(212) Ravel, B.; Newville, M. *J. Synchrotron Radiat.* **2005**, *12*, 537.

(213) Newville, M.; Boyanov, B. I.; Sayers, D. E. *J. Synchrotron Radiat.* **1999**, *6*, 264.

(214) Zhang, W.; Duchesne, P. N.; Gong, Z.; Wu, S.; Ma, L.; Jiang, Z. *J. Phys. Chem. C* **2013**, *117*, 11498.

(215) Rehr, J. J.; Mustre de Leon, J.; Zabinsky, S. I.; Albers, R. C. *J. Am. Chem. Soc.* **1991**, *113*, 5135.

(216) Ankudinov, A. L.; Ravel, B.; Rehr, J. J.; Conradson, S. D. *Phys. Rev. B* **1998**, *58*, 7565.

(217) Desclaux, J. P. *Comput. Phys. Commun.* **1975**, *9*, 31.

(218) von Barth, U.; Hedin, L. *J. Phys. C Solid State Phys.* **1972**, *5*, 1629.

(219) Beleznay, F.; Lawrence, M. J. *J. Phys. C* **1968**, *1*, 1288.

(220) Einstein, A. *Ann. Phys.* **1905**, *17*, 132.

(221) Ghosh, P. *Introduction to photoelectron spectroscopy*; Wiley-Interscience: New York, 1983.

(222) Wu, Z.; MacDonald, M. A.; Chen, J.; Zhang, P.; Jin, R. *J. Am. Chem. Soc.* **2011**, *133*, 9670.

(223) Zeng, C.; Li, T.; Das, A.; Rosi, N. L.; Jin, R. *J. Am. Chem. Soc.* **2013**, *135*, 10011.

(224) Meng, X.; Xu, Q.; Wang, S.; Zhu, M. *Nanoscale* **2012**, *4*, 4161.

(225) Jiang, D.; Tiago, M. L.; Luo, W.; Dai, S. *J. Am. Chem. Soc.* **2008**, *130*, 2777.

(226) Simms, G. A.; Padmos, J. D.; Zhang, P. *J. Chem. Phys.* **2009**, *131*, 214703.

(227) Turner, M.; Golovko, V. B.; Vaughan, O. P. H.; Abdulkin, P.; Berenguer-Murcia, A.; Tikhov, M. S.; Johnson, B. F. G.; Lambert, R. M. *Nature* **2008**, *454*, 981.

(228) Zhu, Y.; Qian, H.; Jin, R. *J. Mater. Chem.* **2011**, *21*, 6793.

(229) Herzing, A. A.; Kiely, C. J.; Carley, A. F.; Landon, P.; Hutchings, G. J. *Science*

2008, *321*, 1331.

(230) Shao, N.; Huang, W.; Gao, Y.; Wang, L.-M.; Li, X.; Wang, L.-S.; Zeng, X. C. *J. Am. Chem. Soc.* **2010**, *132*, 6596.

(231) Jiang, D.; Walter, M. *Phys. Rev. B* **2011**, *84*, 38.

(232) Frenkel, A. I.; Nemzer, S.; Pister, I.; Soussan, L.; Harris, T.; Sun, Y.; Rafailovich, M. H. *J. Chem. Phys.* **2005**, *123*, 184701.

(233) Macdonald, M. A.; Zhang, P.; Chen, N.; Qian, H.; Jin, R. *J. Phys. Chem. C* **2011**, *115*, 65.

(234) Wu, Z.; Suhan, J.; Jin, R. *J. Mater. Chem.* **2009**, *19*, 622.

(235) Zanchet, D.; Tolentino, H.; Martins Alves, M.; Alves, O.; Ugarte, D. *Chem. Phys. Lett.* **2000**, *323*, 167.

(236) Lopez-Acevedo, O.; Akola, J.; Whetten, R. L.; Gronbeck, H.; Häkkinen, H. *J. Phys. Chem. C* **2009**, *113*, 5035.

(237) Taylor, K. J.; Jin, C.; Conceicao, J.; Wang, L.-S.; Cheshnovsky, O.; Johnson, B. R.; Nordlander, P. J.; Smalley, R. E. *J. Chem. Phys.* **1990**, *93*, 7515.

(238) Zeng, C.; Liu, C.; Pei, Y.; Jin, R. *ACS Nano* **2013**, *7*, 6138.

(239) Zeng, C.; Li, T.; Das, A.; Rosi, N. L.; Jin, R. *J. Am. Chem. Soc.* **2013**, *135*, 10011.

(240) Li, W.-H.; Wu, S.; Yang, C.; Lai, S.; Lee, K.; Huang, H. L.; Yang, H. D. *Phys. Rev. Lett.* **2002**, *89*, 135504.

(241) Comaschi, T.; Balerna, a.; Mobilio, S. *Phys. Rev. B* **2008**, *77*, 75432.

(242) Zhang, P.; Sham, T. *Phys. Rev. Lett.* **2003**, *90*, 245502.

(243) Chevrier, D. M.; Macdonald, M. A.; Chatt, A.; Zhang, P.; Wu, Z.; Jin, R. *J. Phys. Chem. C* **2012**, *116*, 25137.

(244) Zeng, C.; Chen, Y.; Li, G.; Jin, R. *Chem. Commun. (Camb).* **2014**, *50*, 55.

(245) Crasto, D.; Malola, S.; Brosofsky, G.; Dass, A.; Häkkinen, H. *J. Am. Chem. Soc.* **2014**, *136*, 5000.

(246) Jiang, D.; Whetten, R. L.; Luo, W.; Dai, S. *J. Phys. Chem. C* **2009**, *113*, 17291.

(247) Pei, Y.; Lin, S.; Su, J.; Liu, C. *J. Am. Chem. Soc.* **2013**, *135*, 19060.

(248) Knoppe, S.; Malola, S.; Lehtovaara, L.; Bürgi, T.; Häkkinen, H. *J. Phys. Chem. A* **2013**, *117*, 10526.

(249) Song, Y.; Wang, S.; Zhang, J.; Kang, X.; Chen, S.; Li, P.; Sheng, H.; Zhu, M. *J. Am. Chem. Soc.* **2014**, *24*, 5.

(250) Häkkinen, H.; Walter, M.; Gronbeck, H. *J. Phys. Chem. B* **2006**, *110*, 9927.

(251) Chevrier, D. M.; Chatt, A.; Zhang, P.; Zeng, C.; Jin, R. *J. Phys. Chem. Lett.* **2013**, *36*, 3186.

(252) Yee, C. K.; Ulman, A.; Ruiz, J. D.; Parikh, A.; White, H.; Rafailovich, M. *Langmuir* **2003**, *19*, 9450.

(253) Zelakiewicz, B. S.; Yonezawa, T.; Tong, Y. *J. Am. Chem. Soc.* **2004**, *126*, 8112.

(254) Li, Y.; Zaluzhna, O.; Xu, B.; Gao, Y.; Modest, J. M.; Tong, Y. J. *J. Am. Chem. Soc.* **2011**, *133*, 2092.

(255) Negishi, Y.; Kurashige, W.; Kamimura, U. *Langmuir* **2011**, *27*, 12289.

(256) Kurashige, W.; Yamaguchi, M.; Nobusada, K.; Negishi, Y. *J. Phys. Chem. Lett.* **2012**, *3*, 2649.

(257) Kurashige, W.; Munakata, K.; Nobusada, K.; Negishi, Y. *Chem. Commun. (Camb).* **2013**, *49*, 5447.

(258) Xu, Q.; Wang, S.; Liu, Z.; Xu, G.; Meng, X.; Zhu, M. *Nanoscale* **2013**, *5*, 1176.

(259) Kurashige, W.; Yamazoe, S.; Kanehira, K.; Tsukuda, T.; Negishi, Y. *J. Phys. Chem. Lett.* **2013**, *4*, 3181.

(260) Kresse, G.; Furthmüller, J. *Phys. Rev. B. Condens. Matter* **1996**, *54*, 11169.

(261) Perdew, J.; Burke, K.; Ernzerhof, M. *Phys. Rev. Lett.* **1996**, *77*, 3865.

(262) Blöchl, P. *Phys. Rev. B* **1994**, *50*, 17953.

(263) Marsh, R. E. *Acta Crystallogr.* **1952**, *5*, 458.

(264) Schmidbaur, H. *Gold Bull.* **2000**, *33*, 3.

(265) Goodwin, A. L.; Calleja, M.; Conterio, M. J.; Dove, M. T.; Evans, J. S. O.; Keen, D. A.; Peters, L.; Tucker, M. G. *Science* **2008**, *319*, 794.

(266) Korcok, J. L.; Katz, M. J.; Leznoff, D. B. *J. Am. Chem. Soc.* **2009**, *131*, 4866.

(267) Bachman, R. E.; Fioritto, M. S.; Fetics, S. K.; Cocker, T. M. *J. Am. Chem. Soc.* **2001**, *123*, 5376.

(268) Häberlen, O. D.; Chung, S.-C.; Stener, M.; Rösch, N. *J. Chem. Phys.* **1997**, *106*, 5189.

(269) Fernández, E.; Soler, J.; Garzón, I.; Balbás, L. *Phys. Rev. B* **2004**, *70*, 165403.

(270) Sanchez, S. I.; Menard, L. D.; Bram, A.; Kang, J. H.; Small, M. W.; Nuzzo, R. G.; Frenkel, A. I. *J. Am. Chem. Soc.* **2009**, *131*, 7040.

(271) Shibu, E. S.; Habeeb Muhammed, M. A.; Tsukuda, T.; Pradeep, T. *J. Phys. Chem. C* **2008**, *112*, 12168.

(272) Tlahuice-Flores, A.; Whetten, R. L.; Jose-Yacaman, M. *J. Phys. Chem. C* **2013**, *117*, 20867.

(273) Yu, Y.; Chen, X.; Yao, Q.; Yu, Y.; Yan, N.; Xie, J. *Chem. Mater.* **2013**, *25*, 946.

(274) Ghosh, A.; Udayabhaskararao, T.; Pradeep, T. *J. Phys. Chem. Lett.* **2012**, *3*, 1997.

(275) Pyo, K.; Thanthirige, V. D.; Kwak, K.; Pandurangan, P.; Ramakrishna, G.; Lee, D. *J. Am. Chem. Soc.* **2015**, *137*, 8244.

(276) Das, A.; Liu, C.; Byun, H. Y.; Nobusada, K.; Zhao, S.; Rosi, N.; Jin, R. *Angew. Chem.* **2015**, *54*, 3140.

(277) Rojas-Cervellera, V.; Rovira, C.; Akola, J. *J. Phys. Chem. Lett.* **2015**, *25*, 3859.

(278) Car, R.; Parrinello, M. *Phys. Rev. Lett.* **1985**, *55*, 2471.

(279) Goedecker, S.; Teter, M.; Hutter, J. *Phys. Rev. B* **1996**, *54*, 1703.

(280) Hartwigsen, C.; Goedecker, S.; Hutter, J. *Phys. Rev. B* **1998**, *58*, 3641.

(281) Troullier, N.; Martins, J. L. *Phys. Rev. B* **1991**, *43*, 8861.

(282) Krüger, D.; Fuchs, H.; Rousseau, R.; Marx, D.; Parrinello, M. *J. Chem. Phys.* **2001**, *115*, 4776.

(283) Phillips, J. C.; Braun, R.; Wang, W.; Gumbart, J.; Tajkhorshid, E.; Villa, E.; Chipot, C.; Skeel, R. D.; Kalé, L.; Schulten, K. *J. Comput. Chem.* **2005**, *26*, 1781.

(284) Zhang, Y. K.; Lee, T. S.; Yang, W. T. *J. Chem. Phys.* **1999**, *110*, 46.

(285) Laio, A.; VandeVondele, J.; Rothlisberger, U. *J. Chem. Phys.* **2002**, *116*, 6941.

(286) Chen, S.; Wang, S.; Zhong, J.; Song, Y.; Zhang, J.; Sheng, H.; Pei, Y. *Angew. Chemie Int. Ed.* **2015**, *54*, 1.

(287) Kurashige, W.; Yamazoe, S.; Yamaguchi, M.; Nishido, K.; Nobusada, K.; Tsukuda, T.; Negishi, Y. *J. Phys. Chem. Lett.* **2014**, *5*, 2072.

(288) Forward, J. M.; Bohmann, D.; Fackler, J. P.; Staples, R. J. *Inorg. Chem.* **1996**, *34*, 6330.

(289) Cha, S.; Kim, J.; Kim, K.; Lee, J. *Chem. Mater.* **2007**, *19*, 6297.

(290) Yam, V. W.; Lo, K. K. *Chem. Soc. Rev.* **1999**, *28*, 323.

(291) Li, Z. Y.; Young, N. P.; Di Vece, M.; Palomba, S.; Palmer, R. E.; Bleloch, A. L.; Curley, B. C.; Johnston, R. L.; Jiang, J.; Yuan, J. *Nature* **2008**, *451*, 46.

(292) Chen, S.; Ingram, R.; Hostetler, M.; Pietron, J.; Murray, R.; Schaaff, T.; Khoury, J.; Alvarez, M.; Whetten, R. *Science* **1998**, *280*, 2098.

(293) Azubel, M.; Koivisto, J.; Malola, S.; Bushnell, D.; Hura, G. L.; Koh, A. L.; Tsunoyama, H.; Tsukuda, T.; Pettersson, M.; Hakkinen, H.; Kornberg, R. D. *Science* **2014**, *345*, 909.

(294) Shankar, S. S.; Rai, A.; Ankamwar, B.; Singh, A.; Ahmad, A.; Sastry, M. *Nat. Mater.* **2004**, *3*, 482.

(295) Sarikaya, M.; Tamerler, C.; Jen, A. K.; Schulten, K.; Baneyx, F. *Nat. Mater.* **2003**, *2*, 577.

(296) Wei, H.; Wang, Z.; Zhang, J.; House, S.; Gao, Y. G.; Yang, L.; Robinson, H.; Tan, L. H.; Xing, H.; Hou, C.; Robertson, I. M.; Zuo, J.; Lu, Y. *Nat. Nanotechnol.* **2011**, *6*, 93.

(297) Xavier, P. L.; Chaudhari, K.; Verma, P. K.; Pal, S. K.; Pradeep, T. *Nanoscale* **2010**, *2*, 2769.

(298) Stern, E. A. *Phys. Rev. B* **1993**, *48*, 9825.

(299) Arbeloa, F. L.; Ojeda, P. R.; Arbeloa, I. L. *J. Lumin.* **1989**, *44*, 105.

(300) Vydrov, O. A.; Scuseria, G. E. *J. Chem. Phys.* **2006**, *125*, 234109.

(301) Vydrov, O. A.; Heyd, J.; Krukau, A.; Scuseria, G. E. *J. Chem. Phys.* **2006**, *125*, 74106.

(302) Vydrov, O. A.; Scuseria, G. E.; Perdew, J. P. *J. Chem. Phys.* **2007**, *126*, 154109.

(303) Becke, A. D.; Johnson, E. R. *J. Chem. Phys.* **2007**, *127*, 154108.

(304) Otero-de-la Rozza, A.; Johnson, E. R. *J. Chem. Phys.* **2013**, *138*, 204109.

(305) Couty, M.; Hall, M. B. *J. Comput. Chem.* **1996**, *17*, 1359.

(306) Peterson, K. A.; Puzzarini, C. *Theor. Chem. Acc.* **2005**, *114*, 283.

(307) Dunning, J. T. H. *J. Chem. Phys.* **1989**, *90*, 1007.

(308) Woon, D. E.; Dunning, J. T. H. *J. Chem. Phys.* **1993**, *98*, 1358.

(309) Otero-De-La-Roza, A.; Mallory, J. D.; Johnson, E. R. *J. Chem. Phys.* **2014**, *140*, 18A504.

(310) Frisch, M. J.; Trucks, G. W.; Schlegel, H. B.; Scuseria, G. E.; Robb, M. A.; Cheeseman, J. R.; Scalmani, G.; Barone, V.; Mennucci, B.; Petersson, G. A.; Nakatsuji, H.; Caricato, M.; Li, X.; Hratchian, H. P.; Izmaylov, A. F.; Bloino, J.; Zheng, G.; Sonnenberg, J. L.; Hada, M.; Ehara, M.; Toyota, K.; Fukuda, R.; Hasegawa, J.; Ishida, M.; Nakajima, T.; Honda, Y.; Kitao, O.; Nakai, H.; Vreven, T.; Montgomery, J. A.; Peralta, J. E.; Ogliaro, F.; Bearpark, M.; Heyd, J. J.; Brothers, E.; Kudin, K. N.; Staroverov, V. N.; Kobayashi, R.; Normand, J.; Raghavachari, K.; Rendell, A.; Burant, J. C.; Iyengar, S. S.; Tomasi, J.; Cossi, M.; Rega, N.; Millam, J. M.; Klene, M.; Knox, J. E.; Cross, J. B.; Bakken, V.; Adamo, C.; Jaramillo, J.; Gomperts, R.; Stratmann, R. E.; Yazyev, O.; Austin, A. J.; Cammi, R.; Pomelli, C.; Ochterski, J. W.; Martin, R. L.; Morokuma, K.; Zakrzewski, V. G.; Voth, G. A.; Salvador, P.; Dannenberg, J. J.; Dapprich, S.; Daniels, A. D.; Farkas; Foresman, J. B.; Ortiz, J. V; Cioslowski, J.; Fox, D. J. *Gaussian 09, Revision E.01, Gaussian, Inc., Wallingford CT*. 2013,.

(311) Schuchardt, K. L.; Didier, B. T.; Elsethagen, T.; Sun, L.; Gurumoorthi, V.; Chase, J.; Li, J.; Windus, T. L. *J. Chem. Inf. Model.* **2007**, *47*, 1045.

(312) Wiseman, M. R.; Marsh, P. A.; Bishop, P. T.; Brisdon, B. J.; Mahon, M. F. *J. Am. Chem. Soc.* **2000**, *122*, 12598.

(313) Simpson, C. A.; Farrow, C. L.; Tian, P.; Billinge, S. J. L.; Huffman, B. J.; Harkness, K. M.; Cliffel, D. E. *Inorg. Chem.* **2010**, *49*, 10858.

(314) LeBlanc, D. J.; Lock, C. J. L. *Acta Crystallogr. Sect. C Cryst. Struct. Commun.* **1997**, *53*, 1765.

(315) Bau, R. *J. Am. Chem. Soc.* **1998**, *7863*, 9380.

(316) Chui, S. S.-Y.; Chen, R.; Che, C.-M. *Angew. Chemie Int. Ed.* **2006**, *45*, 1621.

(317) Cha, S.; Kim, J.; Kim, K.; Lee, J. *Chem. Mater.* **2007**, *19*, 6297.

(318) Yam, V. W.-W.; Chan, C.-L.; Li, C.-K.; Wong, K. M.-C. *Coord. Chem. Rev.* **2001**, *216–217*, 173.

(319) Dou, X.; Yuan, X.; Yu, Y.; Luo, Z.; Yao, Q.; Leong, D. T.; Xie, J. *Nanoscale*

2014, *6*, 157.

(320) Negishi, Y.; Tsukuda, T. *Chem. Phys. Lett.* **2004**, *383*, 161.

(321) Kumar, S.; Bolan, M. D.; Bigioni, T. P. *J. Am. Chem. Soc.* **2010**, *132*, 13141.

(322) He, S.; Yao, J.; Jiang, P.; Shi, D.; Zhang, H.; Xie, S.; Pang, S.; Gao, H. *Langmuir* **2001**, *17*, 1571.

(323) Standridge, S. D.; Schatz, G. C.; Hupp, J. T.; Standridge, S. D.; Schatz, G. C.; Hupp, J. T. *Langmuir* **2009**, *25*, 2596.

(324) Conn, B. E.; Desireddy, A.; Atnagulov, A.; Wickramasinghe, S.; Bhattarai, B.; Yoon, B.; Barnett, R. N.; Abdollahian, Y.; Kim, Y. W.; Griffith, W. P.; Oliver, S. R. J.; Landman, U.; Bigioni, T. P. *J. Phys. Chem. C* **2015**, *119*, 11238.

(325) Urushizaki, M.; Kitazawa, H.; Takano, S.; Takahata, R.; Yamazoe, S.; Tsukuda, T. *J. Phys. Chem. C* **2015**, *119*, 27483.

(326) Yoon, B.; Luedtke, W. D.; Barnett, R. N.; Gao, J.; Desireddy, A.; Conn, B. E.; Bigioni, T.; Landman, U. *Nat. Mater.* **2014**, *13*, 807.

(327) Ahn, B. Y.; Duoss, E. B.; Motala, M. J.; Guo, X.; Park, S.-I.; Xiong, Y.; Yoon, J.; Nuzzo, R. G.; Rogers, J. A.; Lewis, J. A. *Science (80-.).* **2009**, *323*, 1590.

(328) Ding, I.-K.; Zhu, J.; Cai, W.; Moon, S.-J.; Cai, N.; Wang, P.; Zakeeruddin, S. M.; Grätzel, M.; Brongersma, M. L.; Cui, Y.; McGehee, M. D. *Adv. Energy Mater.* **2011**, *1*, 52.

(329) Standridge, S. D.; Schatz, G. C.; Hupp, J. T. *J. Am. Chem. Soc.* **2009**, *131*, 8407.

(330) Guo, J.; Kumar, S.; Bolan, M.; Desireddy, A.; Bigioni, T. P.; Gri, W. P. *Anal. Chem.* **2012**, *84*, 5304.

(331) Padmos, J. D.; Boudreau, R. T. M.; Weaver, D. F.; Zhang, P. *J. Phys. Chem. C* **2015**, *119*, 24627.

(332) Zeng, C.; Chen, Y.; Iida, K.; Nobusada, K.; Kirschbaum, K.; Lambright, K. J.; Jin, R. *J. Am. Chem. Soc.* **2016**, jacs. 5b12747.

(333) Ohyama, J.; Teramura, K.; Higuchi, Y.; Shishido, T.; Hitomi, Y.; Kato, K.; Tanida, H.; Uruga, T.; Tanaka, T. *ChemPhysChem* **2011**, *12*, 127.

Appendix A - Supporting Information for Chapter 8

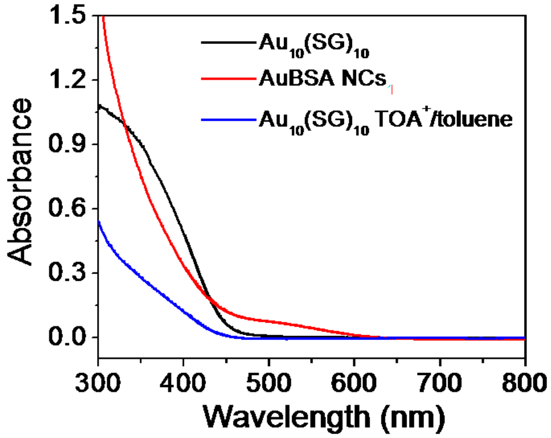

Figure A.1 UV-Vis absorption of AuBSA NCs, $Au_{10}(SG)_{10}$ and $Au_{10}(SG)_{10}$ after phase-transfer with TOA^+/toluene (TOA^+-$Au_{10}(SG)_{10}$ clusters were ~3X less concentrated than original $Au_{10}(SG)_{10}$ at the time of measurement).

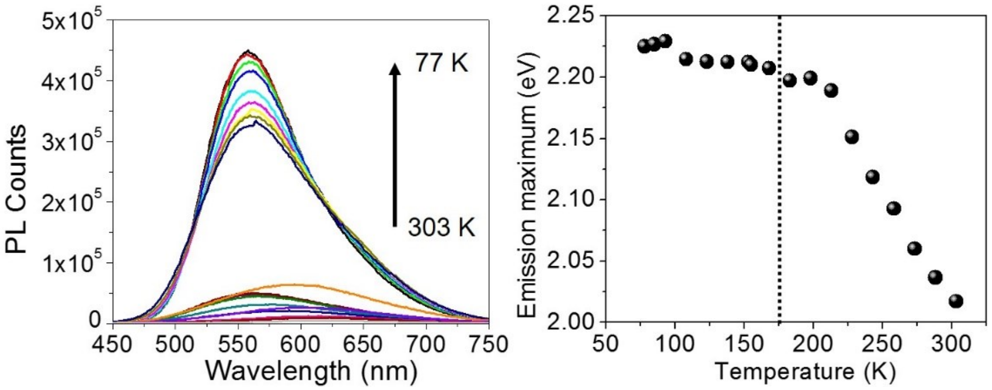

Figure A.2 Temperature dependent photoluminescence of $Au_{10}(SG)_{10}$ NCs in water/glycerol mixture. Temperature-dependent emission maximum energy and emission yield for $Au_{10}(SG)_{10}$ NCs in water/glycerol mixture.

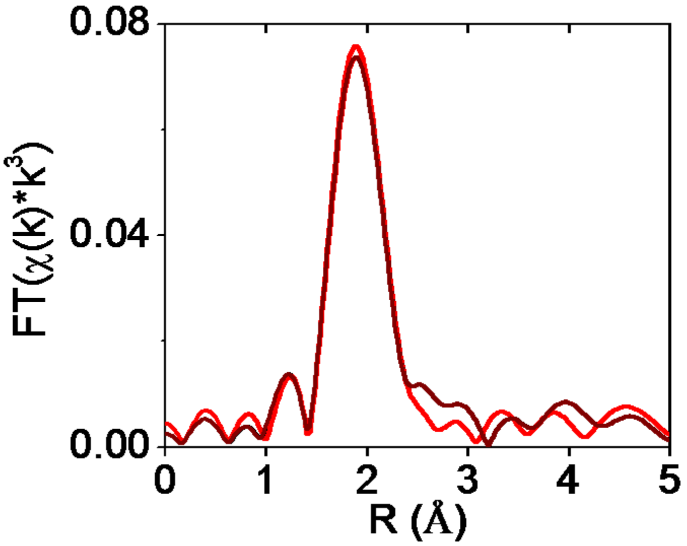

Figure A.3 **Au L₃-edge EXAFS of original AuBSA NCs (red line) and after trypsin digestion (maroon line).**

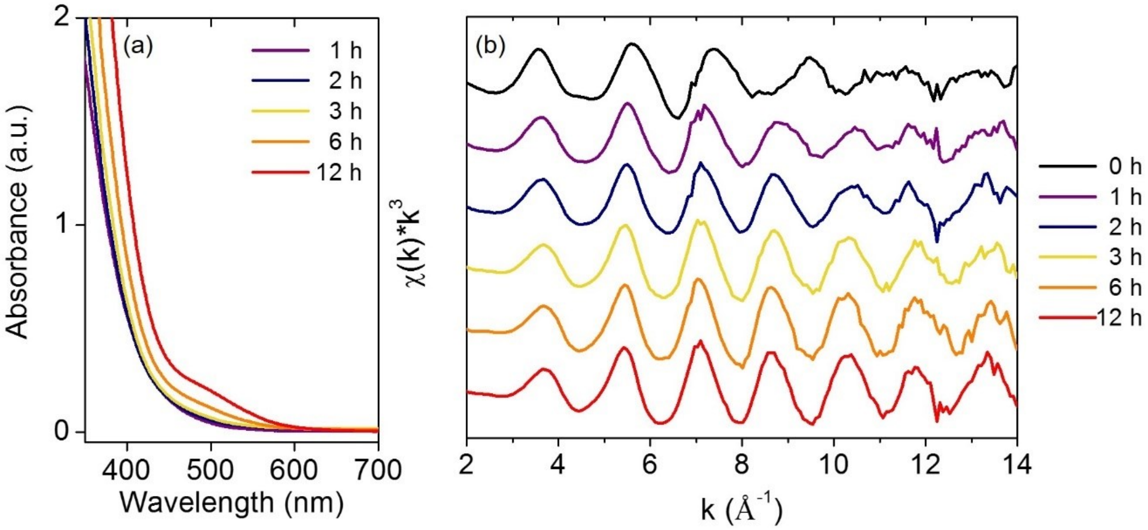

Figure A.4 **(a) UV-Vis absorbance spectra following the synthesis of AuBSA NCs and (b) Au L₃-edge** ***k*****-space spectra of time-dependent AuBSA NC samples.**

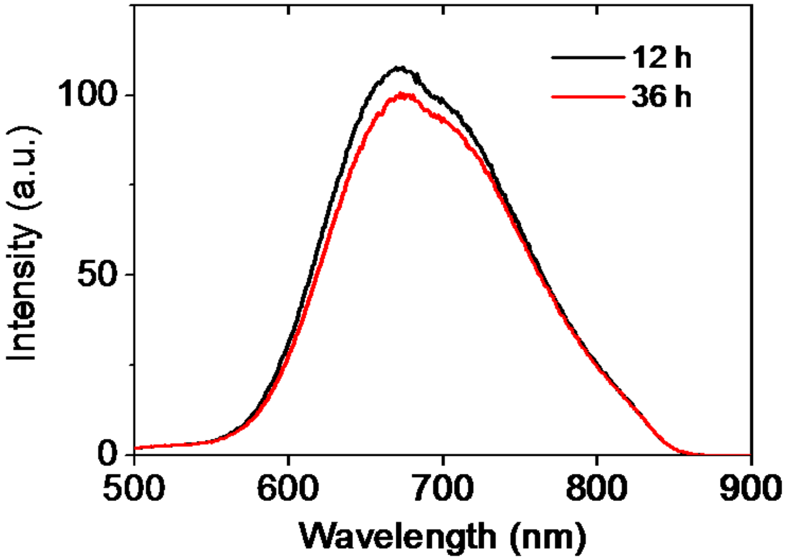

Figure A.5 Photoluminescence of AuBSA NCs at 12 and 36 h from excitation at 470 nm.

Table A.1 EXAFS refinement results for the time-dependent study of AuBSA NC formation. Values not reported "-" were unobtainable due to fitting constraints or the absence of that scattering path. Uncertainties in fitted parameters are shown in parentheses.

	Parameters	0 h	1 h	2 h	3 h	6 h	12 h	36 h
Au-O	CN	2.8(2)	0.9(2)	0.6(4)	-	-	-	
	R (Å)	2.02(1)	2.04(2)	2.0(1)	-	-	-	
	σ^2 (Å^2)	0.0059(6)	0.002(2)	0.006(5)	-	-	-	
	ΔE_0 (eV)	6(1)	5(4)	2(3)	-	-	-	
Au-S	CN	-	1.1(1)	1.4(2)	2.3(1)	2.2(1)	2.2(1)	2.16(8)
	R (Å)	-	2.31(1)	2.31(2)	2.31(1)	2.323(5)	2.321(8)	2.321(2)
	σ^2 (Å^2)	-	0.003(1)	0.003(2)	0.0046(5)	0.0039(3)	0.0036(3)	0.0036(3)
	ΔE_0 (eV)	-	4(2)	2(3)	2(1)	1.7(4)	1.1(3)	0.9(4)
Au-Au	CN	-	-	-	2(1)	1.3(8)	0.8(5)	0.9(5)
	R (Å)	-	-	-	3.02(2)	3.03(2)	3.02(2)	3.02(1)
	σ^2 (Å^2)	-	-	-	0.018(6)	0.015(5)	0.011(4)	0.012(4)
	ΔE_0 (eV)	-	-	-	2(1)	1.7(4)	1.1(3)	0.9(4)

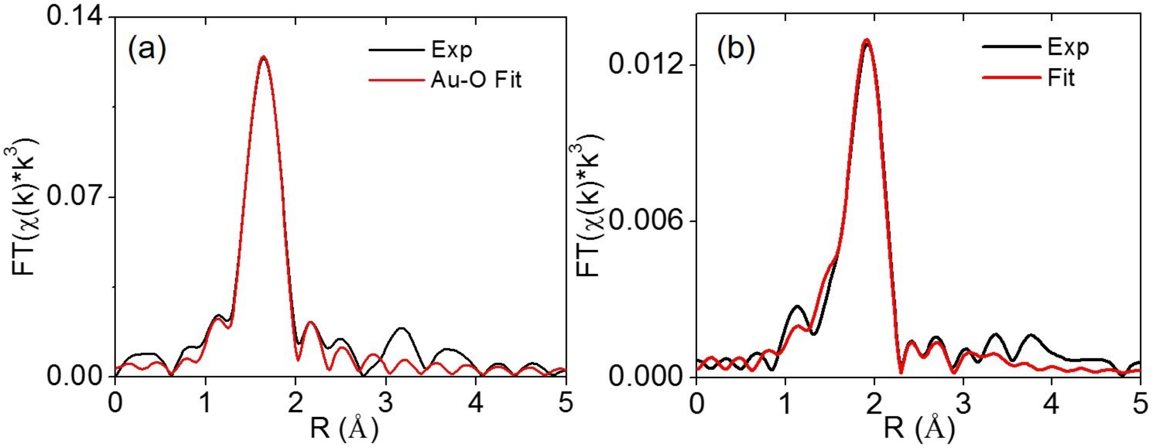

Figure A.6 (a) Au L$_3$-edge EXAFS of Au(OH)$_3$ reference material with fitted Au-O scattering shell. From fit, CN = 3.4(3), R = 2.005(4) Å, σ^2= 0.0015(6) Å^2, E_0 shift = 6.4(7) eV. (b) Au L$_3$-edge EXAFS and two-shell fit of AuBSA NCs at 36 h.

Table A.2 Formation energy DFT calculations for the conversion of AuCl$_3$ to Au(OH)$_3$.

<table>
<tr><td colspan="2">$AuCl_3 + 3OH^- \rightarrow Au(OH)_3 + 3Cl^-$</td></tr>
<tr><td>Individual Reaction Steps</td><td>(Products - Reactants) Total energy (SCF+XDM) /eV</td></tr>
<tr><td>$AuCl_3 + OH^- \rightarrow AuCl_2OH + Cl^-$</td><td>-1.96 eV</td></tr>
<tr><td>$AuCl_2OH + OH^- \rightarrow AuCl(OH)_2 + Cl^-$</td><td>-1.86 eV</td></tr>
<tr><td>$AuCl(OH)_2 + OH^- \rightarrow Au(OH)_3 + Cl^-$</td><td>-1.82 eV</td></tr>
</table>

Table A.3 Formation energy DFT calculations for the conversion of $AuCl_4^-$ to $Au(OH)_4^-$.

<table>
<tr><td colspan="2">$AuCl_4^- + 4OH^- \rightarrow Au(OH)_4^- + 4Cl^-$</td></tr>
<tr><td>Individual Reaction Steps</td><td>(Products - Reactants) Total energy (SCF+XDM) /eV</td></tr>
<tr><td>$AuCl_4^- + OH^- \rightarrow AuCl_3OH^- + Cl^-$</td><td>-1.75 eV</td></tr>
<tr><td>$AuCl_3OH^- + OH^- \rightarrow$ *cis*-$AuCl_2(OH)_2^- + Cl^-$
$AuCl_3OH^- + OH^- \rightarrow$ *trans*-$AuCl_2(OH)_2^- + Cl^-$</td><td>-1.73 eV
-1.69 eV</td></tr>
<tr><td>*cis*-$AuCl2(OH)_2^-$ + OH- $\rightarrow AuCl(OH)_3^- + Cl^-$
trans-$AuCl2(OH)_2^-$ + OH- $\rightarrow AuCl(OH)_3^- + Cl^-$</td><td>-1.64 eV
-1.67 eV</td></tr>
<tr><td>$AuCl(OH)_3^- + OH^- \rightarrow Au(OH)_4^- + Cl^-$</td><td>-1.40 eV</td></tr>
</table>

Table A.4 Formation energy DFT calculations for the conversion of $AuCl_3$ and $Au(OH)_3$ to their anionic complex form.

Reaction	(Products - Reactants) Total energy (SCF+XDM) /eV
$Au(OH)_3 + OH^- > Au(OH)_4^-$	-4.60 eV
$AuCl_3 + Cl^- \rightarrow AuCl_4^-$	-3.73 eV

Appendix B - Copyright Agreement for Chapter 3

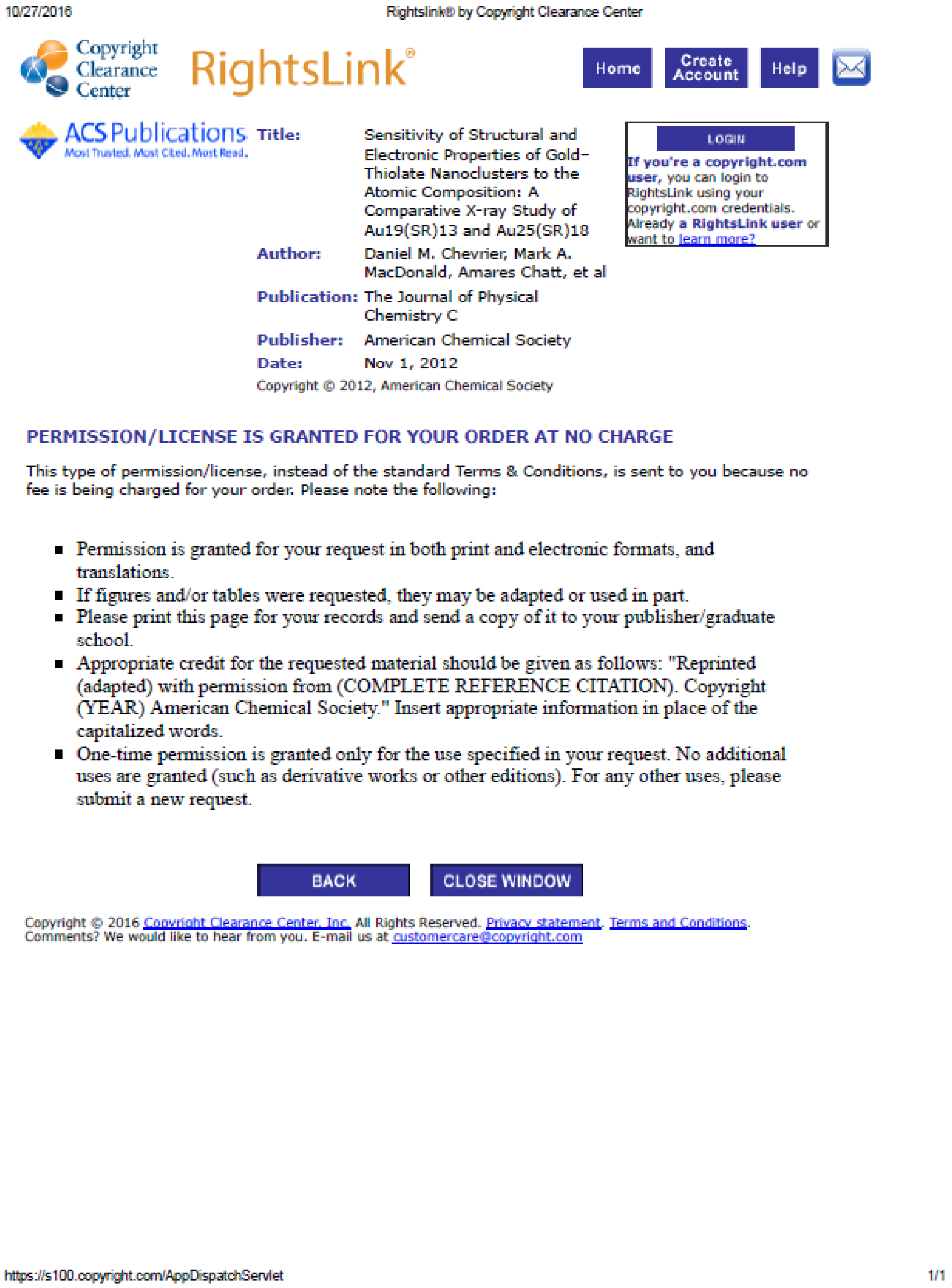

10/27/2016 Rightslink® by Copyright Clearance Center

Title:	Sensitivity of Structural and Electronic Properties of Gold–Thiolate Nanoclusters to the Atomic Composition: A Comparative X-ray Study of Au19(SR)13 and Au25(SR)18
Author:	Daniel M. Chevrier, Mark A. MacDonald, Amares Chatt, et al
Publication:	The Journal of Physical Chemistry C
Publisher:	American Chemical Society
Date:	Nov 1, 2012

Copyright © 2012, American Chemical Society

If you're a copyright.com user, you can login to RightsLink using your copyright.com credentials. Already **a RightsLink user** or want to learn more?

PERMISSION/LICENSE IS GRANTED FOR YOUR ORDER AT NO CHARGE

This type of permission/license, instead of the standard Terms & Conditions, is sent to you because no fee is being charged for your order. Please note the following:

- Permission is granted for your request in both print and electronic formats, and translations.
- If figures and/or tables were requested, they may be adapted or used in part.
- Please print this page for your records and send a copy of it to your publisher/graduate school.
- Appropriate credit for the requested material should be given as follows: "Reprinted (adapted) with permission from (COMPLETE REFERENCE CITATION). Copyright (YEAR) American Chemical Society." Insert appropriate information in place of the capitalized words.
- One-time permission is granted only for the use specified in your request. No additional uses are granted (such as derivative works or other editions). For any other uses, please submit a new request.

Copyright © 2016 Copyright Clearance Center, Inc. All Rights Reserved. Privacy statement. Terms and Conditions.
Comments? We would like to hear from you. E-mail us at customercare@copyright.com

https://s100.copyright.com/AppDispatchServlet 1/1

Appendix C - Copyright Agreement for Chapter 4

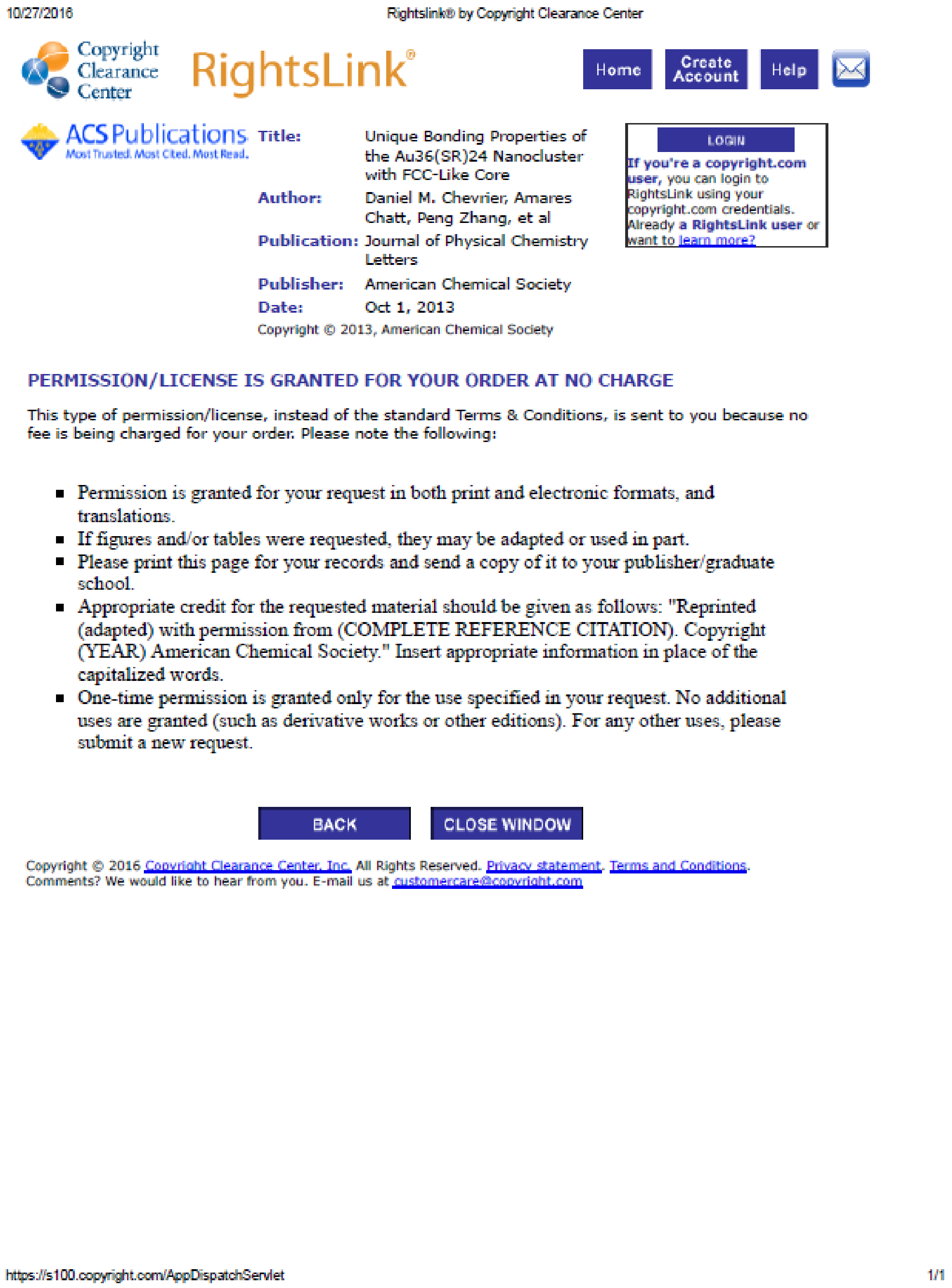

10/27/2016 Rightslink® by Copyright Clearance Center

Title:	Unique Bonding Properties of the Au36(SR)24 Nanocluster with FCC-Like Core
Author:	Daniel M. Chevrier, Amares Chatt, Peng Zhang, et al
Publication:	Journal of Physical Chemistry Letters
Publisher:	American Chemical Society
Date:	Oct 1, 2013

Copyright © 2013, American Chemical Society

If you're a copyright.com user, you can login to RightsLink using your copyright.com credentials. Already **a RightsLink user** or want to learn more?

PERMISSION/LICENSE IS GRANTED FOR YOUR ORDER AT NO CHARGE

This type of permission/license, instead of the standard Terms & Conditions, is sent to you because no fee is being charged for your order. Please note the following:

- Permission is granted for your request in both print and electronic formats, and translations.
- If figures and/or tables were requested, they may be adapted or used in part.
- Please print this page for your records and send a copy of it to your publisher/graduate school.
- Appropriate credit for the requested material should be given as follows: "Reprinted (adapted) with permission from (COMPLETE REFERENCE CITATION). Copyright (YEAR) American Chemical Society." Insert appropriate information in place of the capitalized words.
- One-time permission is granted only for the use specified in your request. No additional uses are granted (such as derivative works or other editions). For any other uses, please submit a new request.

Copyright © 2016 Copyright Clearance Center, Inc. All Rights Reserved. Privacy statement. Terms and Conditions.
Comments? We would like to hear from you. E-mail us at customercare@copyright.com

https://s100.copyright.com/AppDispatchServlet 1/1

Appendix D - Copyright Agreement for Chapter 5

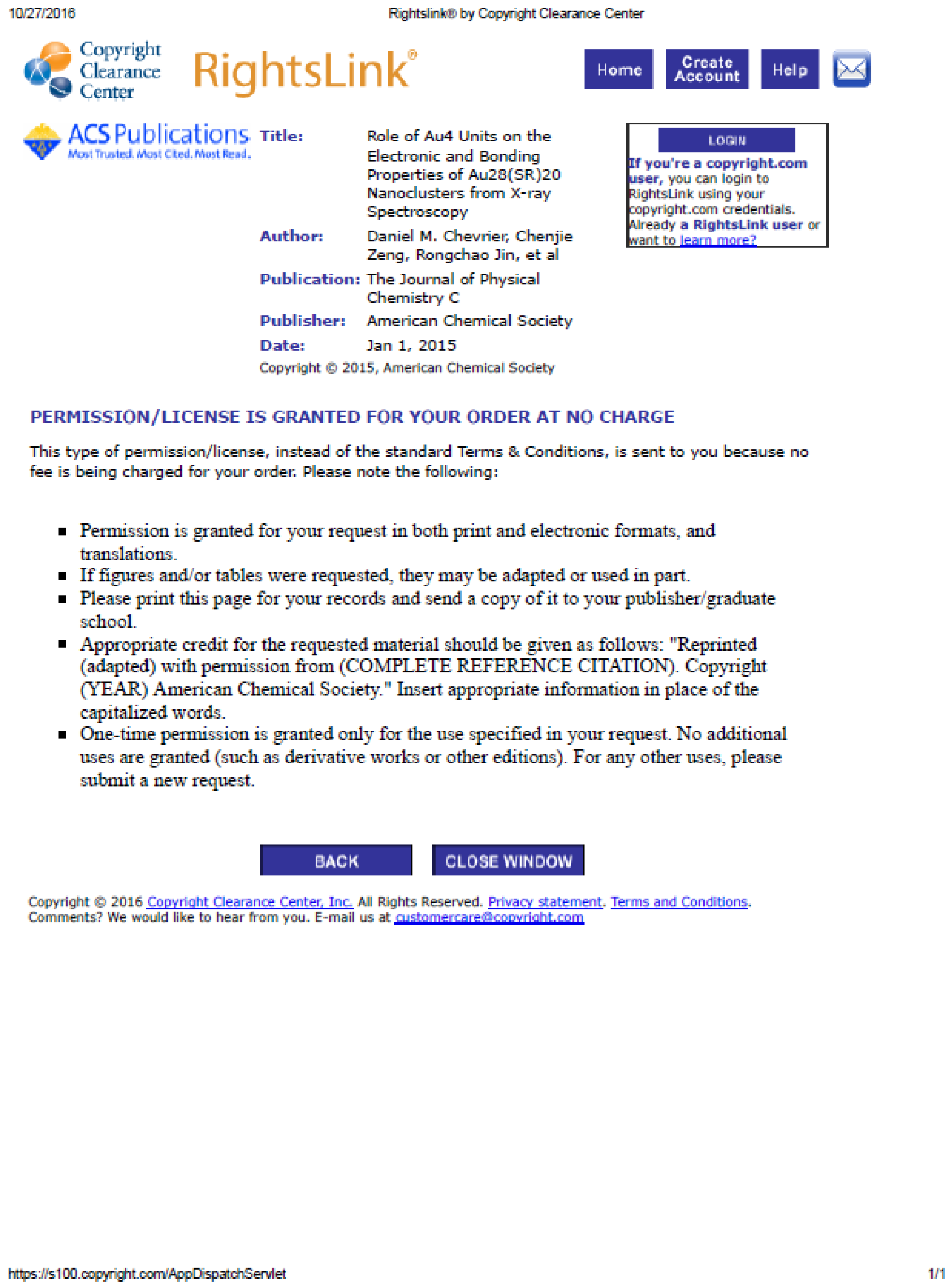

10/27/2016 Rightslink® by Copyright Clearance Center

Title:	Role of Au4 Units on the Electronic and Bonding Properties of Au28(SR)20 Nanoclusters from X-ray Spectroscopy
Author:	Daniel M. Chevrier, Chenjie Zeng, Rongchao Jin, et al
Publication:	The Journal of Physical Chemistry C
Publisher:	American Chemical Society
Date:	Jan 1, 2015

Copyright © 2015, American Chemical Society

If you're a copyright.com user, you can login to RightsLink using your copyright.com credentials. Already **a RightsLink user** or want to learn more?

PERMISSION/LICENSE IS GRANTED FOR YOUR ORDER AT NO CHARGE

This type of permission/license, instead of the standard Terms & Conditions, is sent to you because no fee is being charged for your order. Please note the following:

- Permission is granted for your request in both print and electronic formats, and translations.
- If figures and/or tables were requested, they may be adapted or used in part.
- Please print this page for your records and send a copy of it to your publisher/graduate school.
- Appropriate credit for the requested material should be given as follows: "Reprinted (adapted) with permission from (COMPLETE REFERENCE CITATION). Copyright (YEAR) American Chemical Society." Insert appropriate information in place of the capitalized words.
- One-time permission is granted only for the use specified in your request. No additional uses are granted (such as derivative works or other editions). For any other uses, please submit a new request.

Copyright © 2016 Copyright Clearance Center, Inc. All Rights Reserved. Privacy statement. Terms and Conditions.
Comments? We would like to hear from you. E-mail us at customercare@copyright.com

https://s100.copyright.com/AppDispatchServlet 1/1

Appendix E - Copyright Agreement for Chapter 6

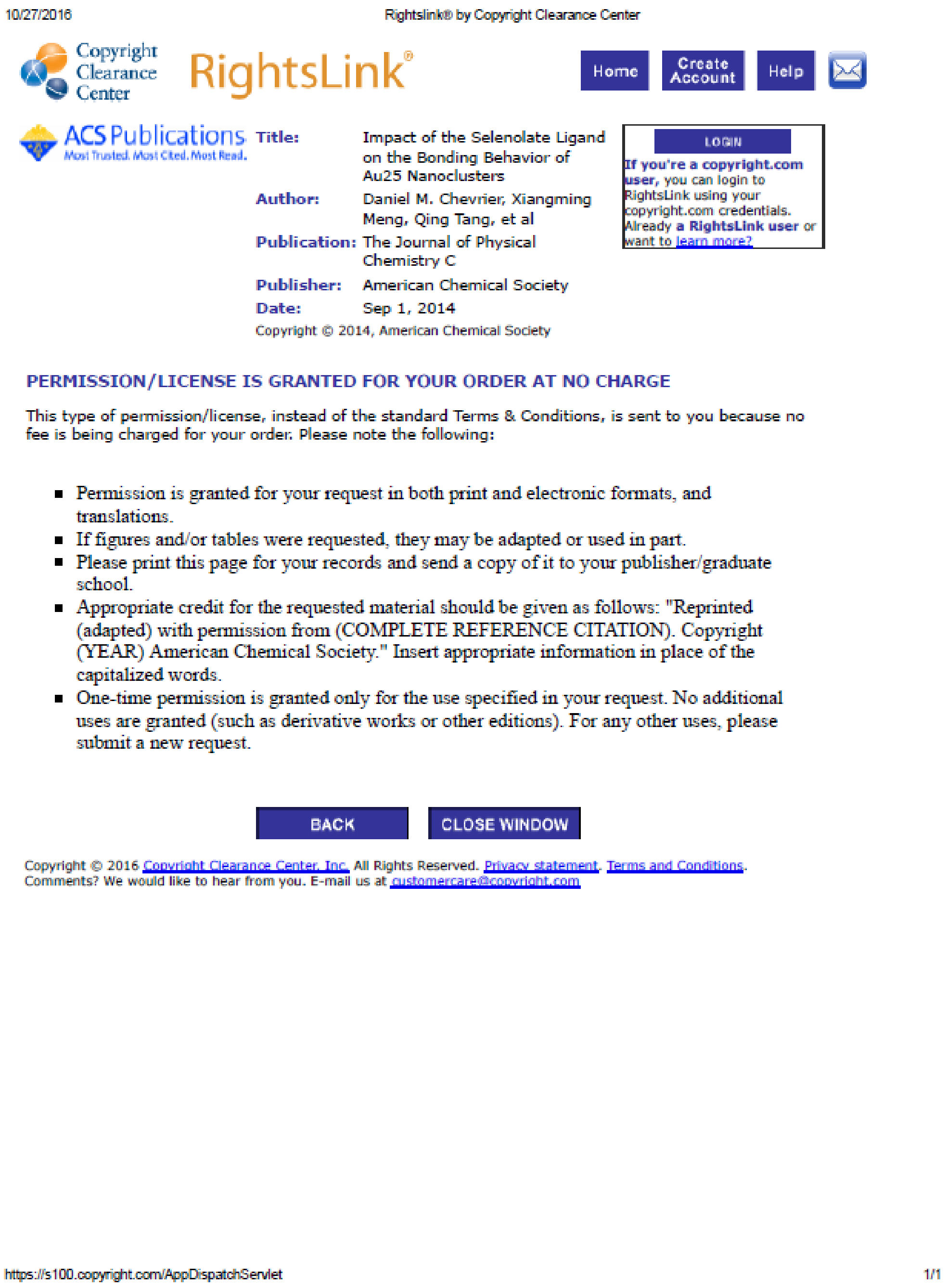

10/27/2016 Rightslink® by Copyright Clearance Center

Title: Impact of the Selenolate Ligand on the Bonding Behavior of Au25 Nanoclusters

Author: Daniel M. Chevrier, Xiangming Meng, Qing Tang, et al

Publication: The Journal of Physical Chemistry C

Publisher: American Chemical Society

Date: Sep 1, 2014

Copyright © 2014, American Chemical Society

If you're a copyright.com user, you can login to RightsLink using your copyright.com credentials. Already **a RightsLink user** or want to learn more?

PERMISSION/LICENSE IS GRANTED FOR YOUR ORDER AT NO CHARGE

This type of permission/license, instead of the standard Terms & Conditions, is sent to you because no fee is being charged for your order. Please note the following:

- Permission is granted for your request in both print and electronic formats, and translations.
- If figures and/or tables were requested, they may be adapted or used in part.
- Please print this page for your records and send a copy of it to your publisher/graduate school.
- Appropriate credit for the requested material should be given as follows: "Reprinted (adapted) with permission from (COMPLETE REFERENCE CITATION). Copyright (YEAR) American Chemical Society." Insert appropriate information in place of the capitalized words.
- One-time permission is granted only for the use specified in your request. No additional uses are granted (such as derivative works or other editions). For any other uses, please submit a new request.

Copyright © 2016 Copyright Clearance Center, Inc. All Rights Reserved. Privacy statement. Terms and Conditions.
Comments? We would like to hear from you. E-mail us at customercare@copyright.com

https://s100.copyright.com/AppDispatchServlet 1/1